TESIS DE DOCTORADO EN CIENCIAS BIOLÓGICAS

PEDECIBA BIOLOGÍA - Sub-área BIOLOGÍA CELULAR Y MOLECULAR

Aptámero Sgc8-c como sonda para imagenología y terapia en cáncer

Lic. Estefanía Sicco

Directores de tesis: Dr. Hugo Cerecetto, Dra. María Moreno y Dra. Victoria Calzada

Área de Radiofarmacia, Centro de Investigaciones Nucleares, Facultad de Ciencias y Departamento de Desarrollo Biotecnológico, Instituto de Higiene, Facultad de Medicina, Universidad de la República. Montevideo, Uruguay

- 2023 -

Tabla de contenido

1. Resumen

Los aptámeros son oligonucleótidos de cadena sencilla (ADN o ARN) que reconocen su diana con alta especificidad y afinidad, teniendo propiedades equiparables a las de los anticuerpos. Sin embargo, por su composición no proteica presentan ventajas significativas en cuanto a su tamaño, producción y modificación, además, no generan inmunogenicidad o efectos tóxicos. Estas características los hacen excelentes candidatos para el desarrollo de nuevas plataformas biotecnológicas, para su aplicación como agentes de imagen o terapia.

El aptámero truncado Sgc8-c es de ADN (41 bases) y fue modificado previamente por este grupo de trabajo agregándole, en el extremo 5', un grupo aminohexilo. Sgc8-c reconoce específicamente y con alta afinidad al receptor PTK7 (K_d=0,78 nM). Este receptor, que actúa como co-receptor en varias vías celulares, es un biomarcador tumoral que se sobreexpresa en diferentes tipos de leucemia, tumores gástricos, cánceres de colon, pulmón, mama y próstata, e incluso en metástasis.

Durante este posgrado, en el capítulo I de esta tesis se describe la evaluación de la marcación de Sgc8-c como agente de imagenología molecular en cáncer, generando una sonda fluorescente y otra portadora de un radionucleido emisor gamma. Para ello, se realizaron modificaciones químicas en el extremo 5´ del aptámero incorporando:

(I) un fragmento estructural derivado del fluoróforo Alexa Fluor™ 647 (**Sgc8-c-Alexa647**), lo que permitió hacer estudios de imagen óptica en la región del infrarrojo cercano, logrando un contraste óptimo, debido a que las moléculas presentes en los tejidos no exhiben importante absorción en esa región espectral;

(II) un fragmento estructural derivado de ácido 1,4,7-triazaciclononano-1,4,7-triacético, lo que permitió la coordinación con el radionucleido emisor gamma galio-67 (**Sgc8-c-NOTA-⁶⁷Ga**) para poder realizar imágenes gamma con una mayor penetración en el tejido y mejorando la capacidad de medir las señales con alta sensibilidad, adquiriendo imágenes cuantitativas de todo el cuerpo.

Se evaluaron condiciones de reacción y purificación, y posteriormente se realizó la caracterización fisicoquímica, así como la verificación del reconocimiento por su receptor, mediante ensayos en diferentes líneas celulares tumorales. Para la evaluación biológica, se estudiaron las características farmacocinéticas, se adquirieron imágenes *in vivo* y *ex vivo* con ambas sondas y se evaluó su biodistribución, en diferentes modelos de ratones

portadores de tumor, siendo la primera vez que estas sondas son ensayada en un modelo de melanoma metastásico. Estos estudios indican que ambas sondas reconocen con alta especificidad su blanco y, junto con la rápida depuración en sangre, resultan en una captación con excelente relación tumor/no-tumor.

Los resultados previos, junto con otros descriptos por nuestro grupo, proporcionaron las bases para el desarrollo del capítulo II de esta tesis, donde se evaluó la capacidad del aptámero Sgc8-c para dirigir fármacos al sitio de acción. Para ello, se desarrollaron conjugados aptámero-fármaco para terapia a través de la incorporación covalente de una subestructura derivada del fármaco dasatinib en el extremo 5´ del aptámero Sgc8-c. Así, se estudiaron diferentes condiciones de reacción variando el disolvente, el tiempo, la temperatura, la fuente de calor, el pH y los contraiones. El conjugado aptámero-fármaco, **Sgc8-c-carb-da**, se caracterizó fisicoquímicamente y se evaluó su capacidad de liberar dasatinib a distintos pH. Por último, se realizó una evaluación biológica *in vitro* en un modelo de linfoma, proporcionando una prueba de concepto del valor terapéutico de **Sgc8-c-carb-da**.

En conjunto, los resultados de este trabajo con el aptámero Sgc8-c abren las puertas al desarrollo de herramientas biotecnológicas versátiles con aplicación en biomedicina.

Palabras clave: Aptámero, Cáncer, Imagenología Molecular, Terapia, Sondas imagenológicas, Conjugados aptámero-fármaco, Entrega activa

2. Introducción y Antecedentes

2.1. Aspectos generales del cáncer

El cáncer es la segunda causa de muerte entre enfermedades no transmisibles, siendo responsable de más de 9 millones de defunciones anuales a nivel mundial (Globocan, 2020; Sung, 2020). Una de cada cinco personas en todo el mundo desarrolla cáncer durante su vida (Globocan, 2020; Sung, 2020). En Latinoamérica, Uruguay es el país que presenta las tasas de incidencia y mortalidad más altas por cáncer (Globocan, 2020; Garau, 2022). Según la *International Agency for Research on Cancer*, la tasa de incidencia estimada estandarizada por edad para el año 2020 fue de 269,3 cada 100.000 personas al año para todos los tipos de cáncer, en ambos sexos (Globocan, 2020; Ferlay, 2021).

En el período analizado entre los años 2015 y 2019 por el *Registro Nacional De Cáncer* se describió que en el sexo femenino los tipos de cáncer con mayor incidencia fueron de mama (75,33 cada 100.000 mujeres), colo-recto (25,17), pulmón (14,87), cuello uterino (14,35) y tiroides (12,50). Mientras que los tipos de cáncer más frecuentes en el sexo masculino fueron de próstata (58,78 cada 100.000 hombres), pulmón (45,69), colo-recto (37,05), vejiga (16,97) y riñón (18,57) (Figura 1) (CHLCC, 2020; Garau 2022).
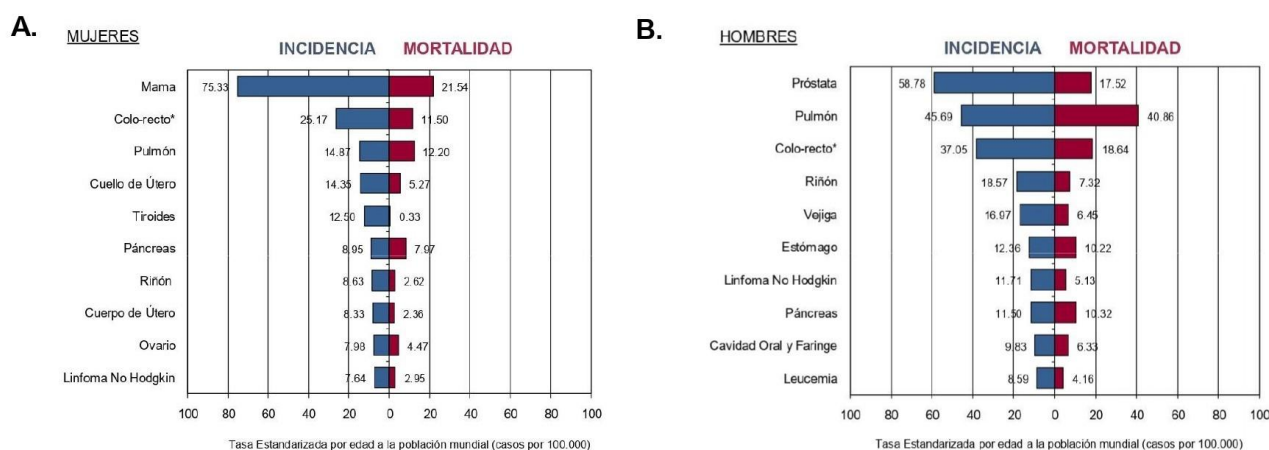
Figura 1. Incidencia del cáncer en Uruguay entre los años 2015 y 2019. Principales sitios de Incidencia con su respectiva Mortalidad en Mujeres **A**. y Hombres **B**. (*) La categoría colo-recto involucra los códigos C18-C20 de la CIE-O 3ª Ed. IARC-OMS (colon, recto sigmoidea y recto). Extraída y adaptada de CHLCC, 2020.

El cáncer se considera una enfermedad de etiología multifactorial, que posee la potencialidad de afectar a cualquier célula del organismo (Alberts, 2004; PDQ, 2023). Dentro de los factores involucrados se encuentran los genéticos, hormonales, problemas inmunitarios, la edad y los factores ambientales o externos, como la exposición a agentes infecciosos, a diferentes fuentes de radiación y al estilo de vida, como el tabaquismo y una mala alimentación (PDQ, 2023). Dichos factores pueden interactuar ejerciendo su acción en conjunto o en serie, y afectar las funciones de las células, incidiendo principalmente en su división y crecimiento (Islami, 2021). Esto puede derivar en la proliferación celular incontrolada, lo que conduce a la formación de agregados celulares que crecen y terminan originando o promoviendo el desarrollo del cáncer (Islami, 2021; PDQ, 2023). Además, estas células tumorales pueden migrar e invadir tejidos circundantes o distantes, continuando con su crecimiento y originar metástasis (Michor, 2004; Islami, 2021).

Entre los diversos rasgos que caracterizan a las células tumorales se encuentran las alteraciones fenotípicas de las células que van a determinar cambios morfológicos y funcionales (Baba, 2007; Hanahan, 2011). A nivel funcional se pueden encontrar los siguientes cambios: evasión de los factores supresores del crecimiento y mantenimiento de la señalización proliferativa; evasión del sistema inmunológico; promoción de la inmortalidad replicativa; resistencia a la muerte celular; desregularización del metabolismo celular; inducción de la angiogénesis y activación de la invasión y la metástasis; inestabilización y mutación del genoma; inflamación promotora de tumores (Hanahan, 2011; Sanchez, 2013). A nivel morfológico se puede encontrar la sobreexpresión de moléculas a nivel de la superficie celular, u otros compartimientos celulares o promover la situación opuesta, entre otras (Sanchez, 2013). En el 2022 Hanahan describió nuevos parámetros para incorporarse como componentes centrales de las características distintivas de la conceptualización del cáncer. Estos son: plasticidad fenotípica; reprogramación epigenética no mutacional; microbiomas polimórficos y senescencia celular (Hanahan, 2022).

Es fundamental identificar los mecanismos de estímulo y proliferación celular, con el fin de crear estrategias específicamente dirigidas contra dianas celulares que participan en estos procesos (Pinheiro, 2021). Asimismo, el análisis de los genes, proteínas y microambiente que caracteriza a los tumores, otorga información específica para la búsqueda de biomarcadores tumorales y la identificación de potenciales blancos

terapéuticos (Sanchez, 2013; Pinheiro, 2021). Mediante estrategias de detección precoz de tumores se han reducido las tasas de mortalidad de todos los tipos de cáncer (Globocan, 2020; Ferlay, 2021). En este sentido, se ha demostrado que el factor pronóstico más eficaz está relacionado con la extensión de la enfermedad al momento del diagnóstico (Klein, 2020; Pinheiro, 2021). Es por ello que las investigaciones adquieren gran relevancia al buscar optimizar los métodos de diagnóstico, así como los tratamientos existentes, e incorporar el desarrollo de nuevas estrategias y enfoques.

2.2 Aptámeros

2.2.1. Características de los aptámeros

Los aptámeros han ganado una posición destacada en el campo de la biotecnología. El nombre en sí, que deriva de una combinación de la palabra latina *aptus*, que significa "ajustar a", y el término griego *meros*, que significa "partícula"; sugiere fuertemente la versatilidad de estos compuestos (González, 2016).

Los aptámeros son oligonucleótidos monocatenarios pequeños, de ácido desoxirribonucleico (ADNss) o de ácido ribonucleico (ARN), de entre 20 y 100 bases de largo. Presentan una estructura tridimensional única y estable, caracterizada por bucles, tallos, u horquillas. Se unen a blancos moleculares selectivamente, con alta afinidad y especificidad mediante enlaces no-covalentes. Los aptámeros interaccionan con el ligando, principalmente, a través de las fuerzas electrostáticas y motivos conformacionales. Participan en la unión fuerzas de van der Waals, interacciones de carga y enlaces de hidrógeno. La estructura tridimensional que presentan los aptámeros favorece una mayor interacción, formando complejos fuertes a través de ajustes conformacionales (Musumeci, 2017; Calzada, 2020). La unión del blanco con el aptámero se ve afectada por la complementariedad de conformación espacial; por lo tanto, investigar estructuras tridimensionales de interacciones aptámero/blanco, a nivel atómico y molecular, pueden ayudar al descubrimiento de fármacos basado en estas estructuras (Reinemann, 2014).

Los aptámeros son capaces de unirse a moléculas que no son ácidos nucleicos, como moléculas orgánicas e inorgánicas, iones metálicos, péptidos, proteínas, diversos

componentes celulares, toxinas, bacterias, e incluso se pueden unir a blancos no inmunogénicos contra los que es difícil generar anticuerpos de alta afinidad y especificidad (Smith, 2018; Calzada, 2020; García Melián, 2023).

Los aptámeros son seleccionados a partir de bibliotecas masivas mediante el proceso *in vitro* denominado Evolución Sistemática de Ligandos por Enriquecimiento Exponencial (SELEX) (Ellington, 1990; Tuerk, 1990). Este proceso utiliza una biblioteca de secuencias de ácidos nucleicos (> 10^{15} oligonucleótidos aleatorios). Estas secuencias son incubadas con un blanco molecular de interés, y las secuencias que presenten reconocimiento con el blanco, son aisladas y amplificadas por PCR o RT-PCR, y el pool enriquecido es expuesto nuevamente a una nueva ronda de selección. Por lo general, se realizan entre 6 y 10 rondas de selección. Luego de la selección, se realiza una secuenciación y un análisis informático exhaustivo y finalmente, las secuencias seleccionadas son sintetizadas químicamente y caracterizadas individualmente, evaluando su afinidad por el blanco (González, 2016; Calzada 2020). En suma, SELEX es una técnica que, por sus características, permite obtener aptámeros con la selectividad por su blanco y valores de constante de disociación (K_d) deseables (Kinghorn, 2017; Calzada, 2020).

Sin embargo, la técnica de SELEX se ha ido perfeccionando para que el procedimiento de selección sea aún más eficiente. Dentro de sus variantes se encuentra Cell-SELEX, que agrega células como blanco de interés (Figura 2). En contraste con los otros enfoques, Cell-SELEX elige un aptámero enfrentándolo a toda la célula, esto asegura que los blancos moleculares en la membrana celular estén en su estado natural y representen su estructura de plegamiento normal. Por lo que, Cell-SELEX permite seleccionar aptámeros con un gran potencial de selectividad por su blanco, identificar nuevos blancos presentes en líneas celulares tumorales, y también, distinguir entre *"molecular signatures"* de varios tipos de células sin conocimiento previo de sus propiedades moleculares (Kaur, 2018; Li, 2021).
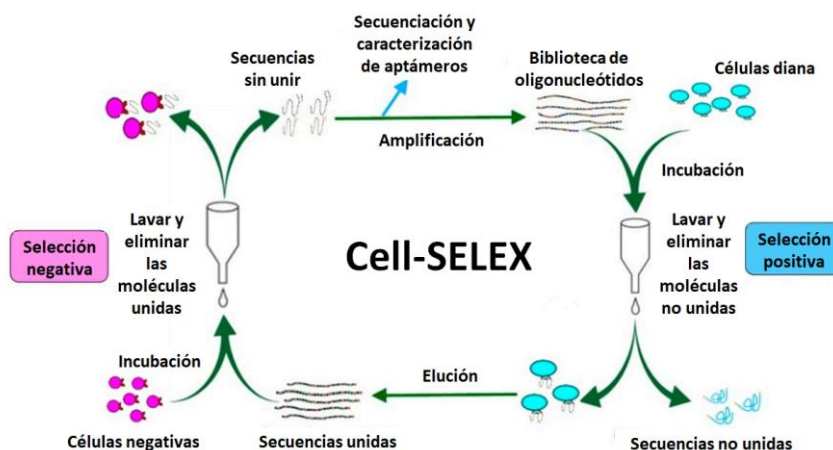
Figura 2. Representación esquemática de la selección de aptámeros utilizando la técnica Cell-SELEX. Extraída de Chen, 2016.

Luego de ser seleccionados y sintetizados, los aptámeros puedes ser modificados post-SELEX con el objetivo de mejorar sus características intrínsecas (Gao, 2016). Los aptámeros pueden lograr afinidades por su blanco similares a las que presentan los anticuerpos, pero con varias ventajas (Tabla 1) (Zhang, 2019; Calzada 2020). Entre estas se destacan el bajo peso molecular de los aptámeros entre 8 a 15 kDa, lo que mejora la absorción tisular y la internalización celular, y también la depuración sanguínea (Zhang, 2019). Las metodologías de síntesis química son rápidas, reproducibles y robustas, obteniendo un producto que es estable en amplio rango de pH y temperatura. Los productos además tienen escasa toxicidad y no presentan inmunogenicidad como los anticuerpos. Esto último, brinda un perfil de seguridad biológica para los enfoques farmacéuticos (Bouchard, 2010; Lui, 2017; Calzada, 2020).

Los aptámeros permiten ser fácilmente modificados químicamente sin afectar el reconocimiento por su blanco, para incorporar funcionalidades, incrementar su estabilidad biológica y diversificar sus aplicaciones clínicas. Las modificaciones químicas se pueden generar a nivel de los fosfatos, en los extremos 3' y 5' terminal, en las ribosas y en las bases nitrogenadas, incorporando grupos funcionales de interés. Esto asegura y facilita la conjugación específica con una amplia variedad de biomateriales (Famulok, 2011; Calzada, 2017a; Calzada, 2017b; Adachi, 2019; Odeh, 2020). Las principales desventajas de los aptámeros son la degradación por la acción de las nucleasas, lo cual genera mayor filtración renal y menor vida media en plasma. Sin embargo, los aptámeros cuentan con una estabilidad intrínseca, mayor a la esperada para un oligonucleótido convencional, pero

además las modificaciones químicas también pueden mejorar enormemente esta característica. Por ejemplo, para aumentar el tiempo de circulación en sangre es posible acoplarlos a otras moléculas como fragmentos derivados de polietilenglicol (PEG), nanopartículas, fragmentos derivados de biotina, lo que aumenta su masa molecular (Tabla 1) (Haruta, 2017).

Las ventajas que presentan los aptámeros garantizan biodisponibilidad e integridad química en condiciones fisiológicas (Adachi, 2019; Calzada 2020). Asimismo, los convierte en moléculas versátiles para un amplio rango de aplicaciones: cuantificación de la expresión de un blanco tumoral a través de biosensores, terapia, diagnóstico e imagenología molecular (Famulok, 2011; Zhang, 2019; Calzada 2020).

Tabla 1. Ventajas y desventajas de los aptámeros. Extraída y adaptada de Ospina, 2020.

|	
No requieren modelos biológicos para su producción	Su desarrollo apenas comienza
Tiempo de producción breve (1 a 3 meses)	Farmacocinética variable
Fácil de escalar	Proclives a filtración renal
Pueden modificarse químicamente para evitar degradación	Corta vida media
Largo tiempo de almacenamiento a temperatura ambiente	
Se unen a una amplia variedad de blancos inmunógenos y no inmunógenos	Los aptámeros no modificados químicamente se degradan fácilmente en el plasma
Menor tamaño para acceder a tejidos o células (12-15 kDa)	
Bajo costo de producción	
La síntesis química disminuye la variabilidad entre lotes	
La secuencia de nucleótidos se almacena para posteriores producciones	
Especificidad y afinidad iguales o mejores que las de los anticuerpos monoclonales	

2.2.2. Sgc8-c: aptámero de estudio

El grupo de investigación de Shangguan y colaboradores desarrollaron un panel de aptámeros de ADNss, que llamaron aptámeros Sgc, para el reconocimiento específico en células T de leucemia linfoblástica aguda (T-ALL), mediante la técnica de selección Cell-SELEX. En ese proceso, una biblioteca de ADNss que contenía regiones de secuencias aleatorias, se incubó con la línea celular CCRF-CEM (células diana).

Entre las secuencias identificadas, Sgc8, un aptámero de 88 bases, mostró unirse con alta especificidad y afinidad a un blanco en la superficie celular presente en células de T-ALL, presentando una K_d de 0,80 ± 0,09 nM (Figura 3) (Shangguan, 2006; Shangguan, 2007).

Este mismo grupo de trabajo continuó profundizando en la caracterización del aptámero Sgc8, e identificó que el blanco molecular selectivo es la proteína transmembrana tirosina quinasa 7 (PTK7). Este receptor se sobreexpresa en la línea celular CCRF-CEM (T-ALL) que utilizaron para su selección (Shangguan, 2008) y en varios tipos de tumores (Xiao, 2008). Además, comprobaron que Sgc8 se internaliza mediante endocitosis al igual que el anticuerpo anti-PTK7, luego de la unión a la proteína, siendo una interacción receptor-dependiente (Xiao, 2008). Sin embargo, también evidenciaron que el anticuerpo anti-PTK7 no competía con el aptámero Sgc8 (Shangguan, 2008), esto se debe a que la unión a PTK7 sucede en diferentes sitios de reconocimiento. La distancia entre los sitios de unión del aptámero Sgc8 y el anticuerpo en la proteína de membrana PTK7 de las células CCRF-CEM, en el entorno fisiológico natural, es de 13,4 ± 1,4 nm (Chen, 2010a).

Durante el análisis de la estructura del aptámero Sgc8 para estudiar el reconocimiento por su blanco, se realizaron modificaciones en la secuencia de Sgc8. Se encontró que la secuencia truncada, Sgc8-c, de 41 bases y con una estructura de tallo-bucle, presenta una K_d igual a 0,78 nM por PTK7 (Figura 3). De todas las secuencias analizadas, Sgc8-c presenta características muy similares al aptámero original, por lo que la secuencia de Sgc8-c es la mínima requerida para la óptima unión al blanco (Shangguan, 2007).
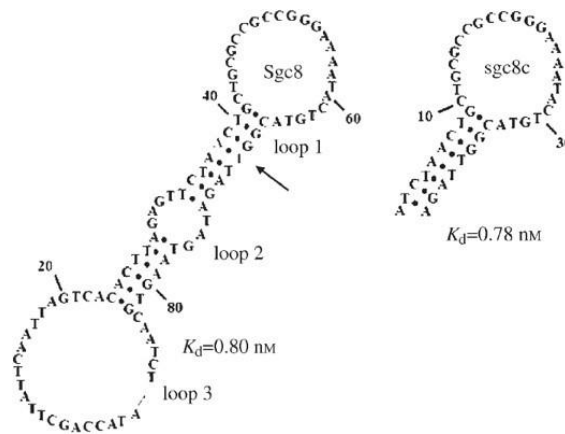
Figura 3. Estructura de los aptámeros Sgc8 (izquierda) y Sgc8-c (derecha), con sus K_d para PTK7. Extraída y adaptada de Shangguan, 2007.

Debido a su especificidad de unión por el PTK7, Sgc8-c es una biomolécula de reconocimiento de gran interés en el campo de la imagenología molecular para el desarrollo de nuevos agentes imagenológicos. Por su naturaleza química y tamaño molecular, así como los fundamentados antecedentes, fue el aptámero de elección para explorar nuevas posibilidades. Para realizar la marcación del aptámero y generar nuevas sondas imagenológicas, nuestro grupo de trabajo modificó el extremo 5' del Sgc8-c, donde se incorporó una cadena alifática de 6 carbonos y un grupo amino libre para sus posteriores conjugaciones (Figura 4). Este aptámero, de aquí en más llamado Sgc8-c-NH_2, presenta una masa molecular de 13 kDa (Calzada, 2017a).


Figura 4. Estructura representativa del aptámero Sgc8-c-NH_2.

2.2.3.PTK7: blanco molecular de Sgc8-c

Los receptores de tirosina quinasa (RTK) son receptores transmembrana y constituyen el mayor grupo de receptores que presentan un rol fundamental en las vías de señalización celular, en diversos procesos biológicos durante el desarrollo y la vida adulta (Grassot, 2006). Los RTK generalmente son proteínas grandes que contienen entre 800 y 1600 aminoácidos y están compuestos por tres dominios. Un dominio *N*-terminal en la región extracelular altamente variable y responsable de la unión y especificidad por el ligando. Un dominio transmembrana único y un dominio tirosina quinasa intracelular altamente conservado en el extremo *C*-terminal, que se une y fosforila al sustrato, siendo el responsable de la actividad catalítica (Grassot, 2006; Sun, 2014). Estos receptores son activados por la unión al ligando, produciendo la dimerización del receptor, lo que genera una cascada de señales a nivel intracelular, que da como resultado numerosos cambios celulares involucrados en la regulación de procesos celulares, incluyendo el ciclo celular, proliferación, metabolismo, diferenciación, migración y la comunicación célula-célula (Regad, 2015; Butti, 2018). Los RTK se subdividen en varias familias en función de la similitud del dominio tirosina quinasa, del dominio extracelular o su organización génica (Chen, 2015). Dentro de las 20 subfamilias se encuentra la proteína tirosina quinasa 7 (PTK7) (Lapraz, 2006; Butti, 2018), siendo el blanco molecular del aptámero que se ha evaluado en esta tesis.

Los transcriptos que codifican la proteína PTK7 se identificó inicialmente en el ARNm de melanocitos y posteriormente, en carcinoma de colon, por esto también es denominada como quinasa-4 de carcinoma de colon (CCK4) (Peradziryi, 2012). PTK7 es una pseudoquinasa de membrana, que contiene 1070 aminoácidos y su masa molecular es de 118,5 kDa (Jung, 2002). Está constituida por siete dominios extracelulares similares inmunoglobulinas, una región transmembrana y yuxtamembrana y un dominio *C*-terminal catalíticamente inactivo con homología con la familia de tirosina quinasas (Figura 5) (Murphy, 2014). En humanos, se han identificado cinco isoformas de PTK7 en testículos, que se generan por *"splicing"* alternativo (Jung, 2002).
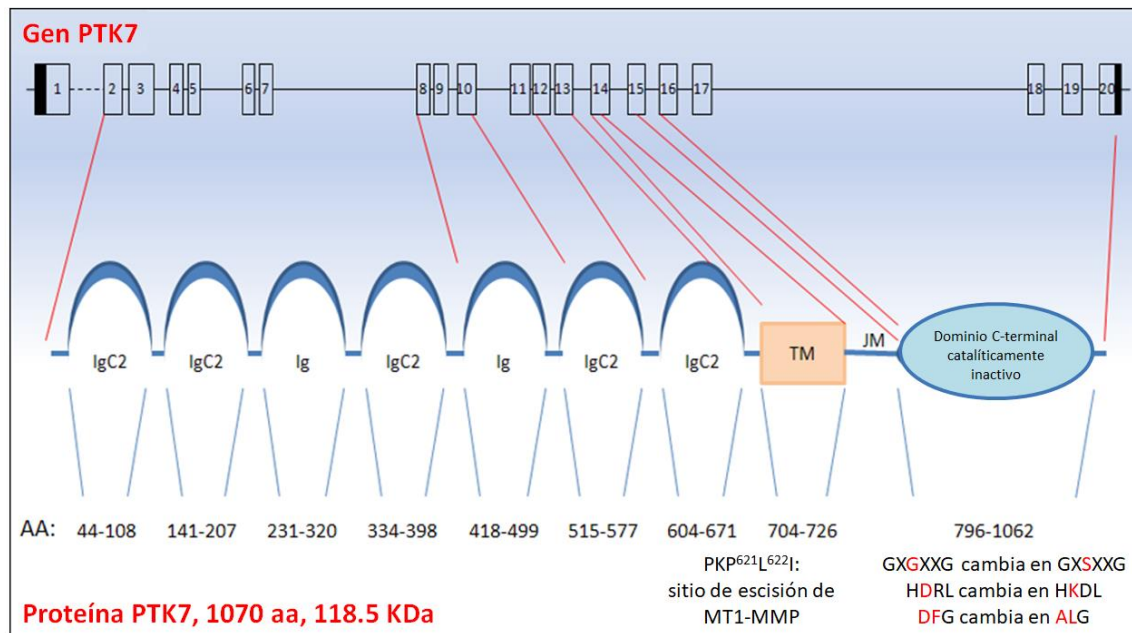
Figura 5. Estructura y organización de PTK7. Gen PTK7, donde cada cuadro representa un exón; y proteína PTK7 donde se observa las tres regiones y el sitio de proteólisis mediada por MT1-MMP. Ig: dominio inmunoglobulina.TM: dominio transmembrana. JM: yuxtamembrana. Extraída de Lhoumeau, 2012.

A pesar de que aún no se ha identificado ningún ligando específico y que no presenta actividad quinasa, PTK7 regula diversas actividades celulares como la polaridad celular planar, la motilidad celular polarizada, la morfogénesis y la migración celular, que son esenciales en la sobrevida de los organismos (Lin, 2012; Xu, 2016). PTK7 participa en señales de polaridad celular involucrando la vía de señalización Wingless (Wnt), regula las vías Wnt canónicas y no canónicas, principalmente en el desarrollo embrionario (Peradziryi, 2012). Se ha descrito que ocurre proteólisis en el dominio extracelular de PTK7 mediado por la metaloproteinasa de matriz tipo 1 (MT1-MMP) (Figura 5), afectando la polaridad planar celular y la migración celular (Lichtig, 2019).

En humanos, se ha descripto la sobreexpresión de PTK7 en distintos tipos de cáncer, incluidos cáncer de colon (Mossie, 1995), adenocarcinoma pulmonar (Endoh, 2004), cáncer gástrico (Gorringe, 2005), cáncer de mama (Ataseven, 2014), leucemia mieloide aguda (Jiang, 2012), linfoma (Calzada, 2017a), carcinoma de células escamosas de esófago (Shin, 2013), cáncer de próstata (Zhang, 2014), colangiocarcinoma intrahepático (Jin, 2014), células de glioma (Liu, 2015), melanoma (Easty, 1997, Calzada, 2017a) e incluso en metástasis (Dong, 2017).

En células tumorales, PTK7 regula la migración e invasión endotelial (Shin, 2008). PTK7 puede heterodimerizar con el receptor 1 del factor de crecimiento endotelial vascular (VEGFR1) y favorecido por VEGF-A, consigue promover la migración e invasión en células y formación de tubos durante la angiogénesis (Lee, 2011). También se ha encontrado que en un grupo de células progenitoras mieloides, PTK7 induce señales promigratorias y antiapoptóticas (Prebet, 2010). Asimismo, se ha observado que la interrupción de la expresión de PTK7 puede reprimir la proliferación celular y promover la apoptosis en cáncer de colon e hígado (Meng, 2010). Por otro lado, se ha asociado la sobreexpresión de PTK7 a resultados clínicos adversos en el cáncer colorrectal y a la invasividad de las células tumorales, por lo que PTK7 podría servir como predictor del pronóstico de dichas patologías (Lhoumeau, 2015).

2.3. Aptámeros en el desarrollo de agentes de imagenología molecular para diagnóstico en cáncer

2.3.1. Imagenología molecular

La imagenología molecular es la visualización, caracterización y medición *in vivo* de procesos biológicos, tanto a nivel molecular como a nivel celular (Weissleder, 2001). Es una técnica que permite monitorear y registrar la distribución espaciotemporal de procesos moleculares o celulares, así como también realizar imágenes en 2D o 3D, otorgando información anatómica y fisiológica del paciente, mediante la administración de sondas al paciente o mediante equipamiento externo (Weissleder, 2006; Calzada, 2020).

Es una modalidad imagenológica que combina biología molecular, química nuclear, medicina de radiación y ciencias de la computación. Puede proporcionar una lectura de todo el cuerpo, siendo un sistema no invasivo y permitiendo la evaluación de la patología en su contexto, lo cual es clave para entender la progresión del tumor sin alterar el entorno biológico (Chen, 2015; Calzada, 2020). Asimismo, la detección es cuantitativa mediante la detección de procesos biológicos que están alterados en el organismo, más específicamente biomarcadores. Esta detección se puede realizar por medio de sondas imagenológicas específicas para cada biomarcador o blanco (Alford, 2009).

Esta herramienta tiene un gran potencial en el diagnóstico y manejo de enfermedades como el cáncer, enfermedades neurológicas y cardiovasculares (Aebersold, 2005). La detección no invasiva de marcadores moleculares puede proporcionar: un diagnóstico más temprano, la estadificación tumoral, la cuantificación de una lesión, y seguimiento de la misma (resultados estadísticamente más precisos a través de estudios longitudinales que se pueden realizar en el mismo paciente), ayuda en la elección de un tratamiento más efectivo, la precisión de la dosis, un pronóstico más preciso; facilitar la detección de metástasis; y permitir la cirugía guiada, entre otros (Weissleder, 2006; Hartewell, 2006; Cai, 2006; Gibbs, 2012).

Existen diversas modalidades de imágenes para la investigación biomédica y aplicación clínica. Las modalidades de imagen predominantes se pueden clasificar en dos categorías. Por un lado, algunas modalidades de imagen, como la ecografía, la resonancia magnética nuclear y la tomografía computarizada proporcionan información anatómica que depende de los cambios asociados a la enfermedad. En cambio, las de segunda categoría pueden ofrecer información funcional de la enfermedad y rastrear procesos biológicos *in vivo*. Estas modalidades de imagen incluyen tomografía por emisión de positrones (PET), tomografía computarizada por emisión de fotón único (SPECT), imágenes de bioluminiscencia óptica/fluorescencia, imágenes de resonancia magnética molecular (mMRI) y espectroscopia de resonancia magnética (MRS) (Massoud, 2003). PET y SPECT ofrecen además la posibilidad de cuantificación de procesos biológicos asociados a enfermedades. Además, se utilizan comúnmente sistemas híbridos que combinan dos o más modalidades (Catana, 2006; Even-Sapir, 2003). Las modalidades más utilizadas y sus ventajas y desventajas relativas, junto con aspectos claves, se muestran en la Tabla 2.

Entre las diversas modalidades de imágenes, algunas modalidades, como PET, SPECT e imágenes ópticas, requieren la inyección de sondas moleculares al paciente para adquirir la señal de imagen, mientras que otras, como imágenes ópticas y mMRI, pueden seguir la enfermedad ya sea a través de las sondas moleculares exógenas o a través de las moléculas endógenas (Massoud, 2003). Debido al papel fundamental que presentan las sondas moleculares para generar una óptima imagen molecular, es necesario que el diseño y desarrollo de la sonda biológicamente activa cumpla con ciertas características, las cuales se describen en la siguiente sección (Gambhir, 2002; Gibbs, 2012; Calzada, 2020).

Tabla 2. Modalidades seleccionadas para imágenes moleculares en oncología. Ventajas y desventajas relativas. Extraída y adaptada de Rowe, 2022.

|		
Óptico		
Fluorescencia	Orientación quirúrgica	Radiación no ionizante; fotodinámica y fotoinmunoterapia/Profundidad de penetración moderada (investigación, traslacional)
Fotoacústica	Caracterización de tejidos; guía quirúrgica	Radiación no ionizante; alta especificidad óptica/Profundidad de penetración en tiempo real/moderada (investigación)
Ultrasonido	Entrega dirigida de medicamentos; alteración de la barrera hematoencefálica; caracterización tumoral	Radiación no ionizante; escáneres fácilmente disponibles; bajo costo (investigación traslacional y clínica)
Resonancia magnética		
Espectroscopía	Tumores cerebrales, cáncer de próstata	Contraste endógeno; amplia disponibilidad/Baja sensibilidad; metabolitos limitados (investigación traslacional y clínica)
Partículas de óxido de hierro ultrapequeña y superparamagnética (USPIO)	Seguimiento de células detección de fagocitos; metástasis en los ganglios linfáticos	Alternativa al gadolinio; teranóstico/Puede alterar los estudios de resonancia magnética nuclear posteriores; algunas reacciones adversas; ralentiza el flujo de trabajo; utilidad clínica incierta (investigación clínica)
Hiperpolarización	Caracterización del metabolismo tumoral	Señal alta; potencial para investigar una amplia gama de vías metabólicas/Caro; las vías en estudio pueden verse perturbadas por una alta concentración de agentes hiperpolarizados (investigación)
Radionucleido		
SPECT	Gammagrafías óseas; tumores cerebrales; mapeo de ganglio centinela; dosimetría de radiación para teranóstica	Ampliamente disponible/Baja sensibilidad; baja resolución; uso decreciente en oncología (clínica)
PET	Blancos moleculares específicos;	Alta sensibilidad y potencial para alta especificidad/Infraestructura compleja;

| | metabolismo (glucosa/glutamina) | agentes costosos (investigación traslacional y clínica) |

Abreviaturas: SPECT = single photon emission computed tomography; PET = positron emission tomography; USPIO = ultrasmall superparamagnetic iron oxide nanoparticles.

## 2.3.2. Diseño de sonda para diagnóstico basadas en aptámeros

El desarrollo de sondas en base a aptámeros es una herramienta de gran potencial para diagnóstico en cáncer mediante imagenología molecular, debido a sus características para reconocer con alta afinidad y especificidad biomarcadores que se sobreexpresan en las diferentes células tumorales (Weissleder, 2001; Calzada, 2020; García Melian, 2023).

Las sondas para imagenología molecular son moléculas utilizadas para visualizar, caracterizar y cuantificar los procesos biológicos de forma no invasiva (Weissleder, 2001). Brevemente, las imágenes se logran mediante la administración sistémica o localizada de la sonda imagenológica, seguida de un tiempo para la acumulación de la sonda en el sitio específico en paralelo a la depuración del resto del organismo para lograr una alta relación señal/fondo (Figura 6) (Bohrmann, 2022). En dicho momento, se realiza la adquisición de la imagen por un equipo imagenológico externo. Es de destacar que no se busca ningún efecto farmacológico tras la administración al paciente de la sonda (Calzada, 2020).
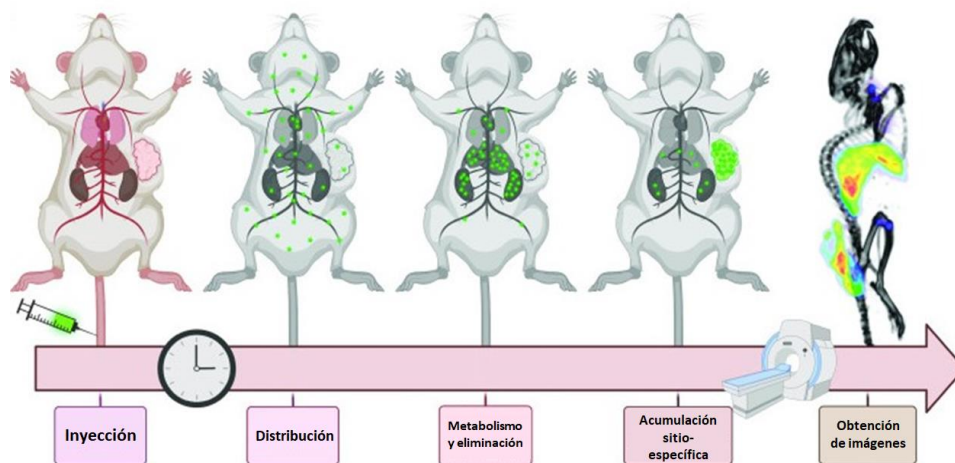
Figura 6. Imágenes moleculares representativas *in vivo* en un ratón. Para obtener la imagen se inyecta por vía intravenosa una dosis de la sonda y se distribuye por todo el cuerpo. La sonda se acumula en el sitio específico (en este caso en el tumor) y se elimina a través de los órganos excretores. La obtención de imágenes se realiza cuando la relación entre la señal específica y el fondo es favorable. Extraída y adaptada de Bohrmann, 2022.

Una sonda para imagenología molecular tiene tres componentes fundamentales: un agente de imagen, un conector y una molécula de reconocimiento (en este caso un aptámero) (Figura 7) (Calzada, 2020; Bohrmann, 2022). El agente de imagen produce una señal y para las distintas modalidades de formación de imágenes se necesitan sondas con agentes diferentes. Por ejemplo, para la formación de imágenes SPECT se usan emisores gamma puros como agentes de imagen, mientras que para realizar imágenes ópticas se utilizan moléculas fluorescentes (Chen, 2010b).
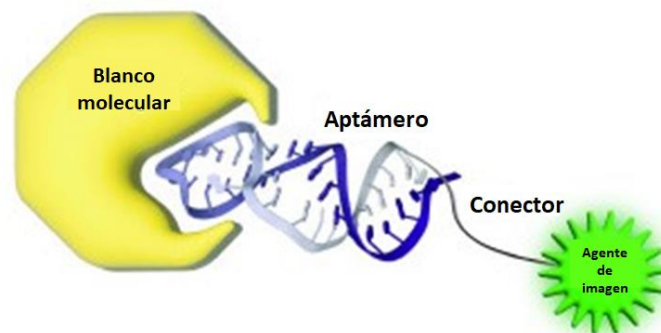
Figura 7. Esquema de una sonda basada en aptámeros para imagenología molecular. Se observa el agente de imagen (verde), el conector, el aptámero y el blanco molecular (amarillo). Extraída y adaptada de Bohrmann, 2022.

En este caso, la molécula de reconocimiento son los aptámeros que dirigen e interactúan con el biomarcador que se sobreexpresa en las células tumorales (Weissleder, 2001; Weissleder, 2006). El conector utilizado en las sondas puede acoplar la molécula de reconocimiento con el agente de imagen (imagenóforo). Esto favorece que no se modifique la especificidad o afinidad de la molécula de reconocimiento. También se puede modificar la farmacocinética y la biodistribución de la sonda, en base a sus características como la longitud, la flexibilidad y la hidrofilia (Weissleder, 2001).

Debido a que es necesario optimizar muchos aspectos para obtener el mejor resultado de imagen, es necesario tener varias consideraciones para desarrollar una sonda para imagenología molecular (Calzada, 2020).

Las estrategias de imágenes moleculares se basan en gran medida en la naturaleza de los biomarcadores, lo que a su vez afecta el diseño de la sonda. Entonces, el biomarcador apropiado asociado con el proceso biológico de la enfermedad debe identificarse, seleccionarse e incluso validarse en un sistema de prueba. Por ello, el diseño de estas sondas comienza con la selección adecuada del aptámero para el blanco molecular de interés (Chen, 2010b; Calzada, 2020). Asimismo, la alta afinidad con el blanco molecular o biomarcador es un requisito para lograr una alta captación tumoral. Requiere valores de K_d en el rango de nM o menores y cualquier incorporación puede afectar ese valor, al cambiar la carga u otras características de unión (Calzada, 2020).

La alta especificidad es un parámetro que permite que la sonda interactúe con el biomarcador particular y discrimine el blanco molecular específico entre otros. Gracias a esta especifidad, las sondas pueden proporcionar información de distintos procesos biológicos, las cuales son muy útiles para comprender la biología de enfermedades específicas. La unión altamente específica reduce la captación no específica de la sonda de imagen en otros tejidos. Además, la pureza de la sonda de imagen tiene estrecha relación con el contraste de la imagen, debido a que el agente de señal libre aumenta el ruido de fondo, afectando la medición real. A su vez, el aptámero sin conjugar compite con el sitio específico, disminuyendo la señal observada por la sonda, por lo que el proceso de preparación de la sonda debe tener altísimos rendimientos o estrictos procesos de purificación (Chen, 2010b; Calzada, 2020). La actividad específica es importante, ya que cuanto más componente de señal posea la sonda, mejor será la imagen (Calzada, 2020).

La estabilidad *in vivo* de una sonda de imagenología es un gran desafío porque los numerosos sistemas metabolizantes presentes en el suero o en el tejido específico pueden degradar la sonda (Calzada, 2020). Las sondas deben presentar una alta sensibilidad, ya que es crucial reducir la perturbación y los efectos farmacológicos en los sistemas y procesos biológicos a un nivel mínimo (Chen, 2010b). Esto va acompañado de la baja inmunogenicidad y toxicidad, si bien por lo general las sondas se administran en dosis bajas, es necesario controlar sus efectos farmacológicos (Chen, 2010b).

Por último, la producción, reproducibilidad y factibilidad económica deben optimizarse. El bajo costo y la disponibilidad de las sondas, junto con una metodología reproducible, hará que estas herramientas sean ventajosas para su uso clínico (Chen, 2010b; Calzada, 2020).

2.3.3. Aptámeros en el diagnóstico

La detección temprana del cáncer aumenta significativamente las posibilidades de supervivencia y efectividad al tratamiento. Los métodos comúnmente utilizados para la detección temprana del cáncer son la ecografía, la tomografía computarizada, la resonancia magnética nuclear y los ensayos bioquímicos, genéticos y moleculares como los ensayos de biomarcadores presentes en suero o plasma, e inmunohistoquímica. Sin embargo, los biomarcadores de cáncer se encuentran comúnmente en bajas concentraciones, dispersos en forma heterogénea y, a menudo, se mezclan con otras proteínas, lo que dificulta su detección temprana (Ciancio, 2018).

Los aptámeros son una herramienta extremadamente prometedora para el diagnóstico temprano del cáncer debido a sus características de alta afinidad, especificidad y sensibilidad (Kurt, 2016). De esta forma hay una gran variedad de aptámeros que se están empleando en el diagnóstico en cáncer. Por ejemplo, se utiliza un aptámero que reconoce CD30 marcado con IRD800CW para obtener imágenes *in vivo* del linfoma (Zeng, 2014), así como un aptámero específico del cáncer de páncreas marcado con una subestructura derivada del fluoróforo Cy5 para la obtención de imágenes *in vivo* de este cáncer (Wu, 2015). El aptámero AS1411 junto con el péptido dirigido a la barrera hematoencefálica es utilizado para la obtención de imágenes *in vivo* de gliomas (Ma, 2014). Por otro lado, el aptámero D3P-21 fue desarrollado para diagnosticar tumores de próstata independientes de andrógenos en ratones (Civit, 2019). Todos ellos muestran una capacidad de orientación tumoral rápida y específica, alta relación señal/ruido y óptimas propiedades farmacocinéticas.

Además de obtener imágenes con fluoróforos, los aptámeros se pueden conjugar con perlas magnéticas para mejorar la resonancia magnética (Yu, 2011), como es el caso del aptámero del receptor 2 del factor de crecimiento endotelial vascular (VEGFR2) conjugado con nanomateriales magnéticos para la obtención de imágenes por resonancia magnética del glioma (Kim, 2013). El aptámero de la molécula de adhesión epidérmica (EpCAM) también se ha conjugado con nanomateriales magnéticos para imágenes de resonancia magnética del cáncer gástrico (Heo, 2014). Todos mejoran significativamente la sensibilidad y la biocompatibilidad de las imágenes dirigidas al tumor y reducen la

citotoxicidad, mejorando aún más el potencial de aplicación clínica de la resonancia magnética.

También se ha diseñado una técnica sensible para el diagnóstico de células cancerosas en la sangre utilizando el sistema conjugado aptámero-nanopartícula, que comprende el aptámero Sgc8 y nanopartículas de sílice marcadas fluorescentemente (Tan, 2016). En otra modificación, el aptámero Sgc8 fue conjugado con nanopartículas de oro con una capa de óxido férrico magnético para desarrollar un biosensor altamente sensible para detectar la leucemia de células T (Khoshfetrat, 2017).

Recientemente, con el éxito de las terapias que modulan los puntos de control del sistema inmune, se describen varias sondas de aptámeros anti PD1, PD-L1, y CTLA-4, entre otros, con fines diagnósticos, así como terapéuticos (García Melián, 2023).

## 2.3.4. Características de los agentes de imagen de este estudio

2.3.4.1. Características del fluoróforo Alexa Fluor™ 647

Realizar imágenes ópticas en el rango de 600 a 1000 nm del espectro electromagnético del infrarrojo cercano (NIR) otorga varias ventajas. Por ejemplo, los cromóforos biológicos, en particular la hemoglobina, absorben fuertemente la luz visible, limitando así la profundidad de penetración en longitudes de ondas cortas a unos pocos milímetros. Sin embargo, en el NIR, el coeficiente de absorción de luz de las moléculas biológicas es mínima y permite mejorar la penetración de los fotones a través del tejido, a nivel de profundidad y de uniformidad (Hilderbrand, 2010; Zhao, 2018). Asimismo, a alta longitud de onda, los tejidos tienen menor autofluorescencia y la dispersión de luz disminuye en el NIR, generando así, menor interferencia de fondo con una mayor relación señal/fondo; lo que permite obtener imágenes ópticas con alto contraste (Hilderbrand, 2010).

Estos requisitos son claves para su uso como agentes de imagen *in vivo*. Por tanto, las sondas de imágenes generadas con moléculas que absorben en el NIR se utilizan predominantemente en investigación (Borlan, 2021). Además, algunas han recibido la

aprobación de la Administración de Alimentos y Medicamentos (FDA) para uso clínico (Yu, 2016) debido a que, por ejemplo, tienen baja toxicidad, efectos secundarios insignificantes. Estas se usan para monitorear la función cardíaca, el gasto hepático y la angiografía retiniana (Boumaza, 2001; Berlier, 2003).

El éster *N*-hidroxisuccinimidilo (NHS) de Alexa Fluor™ 647 (Figura 8), cuyo fluoróforo pertenece a la familia de Alexa Fluor, ha sido utilizado para conjugación a bio-sistemas a través de un enlace covalente. Las moléculas fluorescentes Alexa Fluor presentan un amplio rango de longitudes de onda de emisión y de excitación. Los fluoróforos de dicha familia también resultan interesantes por su composición química ya que poseen una adecuada lipofilia, comparados con otros fluoróforos, y no presentan problemas de solubilidad en medios biológicos (Berlier, 2003). Alexa Fluor™ 647, presenta un espectro de excitación/emisión de 650/668 (Figura 9) y se ha descripto su uso en el desarrollo de agentes imagenológicos en cáncer a nivel pre-clínico y como potencial herramienta en cirugías guiadas (Saccomano, 2016; Calzada, 2017a; Comeo, 2020; Castelli, 2021; Arévalo, 2022).
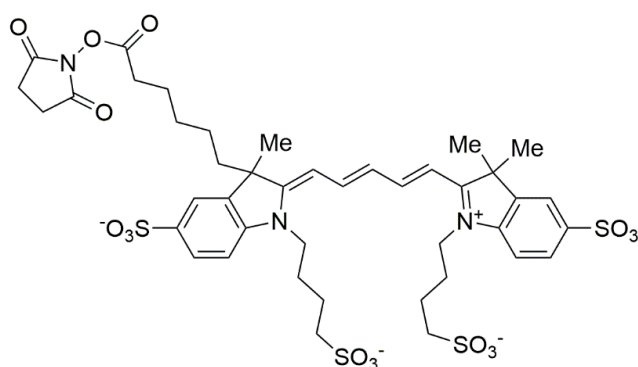
Figura 8. Estructura del éster *N*-hidroxisuccinimidilo de Alexa Fluor™ 647. Utilizado en esta tesis como agente acoplante.
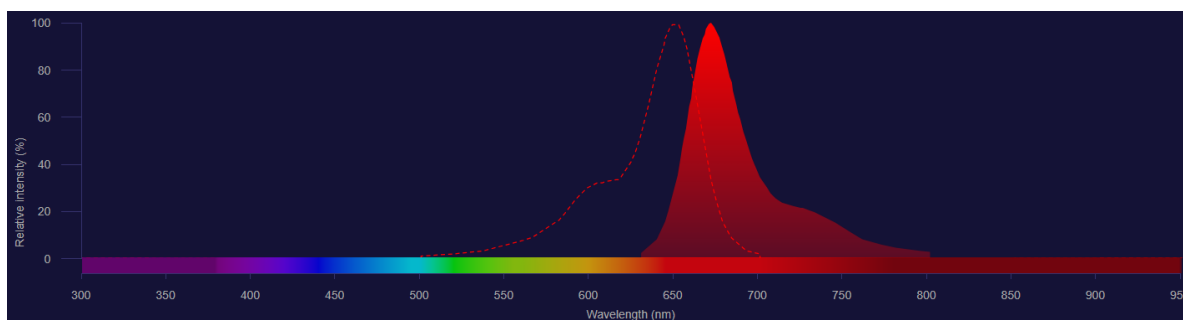
Figura 9. Espectro de emisión y excitación de Alexa Fluor™ 647. Extraído de la plataforma "SpectraViewer" de Thermofisher Scientific Inc.

2.3.4.2. Química de galio-67

El radionucleido metálico galio-67 (^{67}Ga) se produce en ciclotrón a partir de zinc-68 y se comercializa en forma de citrato o cloruro de Galio. El ^{67}Ga decae por captura electrónica al nucleido estable ^{67}Zn, con un período de semidesintegración de 78,3 horas (3,26 días). En su decaimiento se emiten varios fotones gamma, siendo los principales los de 93 keV con 37 % de abundancia, 185 keV con 20 % de abundancia, 300 keV con 17 % de abundancia y 394 keV con 5 % de abundancia (Figura 10) (Mattsson, 2015; Drugs and Lactation Database, 2021). Estas propiedades radiofísicas, hacen a ^{67}Ga adecuado para generar sondas emisoras gamma para el uso en imagenología molecular, principalmente para la toma de imágenes *in vivo* hasta las 72 horas (Calzada, 2017a; Calzada, 2017b; Zhang, 2017).

A su vez, otra característica de ^{67}Ga es la emisión de electrones Auger durante el decaimiento, que son de baja energía, por lo que también se consideran partículas adecuadas para la inactivación de células tumorales, produciendo una acción citotóxica en las mismas. Estas partículas son extremadamente radiotóxicas ya que, si en su recorrido colisionan con el ADN, pueden inducir la ruptura del mismo (Williams, 2008). Sin embargo, es una terapia de corto alcance, es decir, solo es eficiente si la desintegración radiactiva ocurre cerca del ADN. Entonces, para que ^{67}Ga pueda ser utilizado como potencial radionucleido terapéutico, es necesario que la sonda o radiofármaco se internalice en la célula, se transloque al núcleo e, idealmente, se incorpore al ADN (Williams, 2008; Othman, 2017).
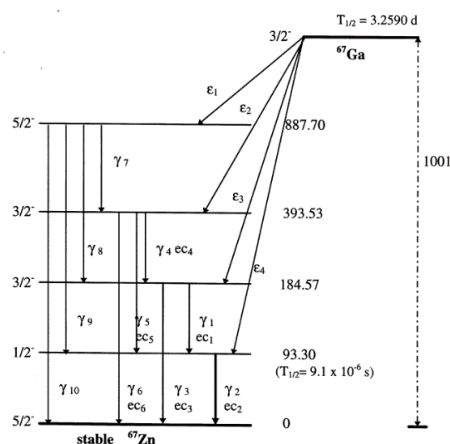
Figura 10. Diagrama del decaimiento de galio-67. Extraído y adaptado de Attie, 1998.

Para lograr radiomarcar una molécula con $^{67}Ga^{3+}$, que es un ión metálico, es necesaria la incorporación de un quelante bifuncional, para que sea coordinado fuertemente, formando así un complejo termodinámicamente estable. Un quelante bifuncional, posee grupos funcionales para la quelación del radiometal (primera función) y otros para el acoplamiento de una molécula (segunda función) como un péptido, aptámero, entre otros (Tolmachev, 2008). Mayoritariamente se utilizan para lograr minimizar la interrupción o alteración de la actividad biológica del agente de reconocimiento tras la incorporación del radionucleido metálico (Okoye, 2019). De esta forma, se pretende no modificar sustancialmente la interacción de la molécula, luego del marcado, con su blanco molecular (Okoye, 2019). El quelante bifuncional a utilizar se selecciona en base a la naturaleza y estado de oxidación del ión metálico, así como la estabilidad del complejo final, entre otras propiedades de interés (Liu, 2004). En este posgrado se utilizó $^{67}GaCl_3$ como forma química del radionucleido galio-67, en el que el galio se encuentra con estado de oxidación +3, por lo que los quelantes bifuncionales ideales para ser usados son los polidentados con átomos donadores como aminas y carboxilatos. Entre ellos se puede mencionar a los derivados del ácido 1,4,7,10-teraazaciclododecano-*N,N´,N´´,N´´´*-tetraacético (DOTA) (Guo, 2009) y a los derivados de ácido 1,4,7-triazaciclononano-*N,N´,N´´*-triacético (NOTA) (Valdovinos, 2017). Estos quelantes son preferidos en la complejación por el incremento de la estabilidad termodinámica y, por ende, la baja inercia química de los complejos de Ga^{+3} formados, comparado con los análogos de cadena abierta (por ejemplo, derivados de ácido dietilentriaminopentaacético, DTPA) (Šimeček, 2012). Adicionalmente, la geometría de la cavidad de DOTA y la preferencia del ión Ga^{3+} por la coordinación octaédrica regular promueve como resultado un inadecuado ajuste del

ión metálico en el macrociclo de este ligando. Por el contrario, el ligando NOTA presenta una cavidad que es casi ideal para pequeños iones metálicos que dan complejos octaédricos como el Ga^{3+} (Šimeček, 2012). Además, en cuanto a los radiofármacos portadores de un macrociclo derivado de NOTA se han descripto muy buenas estabilidades frente a diferentes desafíos biológicos (Jain, 2018).

Un quelante bifuncional derivado de DOTA se utilizó en nuestro laboratorio para la generación de aptámeros radiomarcados para imagenología molecular teniendo excelentes resultados (Calzada, 2017b). Con el objetivo de continuar profundizando en el desarrollo de sondas radiomarcadas basadas en el aptámero Sgc8-c, en este trabajo de posgrado se eligió utilizar derivados del quelante bifuncional NOTA, por las potenciales ventajas mencionadas en el párrafo anterior, para finalmente generar la sonda portadora del emisor gamma ^{67}Ga.

Así, en este trabajo, se utilizó el quelante bifuncional ácido 2-S-(*p*-isotiocianatobencil)-1,4,7-triazaciclononano-*N,N´,N´´*-triacético (*p*-SCN-Bn-NOTA) que exhibe un grupo isotiocianato activado para reaccionar con nucleófilos y una estructura macrocíclica, con tres grupos carboxílicos, presentando un núcleo más pequeño que el del ciclo de DOTA (Figura 11).
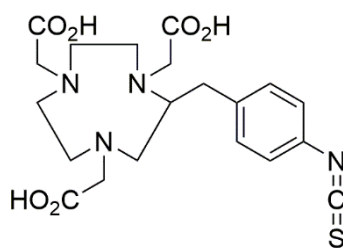
Figura 11. Estructura del agente acoplante utilizado en este trabajo, para incorporar el quelante NOTA al aptámero Sgc8-c.

2.4. Aptámeros en el desarrollo de biofármacos para terapia en cáncer

2.4.1. Diseños de conjugados aptámero-fármaco

La terapia dirigida tiene como objetivo aumentar la toxicidad específicamente en los tejidos tumorales mientras reduce la toxicidad en los tejidos sanos (American Cancer Society, 2008). Así como los "*Antibodies Drug Conjugates*" (ADC), los aptámeros son candidatos prometedores para su aplicación en terapia dirigida debido a sus características, principalmente su alta especificidad, selectividad, fácil internalización celular, rápida capacidad de acumulación tisular y capacidad de modificación (Ni, 2021).

La terapia dirigida basada en aptámeros ha empleado dos estrategias:

(1) aptámero *per se* como agente terapéutico, como antagonista para bloquear la interacción de dianas asociadas a la enfermedad o agonista para activar la función de los receptores específicos;

(2) aptámero como agente de entrega activa, para dirigir otros agentes terapéuticos a las células o tejidos específicos (conjugado aptámero-fármaco - ApDC) (Huang, 2014). En este caso, el aptámero no necesariamente debe tener un efecto farmacológico.

El conjugado aptámero-fármaco, al igual que la sonda imagenológica, puede constar de tres componentes: el aptámero, el conector y el fármaco (porción que tiene actividad bilógica) (Kim, 2021). Aunque existen ejemplos de desarrollos de sistemas más sencillos.

En los conjugados, los ligandos reconocen específicamente los biomarcadores asociados con el cáncer y administran fármacos a las células tumorales específicas. Los fármacos se conjugan al aptámero, en general a través de conectores con grupos funcionales que aseguran la estabilidad de los conjugados y también permiten la liberación selectiva del fármaco en células o tejidos tumorales (Zhu, 2018).

La estabilidad general y la reversibilidad estructural de los aptámeros permite diseñar varios tipos de conjugados aptámero-fármaco para dirigirse a las células específicamente, mejorando la concentración local del fármaco y eficacia terapéutica (Kim, 2021).

Uno de los tipos de conjugados covalentes aptámero-fármaco son los construidos en base a análogos de nucleótidos (Figura 12A). Los análogos de nucleósidos citotóxicos y las nucleobases estuvieron entre los primeros agentes quimioterapéuticos que se introdujeron para el tratamiento médico del cáncer (Galmarini, 2002). Los análogos de nucleótidos son familias farmacológicamente diversas, que incluyen: agentes antitumorales, agentes antivirales y moléculas inmunosupresoras (Kim, 2021). Estos conjugados se pueden realizar mediante la inserción de análogos de nucleótidos, biológicamente activos, entre la secuencia del aptámero. El fármaco actúa como un antagonista metabólico o compite con los ácidos nucleicos fisiológicos o interactúa con muchos blancos intracelulares para inducir citotoxicidad. Sin embargo, podría ocurrir una acción dual si el aptámero presenta también efecto anticancerígeno (Galmarini, 2002; Ni, 2021).

Otro tipo de conjugados aptámero-fármaco son los conjugados por intercalación, u otro tipo de interacción de baja energía, reversible del fármaco (Figura 12B). Los conjugados físicos, no covalentes, se generan mediante la interacción del fármaco a la estructura del aptámero. Las estrategias que se utilizan para la inserción al aptámero, es similar a la que ocurre en el ADN celular, donde, por ejemplo, se intercalan moléculas entre dos pares de bases adyacentes en la doble hélice del ADN (Zeng Z, 2021). Aunque aún se continúa estudiando como es este mecanismo, estos conjugados tienen la ventaja de poder acoplar fácilmente fármacos a aptámeros, sin pasar por un proceso de síntesis química o proceso de modificación complicado (Kim, 2019). Hay muchos estudios que utilizan este tipo de conjugación, intercalando fármacos como doxorrubicina con grandes resultados (Bagalkot, 2006). Sin embargo, esta estrategia presenta la desventaja de que el reconocimiento y afinidad del aptámero por el blanco molecular puede verse afectado, al intercalarse el fármaco, debido a los cambios tridimensionales del oligonucleótido (Zeng, 2021).
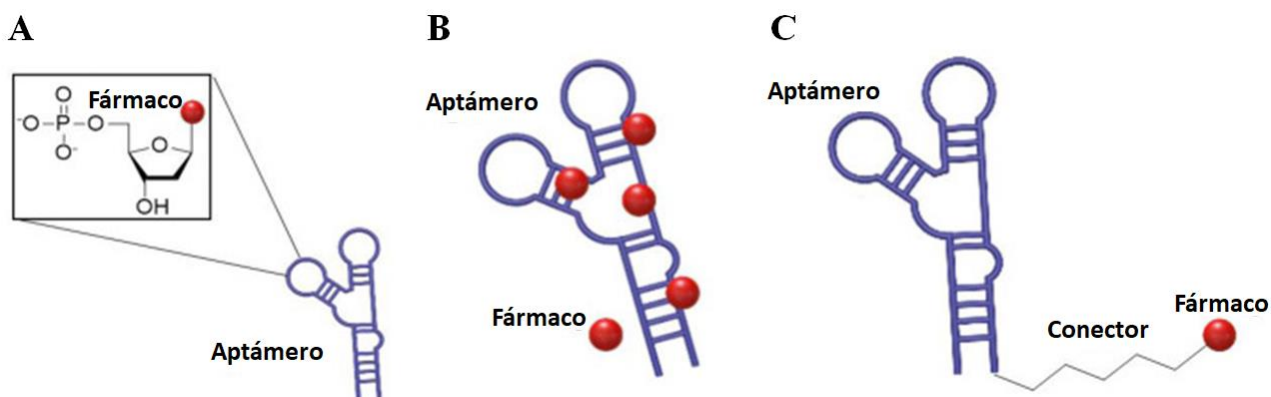
Figura 12. Diferentes conjugados aptámeros-fármacos. ApDC construido por análogos de nucleótidos **A**. ApDC por intercalación u otro tipo de interacción de baja energía del fármaco al aptámero **B**. ApDC mediante el uso de un conector entre el fármaco y un aptámero **C**. Extraída de Kim, 2021.

Otro tipo de conjugado aptámero-fármaco es el que se obtiene por el uso de un conector químico (Figura 12C). La unión covalente de fármacos a aptámeros mediante conectores se ha explorado ampliamente y es el más utilizado para la generación de los conjugados. Además, presenta mayor potencial para modificaciones específicas y tienen una función escindible para luego liberar el fármaco en el sitio de acción. La escisión puede ser dependiente de temperatura, por dinámicas lábiles al pH, por productos químicos, por reacciones enzimáticas, entre otros (Zhu, 2018, Ni, 2021).

Han sido descripto tres tipos de métodos para unir un conector a un aptámero. El primero es formando una hidrazona que implica contar con cetonas y aldehídos y un agrupamiento hidracina. El grupo hidrazona, inestable en medio ácido, se descompone por hidrólisis cuando el aptámero y el fármaco son internalizados por endosomas y lisosomas ácidos; de esta forma se libera el fármaco (Zhu, 2018).

El segundo es la química relacionada con agrupamientos de tioles. Esta estrategia se usa comúnmente en mercapto-fármacos (portadores de agrupamiento -SH) y se los hace reaccionar con un aptámero portador de un grupo –SH para formar un enlace disulfuro. También se ha descripto el uso de fragmentos derivados de mercapto-PEG en el fármaco y en el aptámero que concomitantemente aumenta la estabilidad del compuesto (Da Pieve, 2010).

El tercer tipo de conector son los que pueden ser escindidos por la catepsina B, que es una proteasa de lisosomas que se sobreexpresa en varias células tumorales y está involucrada en numerosos procesos de carcinogénesis en humanos. La catepsina B tiene varios sustratos, sin embargo, secuencias como fenilalanillisina (*Phe-Lys*) son más específicas. El conjugado aptámero-fármaco se internaliza por endocitosis y se transporta al lisosoma, donde la catepsina B escinde selectivamente el conector, logrando la liberación intracelular controlada del fármaco (Qi, 2022).

En este trabajo de tesis se utilizó otro tipo de conector, carbamato, tanto por las características de estabilidad del mismo como por motivos estructurales, descripto en el artículo IV (Sicco, 2021).

2.4.2. Aptámeros en terapia

Si bien la terapia con aptámeros *per se* no fue enfoque de este posgrado, resulta importante destacar los recientes avances en el campo de la biomedicina.

La mayoría de los tratamientos contra el cáncer implican radiación, extracción quirúrgica o quimioterapia combinada con farmacología más reciente como la inmunoterapia (Yildizhan, 2018). Sin embargo, estos enfoques son, en algunos casos, invasivos o, en otros, tienen una amplia gama de blancos moleculares que causan efectos indeseables en el tejido sano circundante, lo que lleva a efectos secundarios en los pacientes. Nuevos tratamientos intentan eliminar las células tumorales de manera más precisa y con un impacto mínimo en las células sanas adyacentes. Los aptámeros son candidatos prometedores para su aplicación en terapia dirigida (Ni, 2021).

La primera formulación de un aptámero que fue aprobada por la FDA para su uso clínico es Macugen (Pegaptanib). Este aptámero se utiliza para el tratamiento de pacientes con degeneración neovascular macular de la edad, por inhibición de la expresión del factor de crecimiento endotelial (Gryziewicz, 2005). Aparte de Pegaptanib, el aptámero más avanzado para la terapia en cáncer es AS1411 y se encuentra en fase II (Ireson, 2006). El aptámero AS1411, dirigido a la proteína nucleolina, también se ha utilizado como conjugado aptámero-fármaco. Este se conjugó con doxorrubicina y se observó la utilidad del conjugado para la administración dirigida del fármaco en la línea celular de cáncer de

hígado humano (células Huh7) *in vitro* y en un modelo de xenoinjerto murino de carcinoma hepatocelular (Trinh, 2015). Recientemente, el aptámero ApTOLL se encuentra en estudios de fase 1b/2a, donde se evaluó su seguridad y eficacia en combinación con el tratamiento endovascular para pacientes con accidente cerebrovascular isquémico, surgiendo así nuevos candidatos con excelentes resultados (Hernández, 2023). En la Tabla 3 se detallan aptámeros en fases de desarrollo clínico (Opsina, 2020).

Tabla 3. Aptámeros en fases de desarrollo clínico. Extraída y adaptada de Ospina, 2020.

Pegaptanib™ (Macugen)	Factor de crecimiento vascular endotelial (VSGF)	Degeneración macular relacionada con la edad	Aprobado por la FDA Fase IV
REG1™	Factor de coagulación IXa	Enfermedad de la arteria coronaria	Fase III
E10030™ (Ophthotech Corporation)	Factor de crecimiento derivado de plaquetas (PDGF)	Degeneración macular relacionada con la edad	Fase III
AS1411™ (antisoma)	Nucleolina	Leucemia mieloide aguda	Fase II
REG1™	Factor de coagulación IXa	Intervención coronaria percutánea	Fase II
ARC1779™ (Archemix)	Dominio A1, factor de von Willebrand	Microangiopatías trombóticas y enfermedad de la arteria carótida	Fase II
NOX-E36™ (Noxxon Pharma)	Citocina CCL2	Diabetes mellitus de tipo 2	Fase II
NU172™ (ARCA)	Trombina	Derivación cardiopulmonar para mantener el estado de la anticoagulación	Fase II
ARC19499™ (Baxter)	Inhibidor de vía del factor tisular (TFPI)	Hemofilia	Fase I
ARC1905™ (Ophthotech)	Componente 5 del complemento	Degeneración macular relacionada con la edad	Fase I

En fase preclínica, el aptámero Sgc8 también fue conjugado para administrar doxorrubicina específicamente en las células T de leucemia linfoblástica aguda (Taghdisi, 2010). Pero para mejorar la estabilidad de ese conjugado, el aptámero se unió

covalentemente al fármaco mediante un conector lábil en medio ácido (Huang, 2009). Luego, con el objetivo de aumentar la capacidad de carga útil de aptámero-fármaco, se informó sobre otro sistema de administración de doxorrubicina, denominado *"nanotrains"* de ADN anclado en aptámero (aptNTrs) con una relación molar fármaco/Sgc8 aptámero-NTr de 50:1. Este compuesto muestra la inhibición del crecimiento de células tumorales *in vitro* e *in vivo* (Zhu, 2013).

Otros portadores de nanopartículas, como las nanopartículas de sílice mesoporosas (MSN), también han sido evaluados como método para mejorar la eficacia terapéutica. Se desarrolló un MSN modificado con el aptámero Sgc8 para administrar doxorrubicina a las células leucémicas con alta eficacia terapéutica y reducción de la toxicidad (Yang, 2019). En cuanto a la terapia génica, se desarrolló un conjugado aptámero-ADNzima en forma de Y circular para una terapia génica *in vivo* altamente eficaz a través de la escisión del ARN por ADNzima Este fármaco oligonucleótido proporcionó un enfoque novedoso para aplicaciones terapéuticas prácticas (Zhang, 2020).

Se ha desarrollado el aptámero A9g, de ARN, anti-PSMA (antígeno prostático específico de membrana) con capacidad de inhibir la actividad enzimática de PSMA, reduciendo la capacidad migratoria e invasiva de las células cancerosas prostáticas *in vitro*. El aptámero A9g demostró ser seguro y no tóxico en estudios *in vivo* (Ning, 2020). Por otro lado, el aptámero de ARN Apt63 puede discriminar fácilmente entre líneas celulares de cáncer de próstata en función de su potencial metastásico. Las células cancerosas sin propiedades metastásicas no se unen a Apt63, mientras que el aptámero podría unirse a la subunidad b de la ATP sintasa presente en la membrana plasmática de las células tumorales metastásicas. Esta unión tiene el potencial de destruir el mecanismo de existencia fundamental de las células tumorales y puede causar una muerte celular rápida (Speransky, 2019).

Por último, como se mencionó anteriormente, hay un gran desarrollo en lo que refiere a aptámeros contra los puntos de control del sistema inmune como terapia, que intentan reproducir el éxito de estas terapias basadas en anticuerpos, con las ventajas que los aptámeros representan (García Melián 2023).

2.4.3. Dasatinib: fármaco utilizado en este estudio

Dasatinib es un inhibidor de la tirosina quinasa de amplio espectro, incluidas las quinasas de la familia BCR-ABL y SRC, que presenta una masa molecular de 488,0 Da, y que se administra por vía oral (Figura 13) (Braun, 2020). En el 2006, recibió la aprobación de la FDA para tratar la fase leucemia mieloide crónica (LMC), leucemia linfoblástica crónica y la leucemia linfoblástica aguda Philadelphia positiva (LLA Ph positiva), con resistencia o intolerancia a la terapia previa (Talpaz, 2006; Simoneau, 2013). Demostró ser un fármaco más potente y efectivo, durante más tiempo que otros tratamientos anteriores para la LMC, como imatinib y nilotinib (O'Hare, 2005).
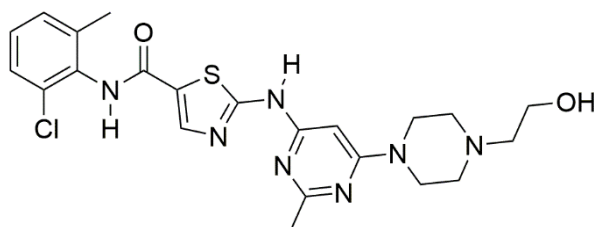

Figura 13. Estructura de dasatinib.

Dasatinib se une fuertemente a la quinasa BCR-ABL y tiene actividad contra muchas de las formas mutantes de BCR-ABL, tanto las conformaciones activas como inactiva (McCormack, 2011). Consecuentemente, se ha visto que dasatinib es eficaz contra las mutaciones BCR-ABL resistentes a imatinib, que han alterado la conformación inactiva (Hiwase, 2008; McCormack, 2011).

La absorción de dasatinib es principalmente un proceso pasivo, se une en gran medida a las proteínas plasmáticas (96 %) y se distribuye ampliamente en el espacio extravascular. Los transportadores de cationes orgánicos (OCT1, OCT-2 y OCT-3) no desempeñan ningún papel en la captación celular de dasatinib, pero este fármaco es un sustrato de los transportadores de salida (ABCB1 y ABCG2) en las células leucémicas (Furmanski, 2013). Además, la absorción de dasatinib depende del pH ácido, por lo que el transportador ABCC4 ubicado en el estómago y el tracto gastrointestinal, junto con el pH ácido, facilitan la absorción gástrica del fármaco (Eley, 2009).

La vía principal de eliminación de dasatinib es la biotransformación oxidativa a través de la cual se forman los metabolitos circulantes. Estos metabolitos incluyen productos de hidroxilación, oxidación de alcohol, *N*-oxidación, *N*-desalquilación, conjugación de sulfato y glucuronidación, y metabolitos secundarios que son subproductos de metabolitos primarios (Figura 14) (Kumar, 2022).
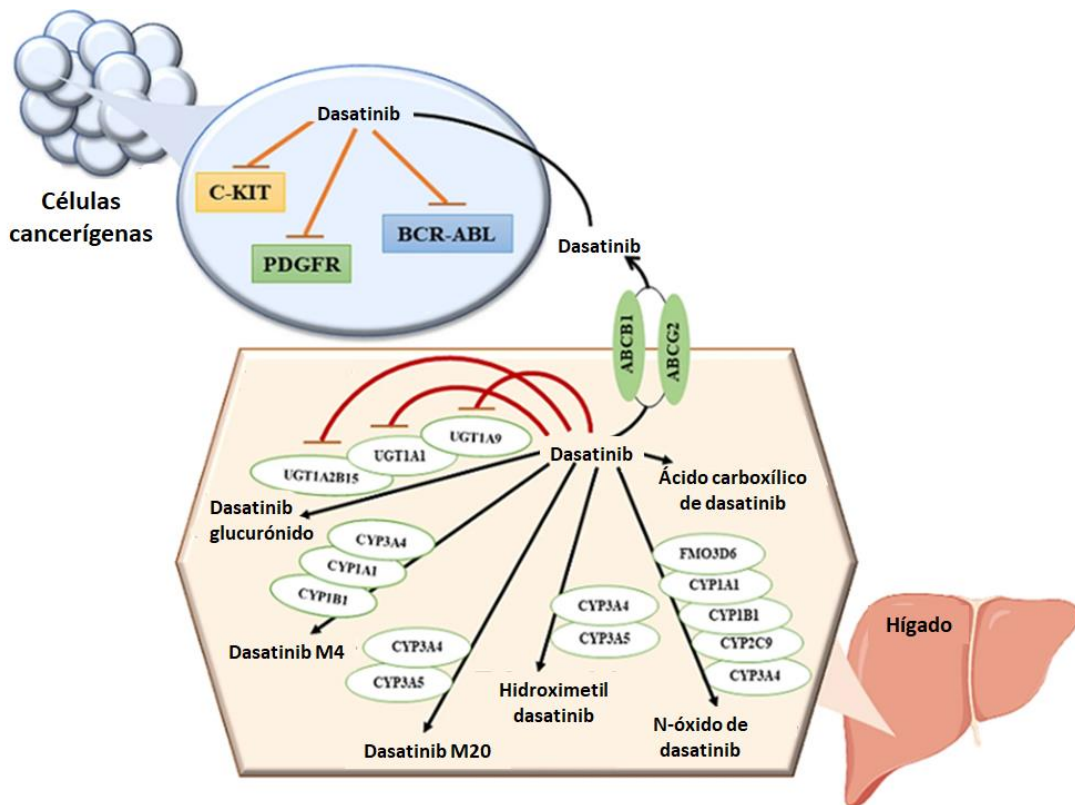
Figura 14. Vía metabólica de dasatinib. Extraído de Kumar, 2022.

El uso de dasatinib en terapias dirigida que inhiba la actividad de la quinasa BCR-ABL puede provocar respuestas hematológicas y citogenéticas en las personas afectadas. En un ensayo clínico con hepatocitos primarios de rata, se observó que dasatinib aumenta el nivel de especies reactivas de oxígeno, reduce el glutatión en la célula, disminuye el potencial de membrana de las mitocondrias y, eventualmente, mejora otros eventos para promover el estrés oxidativo (Xue, 2012). Además, dasatinib puede inducir una respuesta apoptótica a través de distintos mecanismos, como el de la regulación de la actividad de Akt/mTOR, al mismo tiempo que evita la liberación exosómica (Figura 15) (Liu, 2016; Vaidya, 2018).
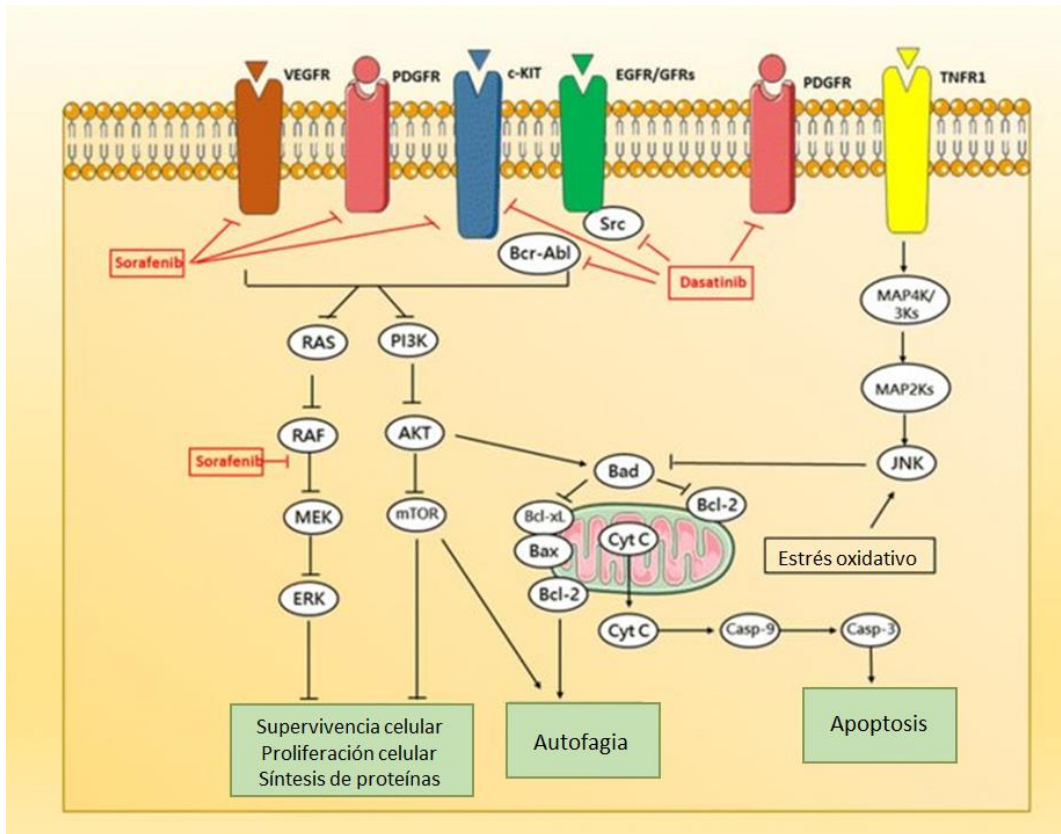
Figura 15. Vías de señalización implicadas en la toxicidad inducida por dasatinib. Extraída de Vaidya, 2018.

Se ha profundizado en la evaluación de dasatinib, en estudios preclínicos y clínicos, para el tratamiento de tumores malignos sólidos, incluido cáncer de mama (Reissig, 2001), cáncer de células renales (Sun, 2018), cáncer de pulmón de células no pequeñas, cáncer de próstata y glioma (Araujo, 2010).

Recientemente, se realizaron estudios clínicos en humanos utilizando un agente derivado de dasatinib, donde se evaluó la factibilidad de usar ^{18}F-dasatinib (^{18}F-SKI) para imágenes PET en pacientes con neoplasias malignas. También se validó su uso para la detección de tumores no invasivos *in vivo* dirigidos por tirosina quinasa en modelos preclínicos. A pesar de las dosis bajas inyectadas y una eliminación rápida de la sangre, los ensayos mostraron una captación tumoral significativa y un buen contraste de imagen (Krebs, 2020).

3. Objetivos

3.1. Objetivo general

- Evaluar la potencialidad del aptámero Sgc8-c para su aplicación en imagenología molecular y terapia en cáncer.

3.2. Objetivos específicos

- **Capítulo I: Sgc8-c como agente de imagenología molecular en cáncer**

    A- Sintetizar y caracterizar fisicoquímicamente derivados del aptámero Sgc8-c con la capacidad de generar sondas portadoras de emisores gamma.

    B- Profundizar en la síntesis y caracterización *in vitro* de una sonda fluorescente derivada del aptámero Sgc8-c.

    C- Sintetizar y caracterizar *in vitro* e *in vivo* una sonda derivada del aptámero Sgc8-c portadora de un emisor gamma, como potencial agente diagnóstico en cáncer en un modelo tumoral de linfoma.

    D- Profundizar en la caracterización biológica *in vitro* e *in vivo* de las sondas fluorescente y portadora de un emisor gamma desarrolladas en dos modelos tumorales de melanoma.

- **Capítulo II: Sgc8-c como agente potencial bioterapéutico selectivo en cáncer**

    A- Generar nuevos conjugados aptámero-fármaco mediante la incorporación covalente al aptámero Sgc8-c.

    B- Evaluar biológicamente *in vitro* la capacidad del aptámero Sgc8-c para dirigir el fármaco antitumoral al sitio de acción.

4. Capítulo I: Sgc8-c como agente de imagenología molecular en cáncer

4.1. Artículo I: Síntesis, purificación y caracterización fisicoquímica de los derivados del aptámero Sgc8-c y de una sonda fluorescente.

RESEARCH ARTICLE

WILEY C&B

Derivatizations of Sgc8-c aptamer to prepare metallic radiopharmaceuticals as imaging diagnostic agents: Syntheses, isolations, and physicochemical characterizations

Estefanía Sicco[1,2] | Jessica Báez[1,3] | Jimena Margenat[1] | Fernanda García[1] | Manuel Ibarra[3] | Pablo Cabral[1] | María Moreno[2] | Hugo Cerecetto[1] (ORCID) | Victoria Calzada[1]

[1]Área de Radiofarmacia, Facultad de Ciencias, Centro de Investigaciones Nucleares, Universidad de la República, Montevideo, Uruguay

[2]Departamento de Desarrollo Biotecnológico, Facultad de Medicina, Instituto de Higiene, Universidad de la República, Montevideo, Uruguay

[3]Facultad de Química, Centro de Evaluación de Biodisponibilidad y Bioequivalencia de Medicamentos, Universidad de la República, Montevideo, Uruguay

Correspondence
Hugo Cerecetto and Victoria Calzada, Área de Radiofarmacia, Centro de Investigaciones Nucleares, Facultad de Ciencias, Universidad de la República, Montevideo, Uruguay.
Emails: hcerecetto@cin.edu.uy and victoriacz@gmail.com

Aptamers, oligonucleotides with the capability to bind to a target through non-covalent bonds with high affinity and specificity, have a great number of advantages as scaffold to prepare molecular imaging agents. In this sense, we have performed post-SELEX modifications of a truncated aptamer, Sgc8-c, which bind to protein tyrosine kinase 7 to obtain a specific molecular targeting probe for in vivo diagnosis and in vivo therapy. Herein, we describe the synthetic efforts to prepare conjugates between Sgc8-c and different metallic ions chelator moieties in short times, high purities, and adequate yields. The selected chelator moieties, derived from 1,4,7,10-tetraazacyclo dodecane-1,4,7,10-tetraacetic acid, 2-benzyl-1,4,7-triazacyclononane-1,4,7-triacetic acid, and 6-hydrazinonicotinic acid, were covalently attached at the 5′-aptamer position yielding the expected products which were stable in aqueous solution up to 75°C and in typical aptamer storage conditions at least for 30 days.

KEYWORDS
aptamer, DOTA, HYNIC, NOTA, post-SELEX modifications, radiopharmaceutical

1 | INTRODUCTION

Molecular imaging consists of the in vivo visualization, characterization, and measure of biological processes at the cellular or molecular level.[1] Details such as localization, size, morphology, and structural changes of an affected area could be seen through conventional imaging techniques.[2] Visualization of molecular characteristics non-invasively through imaging allows the evaluation of pathology without disturbing the biological environment. In cancer, tumor stratification, metastasis detection, guided surgery, as well as quantification of an injury are different applications in this field.[3–5]

Identification of new molecular biomarkers and the development of specific molecular targeting agents against them are very important for image diagnosis and therapy.[6] In this sense, aptamers, which are oligonucleotides (ssDNA or RNA)

with a three-dimensional structure characterized by loops or hairpins, have the ability to bind to a target through non-covalent bonds with high affinity and specificity.[7–9] Aptamers are selected through massive complex combinatorial libraries by an in vitro process well-known as Systematic Evolution of Ligands by Exponential Enrichment (SELEX).[9] Thus, it offers advantages over other conventional-specific recognition molecules commonly used as therapy or imaging agents, such as antibodies. In vitro selection and chemical modifications are fast, inexpensive, and have less variability compared with antibodies and do not generate in vivo immunogenicity or toxicity.[10] Moreover, the low molecular weight (~15 kDa) and charges of most aptamers promote rapid tissue penetration and fast clearance, achieving high target/non-target ratios.[11] Furthermore, FDA approved aptamers as therapeutic agent,[12] and several researches are carrying out.[13–18]

Sgc8-c is a truncated sequence of the original aptamer Sgc8, which showed binding properties to protein tyrosine kinase 7 (PTK7) membrane receptor. Although Sgc8-c has only 41 nucleotides, the K_d value is 0.78 nM for the PTK7 receptor.[19] PTK7 is able to participate as a co-receptor, its proteolysis by MT1-MMP is involved in the progression of cancer, and furthermore, the participation of PTK7 in angiogenesis, cellular migration, and invasion, via VEGF pathways, has been described.[20–23] PTK7 overexpression has been observed in several colon, differentiated gastric, lung, prostate, and breast tumors and their metastases.[24–27]

Recently, we have explored Sgc8-c aptamer as the base of a molecular probe tagging with the fluorophore AlexaFluor647® (Sgc8-c-Alexa647) and radiolabeling with ^{99m}Tc via the HYNIC chelator.[28] Near-infrared probe was able to recognize melanoma and lymphoma in vivo. However, lack of in vivo targeting of the radiolabeled probe could be explained by labeling modifications. Gamma rays have better tissue penetration and the ability to accurately measure in tissue, which permit whole-body quantitative imaging.[29] For this reason, we were interested to exploring new Sgc8-c-radiolabeled probes and how chemical modifications could be change in vivo targeting.

Herein, we reported the optimization of the Sgc8-c derivative preparations, able to co-ordinate metallic radionuclides. For this reason, we selected the frameworks derivatives from 1,4,7,10-tetraazacyclododecane-1,4,7,10-tetraacetic acid (DOTA), and 2-benzyl-1,4,7-triazacyclononane-1,4,7-triacetic acid (NOTA) which are able to co-ordinate, for example, with metallic ions such as Ga^{3+}, Zr^{4+}, Cu^{2+}, In^{3+}, Lu^{3+}, Y^{3+}, or Bi^{3+}, among others. Furthermore, we optimized the derivatization of Sgc8-c with the moiety 6-hydrazinonicotinyl (from HYNIC), using a different precursor that it was previously described,[28] which is able to co-ordinate, for example, with metallic ions such as Tc^{5+}, or Re^{5+}, among others. Additionally, we analyzed properties of the aptamer conjugates in different conditions.

2 | METHODS AND MATERIALS

2.1 | Chemistry

All commercially available starting materials, reagents, and solvents were used without further purification unless otherwise stated. 5′-Aminohexyl-modified Sgc8-c aptamer (~13 kDa, 5′-/AM/ATC TAA CTG CTG CGC CGC CGG GAA AAT ACT GTA CGG TTA GA-3′, Sgc8-c-NH$_2$) was purchased by IDT technologies (Integrated DNA Technologies, Coralville, USA). ESI-MS was performed by IDT technologies. All buffers were prepared with sterilized MilliQ water.

Advance of the reaction and quality of the product were followed by reverse-phase HPLC chromatography (RP-HPLC) (Agilent 1200 Series Infinity Star, Santa Clara-USA) with a 5 μm C-18 Kinetex column (Phenomenex) run with aqueous solution of triethylamine (50 mM, pH 7.5)/5% acetonitrile (solvent A) and methanol (solvent B), flow rate 1 ml/min, and performed in a gradient of A:B (90:10) to A:B (40:60) over 30 min (UV detection). Purifications in the scaling-up procedures were performed in same conditions.

2.1.1 | Synthesis of Sgc8-c-DOTA (1)

Sgc8-c-NH$_2$ was reacted with 1,4,7,10-tetraazacyclododecane-1,4,7,10-tetraacetic acid mono-N-hydroxysuccinimide ester as HPF6 · CF$_3$CO$_2$H salt (NHS-DOTA, B-280, Macrocyclics, Inc. TX-USA) as: NHS-DOTA (26.0 mg, 34 μmol) dissolved in dry DMSO (3.85 μl) was added to a solution of Sgc8-c-NH$_2$ (2.2 mg, 0.17 μmol) dissolved in a mixture of equal volume of sodium phosphate buffer (0.1 M) and sodium bicarbonate (0.1 M), at final volume of 400 μl, pH = 8.3. The mixture of reaction was stirred at room temperature for 2 hr. Reaction was stopped by MilliQ washing of Sgc8-c-DOTA by microcon® Centrifugal Filters (10 kDa cutoff) or PD10 column (GE Healthcare Life Sciences, Little Chalfont-UK) and followed by spectrophotometry at 260 nm. Yield (by RP-HPLC) = 77%; ESI-MS = 13238.5 Da (with co-ordinated potassium); expected: 13238.5 Da (with co-ordinated potassium). In addition, molecular weight changes were followed by gel electrophoresis (native polyacrylamide (15%)).

After purification by RP-HPLC, fractions, corresponding to the product, were stored at −20 and 4°C dissolved in MilliQ water or lyophilized.

2.1.2 | Synthesis of Sgc8-c-NOTA (2)

Sgc8-c-NH$_2$ was reacted with 2-S-(4-isothiocyanatobenzyl)-1,4,7-triazacyclononane-1,4,7-triacetic acid as 3 HCl salt (p-SCN-Bn-NOTA, B-605, Macrocyclics, Inc. TX-USA)

as: p-SCN-Bn-NOTA (20.0 mg, 36 μmol) dissolved in dry DMSO (4.5 μl) was added to a solution of **Sgc8-c-NH₂** (2.3 mg, 0.18 μmol) dissolved in a mixture of equal volume of sodium phosphate buffer (0.1 M) and sodium bicarbonate (0.1 M), at final volume of 400 μl, pH = 8.3. The mixture of reaction was stirred at room temperature for 2 hr. Reaction was stopped by MilliQ washing of **Sgc8-c-NOTA** by microcon® Centrifugal Filters (10 kDa cutoff) or PD10 column (GE Healthcare Life Sciences, Little Chalfont-UK) and followed by spectrophotometry at 260 nm. Yield (by RP-HPLC) = 70%; ESI-MS = 13325.6 Da (as sodium salt and with co-ordinated potassium); expected: 13325.0 Da (as sodium salt and with co-ordinated potassium). In addition, the molecular weight changes were followed by gel electrophoresis (native polyacrylamide (15%)).

After purification by RP-HPLC, fractions, corresponding to the product, were stored at −20 and 4°C dissolved in MilliQ water or lyophilized.

2.1.3 | Synthesis of Sgc8-c-HYNIC (3)

Sgc8-c-NH₂ was reacted with 6-(2-trifluoroacetylhydrazinyl) nicotinic acid N-hydroxysuccinimide ester (NHS-HYNIC-TFA)[30] as: NHS-HYNIC-TFA (2.7 mg, 7.8 μmol) dissolved in dry DMSO (1.8 μl) was added to a solution of **Sgc8-c-NH₂** (0.5 mg, 0.04 μmol) dissolved in a mixture of equal volume of sodium phosphate buffer (0.1 M) and sodium bicarbonate (0.1 M), at final volume of 400 μl, pH = 8.3. The mixture of reaction was stirred at room temperature for 2 hr. Reaction was stopped by MilliQ washing of **Sgc8-c-HYNIC** by microcon® Centrifugal Filters (10 kDa cutoff) or PD10 column (GE Healthcare Life Sciences, Little Chalfont-UK) and followed by spectrophotometry at 260 nm. Yield (by RP-HPLC) = 48%; ESI-MS = 13044.3 Da; expected: 13045.0 Da. In addition, the molecular weight changes were followed by gel electrophoresis (native polyacrylamide (15%)).

After purification by RP-HPLC, fractions, corresponding to the product, were stored at −20 and 4°C dissolved in MilliQ water or lyophilized.

2.2 | Stability studies

2.2.1 | Physical stability

Thermal stability
Stabilities of the aptamer conjugates, including **Sgc8-c-Alexa647**,[28] were checked at different temperatures, 25, 37, 45, 60, and 75°C, incubating on MilliQ water during 30 min.

After time-points, aliquots of the reaction mixture were filtered (0.22 μm) and analyzed by RP-HPLC (see previous conditions) and gel electrophoresis.

Briefly, for the gel electrophoresis, 1 μg of the sample was suspended on MilliQ water (10 μl), heated at 75°C for 10 min, chilled on ice for 10 min, and mixed with run buffer (1 μl). The samples were loaded into the gel. The gel electrophoreses were performed on 15% native polyacrylamide gel in 1× TAE buffer using a constant voltage of 100 V and an amperage of 0.04 A. Silver nitrate staining was used for visualization. The molecular ruler Bio-Rad 170-8201, for 20 bp, was used as molecular weight marker.

Stability in storage conditions
Additionally, stabilities of the aptamer conjugates, including **Sgc8-c-Alexa647**,[28] were weekly checked storing them, dissolving on MilliQ water, or lyophilized, at −20 and 4°C, during 30 days.

After time-points, aliquots of the reaction mixture were filtered (0.22 μm) and analyzed by RP-HPLC and gel electrophoresis as described above.

2.2.2 | Functional stability

Aptamer conjugates, including **Sgc8-c-Alexa647**,[28] (10 pmol) were incubated with DNAse I (0.2 units) in aqueous solution of NaCl (0.9%) at room temperature during 2 hr.

After time-points, samples were analyzed by gel electrophoresis as described above.

3 | RESULTS AND DISCUSSION

3.1 | Covalent bonding of chelators to aptamer Sgc8-c

Given our previous results,[28] we decided to use the Sgc8-c aliphatic amine derivative, **Sgc8-c-NH₂** (Figure 1), as starting nucleophilic material and evaluate the reaction with various activated bifunctional agents. Gentle and room temperature reactions were chosen for this. In this sense, we used 1,4,7,10-tetraazacyclododecane-1,4,7,10-tetraacetic acid mono-N-hydroxysuccinimide ester (NHS-DOTA), 2-S-(4-isothiocyanatobenzyl)-1,4,7-triazacyclononane-1,4,7-triacetic acid (p-SCN-Bn-NOTA), and 6-(2-trifluorocetylhydrazinyl)nicotinic acid N-hydroxysuccinimide ester (NHS-HYNIC-TFA) as electrophilic reagents (Figure 1). These entities have demonstrated their ability to co-ordinate different metallic ions to produce new radiopharmaceuticals and, according to these structural differences, to produce conjugates ((**1**), (**2**), and (**3**), Figure 1) with different physicochemical properties, that is, lipophilicity, stability, water solubility, and consequently different biodistribution properties.[31,32] On the one hand, due to the potential instability of the aptamer in the reaction milieu conditions and, on the other hand, the need to perform rapid syntheses in the production of radiopharmaceuticals, the following variables were studied that would guarantee
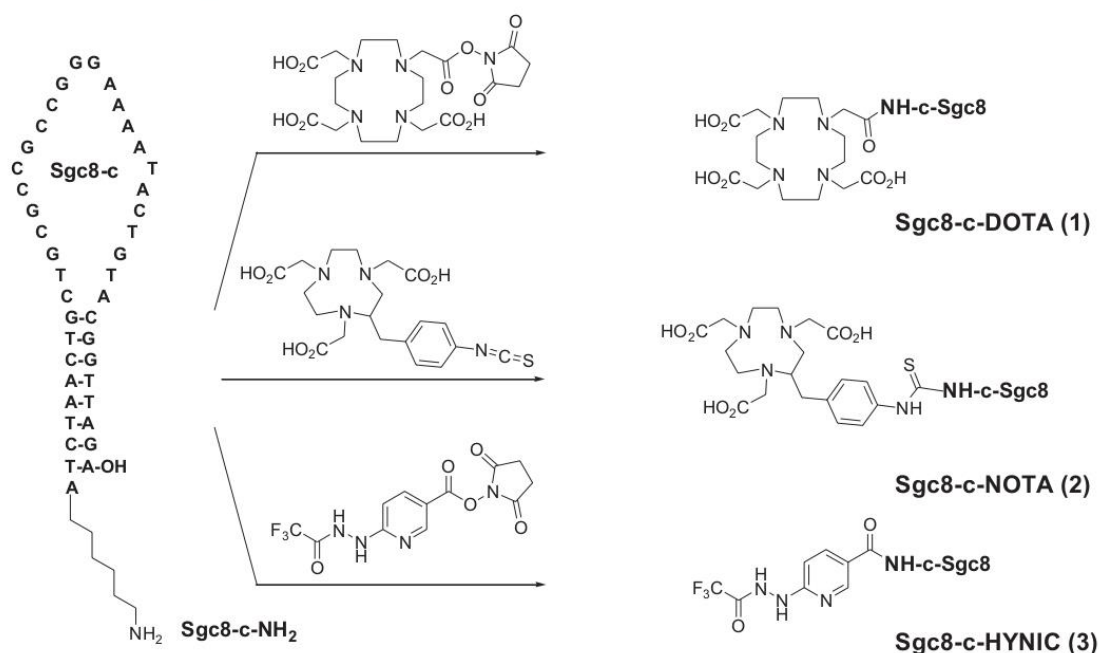
FIGURE 1 Organic chemistry reaction for the syntheses of Sgc8-c-metallic ions coordinators ((**1**)-(**3**))

rapid and efficient procedures: (i) reactants molar ratios; (ii) time; and (iii) solvent of reaction. The advances of the reactions and the desired products yields were studied by reverse-phase HPLC chromatography (RP-HPLC). In reference to the temperature of reactions, although the stability of aptamers is guaranteed even at high temperatures,[33] we performed the optimization studies always at room temperature.

Firstly, the reactants molar ratios were varied, between 1:2 and 1:200 (aptamer:activated chelators), using sodium bicarbonate buffer (0.1 M, pH = 8.3) as solvent of aptamer and DMSO to dissolve NHS-DOTA, *p*-SCN-Bn-NOTA, or NHS-HYNIC-TFA (for details, see Experimental Section), at room temperature and during 2 hr. The results showed that the yields increased with the amount of the electrophiles (Figure 2a) resulting the best conditions, in all the cases, where the ratio was 1:200.

Secondly, due to the low yields in the cases of conjugates **Sgc8-c-DOTA (1)** and, especially **Sgc8-c-HYNIC (3)** (Figure 2a), at 1:200 ratio, led us to analyze different reaction times varying it between 0.5 and 24 hr. The results clearly showed that the increase in reaction time conducted to lower yields of products resulting the best time of incubation 2 hr (Figure 2b). Over 24 hr, no significant changes in yields were observed.

Thirdly, trying to improve the conjugates yields, we analyzed different solvents of reactions assaying different aqueous buffer solutions. The nature and ionic strength of the

buffer, in which aptamer–ligand interaction occurs, could significantly influence in the biological binding.[34] On the other hand, no previous aptamer synthetic studies using different buffers have been performed.[34,35] In this sense, besides sodium bicarbonate buffer (0.1 M, pH = 8.3), sodium phosphate buffer (0.1 M, pH = 8.3), and a mixture of equal volume of both buffers were studied as solvent of reactions. In these studies, we also included the effect of buffers in the yield of **Sgc8-c-Alexa647**[28] preparation. When sodium bicarbonate buffer was changed by sodium phosphate buffer, a clear increment in the yields was observed in all the cases being, especially for **Sgc8-c-HYNIC (3)** (Figure 3a), still low. For this reason, we probed mixtures of both buffers, finding that equal volumes of both buffers produced the best yields of the desired conjugates (Figure 3b) reaching the highest values of 77% for **Sgc8-c-DOTA (1)**, 70% for **Sgc8-c-NOTA (2)**, 48% for **Sgc8-c-HYNIC (3)**, and 52% for **Sgc8-c-Alexa647**.

These syntheses were scaled up to a level of five times with identical results in yields. For future radiolabeling steps is very important to start from a pure sample due to additional radiolabeled reactions could be produced extra impurities turning a poor final product. In this sense, we performed effort to take off the **Sgc8-c-NH₂** from conjugated sample. By RP-HPLC, isolation purities higher than 99% of the conjugates (**1**)–(**3**) were obtained. The RP-HPLC profiles of the scaling-up procedures are shown in Figure 4.

46
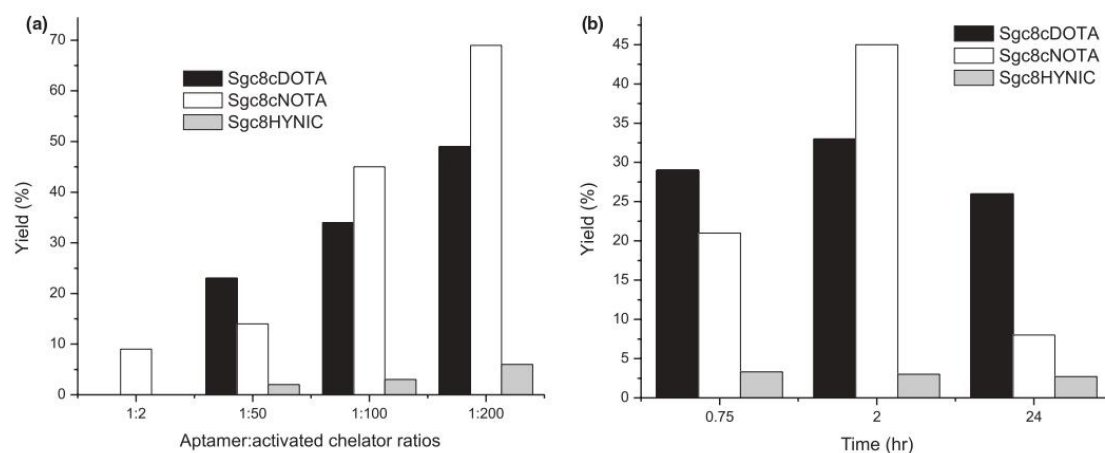
FIGURE 2 Conjugates (1)-(3) yields in different synthetic experimental conditions (a) varying the ratio aptamer:activated chelators (in sodium bicarbonate buffer, 0.1 M, pH= 8.3, at room temperature and during 2 h of incubation); (b) varying the time of reaction (in sodium bicarbonate buffer, 0.1 M, pH= 8.3, at room temperature and in an aptamer:activated chelators ratio of 1:100)
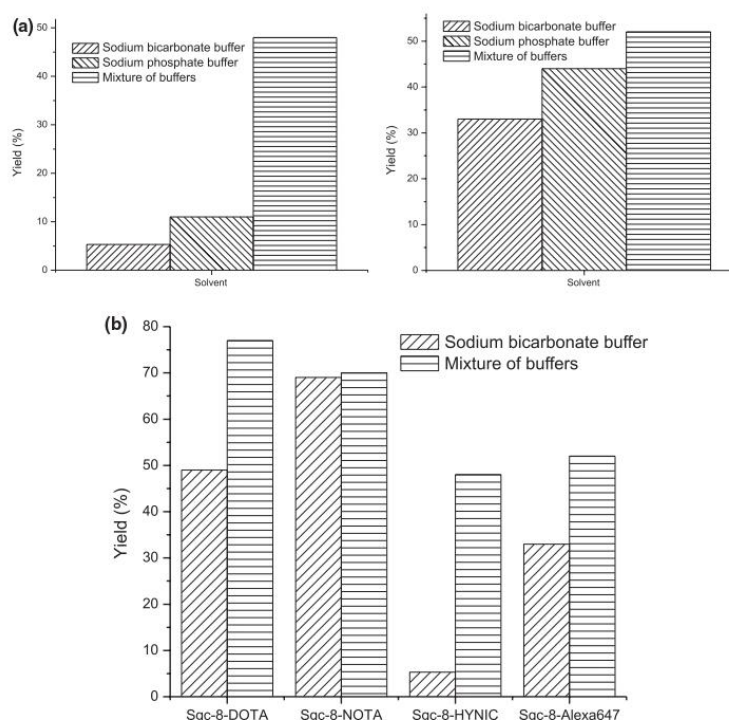
FIGURE 3 Conjugates (1)-(3) and **Sgc8-c-Alexa647**[28] yields using different aqueous buffers of reactions (a) **Sgc8-c-HYNIC** (left) and **Sgc8-c-Alexa647** (right) syntheses (in a **Sgc8-c-NH₂**:NHS-HYNIC-TFA and Sgc8-c-NH2:NHS-Alexa647 ratios of 1:200, at room temperature and during 2 h of incubation); (b) Conjugates (1)-(3) and **Sgc8-c-Alexa647** syntheses (in reactants ratios of 1: 200, at room temperature and during 2 h of incubation)

3.2 | Confirmation of the incorporation of chelators

3.2.1 | ESI-MS studies

The conjugates were obtained free of residual-activated chelators and unreacted chemical reagents by size exclusion filter (10 kDa cutoff). In order to know the incorporation of chelators to the aptamer we isolated, from the RP-HPLC in the scaling-up procedures (Figure 4), and analyzed by ESI-MS each compound present in the synthetic reaction milieus. Surprisingly, significant changes in time retention on RP-HPLC were observed for each isolated probe (Figure 4, $t_{R, Sgc8-c-NH2}$ = 11.4 min, $t_{R, Sgc8-c-DOTA}$ = 12.5 min,
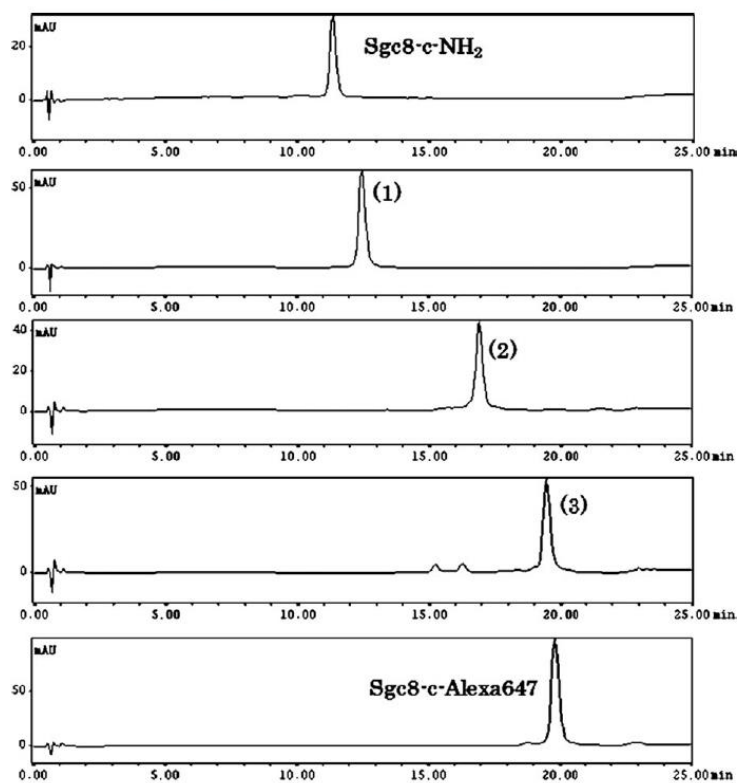
FIGURE 4 RP-HPLC of the products isolated after the scaling-up procedures

$t_{R, \text{Sgc8-c-NOTA}} = 16.9$ min, $t_{R, \text{Sgc8-c-HYNIC}} = 19.4$ min, $t_{R, \text{Sgc8-c-Alexa647}} = 19.8$ min).

The ESI-MS analyses (see example in Fig. S1b) showed that the first RP-HPLC-eluted product corresponded, in all the cases, to **Sgc8-c-NH₂**. Particularly, in the case of the synthesis of **Sgc8-c-HYNIC (3)**, a third product, with intermediate t_R, was isolated (product **(B)** in Fig. S1a) in a yield of <10%. According to the ESI-MS results, product **(B)** corresponded to the **Sgc8-c-NH₂** as trifluoroacetate salt (Figure 5) coming from that counterion of the hydrolysis of NHS-HYNIC-TFA reagent on the reaction condition. Consequently, the lowest yield in the conjugation of **(3)** could be explained by the low nucleophilicity of **Sgc8-c-NH₂** in this condition.

In all the cases, the ESI-MS experiments confirmed the incorporation of one unit of chelators per unit of **Sgc8-c-NH₂**.

3.2.2 | Gel electrophoresis studies

Molecular weight analysis of each conjugate was also performed using gel electrophoresis. The results of these experiments were completely in agreement with those of ESI-MS confirming the molecular weight of the desired conjugates **(1)–(3)** (Figure 5). In these experiments, we included the previously fluorescent probe developed by us,[28] that is, **Sgc8-c-Alexa647**,
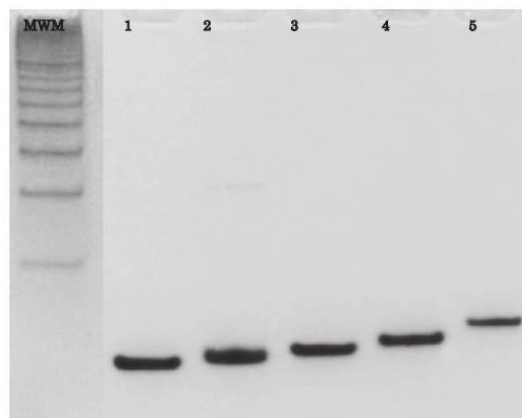
FIGURE 5 Polyacrylamide 15% electrophoresis profiles. **1:** Sgc8-c-NH2; **2:** Sgc8-c-HYNIC; **3:** Sgc8-c-DOTA; **4:** Sgc8-c-NOTA; **5:** Sgc8-c-Alexa647. **MWM:** DNA-molecular weights marker

migrating according to its expected molecular weight. The different conjugates are migrated following their molecular weight: $MW_{\text{Sgc8-c-NH2}} = 12{,}813$ Da, $MW_{\text{Sgc8-c-HYNIC (3)}} = 13{,}045$ Da, $MW_{\text{Sgc8-c-DOTA (1)}} = 13{,}238$ Da, $MW_{\text{Sgc8-c-NOTA (2)}} = 13{,}325$ Da, and $MW_{\text{Sgc8-c-Alexa647}} = 13{,}678$ Da. In
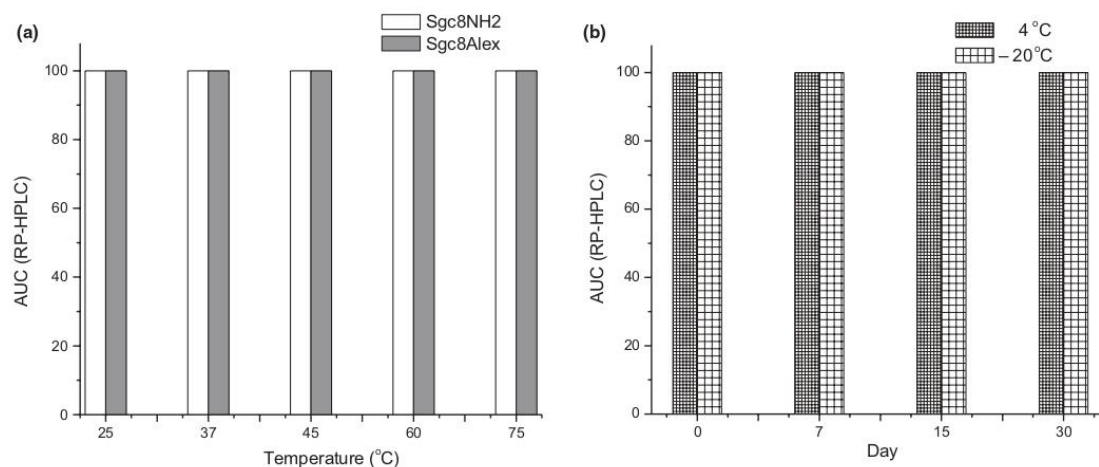
FIGURE 6 Stability results in (a) aqueous solution at different temperatures; and (b) in storage conditions with the time

general, profiles consistent with low molecular weight fragmentation were not detected (Figure 5) ensuring the quality of the synthetic products and the purification processes.

3.3 | Stability studies of the conjugates

Physical stabilities of the conjugates (1)–(3) and **Sgc8-c-Alexa647** were analyzed in MilliQ water, at different temperatures, and under different storage conditions during the time. According to RP-HPLC and gel electrophoresis profiles, the conjugates were stable in water up to 75°C for 30 min of incubation (Figure 6a). Additionally, RP-HPLC and gel electrophoresis results confirmed the integrity of each conjugate, (1)–(3) and **Sgc8-c-Alexa647**, under the different storage assayed conditions, that is, dissolved in MilliQ water and lyophilized, and during the time (at least for 30 days) (Figure 6b). In all the cases, electrophoresis profiles were consistent with the absence of low molecular weight fragmentation.

Functional stabilities toward DNAse showed that after 15 min and 2 hr of incubation, the conjugates (1)–(3) and **Sgc8-c-Alexa647**, such as the parent aptamer **Sgc8-c-NH₂**, suffered from relevant degradation. However, image analyses resulted on the conjugates (1)–(3) were found to be more resistant against degradation than fluorescent probe 15 min after enzyme incubation (Figure 7). After 2 hr, no significant differences are observed but still remaining some aptamer without degradation for all samples.

4 | CONCLUSIONS

The molecular strategy of selectively targeting the supply of radiopharmaceuticals has the potential to improve results while simultaneously minimizing exposure of normal tissues.
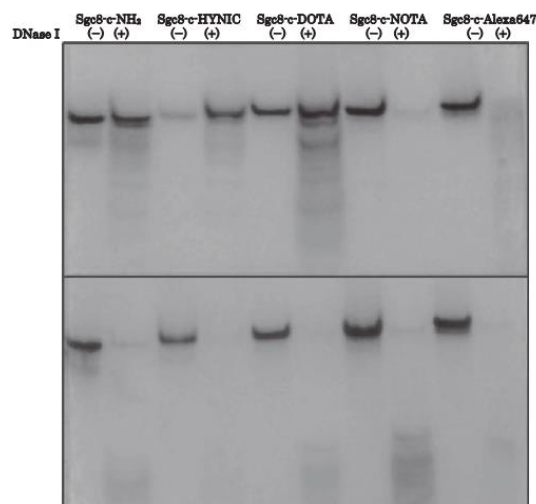
FIGURE 7 Polyacrylamide 15% electrophoresis profiles. Top: 15 min of incubation; Bottom 2 h of incubation

In this sense, the molecular design and the corresponding synthetic organic chemistry that allow the use of covalent bonding to different ionic-metal chelators or bioactive frameworks to a specific aptamer have previously been described.[12,28,36–39]

In this article, a series of Sgc8-c aptamer derivatives with ionic–metallic chelator frameworks were designed, synthesized, and physicochemical characterized as potential chelators of radionuclide to prepare molecular radiopharmaceutical probes. The organic chemistry reactions used herein for the synthesis of conjugates (1), (2), and (3) were performed: (i) in relatively short reactions times; (ii) with organic solvent compatibility, that is, DMSO; (iii) with the absence of secondary

reactions; (iv) with the absence of aptamer degradation; (v) in good-to-excellent yields of the desired products; and (vi) with flexibility to be used with other aptamers. The generated products, (1), (2), and (3), showed different retention times on RP-HPLC. This feature could be explained by significative differences on the lipophilicities of the different used chelator frameworks. Thus, this difference could modify the in vivo biological behavior, especially the biodistribution and clearance, and it should be further studied. The chelator framework could also be the responsible of conjugates stabilities.

High purity of probes is a main step to get good radiopharmaceutical yields. The implemented purification processes, RP-HPLC, allowed to obtain the desired conjugates (1), (2), and (3) with adequate purity, with the absence of any detectable low molecular weight aptamer fragments or large molecular weight aptamer aggregates, and retained biological activity.[28] Additionally, the conjugates displayed good stabilities in conditions for further radiolabeled processes, aqueous milieu up to 70°C, and in typical aptamer storage conditions.

4.1 | Future directions

The generated conjugates potentially could provide a spectrum of desirable new radiopharmaceutical molecular probes with the ability to locate on the exterior surface membrane of tumor cells.

Given this perspective, the covalent aptamer chelators represent potential molecular strategy for enhancing imaging procedures to detect many neoplastic cell types that overexpress PTK7 membrane receptor.

Currently, we are working in the optimization of radiolabeling processes with ^{67}Ga or ^{99m}Tc with (1) and (2) or (3), respectively.

CONFLICT OF INTEREST

The authors declare no conflict of interest.

ORCID

Hugo Cerecetto http://orcid.org/0000-0003-1256-3786

REFERENCES

[1] R. Weissleder, U. Mahmood, *Radiology* **2001**, *219*, 316.

[2] S. N. Histed, M. N. Lindenberg, E. Mena, B. Turkbey, P. L. Choyke, K. A. Kurdziel, *Nucl. Med. Commun.* **2012**, *33*, 349.

[3] S. L. Gibbs, *Quant. Imaging Med. Surg.* **2012**, *2*, 177.

[4] K. M. Tichauer, K. S. Samkoe, K. J. Sexton, S. K. Hextrum, H. H. Yang, W. S. Klubben, J. R. Gunn, T. Hasan, B. W. Pogue, *Mol. Imaging Biol.* **2012**, *14*, 584.

[5] K. Oishi, A. V. Faria, S. Yoshida, L. Chang, S. Mori, *Int. J. Dev. Neurosci.* **2013**, *31*, 512.

[6] M. L. James, S. S. Gambhir, *Physiol. Rev.* **2012**, *92*, 897.

[7] R. R. Breaker, *Nature* **2004**, *432*, 838.

[8] B. J. Hicke, A. W. Stephens, T. Gould, Y. F. Chang, C. K. Lynott, J. Heil, S. Borkowski, C. Hilger, G. Cook, S. Warren, P. G. Schmidt, *J. Nucl. Med.* **2006**, *47*, 668.

[9] H. Shi, W. Cui, X. He, Q. Guo, K. Wang, X. Ye, J. Tang, *PLoS ONE* **2013**, *8*, e70476.

[10] K. E. Borbas, C. S. Ferreira, A. Perkins, J. I. Bruce, S. Missailidis, *Bioconjug. Chem.* **2007**, *18*, 1205.

[11] D. W. Hwang, H. Y. Ko, J. H. Lee, H. Kang, S. H. Ryu, I. Song, D. S. Lee, S. A. Kim, *J. Nucl. Med.* **2010**, *51*, 98.

[12] M. Gijs, A. Aerts, N. Impens, S. Baatout, A. Luxen, *Nucl. Med. Biol.* **2016**, *43*, 253.

[13] V. K. Sharma, R. K. Sharma, S. K. Singh, *Med. Chem. Commun.* **2014**, *5*, 1454.

[14] L. C. Ho, W. C. Wu, C. Y. Chang, H. H. Hsieh, C. H. Lee, H. T. Chang, *Anal. Chem.* **2015**, *87*, 4925.

[15] N. M. Danesh, P. Lavaee, M. Ramezani, K. Abnous, S. M. Taghdisi, *Int. J. Pharm.* **2015**, *489*, 311.

[16] S. M. Khoshfetrat, M. A. Mehrgardi, *Bioelectrochemistry* **2016**, *114*, 24.

[17] W. Niu, W. X. Chen, W. Tan, A. S. Veige, *Angew. Chem. Int. Ed. Engl.* **2016**, *55*, 8889.

[18] X. Ye, H. Shi, X. He, Y. Yu, D. He, J. Tang, Y. Lei, K. Wang, *Nanoscale* **2016**, *8*, 2260.

[19] D. Shangguan, Z. Tang, P. Mallikaratchy, Z. Xiao, W. Tan, *ChemBioChem* **2007**, *8*, 603.

[20] W. S. Shin, Y. S. Maeng, J. W. Jung, J. K. Min, Y. G. Kwon, S. T. Lee, *Biochem. Biophys. Res. Commun.* **2008**, *371*, 793.

[21] F. Puppo, V. Thome, A. C. Lhoumeau, M. Cibois, A. Gangarw, F. Lembo, E. Belotti, S. Marchetto, P. Lecine, T. Prebet, M. Sebbagh, W. S. Shin, S. T. Lee, L. Kodjabachian, J. P. Borg, *EMBO Rep.* **2011**, *12*, 43.

[22] H. K. Lee, S. K. Chauhan, E. Kay, R. Dana, *Blood* **2011**, *17*, 5762.

[23] V. S. Golubkov, N. L. Prigozhina, Y. Zhang, K. Stoletov, J. D. Lewis, P. E. Schwartz, R. M. Hoffman, A. Y. Strongin, *J. Biol. Chem.* **2014**, *289*, 24238.

[24] H. Endoh, S. Tomida, Y. Yatabe, H. Konishi, H. Osada, K. Tajima, H. Kuwano, T. Takahashi, T. Mitsudomi, *J. Clin. Oncol.* **2004**, *22*, 811.

[25] Y. Lin, L. H. Zhang, X. H. Wang, X. F. Xing, X. J. Cheng, B. Dong, Y. Hu, H. Du, Y. A. Li, Y. B. Zhu, N. Ding, Y. X. Du, J. Y. Li, J. F. Ji, *J. Surg. Oncol.* **2012**, *106*, 880.

[26] H. Zhang, A. Wang, S. Qi, S. Cheng, B. Yao, Y. Xu, *Int. J. Mol. Sci.* **2014**, *15*, 11665.

[27] S. Gärtner, A. Gunesch, T. Knyazeva, P. Wolf, B. Högel, W. Eiermann, A. Ullrich, P. Knyazev, B. Ataseven, *PLoS ONE* **2014**, *9*, e84472.

[28] V. Calzada, M. Moreno, J. Newton, J. González, M. Fernández, J. P. Gambini, A. Ibarra, A. Chabalgoity, S. Deutscher, T. Quinn, P. Cabral, H. Cerecetto, *Bioorg. Med. Chem.* **2017**, *25*, 1163.

[29] M. Ogawa, C. A. S. Regino, J. Seidel, M. V. Green, W. Xi, M. Williams, N. Kosaka, P. L. Choyke, H. Kobayashi, *Bioconjug. Chem.* **2009**, *20*, 2177.

[30] M. F. García, V. Calzada, X. Camacho, E. Goicochea, J. P. Gambini, T. P. Quinn, W. Porcal, P. Cabral, *Curr. Radiopharm.* **2014**, *7*, 84.

[31] A. Poschenrieder, M. Schottelius, M. Schwaiger, H. Kessler, H. J. Wester, *EJNMMI Res.* **2016**, *6*, 36.

[32] R. C. King, M. B.-U. Surfraz, S. C. G. Biagini, P. J. Blower, S. J. Mathera, *Dalton Trans.* **2007**, *43*, 4998.

[33] K.-M. Song, S. Lee, C. Ban, *Sensors* **2012**, *12*, 612.

[34] M. Kanoatov, S. N. Krylov, *Anal. Chem.* **2016**, *88*, 7421.

[35] M. Alibolandi, K. Abnous, M. Ramezani, H. Hosseinkhani, F. Hadizadeh, *J. Fluoresc.* **2014**, *24*, 1519.

[36] W. M. Rockey, L. Huang, K. C. Kloepping, N. J. Baumhover, P. H. Giangrande, M. K. Schultz, *Bioorg. Med. Chem.* **2011**, *19*, 4080.

[37] C. E. B. de Almeida, L. N. Alves, E. T. Paulino, J. B. Cabral-Neto, S. Missailidis, *Int. J. Pharm.* **2017**, *525*, 334. https://doi.org/10.1016/j.ijpharm.2017.03.086.

[38] Y. Y. Zhou, X. Zhou, *Chem. Biodivers.* **2012**, *9*, 170.

[39] D. Xie, C. Li, L. Shangguan, H. Qi, D. Xue, Q. Gao, C. Zhang, *Sens. Actuators B Chem.* **2014**, *192*, 558.

SUPPORTING INFORMATION

Additional Supporting Information may be found online in the supporting information tab for this article.

How to cite this article: Sicco E, Báez J, Margenat J, et al. Derivatizations of Sgc8-c aptamer to prepare metallic radiopharmaceuticals as imaging diagnostic agents: Syntheses, isolations, and physicochemical characterizations. *Chem Biol Drug Des*. 2018;91:747–755. https://doi.org/10.1111/cbdd.13135

4.1.1. Material suplementario del artículo I
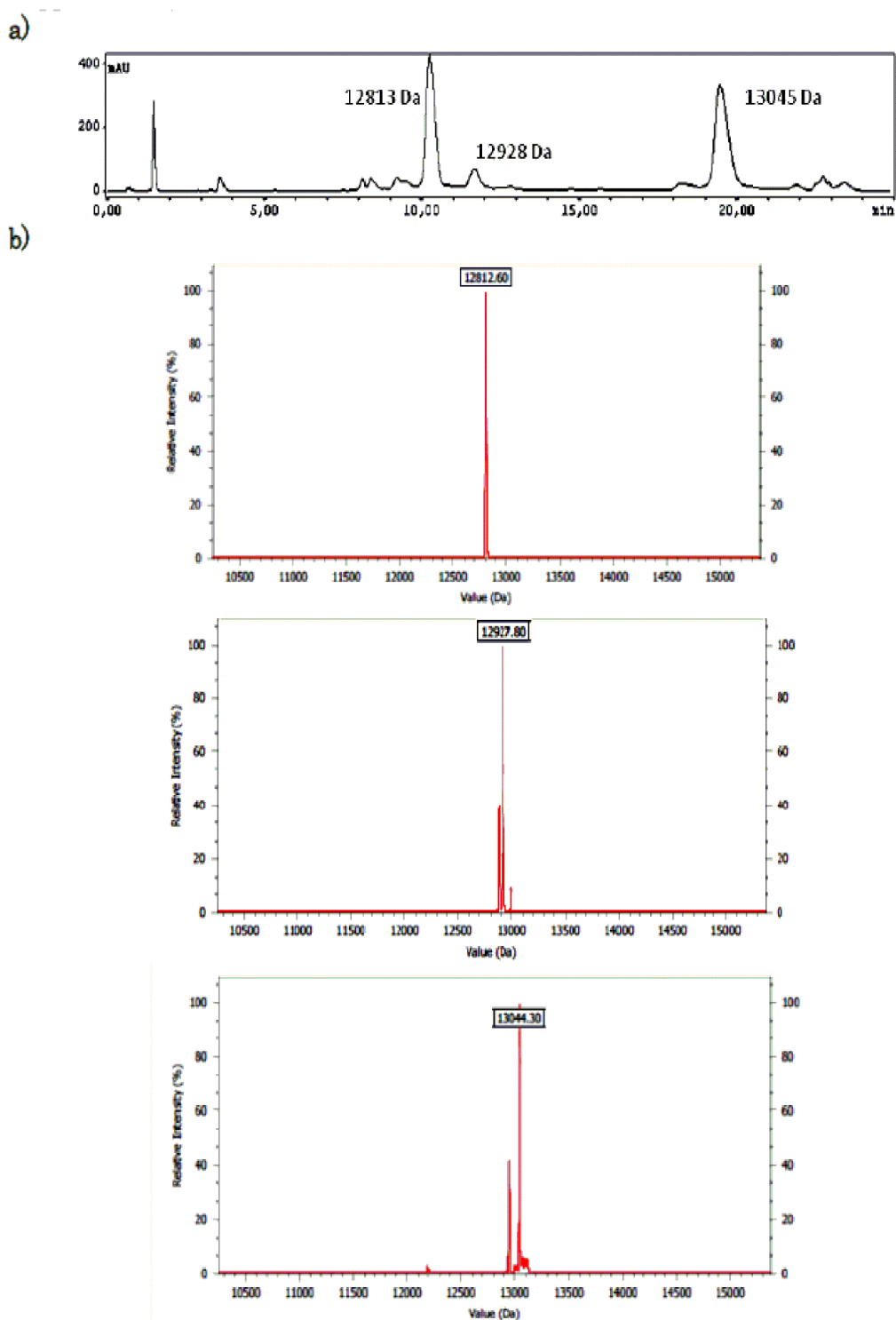
FIGURE S1 (a) RP-HPLC profiles of the scaling-up procedure of the preparation of **Sgc8-c-HYNIC**. The results of the ESI-MS of each isolated product are shown. **(b)** ESI-MS for the main products present in the **Sgc8-c-HYNIC** synthesis reaction milieu. Top to bottom: products according to increasing t_R in RP-HPLC (see Figure S1a).

Síntesis y purificación de la sonda fluorescente: Sgc8-c-Alexa647

La síntesis de la sonda Sgc8-c-Alexa647 se realizó teniendo como base el protocolo descripto anteriormente en el laboratorio (Calzada, 2017a) y el protocolo utilizado para la generación de los tres derivados del aptámero mencionados en el artículo I (Sicco, 2018). Brevemente, el aptámero Sgc8-c-NH$_2$ se disolvió en el buffer de reacción de la mezcla de volúmenes iguales de fosfato de sodio (0,1M) / bicarbonato de sodio (0,1M), y se reaccionó con el doble de concentración de NHS Alexa Fluor™ 647 disuelto previamente en DMSO seco; a pH: 8,32. La reacción se agitó a temperatura ambiente durante 2 h, y se detuvo con lavados con MiliQ mediante filtros centrífugos microcon® (corte de 10 kDa). Se obtuvo un rendimiento por RP-HPLC del 55,1% y se purificó también mediante RP-HPLC, obteniendo una pureza > 99%. Las condiciones utilizadas en el RP-HPLC fueron las mismas que para los derivados generados en el artículo I (Sicco, 2018).

4.2. Artículo II: Síntesis, caracterización y evaluación biológica de la sonda Sgc8-c-NOTA-^{67}Ga.

Los resultados publicados en este artículo fueron destacados en una carta al editor (Filippi, 2020).

Sgc8-c Aptamer as a Potential Theranostic Agent for Hemato-Oncological Malignancies

Estefanía Sicco,[1] Jessica Baez,[1] Manuel Ibarra,[2] Marcelo Fernández,[3]
Pablo Cabral,[1] María Moreno,[4] Hugo Cerecetto,[1] and Victoria Calzada[1]

Abstract

Background: Aptamers represent an emerging class of oligonucleotides that have the ability to bind ligands with high affinity. Sgc8-c aptamer recognizes PTK7, a member of the catalytically defective receptor protein tyrosine kinase family that is upregulated in various cancers, including hemato-oncological malignancies. Herein, an Sgc8-c-NOTA-radiolabeled probe was prepared for theranostic purpose.

Materials and Methods: In this work, an Sgc8-c-radiolabeled probe against PTK7 was prepared, and biological evaluations—pharmacokinetic studies, biodistribution analysis, and *in vivo* molecular imaging—were performed. To obtain the radiolabeled probe, a modified 5′-amino-derivative of the Sgc8-c aptamer was bound to the metal chelator NOTA, and subsequently labeled with ^{67}Ga with high yield and radiochemical purity. The precursor, Sgc8-c-NOTA, the radio probe Sgc8-c-NOTA-^{67}Ga, and its nonradioactive complex, Sgc8-c-NOTA-$^{69/71}$Ga, were purified by reverse-phase high-performance liquid chromatography and characterized by electrospray ionization mass spectrometry. The binding ability of Sgc8-c-NOTA-^{67}Ga was studied *in vitro* against purified PTK7 receptor. In addition, the binding was also evidenced against the hemato-oncological A20 cell line, derived from B lymphocytes, and the corresponding A20-green fluorescent protein (GFP)-transfected cells. The proof of concept was performed on A20-GFP tumor-bearing mice, in which the biodistribution of the radiolabeled probe was evaluated through imaging, using X-ray, fluorescence, and γ modalities. The specific uptake of the probe was confirmed by blocking with the Sgc8-c aptamer in an *in vivo* competition assay.

Results: The biodistribution results showed considerable uptake in tumor since 2 h, with highest at 48 h postinjection. However, the blood and muscle ID/g (injected dose per gram of tissue) activities were decreasing with time and tumor/no-target ratios increasing to 20 at 24 h postinjection. These results are consistent with the *in vivo* images.

Conclusions: This study supports the utility of Sgc8-c-NOTA radiolabeled as a theranostic agent.

Keywords: aptamer, PTK7, lymphoma, theranostic

Introduction

Aptamers are small single-stranded oligonucleotides highly selective for different targets.[1] They can be artificially selected by the Systematic Evolution of Ligands by Exponential Enrichment (SELEX) against a large variety of targets from small molecules to live cells.[2–5] Thus, a wide range of biotechnology purposes have been developed such as biosensors,[6] drug delivery systems,[7] flow cytometry, imaging, diagnostics,[8] and therapeuthics.[9] Aptamers are considered promising tools safe for *in vivo* use, as they have been reported to possess essential clinical aspects, such as

[1]Departamento de Radiofarmacia, Centro de Investigaciones Nucleares, Facultad de Ciencias, Universidad de la República, Montevideo, Uruguay.
[2]Departamento de Ciencias Farmaceuticas, Facultad de Química, Universidad de la República, Montevideo, Uruguay.
[3]Laboratorio de Experimentacion Animal, Centro de Investigaciones Nucleares, Facultad de Ciencias, Universidad de la República, Montevideo, Uruguay.
[4]Departamento de Desarrollo Biotecnológico, Instituto de Higiene, Facultad de Medicina, Universidad de la República, Montevideo, Uruguay.

Address correspondence to: Victoria Calzada; Departamento de Radiofarmacia, Centro de Investigaciones Nucleares, Facultad de Ciencias, Universidad de la República; Mataojo 2055, Montevideo 11200, Uruguay
E-mail: **hcerecetto@cin.edu.uy**

nonimmunogenic and nontoxic properties.[10] However, aptamers have been shown to be rapidly degraded by nucleases, and for this reason, different chemical modifications have been reported for prestabilization and protection.[11] Moreover, chemical modifications could modulate fundamental aspects like residence time circulation and tissue distribution.[12]

Sgc8-c is a 41 nb DNA aptamer selected with cell-SELEX by Tan et al.[13] This aptamer recognizes PTK7, a member of the catalytically defective receptor protein tyrosine kinase family, which is overexpressed in several cancer cell lines. Patient screenings have demonstrated that PTK7 is expressed in hemato-oncological malignancies like acute myeloid leukemia, biphenotypic acute leukemia, and myeloproliferative syndromes.[14] This expression profile makes PTK7 a tumoral marker candidate for developing diagnostic and therapeutic strategies.

In this sense, the authors previously demonstrated the potential of Scg8-c as a molecular imaging agent, for lymphoma and melanoma pathologies, using a fluorescent and two radiolabeled probes. Lymphomas represent a diverse group of neoplastic disorders of lymphocytes and are very frequent, requiring imaging to help the clinician in the therapies.[15] Within the radiolabeled probes, they obtained promising preliminary results with a ^{67}Ga-DOTA Sgc8-c derivative, reporting good tumoral biodistribution and imaging results.[16] This radio probe showed increased liver uptake and bone uptake over time, consistent with hepatobiliary metabolism and some potential degree of instability of coordinated gallium. In addition, tumor/blood and tumor/muscle ratios were higher than 6, increasing with time. This *in vivo* behavior could be modified using a different Ga chelator, such as NOTA (1,4,7-triazacyclononane-1,4,7-triacetic acid).[17] To verify the chelator influence, herein, they report on the synthesis of a second series of ^{67}Ga-radiolabeled Sgc8-c, using 4-{[1,4,7-tri(carboxymethyl)-1,4,7-triazacyclononane-2-yl]methyl}phenylthiourea as a connector/chelator and its evaluation *in vitro* and *in vivo*. *In vitro* studies included the determination of logD, PTK7- and cell-binding abilities. *In vivo* experiments included determination of pharmacokinetic behavior, biodistribution, and imaging using a pre-established model of hemato-tumor-bearing animals.[18]

Materials and Methods

General methods

Chemistry. Pure commercially available materials, reagents, and solvents were used without further purification. 5′-Aminohexyl-modified Sgc8-c aptamer ($\sim$ 13 kDa, Sgc8-c-NH$_2$) was purchased from IDT Technologies (Integrated DNA Technologies, Coralville, IO). All buffers and aqueous solutions were prepared using metal-free MilliQ water. As previously described in detail,[19] advance of the reaction and the product quality were followed by reverse-phase high-performance liquid chromatography (RP-HPLC; Agilent 1200 Series Infinity Star, Santa Clara, CA) with a 5 μm C-18 Kinetex column (Phenomenex). For each run, an aqueous solution was used, consisting of triethylamine (50 mM, pH 7.5)/5% acetonitrile (solvent A) and methanol (solvent B), at a flow of rate 1 mL/min, and performed using a gradient of A:B (90:10) to A:B (40:60) over 30 min (ultraviolet [UV] or γ

detections). Purifications of the precursor and gallium complexes were performed with the same solvent gradient.[16,18,19]

Biology. The A20 cell line derived from mouse B lymphocytes of a naturally occurring reticulum cell sarcoma in an old BALB/cAnN mouse was used and obtained from the American Type Culture Collection (Manassas, VA). In addition, A20/green fluorescent protein (GFP)-transfected cells were constructed in the authors' laboratory based on the method described by Kalil et al.[20] Briefly, 2×10^5 cells were transfected with commercial pEGFP-N1 plasmid (Clontech Lab, Palo Alto, CA) (500 ng) in Dulbecco's modified Eagle's medium (50 μL) with lipofectamine (Life Technologies, Carlsbad, CA) for 48 h. Afterward, the culture media were changed and the cells were grown in the presence of geneticin (200 μg/mL) (Sigma-Aldrich, St. Louis, MO) for 1 month. The highest fluorescent cells (0.4%) were selected using flow cytometry (MoFlo; Beckman Coulter, Pasadena, CA). A20 and A20/GFP cells were grown in suspension in RPMI-1640 media (Sigma-Aldrich) supplemented with 10% (v/v) fetal bovine serum (FBS), 2 mM L-glutamine, and 0.05 mM β-mercaptoethanol (Sigma-Aldrich). All cell lines were cultured at 37°C with 5% (v/v) CO$_2$.

Confirmation of PTK7 expression by A20/GFP cells using flow cytometry. Briefly, expression levels were evaluated by staining the cells with the anti-PTK7-PE (phycoerythrin) antibody (Clone Type: Polyclonal, Catalog No: 033359-PE; United States Biological) and detected in a FACS Canto II flow cytometer (BD Biosciences, San Diego, CA). Data were analyzed using FACS Diva and FlowJo software. The human acute lymphoblastic leukemia cell line CCRF-CEM (ATCC, Manassas, VA) was used as a positive control,[14] while the malignant glioma derived cell line U-87 MG (HTB-14RTM; ATCC) was used as a negative control in this study.[21]

Animals. All protocols for animal experimentation were carried out in accordance with guidelines for the care and use of animals and the procedures were approved by the University's Ethical Committee for Animal Experimentation, Uruguay, to whom this project was previously submitted (Approval No: 240011-001891-17). Animals purchased from DILAVE (Montevideo, Uruguay) were housed in boxes with up to five animals and kept with water and food *ad libitum*, with 14 h of light and 10 h of darkness. They were monitored daily, registering the animals' behavior. In the case of animals bearing tumors, the tumors were palpated to record their presence, location, and volume, where they reached a maximum diameter of 5 mm. Isoflurane was used for anesthesia. At the end of the experiments, all animals were sacrificed by cervical dislocation.

Synthesis of Sgc8-c-NOTA

Sgc8-c-NOTA was prepared according to the authors' previous report.[19]

Sgc8-c-NOTA gallium coordination (Sgc8-c-NOTA-Ga)

Sgc8-c-NOTA was coordinated with stable gallium based on the following: Sgc8-c-NOTA (20 μg, 1.5 nmol) was dissolved in ammonium acetate buffer (0.1 M, pH = 6.0, 300 μL) and $^{69/71}$GaCl$_3$ in excess (427128; Sigma-Aldrich) was added.

The mixture was stirred at 60°C for 30 min, and the reaction was followed using RP-HPLC. The new product (checked at $\lambda = 260$ nm, $t_R = 23.6$ min) was collected from the RP-HPLC analysis and the structure was confirmed by electrospray ionization mass spectrometry (ESI-MS; IDT Technologies). Yield: 50%. ESI-MS, Sgc8-c-NOTA-[69/71]Ga, found: 13327.1 Da (M–2H); expected: 13329.5 Da. The same synthetic procedure was performed using radioactive $^{67}GaCl_3$ solution (Tecnonuclear, Buenos Aires, Argentina), using 30.7 MBq per each 0.4 nmol of Sgc8-c-NOTA in a final volume of 1000 μL with ammonium acetate buffer (0.1 M, pH = 6.0). The RP-HPLC radioactive peak had a $t_R = 23.8$ min. The radiolabeling yield and radiochemical purity were monitored using RP-HPLC with a γ detector comparing with retention time of the UV signal of the precursor and cold complex. Radiochemical purity: 97.2%. The final specific activity, calculated by dividing the obtained radioactivity by the mass unit of Sgc8-c-NOTA used for the reaction, was 76.7 MBq/nmol.

In vitro *characterization*

Media reaction stability studies with time and temperature. Sgc8-c-NOTA-^{67}Ga (0.08 nmol) was maintained in media reaction (400 μL) at room temperature (25°C) for 48 h. After 24 and 48 h, aliquots were studied by RP-HPLC. On the other hand, Sgc8-c-NOTA-^{67}Ga (0.08 nmol) was incubated in media reaction (400 μL) at different temperatures (25°C, 37°C, 45°C, 60°C, and 75°C), for 30 min. After the time points, aliquots from samples at each temperature were studied by radio-RP-HPLC.

Serum fetal bovine stability. The probe (0.08 nmol) was incubated with FBS (200 μL) at 37°C for 24 h. After 30 min, and 2 and 24 h, the mixture was filtered by 10 and 30 kDa microcon® centrifugal filters and studied by RP-HPLC.

Distribution coefficient (logD). To determine the distribution of Sgc8-c-NOTA-^{67}Ga between *n*-octanol and phosphate buffered saline (PBS), pH = 7.5, aliquots of the probe (0.075 nmol) were diluted in 500 μL of PBS, and after adding 500 μL of *n*-octanol, the mixture was centrifugated at 13,000 rpm for 10 min at room temperature. Subsequently, aliquots (200 μL) of both layers were collected and measured in a γ counter (PC-RIA MAS; Stratec), followed by the logD calculation ($n = 4$, eight replicates).

Bioactivity experiments

The maximum binding capacity assay was performed following the Lindmo method.[22] Different amounts of pure receptor PTK7-1 (TP700163; Origene, MD) were prepared in triplicate in 2 mL of PBS (pH = 7.5) to give final concentrations of 9×10^{-3}, 18×10^{-3}, 35×10^{-3}, 71×10^{-3}, 0.140, 0.575, 1.150, and 4.600 nM, subsequently adsorbed in Nunc tubes (Brandt®). After incubating for 24 h at 4°C, with continuous gentle orbital shaking, the tubes were washed two times with PBS. Finally, 100,000 cpm of Sgc8-c-NOTA-^{67}Ga was incubated for 2 h at room temperature in the darkness and with continuous orbital shaking. The tubes were washed two times with PBS and the radioactivity was quantified using a γ counter (PC-RIA MAS; Stratec). Non-specific binding was determined by incubating Sgc8-c-NOTA-^{67}Ga without receptor.

Cell binding was studied in A20 and A20/GFP cell lines. All cells were washed twice by gentle centrifugation with sterile PBS (pH = 7.4) and 1.0×10^6 cells were re-suspended in PBS (final volume of 1 mL) and incubated with 100,000 cpm of Sgc8c-NOTA-^{67}Ga. The probe was incubated for 0.5, 2, and 4 h at 37°C. Cells were washed twice with PBS and radioactivity in the pellets was quantified in a γ counter (PC-RIA MAS; Stratec). Competition binding assays were performed with excess Sgc8-c-NH$_2$ (5 μg, 0.4 nmol) incubated for 30 min at 37°C. After incubation with Sgc8-c-NH$_2$, the cells were washed with PBS and incubated with 100,000 cpm of Sgc8c-NOTA-^{67}Ga. The probe was incubated for 2 h at 37°C. The cells were washed twice with PBS and radioactivity in the pellets was quantified as described above.

Pharmacokinetic studies

The pharmacokinetic profile was assessed by administering an intravenous (IV) bolus of individual doses of 5.5–9.2 MBq of Sgc8c-NOTA-^{67}Ga into the tail vein of female Wistar rats, weighting 200–250 g ($n = 3$). Blood samples were collected in a capillary tube from the orbital sinus at 0.25, 0.5, 1, 2, 4, 6, 18, 24, and 48 h following probe administration. Samples were weighed and radioactivity was measured in a γ counter (PC-RIA MAS; Stratec). Urine and fecal matter were also collected over a 48-h period to assess renal elimination. A compartmental pharmacokinetic analysis was performed for blood and urine data using the software for nonlinear mixed-effects modeling NONMEM 7.4.1.[23] Model development was conducted based on the Akaike information criteria and goodness-of-fit plots.

In vivo *experiments*

Tumor model was generated in female BALB-c mice at 4–6 weeks of age, subcutaneously injected with 1×10^6 A20/GFP cells resuspended in 200 μL of culture media. Formation of tumors was observed 2 weeks later, reaching maximum sizes of 5 mm of diameter.[24] No animal died during the study.

Biodistribution. When the tumors were palpable, Sgc8c-NOTA-^{67}Ga (~1850 kBq) was IV administered through the tail vein. At 0.5, 2, 24, 48, and 72 h after probe administration, the mice ($n = 5$ per time point) were sacrificed by cervical dislocation and the organs were weighed and measured in a γ counter (PC-RIA MAS; Stratec). Radioactivity levels in each tissue were expressed as percentages of the injected dose per gram of tissue (%ID/g) and as percentages of injected dose (%ID). An *in vivo* blocking experiment was performed in a separate group ($n = 5$), with a previous injection of 100-fold excess of Sgc8-c-NH$_2$ aptamer. A half hour before the injection of the radioactive probe (~1850 kBq), 0.5 nmol of Sgc8-c-NH$_2$ was administrated through the tail vein. The mice were sacrificed 2 h after the radioactive probe injection and measurements were performed as previously described. Tissue decay correction and organ weight correction were applied, and the tumor/blood and tumor/muscle ratios were calculated.

Imaging. When the tumors were palpable, Sgc8c-NOTA-^{67}Ga (~1850 kBq) was IV administered through the tail vein. After 2, 24, 48, and 72 h, the mice were anesthetized

with isoflurane. Images were taken with the In-Vivo MS FX PRO instrument (Bruker, Billerica), using the X-ray, fluorescence, and γ modes (10 min acquisition). After each imaging time point, the mice were sacrificed for organ dissection and imaged and counted separately using the same imaging instrument (In-Vivo MS FX PRO instrument; Bruker). The organ weight correction was applied and the tumor/blood and tumor/muscle ratios were calculated.

Statistical analysis

Statistical analysis was performed using the Student's t-test with p-values of significance indicated in each case.

Results

Radiolabeling

The synthesis of Sgc8c-NOTA-^{67}Ga was a one-step procedure from the precursor Sgc8-c-NOTA[19] and ^{67}GaCl$_3$, under optimized conditions (Fig. 1). Aptamers are chemically stable in neutral conditions and low temperatures and are soluble in nonorganic solvents. For these reasons, several radiolabeling conditions (pH/buffer of reaction, temperature, time, Sgc8-c-NOTA concentration, and radioactivity) were studied to produce the desired product with high labeling efficiency, in a short time. In all experiments, the highest purity grade reagents available and metal-free water were used to minimize the effects of metal contaminants interfering with gallium radiolabeling.

At pH values between 3 and 7, Ga^{3+} forms insoluble Ga(OH)$_3$, but deprotonation of NOTA-carboxylic moieties for better complexation requires pH higher than 5. Thus, buffer systems with an adequate pH play a relevant role in the labeling procedure. Within this context, two buffer systems of reaction were studied, sodium acetate (0.1 M, pH = 5.0)[25,26] and ammonium acetate (0.1 M, pH = 5.0),[16] at 37°C for 30 min. In sodium acetate buffer, no radiolabeled (rdl) was observed, while a little degree of rdl was evidenced in the ammonium acetate (Supplementary Table S1). Consequently, using ammonium acetate buffer, the authors modified the temperature and time of the reaction, finding that a modest improvement in the rdl was reached working at 60°C, in accordance with their previous findings,[16] decreasing the rdl when the reaction was carried out for up to 45 min (Supplementary Table S1). Due to the very slow gallium incorporation, which was possibly a result of the low pH, they studied two additional pH conditions, pH = 5.5 and pH = 6.0, finding that a slight change in the rdl was

observed at pH = 5.5 (compare rdl for run 2 in Supplementary Table S1 and run 4 in Supplementary Table S2) with best improvement at the highest pH studied (run 7 in Supplementary Table S2).

To establish a mild radiolabeling method in ammonium acetate buffer (0.1 M, pH = 6.0), the complexation reaction was studied at 37°C during the time (Supplementary Table S3). This temperature did not result in better condition and as it was observed in other experiments, prolonged times produced rdl diminution (see also run 3 in Supplementary Table S1 and run 5 in Supplementary Table S2). In contrast, the rdl efficiency at pH = 6.0, 60°C, and 30-min incubation period was dependent on the molar quantity of the precursor (Supplementary Table S4), increasing from 40% to 77% when using 0.08 and 0.4 nmol (corresponding to concentrations of 0.2 and 0.4 μM), respectively, of Sgc8-c-NOTA. Finally, rdl was studied as a function of the ^{67}Ga activity (Fig. 2 and Supplementary Table S5). The rdl efficiency was activity dependent, reaching the best value at 30.7 MBq of ^{67}GaCl$_3$, with a slight decrease at 37 MBq. It showed that higher volumes of the ^{67}Ga solution (Supplementary Table S5) could incorporate higher concentrations of metal cation contaminants, like Fe(III), decreasing the ^{67}Ga incorporation.[27]

In the optimal condition, pH = 6.0, 60°C, 30 min, 0.4 μM of Sgc8-c-NOTA, and 30.7 MBq of ^{67}GaCl$_3$ (run 19 in Supplementary Table S5), purification of the resulting Sgc8-c-NOTA-^{67}Ga was not required, because the rdl was over 95% and the reaction buffer was compatible with biological systems. The identity of Sgc8-c-NOTA-^{67}Ga was investigated by HPLC and ESI-MS. The HPLC analytical results of the Sgc8-c-NOTA-^{67}Ga were compared with the same conjugate that was complexed with stable $^{69/71}$Ga nuclides, using $^{69/71}$GaCl$_3$, under similar conditions at its radioactive counterpart. Figure 3 shows a clear overlap of the corresponding peaks in the UV detector chromatograms of RP-HPLC for the $^{69/71}$Ga-complexed Sgc8-c derivative, Sgc8-c-NOTA-$^{69/71}$Ga, and the ^{67}Ga-radiolabeled desired product, demonstrating similar identities. In addition, the identity of the Sgc8-c-NOTA-$^{69/71}$Ga was confirmed by ESI-MS (Supplementary Fig. S1).

In vitro characterization

The Sgc8-c-NOTA-^{67}Ga distribution coefficient (logD, pH = 7.5) was -2.41 ± 0.11. The results of the stability in media reaction studies showed that the radio probe was stable at room temperature (25°C) for 48 h and up to 75°C
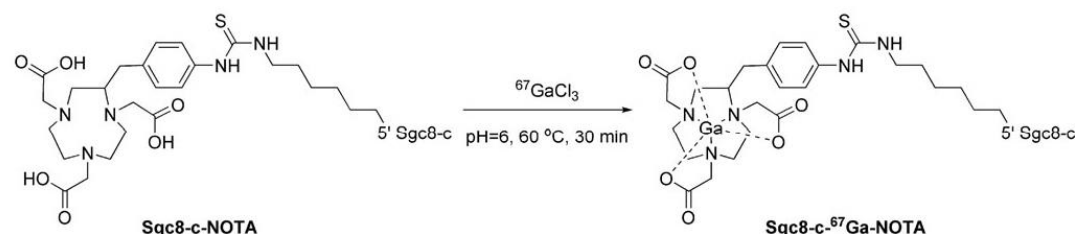

FIG. 1.   Reaction scheme for the complexation of ^{67}Ga^{3+} with Sgc8-c-NOTA.

FIG. 2. Summary of Sgc8-c-NOTA Ga-radiolabeled process as function of the different studied variables (shown results were obtained, apart from the variable indicated conditions, at 60°C for 30 min). The best condition of complexation was ammonium acetate buffer (0.1 M, pH = 6.0), 0.4 nmol of Sgc8-c-NOTA, 30.7 MBq of [67]GaCl$_3$, and at 60°C for 30 min (final volume of reaction 1000 μL).
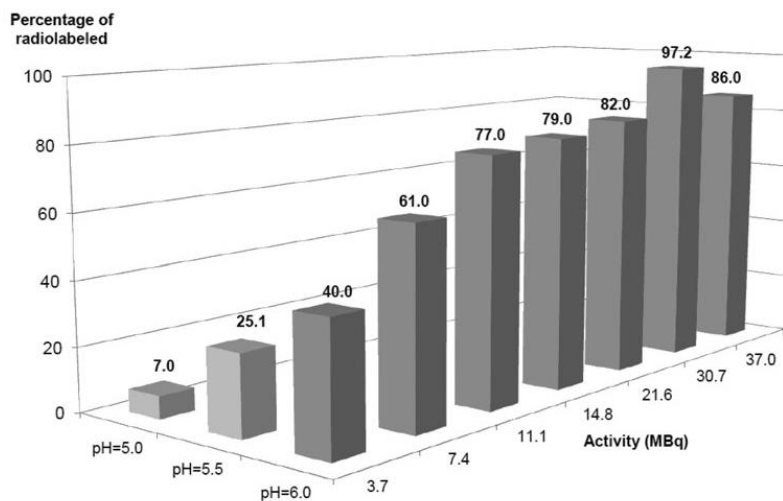
for 30 min (Supplementary Figs. S2 and S3). Probe stability on FBS resulted in high serum protein binding, >90%, and instability of free aptamer (66%) was observed after 2 h of incubation (Supplementary Fig. S4). Similar results were obtained in the authors' previous reports.[16]

The PTK7 receptor affinity studies (Fig. 4) for the radio probe showed a K_d value at the low nanomolar, that is, 0.019 nM, indicating the binding affinity was not modified.

Besides, radio probe binding studies on tumor cell lines were performed based on previous results.[16,18] A signal increase was observed over time for A20 and good binding since the first time point, 30 min, for A20/GFP tumor cell line, demonstrating the Sgc8-c-NOTA-^{67}Ga binding capability (Fig. 4).

In addition, to demonstrate that their model was adequate in the proof-of-concept study, the authors demonstrated that A20/GFP cells are able to express PTK7, using flow cytometry to analyze the A20/GFP cells (Supplementary Fig. S5).

In vivo characterization

The pharmacokinetic analysis showed that Sgc8-c-NOTA-^{67}Ga followed a two-compartment pharmacokinetic disposition in the body, with elimination from the central compartment. All mass transferences were assumed to follow first-order kinetics. Renal clearance was estimated using urine data in a sequential manner (i.e., after estimating pharmacokinetic parameters for probe disposition in body using blood data). Complete results and goodness-of-fit plots are included in the Supplementary Data. The elimination clearance (CL), including renal and no renal elimination pathways, was estimated to be 1.26 mL/h, the volumes of distribution for the central (Vc) and peripheral compartments were 7.39 and 11.4 L, respectively, and the distribution clearance (Q) was 1.22 mL/h. Renal clearance (CLr) was estimated at 0.172 mL/h. Interindividual variability was found significant for Vc (CV = 19.7%), Q (67.0%), and CLr (45.9%). Using these primary pharmacokinetic parameters, a
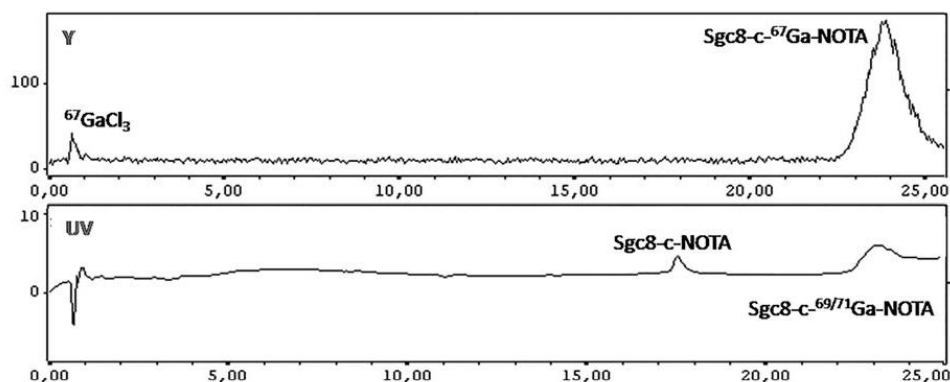
FIG. 3. RP-HPLC analysis (γ-radiodetection, up, and UV detection at 260 nm, down) to assess the identity of the Sgc8-c-NOTA-[67]Ga. RP-HPLC, reverse-phase high-performance liquid chromatography; UV, ultraviolet.
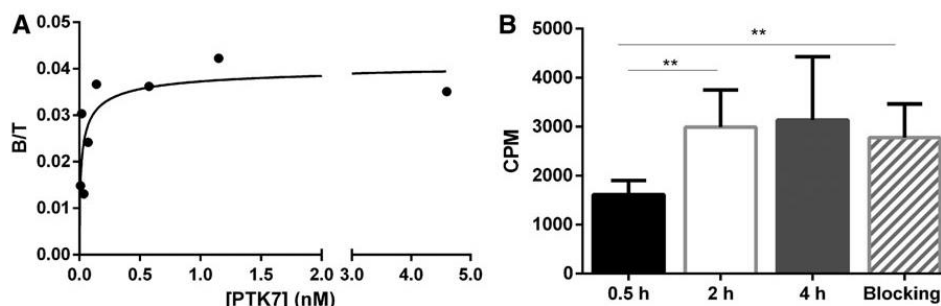
FIG. 4. Binding capacity. **(A)** PTK7-maximum binding capacity assay performed with Sgc8-c-NOTA-^{67}Ga. **(B)** Binding of Sgc8-c-NOTA-^{67}Ga to A20 cell line. **$p < 0.01$ (Student's t-test).

volume of distribution at steady state (Vss) of 18.8 mL and an elimination half-life of 15.1 h were obtained. Also, renal elimination accounted for 14.1% of the administered dosage (Supplementary Fig. S6).

The biodistribution of Sgc8-c-NOTA-^{67}Ga in A20/GFP tumor-bearing BALB-c mice is shown in Figure 5. Low blood values were observed at all assayed time points. After 30 min postinjection, a value of $12.90 \pm 2.06\%$ID/g was observed, which decreased over time to $2.96 \pm 0.49\%$ID/g at 48 h postinjection. The hepatic activity levels remained constant along the assay, close to 20%ID/g, in agreement with hepatobiliary metabolism. In addition, the bone radioactivity did not increase significantly with time, indicating coordinated gallium stability with similar behavior to that previously reported for Sgc8-c-DOTA-^{67}Ga.[16] Bone radioactivity reached the maximum value at 24 h postinjection ($7.99 \pm 1.00\%$ID/g for Sgc8-c-NOTA-^{67}Ga), with no affect on the quality of the images. It could be the result of some level of gallium release from Sgc8-c-NOTA-^{67}Ga under physiological conditions. The urine activity slightly increased up to 24 h.

The tumor uptake increased with the time being significantly higher since 48 h postinjection ($29.87 \pm 0.85\%$ID/g) (Supplementary Fig. S7). *In vivo* blocking studies with Sgc8-c-NH$_2$ showed, a statistically nonsignificant, decrease in tumor signal (Fig. 5). There was no significant uptake in the other no-target organs.

The blood and muscle ID/g activities decreased with time, resulting in better tumor/no-target ratios with time, reaching tumor/blood ratios higher than 7 and tumor/muscle ratios higher than 20, 24 h postinjection, for both ratios (Fig. 6).

In vivo imaging results showed consistent abdominal signal and high tumor uptake, which is mainly in the 24-h time point (Fig. 7).

Discussion

Aptamers are a versatile tool in biotechnology field. Sharing characteristics of peptides and antibodies, aptamers have advantages due to their easy synthesis and facile chemical modification.[18] These biomolecules can be modified to be functional for diverse approaches. In addition, their charge and low molecular weight result in a fast tissue penetration and clearance. Thus, aptamers have properties that make them ideal for theranostics purposes. Theranostics allow imaging visualization and treatment with the same probe, enabling personalized therapy.[28]

Previous studies showed Sgc8-c as a promising aptamer.[18,29] This work studied an Sgc8-c derivative that was performed and radiolabeled with ^{67}Ga. The NOTA conjugation was performed because of good properties as bifunctional chelator for M^{3+},[30,31] as ^{177}Lu, ^{90}Y, ^{213}Bi, and ^{67}Ga, which is a γ emitting radionuclide ($t_{1/2} = 78$ h) used to perform imaging over days. ^{64}Cu, a β and positron emitter
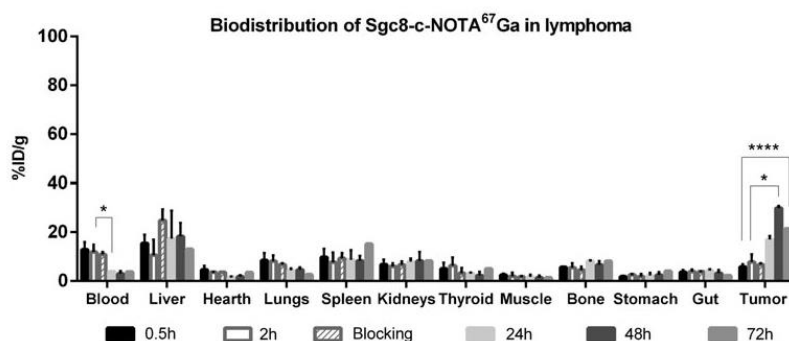
FIG. 5. Biodistribution. Results for Sgc8-c-NOTA-^{67}Ga at 0.5, 2, 24, 48, and 72 h postinjection in A20/GFP tumor-bearing BALB-c mice. ****$p < 0.0001$, *$p < 0.05$ (Student's t-test). GFP, green fluorescent protein.
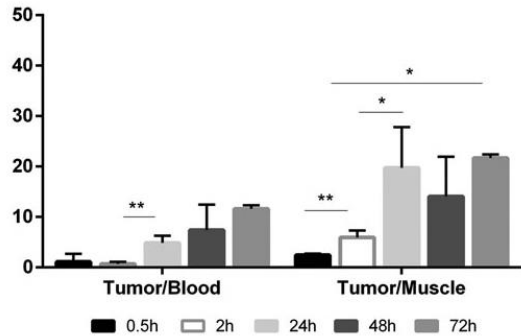
FIG. 6. Tumor/blood and tumor/muscle ratios. $**p < 0.01$, $*p < 0.05$ (Student's t-test).

radionuclide, has also been chelated by NOTA and widely studied for positron emission tomography and theranostics.[32] Previous studies,[33,34] together with the authors' results showed only one peak in the HPLC-analysis and the incorporation of only one gallium atom per molecule of aptamer, according to MS results, and, therefore, allowed us to propose the Ga coordination in the NOTA cage (Fig. 1).

Radiochemical purity and specific activity were evaluated for Sgc8-c-NOTA-^{67}Ga, and optimization procedure showed that the buffer with an adequate pH plays a relevant role in the labeling procedure. The rdl was over 95% and the identity of radio probe was verified using the chromatographic properties of the stable complex, Sgc8-c-NOTA-[69/71]Ga. The Sgc8-c-NOTA-^{67}Ga distribution coefficient ($logD_{7.5}$) was

-2.41 ± 0.11, being a little more hydrophilic than the DOTA analogue previously described by the authors' group, that is, $logD_{7.5} = -1.87 \pm 0.05$ for Sgc8-c-DOTA-[67]Ga.[16] This change could modulate the *in vivo* behavior according to their aims. The radiolabeled probe showed high stability in buffer reaction and high binding serum protein.

Affinity studies showed a K_d value at low nanomolar for the PTK7-receptor, consistent with the data against entire CCRF-CEM cells, that is, K_d 0.80 nM, obtained by Tan et al.[14] The radiolabeled probe was evaluated *in vitro* and *in vivo* in a lymphoma model.

The animal studies resulted in a two-compartment pharmacokinetic disposition in the body of the Sgc8-c-NOTA-[67]Ga. The biodistribution of Sgc8-c-NOTA-^{67}Ga in A20/GFP tumor-bearing BALB-c mice resulted in no significant uptake in the no-target organs. Compared to the ^{67}Ga-radiolabeled analogue prepared using Sgc8-c-DOTA,[16] the authors could state that the change in the NOTA-connector/chelator did not modify the *in vivo* biodistribution as they expected, based on logD values.[16]

Tumor uptake increased with the time being significantly higher for 48 h postinjection (Supplementary Fig. S7). However, the blood and muscle ID/g activities decreased with time, resulting in higher tumor/no-target ratios 24 h postinjection for both ratios (Fig. 6). These results were compared with a blocking control group, obtaining nonsignificant tumor uptake decrease. High serum protein binding can result in lack of blocking. In addition, high receptor expression could impose a low blocking result. The competition could be improved with changes in injected doses of radio probe and blocking agent in the future.

Biodistribution results were consistent with the *in vivo* images using multimodal tools. The authors observed high
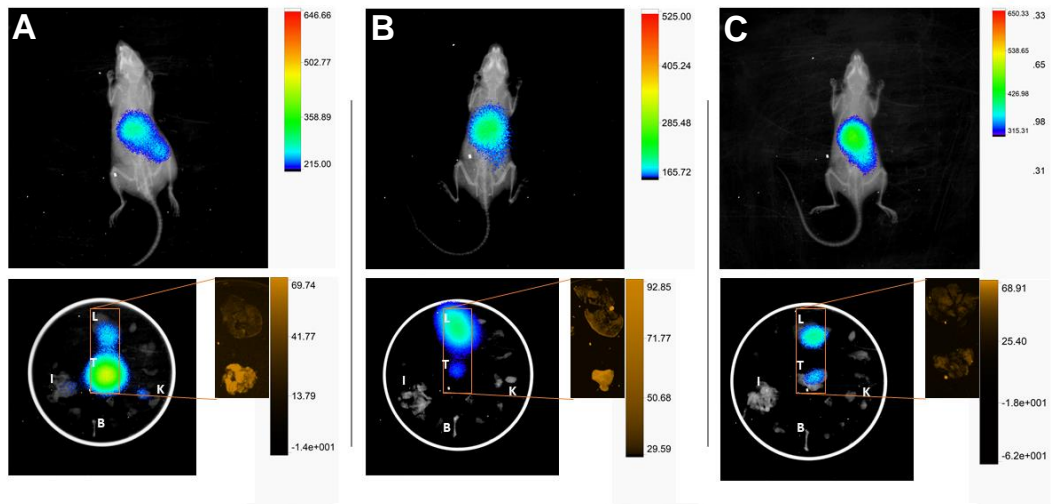
FIG. 7. Examples of multimodal images of radio probe-injected animals. Images were acquired at 24 h (**A**), 48 h (**B**), and 72 h (**C**) postinjection. *Up:* whole animal X-rays and γ live images; tumor is *arrow* indicated. *Down: ex vivo* X-ray and γ images, including T: tumor, L: liver, I: intestine, B: bone, and K: kidneys. *Ex vivo* images also include lungs, blood, heart, muscle, stomach, thyroid, and spleen. *Inset:* additional A20/GFP cells fluorescence acquisition is highlighted in *orange* scale for liver and tumor. GFP, green fluorescent protein.

tumor uptake and an abdominal signal at 24 h postinjection (Fig. 7, up). In addition to the well-defined tumor image at 24 h, at 48 and 72 h, there were image-asymmetries that are evidence of possible tumor presence, which was confirmed with co-localization studies (Fig. 7, down inset). When the organs were analyzed separately (*ex vivo*), it was possible to distinguish high tumor and liver signals (Fig. 7, down), which agreed with the biodistribution studies (Fig. 5). In some cases, the signals from the tumor were the highest. In addition, using the multimodal combination of X-ray, fluorescence, and γ, they could co-localize the fluorescent tumoral cells and the radio probe in the same location where the GFP was visualized in the studied tumors (Fig. 7, inset), being an adequate positive control of specific interaction.

Furthermore, additional investigation is needed to enhance tumor retention over time. However, tumor uptake could be improved with doses and time acquisition adjustments. In addition, studies with human tumor xenograft murine model should be done as previous translational step. Finally, the high tumor/no-target ratios of Sgc8-c-NOTA-^{67}Ga highlight its potential as theranostic agent.

Conclusions

In this study, the authors observed considerable uptake of the radio probe in the A20-tumor since the initial time point, increasing after 24 h, with the concomitant signal decreasing in the blood and muscles. Consequently, target/no-target signal ratios were very high for this mouse model and this effect improved image contrast. Thus, they confirmed the utility of the Sgc8-c aptamer as theranostic agent for hemato-oncological malignancies.

Acknowledgments

Authors' Contributions

E.S. is a PhD student and she worked in all of the experimental activities. J.B. contributed in radiolabeled and quality control experiments. M.I. contributed in pharmacokinetics analyses, discussion of the results, and writing the article. M.F. contributed in all of the animal experiments. P.C. contributed in the discussion of the results. M.M. contributed in the cell studies, discussion of the results, and writing the article. H.C. contributed in the planning of the activities, discussion of the results, and writing the article. V.C. contributed in the planning of the activities, discussion of the results, and writing the article.

Disclosure Statement

There are no existing financial conflicts.

Funding Information

Supplementary Material

Supplementary Table S1
Supplementary Table S2
Supplementary Table S3
Supplementary Table S4
Supplementary Table S5
Supplementary Figure S1
Supplementary Figure S2
Supplementary Figure S3
Supplementary Figure S4
Supplementary Figure S5
Supplementary Figure S6
Supplementary Figure S7

References

1. Bayat P, Nosrati R, Alibolandi M, et al. SELEX methods on the road to protein targeting with nucleic acid aptamers. Biochimie 2018;154:132.
2. Zhou J, Satheesan S, Li H, et al. Cell-specific RNA aptamer against human CCR5 specifically targets HIV-1 susceptible cells and inhibits HIV-1 infectivity. Chem Biol 2015;22:379.
3. Wang CY, Lin BL, Chen CH. An aptamer targeting shared tumor-specific peptide antigen of MAGE-A3 in multiple cancers. Int J Oncol 2016;138:918.
4. Wolter AC, Weickhmann AK, Nasiri AH, et al. A stably protonated adenine nucleotide with a highly shifted pKa value stabilizes the tertiary structure of a GTP-binding RNA aptamer. Angew Chem Int Ed 2017;56:401.
5. Huang Y, Chen X, Duan N, et al. Selection and characterization of DNA aptamers against Staphylococcus aureus enterotoxin C1. Food Chem 2015;166:623.
6. Ramezani M, Abnous K, Taghdisi SM. Optical and electrochemical aptasensors for sensitive detection of streptomycin in blood serum and milk. Methods Mol Biol 2017;1572:403.
7. Alshaer W, Hillaireau H, Fattal E. Aptamer-guided nanomedicines for anticancer drug delivery. Adv Drug Deliv Rev 2018;134:122.
8. Ruiz Ciancio D, Vargas MR, Thiel WH, et al. Aptamers as diagnostic tools in cancer. Pharmaceuticals 2018;11:E86.
9. Yang S, Li H, Xu L, et al. Oligonucleotide aptamermediated precision therapy of hematological malignancies. Mol Ther Nucleic Acids 2018;13:164.
10. Wu X, Liang H, Tan Y, et al. Cell-SELEX aptamer for highly specific radionuclide molecular imaging of glioblastoma *in vivo*. PLoS One 2014;9:e90752.
11. Ni S, Yao H, Wang L, et al. Chemical modifications of nucleic acid aptamers for therapeutic purposes. Int J Mol Sci 2017;18:E1683.
12. Healy JM, Lewis SD, Kurz M, et al. Pharmacokinetics and biodistribution of novel aptamer compositions. Pharm Res 2004;21:2234.
13. Shangguan D, Li Y, Tang Z, et al. Aptamers evolved from live cells as effective molecular probes for cancer study. Proc Natl Acad Sci U S A 2006;103:11838.
14. Prebet T, Lhoumeau AC, Arnoulet C, et al. The cell polarity PTK7 receptor acts as a modulator of the chemotherapeutic response in acute myeloid leukemia and impairs clinical outcome. Blood 2010;116:2315.
15. McCarten KM, Nadel HR, Shulkin BL, et al. Imaging for diagnosis, staging and response assessment of Hodgkin lymphoma and non-Hodgkin lymphoma. Pediatr Radiol 2019;49:1545.

16. Calzada V, Báez J, Sicco E, et al. Preliminary *in vivo* characterization of a theranostic aptamer: Sgc8-c-DOTA-[67]Ga. Aptamers 2017;1:19–27.

17. Notni J, Pohle K, Wester HJ. Comparative gallium-68 labeling of TRAP-, NOTA-, and DOTA-peptides: Practical consequences for the future of gallium-68-PET. EJNMMI Res 2012;2:28.

18. Calzada V, Moreno M, Newton J, et al. Development of new PTK7-targeting aptamer-fluorescent and -radiolabelled probes for evaluation as molecular imaging agents: Lymphoma and melanoma *in vivo* proof of concept. Bioorg Med Chem 2017;25:1163.

19. Sicco E, Báez J, Margenat J, et al. Derivatizations of Sgc8-c aptamer to prepare metallic radiopharmaceuticals as imaging diagnostic agents: Syntheses, isolations, and physicochemical characterizations. Chem Biol Drug Des 2018;91:747.

20. Kalil RA, Teixeira LA, Mastalir ET, et al. Experimental model of gene transfection in healthy canine myocardium: Perspectives of gene therapy for ischemic heart disease. Arq Bras Cardiol 2002;79:223.

21. Jacobson O, Weiss ID, Wang L, et al. Labeled single-stranded DNA aptamer for PET imaging of protein tyrosine kinase-7 expression. J Nucl Med 2015;56:1780.

22. Lindmo T, Bunn PA. Determination of the true immunoreactive fraction of monoclonal antibodies after radiolabeling. Methods Enzymol 1986;121:678.

23. Beal S, Sheiner LB, Boeckmann A, et al. NONMEM User's Guides (1989–2009). Ellicott City, MD: Icon Development Solutions, 2009.

24. Bascuas T, Moreno M, Mónaco M, et al. A novel non-Hodgkin lymphoma murine model closer to the standard clinical scenario. J Transl Med 2016;14:323.

25. Gijs M, Dammicco S, Warnier C, et al. Gallium-68-labelled NOTA-oligonucleotides: An optimized method for their preparation. J Label Compd Radiopharm 2016;59:63.

26. Kryza D, Debordeaux F, Azéma L, et al. Ex vivo and in vivo imaging and biodistribution of aptamers targeting the human matrix metalloprotease-9 in melanomas. PLoS One 2016;11:e0149387.

27. Velikyan I, Beyer GJ, Bergström-Pettermann E, et al. The importance of high specific radioactivity in the performance of ^{68}Ga-labeled peptide. Nucl Med Biol 2008;35:529.

28. Drude N, Tienken L, Mottaghy FM. Theranostic and nanotheranostic probes in nuclear medicine. Methods 2017;130:14.

29. Duan S, Yu Y, Lai C, et al. Vincristine-loaded and Sgc8-modified liposome as a potential targeted drug delivery system for treating acute lymphoblastic leukemia. J Biomed Nanotechnol 2018;14:910.

30. Kretschy D, Koellensperger G, Hann S. Stability assessment of different chelating moieties used for elemental labeling of bio-molecules. Metallomics 2011;3:1304.

31. Kang L, Rosenkrans ZT, Cai W. ^{64}Cu-Labeled aptamers for tumor-targeted radionuclide delivery. Methods Mol Biol 2019;1974:223.

32. Woo SK, Jang SJ, Seo MJ, et al. Development of ^{64}Cu-NOTA-trastuzumab for HER2 targeting: A radiopharmaceutical with improved pharmacokinetics for human studies. J Nucl Med 2019;60:26.

33. Chakraborty S, Goswami D, Chakravarty R, et al. Syntheses and evaluation of [68]Ga- and [153]Sm-labeled DOTA-conjugated bisphosphonate ligand for potential use in detection of skeletal metastases and management of pain arising from skeletal metastases. Chem Biol Drug Des 2018;92:1618.

34. Holub J, Meckel M, Kubíček V, et al. Gallium(III) complexes of NOTA-bis(phosphonate) conjugates as PET radiotracers for bone imaging. Contrast Media Mol Imaging 2015;10:122.

4.2.1. Material suplementario del artículo II

SUPPLEMENTARY TABLE S1. INFLUENCE OF TEMPERATURE AND TIME IN THE SGC8-C-NOTA
^{67}GA-RADIOLABELED USING AMMONIUM ACETATE BUFFER

Run	Sgc8-c-NOTA (nmol)	Activity (MBq)/GaCl$_3$ vol (μL)	Final reaction vol (μL)	Buffer	pH	T (°C)	t (min)	rdl (%)
1	0.08	3.7–7.4/23–46	400	Ammonium acetate (0.1 M)	5.0	37	30	5.0
2						60	30	7.0
3						60	45	5.0

rdl, percentage of radiolabeled (measured by RP-HPLC-γ detection).

SUPPLEMENTARY TABLE S2. INFLUENCE OF TIME AND pH IN THE SGC8-C-NOTA
^{67}GA-RADIOLABELED USING AMMONIUM ACETATE BUFFER

Run	Sgc8-c-NOTA (nmol)	Activity (MBq)/GaCl$_3$ vol (μL)	Final reaction vol (μL)	Buffer	T (°C)	t (min)	pH	rdl[a] (%)
4	0.08	3.7/23	400	Ammonium acetate (0.1 M)	60	30	5.5	25.1
5						60		11.7
7						30	6.0	40.0

SUPPLEMENTARY TABLE S3. INFLUENCE OF TIME IN THE SGC8-C-NOTA ^{67}GA-RADIOLABELED USING AMMONIUM
ACETATE BUFFER (0.1 M, pH = 6.0) AT 37°C

| Run	Sgc8-c-NOTA (nmol)	Activity (MBq)/GaCl$_3$ vol (μL)	Final reaction vol (μL)	Buffer	pH	T (°C)	t (min)	rdl[a] (%)
8	0.08	3.7–7.4/23–46	400	Ammonium acetate (0.1 M)	6.0	37	30	29.5
9							60	34.0
10							90	3.9
11							120	4.2

SUPPLEMENTARY TABLE S4. INFLUENCE OF APTAMER CONCENTRATION IN THE SGC8-C-NOTA
^{67}GA-RADIOLABELED USING AMMONIUM ACETATE BUFFER

| run	Activity (MBq)/GaCl$_3$ vol (μL)	Final reaction vol (μL)	Buffer	pH	T (°C)	t (min)	Sgc8-c-NOTA (nmol)	rdl[a] (%)
12	3.7–11.1/26–78	400	Ammonium acetate (0.1 M)	6.0	60	30	0.08	40.0
13		1000					0.4	77.0

SUPPLEMENTARY TABLE S5. INFLUENCE OF ACTIVITY IN THE SGC8-C-NOTA
^{67}GA-RADIOLABELED USING AMMONIUM ACETATE BUFFER

| Run	Final reaction vol (μL)	Buffer	pH	T (°C)	t (min)	Sgc8-c-NOTA (nmol)	Activity (MBq)/GaCl$_3$ vol (μL)	rdl[a] (%)
14	400	Ammonium acetate (0.1 M)	6.0	60	30	0.08	3.7/26	40.0
15							7.4/52	61.0
16							14.8/104	79.0
17	1000					0.4	11.1/78	77.0
18							21.6/152	82.0
19							30.7/215	97.2
20							37/260	86.0

Supplementary Data
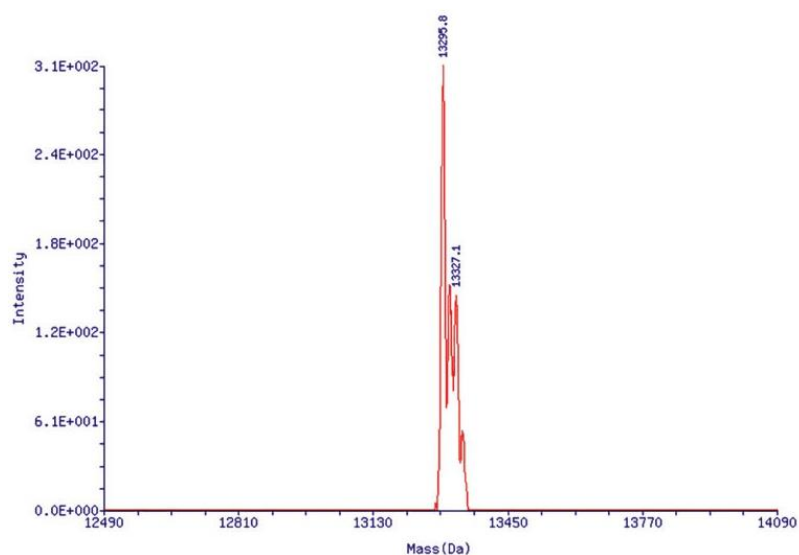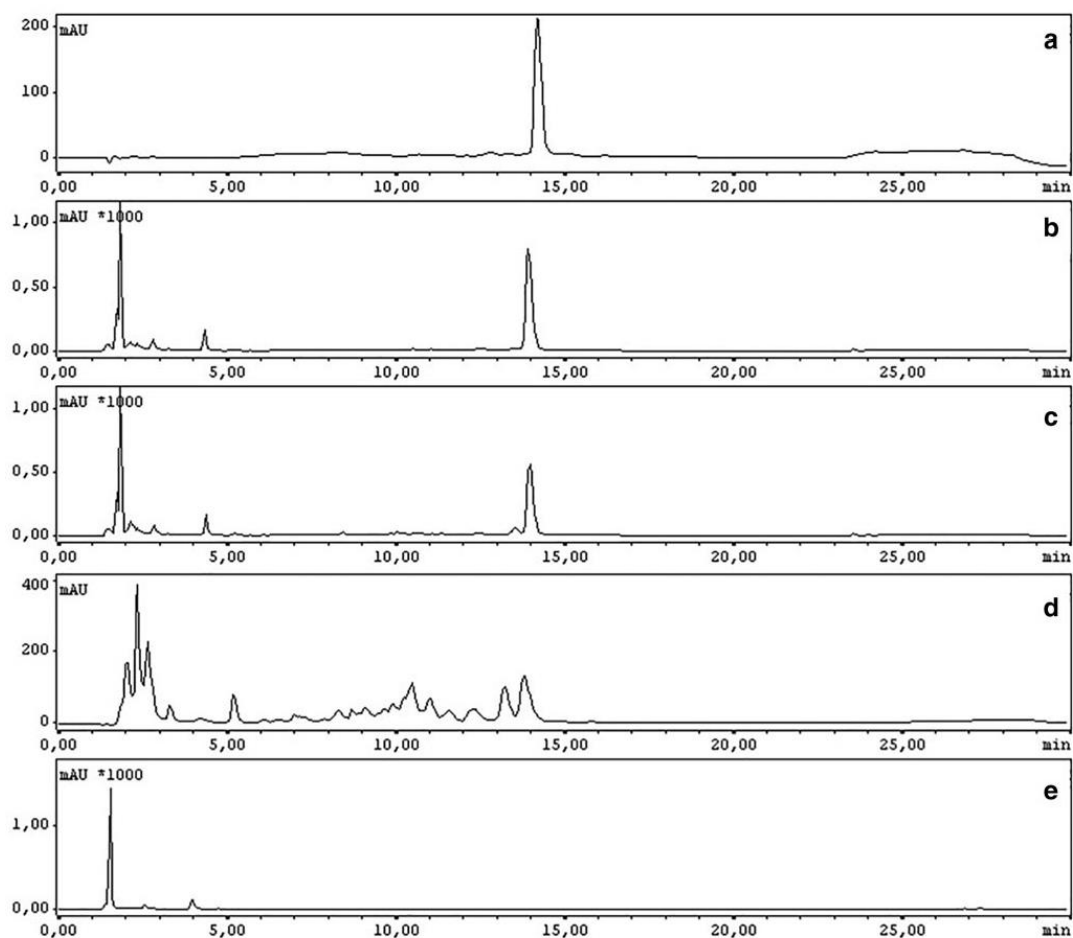

SUPPLEMENTARY FIG. S1. ESI-MS of RP-HPLC-isolated product with $t_R = 23.6$ min from the Sgc8-c-NOTA complexation process with $^{69/71}$GaCl$_3$ (Fig. 3).
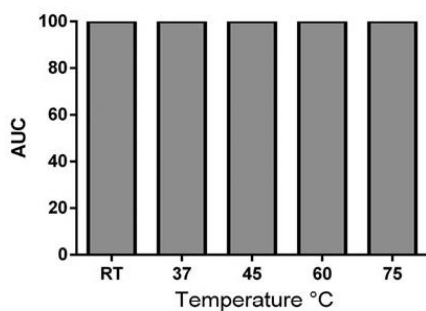
SUPPLEMENTARY FIG. S2. Percentage of intact radiotracer over temperature using ammonium acetate buffer.
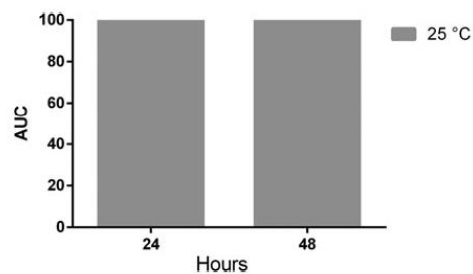
SUPPLEMENTARY FIG. S3. Percentage of intact radiotracer over time using ammonium acetate buffer.

SUPPLEMENTARY FIG. S4. Fetal bovine serum stability by RP-HPLC for t0 **(a)**, 30 min **(b)**, 2 h **(c)**, and 24 h **(d)** of incubation. Serum without aptamer is indicated in **(e)**.
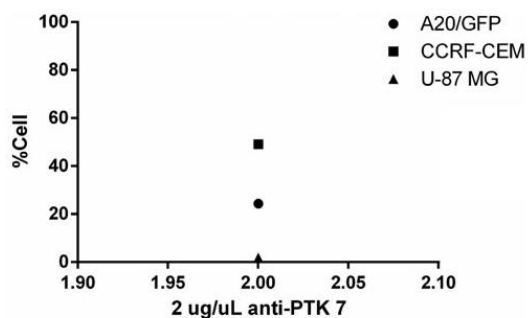
SUPPLEMENTARY FIG. S5. Confirmation of PTK7 expression by A20/GFP cells. Flow cytometry of PTK7 expression results for A20/GFP, CCRF-CEM (positive control), and U-87 MG (negative control) cell lines.
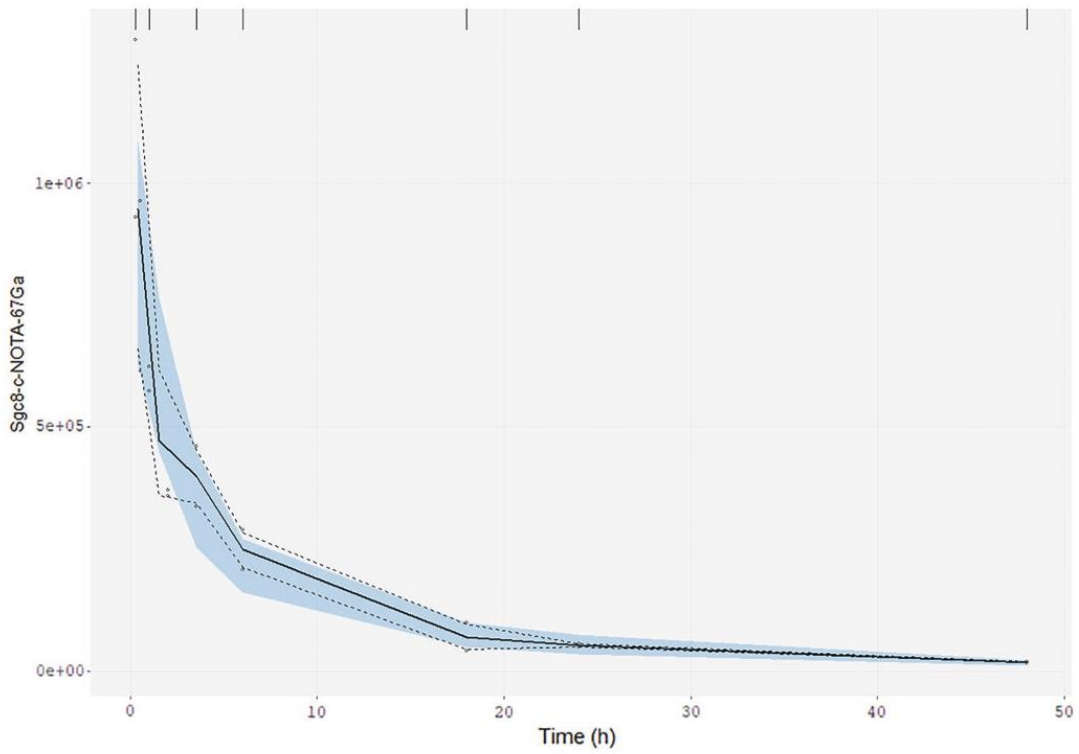
SUPPLEMENTARY FIG. S6. VPC showing the fit to the overall data. Raw observations are shown as *dots*, median for the observation as a continuous *black line*, and its 90% confidence interval as dashed *black lines*. Model-based simulation is included as a *blue* shaded area representing the 90% confidence interval for the median of data obtained after simulating 500 datasets using the final model. VPC, visual predictive check.
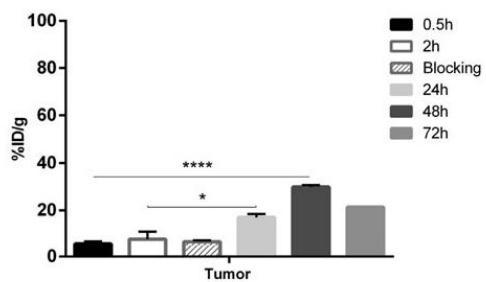
SUPPLEMENTARY FIG. S7. Tumor uptake (%ID/g) for different time points.

4.3. Artículo III: Evaluación biológica de las sondas Sgc8-c-NOTA-^{67}Ga y Sgc8-c-Alexa647, en los modelos de melanoma metastático y no metastático.

scientific reports

Check for updates

OPEN

Metastatic and non-metastatic melanoma imaging using Sgc8-c aptamer PTK7-recognizer

Estefanía Sicco[1,2], Amy Mónaco[2], Marcelo Fernandez[3], María Moreno[2], Victoria Calzada[1]✉ & Hugo Cerecetto[1]

Melanoma is one of the most aggressive and deadly skin cancers, and although histopathological criteria are used for its prognosis, biomarkers are necessary to identify the different evolution stages. The applications of molecular imaging include the in vivo diagnosis of cancer with probes that recognize the tumor-biomarkers specific expression allowing external image acquisitions and evaluation of the biological process in quali-quantitative ways. Aptamers are oligonucleotides that recognize targets with high affinity and specificity presenting advantages that make them interesting molecular imaging probes. Sgc8-c (DNA-aptamer) selectively recognizes PTK7-receptor overexpressed in various types of tumors. Herein, Sgc8-c was evaluated, for the first time, in a metastatic melanoma model as molecular imaging probe for in vivo diagnostic, as well as in a non-metastatic melanoma model. Firstly, two probes, radio- and fluorescent-probe, were in vitro evaluated verifying the high specific PTK7 recognition and its internalization in tumor cells by the endosomal route. Secondly, in vivo proof of concept was performed in animal tumor models. In addition, they have rapid clearance from blood exhibiting excellent target (tumor)/non-target organ ratios. Furthermore, optimal biodistribution was observed 24 h after probes injections accumulating almost exclusively in the tumor tissue. Sgc8-c is a potential tool for their specific use in the early detection of melanoma.

Melanoma is one of the most aggressive and deadly types of skin cancer[1,2], with an annual increase in incidence during the last decade between 15 and 25 per 100,000 individuals[3]. Although histopathological criteria such as tumor thickness, mitotic rate, histologic subtype and ulceration[4,5], are usually used for its prognosis, biomarkers are necessary to identify whether the primary melanoma has metastasized or even differentiate the stages of its evolution[6,7]. Malignant melanomas have been reported to have increased activity of protein tyrosine kinase 7 (PTK7)[8,9]. This membrane receptor is highly conserved in different species and is involved in signal transduction pathways that mediate cell growth, cell polarity, differentiation, and survival[10,11]. However, PTK7 may participate as a co-receptor and its protection by type 1 membrane metalloprotease is implicated in the progression of cancer[12,13]. PTK7 has also been shown to be a key regulator in the Wnt/β-Catenin or Wnt/planar cell polarity pathway, and correlates with aggressive clinicopathological characteristics in cancer[14,15]. In addition, this receptor is overexpressed in different types of leukemia, colon, lung, prostate, breast,Gastric tumors, and even metastases[16–22]. Furthermore, it participates in the migration and endothelial invasion of tumor cells[23–25].

It is possible to identify the expression of tumor biomarkers using molecular imaging, a non-invasive technique that manages to evaluate the strategies for in vivo administration of the tumor target[26,27]. Molecular imaging consists of in vivo visualization, characterization and measurement of biological processes at the cellular or molecular level[27,28], and is a very useful tool for diagnosing cancer. The use of probes that have optimal imaging characteristics provides clinically essential information for this disease, which would allow a correct selection of the treatment to be followed and the monitoring of its effects[29].

In addition, aptamers have been used as a component of molecular imaging probes since they have the ability to bind, through non-covalent interaction bonds, with high affinity and specificity for a molecular target[30,31]. They are oligonucleotides (ssDNAs or RNAs) that have a three-dimensional structure characterized by loops, stems or hairpins. Aptamers have properties equivalent to antibodies in terms of their recognition by the molecular target, however they offer great advantages. The chemical synthetic process of aptamers allows a low cost

[1]Área de Radiofarmacia, Centro de Investigaciones Nucleares, Facultad de Ciencias, Universidad de La República, 11400 Montevideo, Uruguay. [2]Departamento de Desarrollo Biotecnológico, Instituto de Higiene, Facultad de Medicina, Universidad de La República, 11600 Montevideo, Uruguay. [3]Laboratorio de Experimentación Animal, Centro de Investigaciones Nucleares, Facultad de Ciencias, Universidad de La Republica, 11400 Montevideo, Uruguay. ✉email: vcalzada@cin.edu.uy

nature portfolio   1

69

production and no batch to batch variability[32,33]. They have physicochemical properties, such as stability at different temperatures and pH[34,35], and can be easily modified to continue improving their biological stability and pharmacokinetics[26,36,37]. Furthermore, aptamers molecular weight (~ 15000 Da) and charge provide rapid penetration into target tissues and elimination from the body[31,38]. Also, aptamers do not generate immunogenicity or toxic effects. Therefore, the characteristics of aptamers provide great advantages for their use in the development of new molecular imaging agents[39].

Previously, we have modified the Sgc8-c aptamer to generate molecular imaging probes in the diagnosis of cancer[39–42]. The Sgc8-c aptamer is DNA (41 nt) and selectively recognizes the PKT7 receptor with a $K_d = 0.78$ nM[10,43]. We have developed potential molecular imaging probes in different tumor models, through in vitro and in vivo evaluation, with an emphasis on hematological diseases. In this sense, radiolabelled probes (Sgc8-c-NOTA-^{67}Ga, Sgc8-c-DOTA-^{67}Ga, Sgc8-c-HYNIC-^{99m}Tc) have been reported to have better tissue penetration and ability to accurately measure tissue, and as a result, it allows quantitative images of the whole body[39–42]. Likewise, the fluorescent probe (Sgc8-c-Alexa647) allows the generation of optical images in the near infrared region with little interference, achieving optimal contrasts due to the molecules present in the tissues, that do not exhibit high absorption in that spectral region[39,40]. Different versatile platforms have been reported, where the conjugation of Sgc8-c aptamer enhances the cellular uptake capability of the material, achieving specific images in vivo[44–46], even in deep tissues[45]. These features are very useful to perform, for example, guided surgeries in real time[47,48]. Using the appropriate imaging probes, it is even possible to identify metastases[49]. Recently, we have studied these probes as imaging tools in a melanoma model, obtaining interesting results regarding tumor uptake[39]. Moreover, the sensitive and effective detection of PTK7 may represent a good strategy in the early diagnosis of melanoma. Based on this, the present work evaluates for the first time two potential different probes developed with of Sgc8-c in the metastatic melanoma model. Likewise, it also delves into another non-metastatic melanoma model, in order to optimize biological control methods, both biodistribution and imaging, achieving a sensitive and effective detection of PTK7 with these probes.

Results and discussion

PTK7 expression in B16F10 cells.

Firstly, we evaluated the presence of PTK7 in metastatic melanoma B16F10 cells by flow cytometry and Western blot, as it was previously evaluated in non-metastatic B16F1 melanoma cells[39,40]. Flow cytometry assays performed with a commercial anti-PTK7 antibody as probe revealed that approximately 40% of the B16F10 cells expressed detectable levels of PTK7. Of note, near to 80% of the positive control CCRF-CEM cells stained for PTK7, while the negative control, U87MG cells, showed null signal (Fig. 1A). Additionally, the Western blot studies confirmed the presence of PTK7 receptor on B16F10 cells (Fig. 1B, full-length gels are shown in Fig. S1 in Supporting Information). In this assay, it was observed that the probe also recognizes two fractions of PTK7. It has been reported in different cell lines that this receptor has different cleavage sites, which generate different matching cell-associated forms[13,50].

In vitro binding studies.

As it was previously described[39,40], Sgc8-c-NOTA-^{67}Ga and Sgc8-c-Alexa647 probes were stable, according to RP-HPLC and gel electrophoresis results, in water up to 75 °C for 30 min of incubation and in addition the integrity of these conjugates under different storage conditions was confirmed. The observed electrophoresis profiles were consistent with the absence of low molecular weight fragmentation. Furthermore, for the precursor Sgc8-c-NOTA, the probe Sgc8-c-Alexa647 and as well as the original aptamer Sgc8-c-NH$_2$, functional stabilities in DNase I, after 15 min and 2 h of incubation was studied observing similar level of degradation. After 15 min of incubation with the enzyme, it was found that Sgc8-c-NOTA was more resistant to degradation than the fluorescent probe (Sgc8-c-Alexa647). After 2 h, for all the samples, there was still aptamer without degradation. The behavior on fetal bovine serum (FBS) was also studied resulted in > 90% serum protein binding, and 66% instability[40].

Two different strategies were employed to analyze the ability of Sgc8-c probes to interact to B16F10: the use of the radiolabelled probe (Sgc8-c-NOTA-^{67}Ga) that can be measured byGamma counter system, and the use of the fluorescent-probe (Sgc8-c-Alexa647), which allows analysis by flow cytometry and Western blot.

The results showed that the Sgc8-c-NOTA-^{67}Ga probe binds to the B16F10 cell line. It was found that the binding percentage increased with time with significant differences at 4 h of incubation (Fig. 2). Regarding the blocking test of cells with the unlabeled aptamer, it was observed that the percentage of binding to the labeled probe decreases (compare 2 h of incubation and blocking incubation, $p < 0.05$, Fig. 2) indicating that there was a competition between both compounds confirming the probe interaction with PTK7.

For fluorescent flow cytometry assays, melanoma B16F10 cells were incubated with different concentrations of Sgc8-c-Alexa647. Figure 3 shows the percentage of positive cells and the specific mean fluorescence index (MFI). Results showed that the percentage of PTK7 positive cells is dependent on probe concentration, reaching a maximum of 80% of B16F10 cells with approximately 0.5 μM. Furthermore, the MFI indicates the amount of the probe that binds to PTK7, more precisely, the abundance of proteins at individual population cell level[51], thus this suggests that the B16F10 cell line expresses significant high levels of the PTK7 receptor (Fig. 3).

According to cytometry analysis, saturation concentration was reached at 0.3 μM of aptamer without achieving 100% of the B16F10 cells. This phenomenon could be explained by different cell division and differentiation stages in cell culture. In addition, as mentioned above, a molecular cleavage phenomenon has been described upon Sgc8-PTK7 interaction[46]. If the cleaved PTK7 receptor had been excreted into the supernatant of the medium, as result of cleavage mechanism of the aptamer-PTK7 complex, it would be the cause of not reaching saturation when the process was analyzed by flow cytometry. Then, if the cleaved PTK7 receptor is excreted into the supernatant of the medium, its detection by flow cytometry would not be possible. However, all experiments were performed in ice so the chances of cleavage are almost null. Besides, Western blot studies using supernatants

70
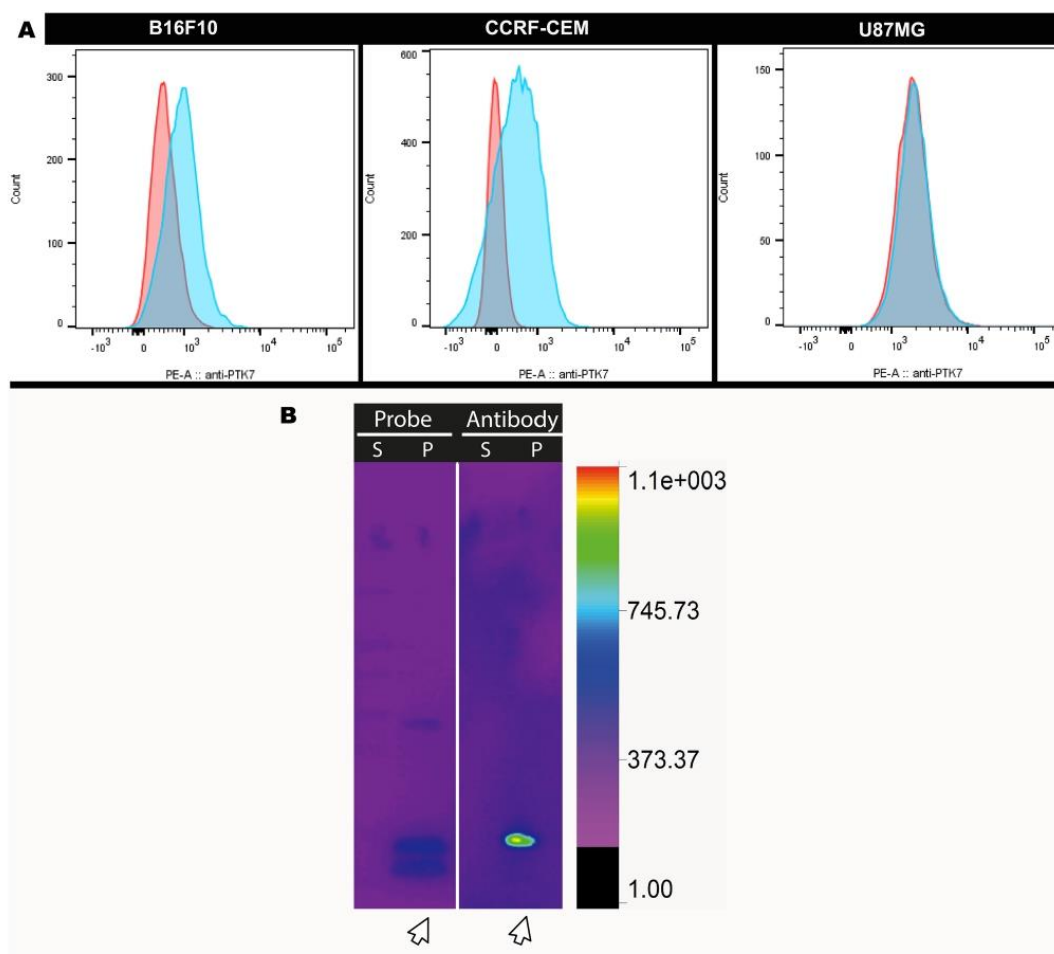
Figure 1. (**A**) Flow cytometry with cell lines B16F10, CCRF-CEM and U87MG. Histograms of cell lines after for incubation with anti-PTK7-PE antibody (in blue) and control (in red). (**B**) Grouping of Western blot cropped of proteins extracted from the supernatant (S) and pellet (P) of B16F10 cells culture. Incubation was performed with the Sgc8-c-Alexa647 probe (Probe) and with the anti-PTK7-PE antibody (Antibody). Arrow indicates the presence of PTK7 only in the cell pellet. White dividing line indicates different gels (performed in parallel) and exposures (full-length gels are shown in Fig. S1 in Supporting Information).

rejected this hypothesis. The results indicated that both the antibody and the fluorescent probe only recognize proteins from the cell pellet (Fig. 1B) showing that there was no detectable molecular cleavage in the supernatant. Based on these results, we propose the hypothesis that the rapid complex internalization does not allowing saturation due to the absence of the membrane receptor[53]. For this reason, fluorescent confocal microscopy studies were performed to demonstrate the internalization of the receptor (see below).

In vivo binding studies. In order to perform the in vivo biological studies we first analyzed the ability of the Sgc-8-c-Alexa647 probe to recognize in vivo the PTK7 presence in target organs. For this, flow cytometry studies were performed on B16F10-tumors, and liver, spleen and bone marrows as negative controls. The results showed that the fluorescent-probe marked, from early times, tumor cells al high levels, while in the rest of the non-target organs the percentage of positive cells was very low (Table 1), showing that the probe binds specifically to the PTK7 receptors that are on melanoma cells. In these studies, it is interesting to observe that the union of the probe to the tumor cells is maintained for a longer time than in the other non-target organs, without observing a significant tendency. This could be due to tissue homogenization to analyze the cells by flow cytometry, because everything that is retained in the extracellular matrix or contained in the different tissues is
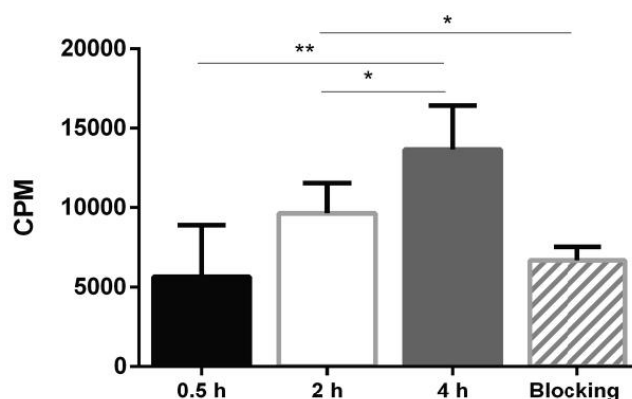
Figure 2. Binding assay with Sgc8-c-NOTA-^{67}Ga in the B16F10 cell line. The probe was incubated for 0.5, 2 and 4 h. Blocking: represents the competition test performed by incubating the cells with an excess of unlabeled aptamer (Sgc8-c-NH$_2$). **$p < 0.01$, *$p < 0.05$ (Student's t test).
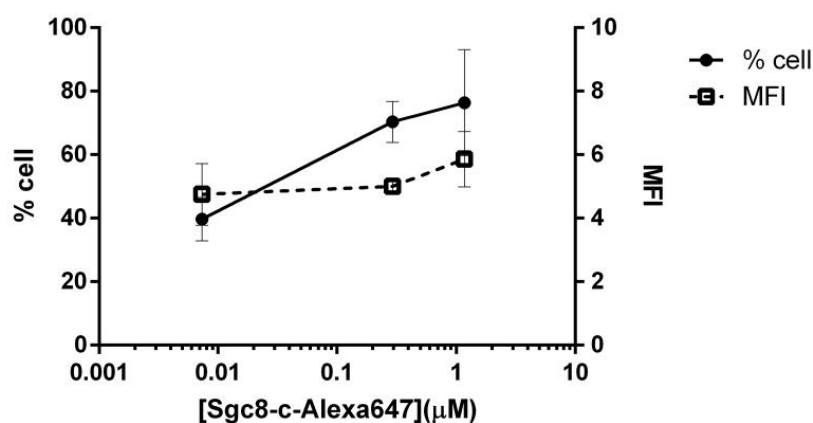

Figure 3. Flow cytometry of B16F10 cell line treated with Sgc8-c-Alexa647. Percentage of positive cells and specific MFI after incubation with the fluorescent probe.

Organ/time (h)	Percentage of positive cells (%)		
	0.5	2	24
Liver	3.80 ± 2.51	0.70 ± 0.35	0.30 ± 0.17
Spleen	1.10 ± 0.40	2.20 ± 1.15	0.60 ± 0.15
Bone marrow	0.93 ± 0.25	1.40 ± 0.49	0.60 ± 0.21
B16F10-tumor	86.40 ± 3.67	81.20 ± 4.55	82.80 ± 5.84

Table 1. Percentage of positive cells for in vivo exposed organs to probe Sgc8-c-Alexa647 analyzed by flow cytometry.

lost, while observing only the specific binding of the probes in the single cells. Additional information can be observed with in vivo imaging and biodistribution studies.

Confocal microscopy. Another mechanism proposed for Sgc8-PTK7 interaction is complex internalization[47]. For this reason, fluorescent confocal microscopy studies were performed to demonstrate the
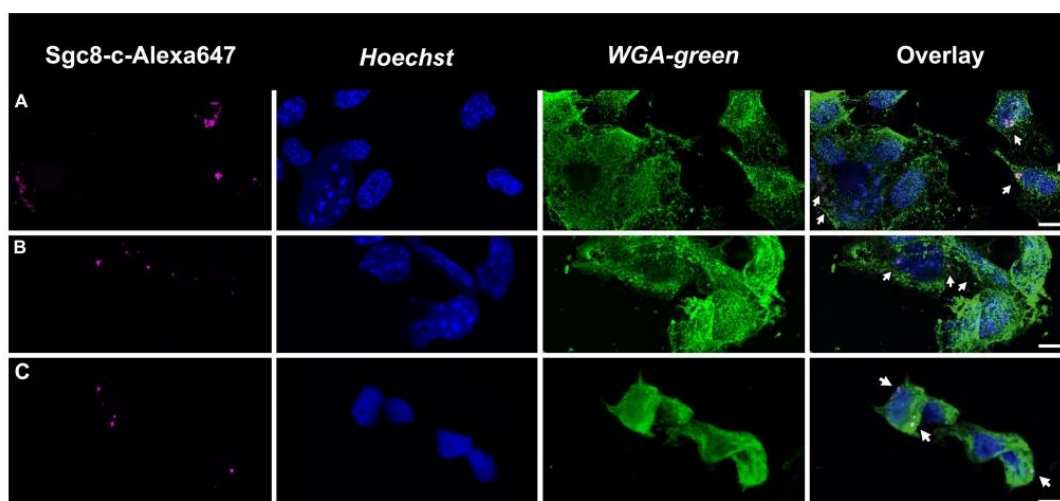
Figure 4. Confocal microscopy of B16F10 tumor cells incubated with fluorescent probe Sgc8-c-Alexa647. Cells were incubated with the probe for (**A**) 2 h, (**B**) 4 h, and (**C**) 16 h. Magenta: Sgc8-c-Alexa647 (white arrows), Blue: *Hoechst* and Green: *WGA-green*. Scale bar: 10 μm.

internalization of the receptor on the studied tumor cells. To perform confocal microscopy assays, B16F10 tumor cells were incubated with the Sgc8-c-Alexa647 probe during different times. At early time point, it was evident that the Sgc8-c-Alexa647 probe was internalized by the cells (Fig. 4).

Since it was observed that Sgc8-c-Alexa647 is internalized, we analyzed if the probe was also co-localized within the endosomes like other aptamers-probes[53]. For that, tumor cells were incubated with the fluorescent probe for different times and subsequently the early endosomes were analyzed. Sgc8-c-Alexa647 was observed to co-localize within endosomes in both melanoma cell lines (Fig. 5 and Fig. S2 in Supporting Information). Similarly, it was observed that the signal from the probe showed a tendency towards polarization. This is in agreement with what has been previously seen, that PTK7 is not uniformly distributed in the cell membrane, presenting a dynamic role in cell polarization[49].

In vivo biological studies. In vivo studies using both Sgc8-c-Alexa647 and Sgc8-c-NOTA-^{67}Ga probes were performed in murine metastatic melanoma model. To do this, once the induced tumors were palpable, probes were i.v. administered, and imaging and biodistribution studies were performed at different times after injection. The results showed interesting characteristics regarding the uptake of the probes in the tumor (Figs. 6, 7). Rapid tissue penetration was visualized, with tumor retention of both probes (Figs. 6, 7). Using the fluorescent probe, a tumor uptake of $32.9 \pm 3.5\%$ was observed at 2 h post-injection, increasing significantly at 24 h ($42.4 \pm 1.5\%$) and at 48 h ($50.3 \pm 1.6\%$) (Figs. 6A, 8). At 2 h post injection of the fluorescent probe, $33.2 \pm 15.6\%$ was eliminated in urine, decreasing to $42.6 \pm 13.8\%$ at 24 h post-injection (Fig. 6). No significant signal was observed in non-target organs (Fig. 6A). A similar tendence was observed in the non-metastatic melanoma model (Fig. S3).

The radiolabeled probe showed an increasing tumor uptake 24 h after injection. At 2 h post-injection, a tumor uptake of $8.4 \pm 1.6\%$ID/g was observed, increasing significantly at 24 h ($28.8 \pm 6.2\%$ID/g). Then, at 72 h after injection, tumor uptake decreased slightly ($17.7 \pm 0.1\%$ ID/g) (Fig. 6B). Urinary excretion was observed at early time points. A value of $9.1 \pm 4.9\%$ ID was observed at 0.5 h post-injection, which decreased to $4.2 \pm 1.6\%$ID at 2 h (Fig. 6). These data were determined by the renal values that were due to the elimination of the probes or their metabolites (Figs. 6B, 8). After 24 h post-injection, it was possible to distinguish signals from liver and intestines in the in vivo and ex vivo images, considering hepatobiliary metabolism for later time points (Figs. 6B, 9). However, non-significant signal comes from other organs, which allowed us to observe a clear signal from the tumor (Fig. 9).

Differences in signal values between organs and tumor were evident with both probes, resulting in an optimal tumor/non-tumor organ ratio, having a significant increase over time (Fig. 7). Mainly at 48 h post-injection with radiolabeled probe in the metastatic model, generated by B16F10 cells, showed a tumor/muscle ratio of 35.5 ± 13.7 (Fig. 7B and Fig. S4 for B16F1 model in Supporting Information), which is an excellent value to consider in vivo images. Likewise, it was observed that tumor uptake increased significantly with time in both models (Fig. S5 in Supporting Information). However, it was observed that the tumor uptake was slightly higher in the metastatic melanoma model, generated with the B16F10 cell line, than with the B16F1 non-metastatic melanoma model (Fig. 6 and Fig. S5 in Supporting Information). This difference could be explained by an increase in the expression of PTK7, since it has been seen that in metastatic melanomas, this receptor is one of the tyrosine kinases that participates in the positive regulation of the formation and function of the invadopodia[9]. Also, this difference in
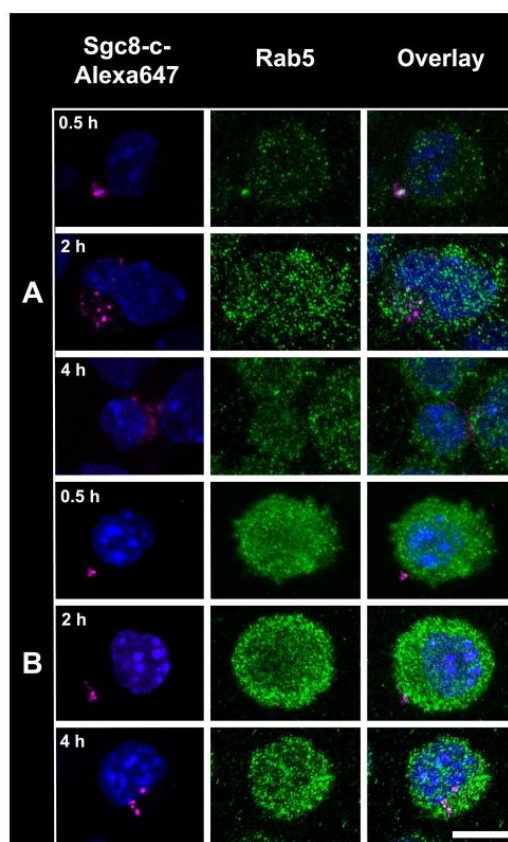
Figure 5. Sgc8-c-Alexa647 co-localize within endosomes. Confocal microscopy of (**A**) B16F10 and (**B**) B16F1 tumor cells incubated for 0.5, 2 and 4 h with the probe. Magenta: Sgc8-c-Alexa647, Blue: *Hoechst* and Green: *Rab5*. Scale bar: 10 μm.

the distribution of the probes, which is also observed in the images obtained by confocal microscopy, could be affected by a structural heterogeneity in the tumor vasculature, since it has been seen that the models generated with the B16F10 line show a significant improvement in vascular density[50].

In vivo blocking studies with Sgc8-c-NH_2 showed a statistically significant decrease of tumor signal for the fluorescent probe (Fig. 6 and Fig. S3, Supporting information), confirming specific probe training. These assays also reproduce the results seen in hematological models[38], indicating that there was competition between the probe and the unlabeled aptamer. In addition with the results of the in vivo binding study (Table 1), we confirm the in vivo specific interaction of the probe with PTK7.

Conclusions

The results described herein together with our previous studies[39,42], showed that both probes developed with the Sgc8-c aptamer are potential tools for their specific use in the early detection of melanoma. The results of in vitro studies were consistent with those obtained for biodistributions and the in vivo imaging. We obtained interesting characteristics related to the uptake of the probes in the tumor, with optimal tumor/non-target organs ratios, which are global benchmarks that encourage us to continue working on this. Although we found the best ratios at 24 h, other acquisition time points can be evaluated to find a better one. Like antibodies, aptamer-based probes are feasible in the clinic. One of most remarkable results is the low backgrounds versus high uptake in tumor which is very good and convenient. These methodologies applied here allowed us to detect differences in the expression of the tumor marker PTK7 in two different melanoma tumor models. However, it should be studied in depth whether this difference in the expression of PTK7 is really involved in signaling pathways that, consequently, grants greater metastatic power to cells.

The optimal tumor uptakes of the probes in metastatic melanoma, make them promising tools to facilitate in vivo diagnosis and thus to select an appropriate therapy. These probes could also be advantageous for
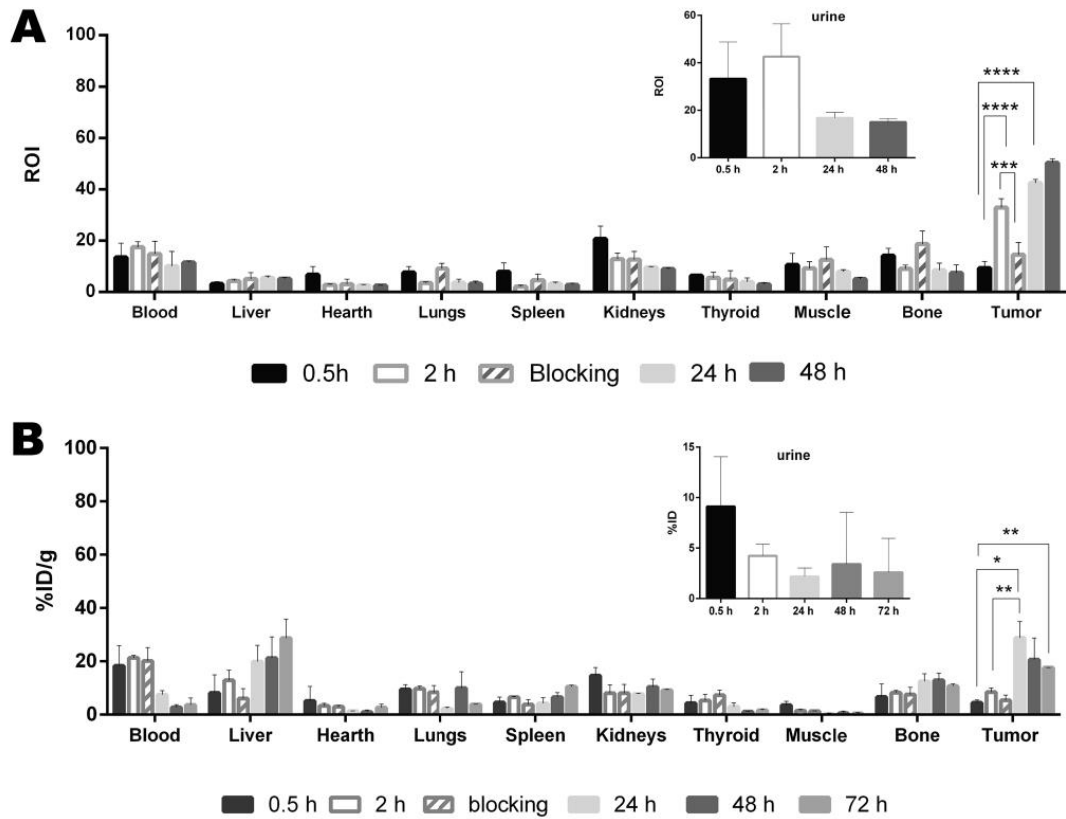
Figure 6. Biodistribution of the probes in B16F10 tumors. (**A**) Biodistribution of Sgc8-cAlexa647 and (**B**) Sgc8-c-NOTA-^{67}Ga. ****$p < 0.0001$; ***$p < 0.001$, **$p < 0.01$; *$p < 0.05$ (Student's t test).
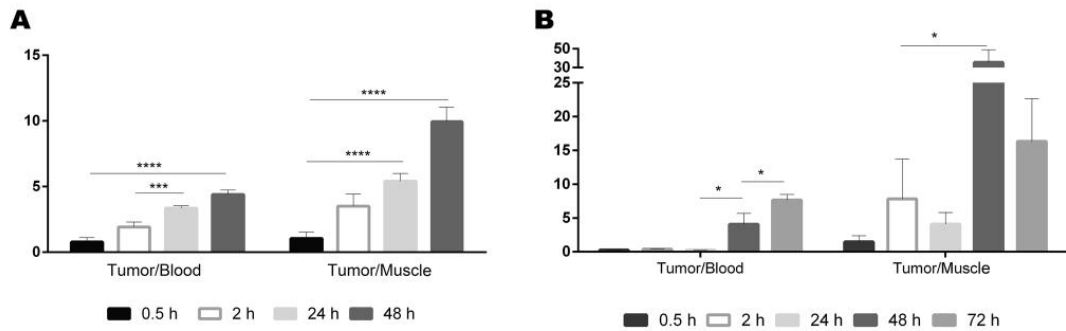
Figure 7. Tumor/blood and tumor/muscle ratios in the tumor model generated with B16F10 cells. (**A**) Sgc8-cAlexa647 and (**B**) Sgc8-c-NOTA-^{67}Ga in the tumor model generated with B16F10 cells. ****$p < 0.0001$, ***$p < 0.001$, *$p < 0.05$ (Student's t test).

developing intraoperative imaging devices, combined or not, the properties of both probes for use in guided surgeries; identifying and pointing out the tumor margins, helping in the surgical resection of tumors and even helpful in detecting metastases[42,51]. A deepened study with the metastatic melanoma model is currently in progress with the aim to improve the use of probes in early diagnosis that allows the selection of an efficient and personalized therapy, and even for monitoring after remission.

75
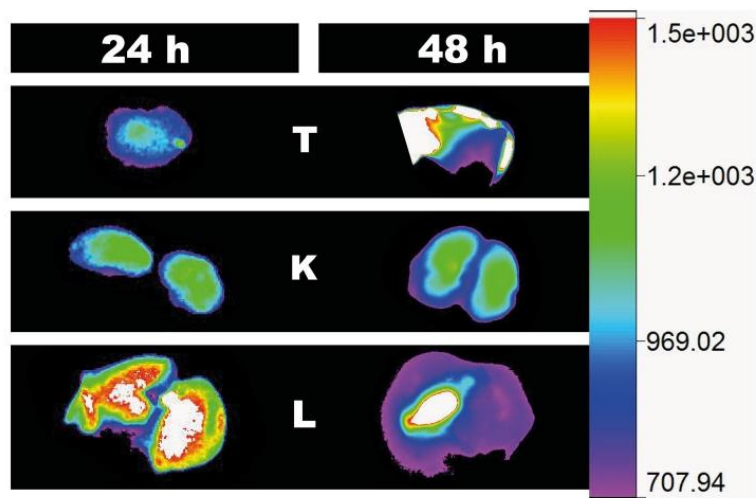
Figure 8. Ex vivo images with Sgc8-c-Alexa647 probe. Tumor (T), kidneys (K) and liver (L) were observed for melanoma tumor model generated with B16F10 cells 24 and 48 h post-injection of the probe.
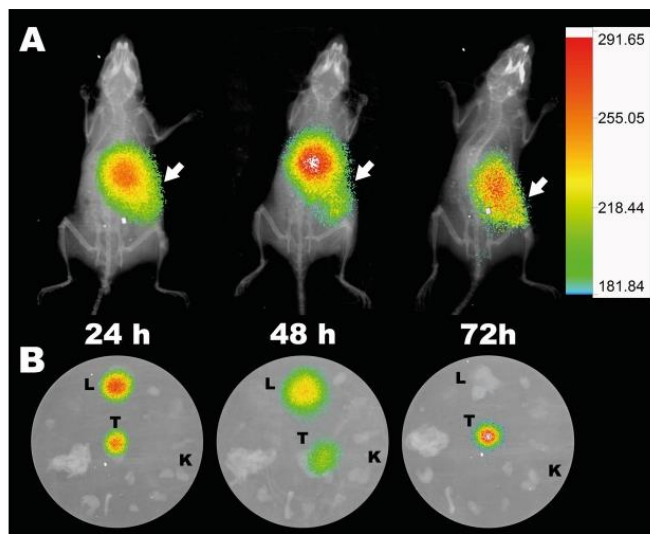
Figure 9. Multimodal images of animals injected with Sgc8-c-NOTA-^{67}Ga probe. (**A**) In vivo and (**B**) Ex vivo images at 24, 48 and 72 h post-injection of the probe. Arrow indicates the locations of the tumors. T: tumor, L: liver and K: kidneys. Ex vivo images also include bone, lungs, blood, heart, muscle, intestine, stomach, thyroid, and spleen.

Our results support the potential role of the Sgc8-c-NOTA-^{67}Ga and Sgc8-c-Alexa647 as molecular imaging probes optimum to improve strategies in non-invasive molecular diagnosis in melanoma, as well as theranostic approaches.

Methods

Synthesis and purification of Sgc8-c-NOTA-^{67}Ga and Sgc8-c-Alexa647. The synthesis and purification of both probes were performed following previous reports from our laboratory[39,41,42].

In vitro biological studies tumor cell lines. *Mus musculus* melanoma B16F1 (ATCC, CRL-6323), *Mus musculus* metastatic melanoma B16F10 (ATCC, CRL-6475) and *Homo sapiens* glioblastoma U87 MG (ATCC, HTB-14) cell lines were grown in adherence in Dulbecco's Modified Eagle's Medium (DMEM) (Capricorn, Ebsdorfergrund, Germany) supplemented with 10% FBS (Sigma-Aldrich, St. Louis, USA) and 2 mM L-glutamine (Sigma-Aldrich, St Louis, USA). *Homo sapiens*, acute lymphoblastic leukaemia CCRF-CEM (ATCC, CCL-119) cell line was grown in a suspension of RPMI-1640 medium (Sigma-Aldrich, St. Louis, USA) supplemented with 10% FBS and 2 mM L-glutamine. The CCRF-CEM and U87 MG cell lines were used as a positive and negative controls, respectively[52,53]. All cell lines were provided from ATCC (American Type Culture Collection, VA, USA) and were cultured at 37 °C with 5% CO_2.

Binding studies for radio-probe. For in vitro cell binding assays, 1.0×10^6 cells from the B16F10 cell line were washed with sterile Phosphate-buffered saline (PBS) pH 7.4, centrifuged at 1000 rpm for 3 min and incubated with 100,000 cpm of the Sgc8-c-NOTA-^{67}Ga probe by 0.5, 2 and 4 h at 37 °C. In addition, a competition assay was performed by incubating cells with an excess of underivatized aptamer (Sgc8-c-NH$_2$, 5 μg, 0.4 nmol) for 0.5 h a 37 °C. After 0.5 h, these same cells were incubated with the labeled probe for an additional 2 h at 37 °C. At the end of the incubation time, the medium was removed, and cells were resuspended and washed twice with PBS, centrifuging at 1000 rpm for 3 min. The test was done in quintupled. The activity retained in the cells was measured on aGamma counter (PC-RIA MAS, Stratec).

Binding studies for fluorescent-probe. The murine tumor cell line B16F10, and the human tumor cell lines CCRF-CEM and U87 MG, were washed with sterile PBS pH 7.4, centrifuged at 1000 rpm for 3 min and approximately, 5×10^5 cells were incubated at 37 °C for 30 min with different concentrations of the Sgc8-c-Alexa647 probe (0.007, 0.3 and 1 μM). After incubation, the medium was removed by centrifugation at 1000 rpm for 3 min and washed with PBS, and centrifuging again at 1000 rpm for 3 min. The test was done in quintupled. For each sample, 10,000 events were detected using a 635 nm excitation, laser detector and BP 660/20 nm. The FACS Canto II flow cytometer (BD Biosciences, San Diego, CA, USA) equipment and data were analyzed using FACS Diva and FlowJo software. These results were validated with an anti-PTK7-PE antibody (United States Biological. Clone Type: Polyclonal. Catalog Number: 033359-PE). Specific mean fluorescence indices (MFIs) were calculated as the mean fluorescence of Sgc8-c-Alexa647 cells positive in the presence of aptamer over the mean fluorescence of the entire cell population in the absence of aptamer.

Western blotting. Supernatants and cell pellets from B16F10 cell cultures were collected separately. Pellets were washed with sterile PBS pH 7.4, centrifuged at 1000 rpm for 3 min and stored at − 20 °C until use. Supernatant proteins were obtained by precipitation with trichloroacetic acid (TCA). Briefly, supernatants were centrifuged for 15 min at 4000*g* at 4 °C recovered and passed through a 0.22 μm filter. Then, TCA (10% final solution) was added and incubated for 1 h on ice. Pellets were obtained by centrifugation, for 30 min at 13,000 rpm and at 4 °C, and further washed three times with 1 mL of acetone and allowed to dry. Finally, proteins were resuspended in 500 μL of PBS pH 7.4. The amount of sample to be used in the Western blot was normalized, quantifying the samples using the bicinchoninic acid assay. Subsequently, these samples were run on a 12% SDS-PAGE gel at 100 V and the blotting membrane was transferred overnight at 400 mA at 4 °C. The membrane was blocked with 5% milk in PBS pH 7.4, for 2 h at room temperature (RT). Subsequently, it was incubated with either the Sgc8-c-Alexa647 probe (10 μg, 0.8 nmol) or the anti-PTK7-PE antibody, at the concentrations recommended by the manufacturer. Three washes with PBS/TBS were performed before the membrane was observed in an imaging equipment (In-Vivo MS FX PRO instrument, Bruker, Billerica, USA).

Confocal microscopy. To perform confocal microscopy assays, 1×10^5 cells from the B16F10 and B16F1 tumor cell lines were grown on round glass coverslips (12 mm) inside 24-well plates. These cells were incubated with the Sgc8-c-Alexa647 probe (10 μg, 0.8 nmol) for different times (2, 4, and 16 h). Cells were washed with sterile PBS pH 7.4 and fixed with 4% paraformaldehyde. Subsequently, the coverslips were placed in a humid chamber, the cells were blocked with 2% bovine serum albumin in PBS for 20 min at RT and then they were blocked for an additional 15 min, also at RT, with the same solution but adding Triton (0.3%). Cells were incubated for 1 h at RT with the *Hoechst 33342* nuclear marker (1:100, Immuno Chemistry Technologies, LLC) and with the *WGA-green* membrane marker (1:100, thermofisher scientific, USA). They were washed three times with PBS pH 7.4 and three more times with mili Q water. The coverslips were mounted with ProLong* (thermofisher Scientific, USA) and the images were acquired in the confocal microscope LEICATCS-SP5-DMI6000 (HeNe laser, 10 mW: 633 nm). To determine if the probe was internalized endosomically, we followed the same protocol as before, incubating for 0.5, 2 and 4 h and instead of using a membrane marker, the early endosomal marker *Rab5* (rabbit, 1:100, C8B1 mAb 3547, Cell Signaling Technology, USA) was used. The secondary antibody anti-rabbit IgG, Alexa 488-conjugated (goat, 1:500, ab 150077 Abcam, USA) was used.

In vivo biological studies. *Animals.* Female C57BL/6 mice, 8–12 weeks of age, were used for the in vivo evaluation. Animal experimentation protocols were approved by the Ethical Committee of the University for Animal Experimentation, Uruguay (approval number: 240011-001891-17), all experiments were performed following the principles outlined in the Declaration of Helsinki and complying with the ARRIVE guidelines. Animals were purchased from URBE (Unidad de Reactivos y Biomodelos de Experimentación, Facultad de Medicina-Universidad de la República, Montevideo, Uruguay). Animals were housed in wire mesh cages (racks with filtered air) at 20 ± 2 °C with cycle of 14 h of light and 10 h of darkness. They were fed ad libitum to standard

pellet diet and given water ad libitum and were used after a minimum of 3 days acclimation to the housing conditions. Animals were monitored daily, recording their behavior and the presence or absence of tumor. Tumor location and volume was recorded, checking that they did not exceed a diameter of 5 mm. Isoflurane was used for anesthesia and at the end of the experiments the animals were sacrificed by cervical dislocation.

Binding studies for fluorescent-probe. For this assay 2.5×10^5 cells/100 mL of the B16F10 cell line were injected subcutaneously into the right flank of C57BL/6 mice. Once tumors were palpable (10–12 days), the Sgc8-c-Alexa647 probe (25 µg, 2 nmol) was injected intravenously (i.v.) through the tail vein. At 0.5, 2 and 24 h post injection, mice were sacrificed to obtain the tumor, liver, spleen and marrow derived from the femur. Organs and tissues were disaggregated by passing through a cell strainer 70 µm (BD Bioscience) and resuspended in sterile PBS pH 7.4. For each sample, 10,000 events were detected using the same laser, detector, and equipment mentioned above. The test was done in quintupled. Data were analyzed using FACS Diva and FlowJo software.

Imaging and biodistribution. To generate the melanoma tumor model murine cells B16F1were inoculated in the C57BL/6 mice, as described above for B16F10. Once melanomas were palpable, the Sgc8-c-Alexa647 probe (25 µg, 2 nmol) was injected i.v. and at 0.5, 2, 24 and 48 h post- injection (n = 5 per time group), mice were sacrificed. Ex vivo images of organs (liver, heart, lungs, spleen, kidneys, thyroid, muscle, bone, blood and tumor) were acquired using the imaging equipment above mentioned, with the X-ray and fluorescence model. The results were expressed in ROI and the tumor/blood and tumor/muscle ratios were calculated. In vivo specificity was evaluated in a competition test. One group of mice (n = 5) was first i.v. injected with Sgc8-c-NH$_2$ in excess of 5 times more than the probe. After 30 min post-injection, the same mice were i.v. injected with the Sgc8-c-Alexa647 probe. After 2 h mice were sacrificed, images acquired and organs weighed. Similar evaluation was performed for the radiolabelled probe. Sgc8-c-NOTA-^{67}Ga was i.v. injected (~ 1850 kBq) and biodistribution of the probe was followed until 72 h post-injection. Over time, the animals were anesthetized with isoflurane to perform the images in vivo. Live images were acquired for 0.5, 2, 24, 48 and 72 h after injection by X-rays andGamma modalities in the imaging equipment. For the biodistributions animals were sacrificed, images were acquired and the levels of radioactivity in the tissue were measured using a Gamma counter (PC-RIA MAS, Stratec). Radioactivity levels were expressed as percentage of injected dose per organ gram (%ID/g) and injected dose (%ID). Competitive blocking assays were also performed, injecting mice first with 0.5 nmol of Sgc8-c-NH$_2$ and after 30 min re-injected with Sgc8-c-NOTA-^{67}Ga and at 2 h the imaging and biodistribution studies were performed.

Statistical analysis. Statistical analysis was performed using the Student's *t* test because the data are independent and have a normal distribution. The *p* values of significance are indicated in each figure.

References

1. rbe, C. & Leiter, U. Epidemiology of melanoma and nonmelanoma skin cancer—The role of sunlight. *Adv. Exp. Med. Biol.* **624**, 89–103 (2008).
2. Carr, S., Smith, C. & Wernberg, J. Epidemiology and risk factors of melanoma. *Surg. Clin. North Am.* **100**, 1–12 (2020).
3. Schadendorf, D. *et al.* Melanoma. *Nat. Rev. Dis. Prim.* **1**, 1–20 (2015).
4. Marsden, J. R. *et al.* Revised UK guidelines for the management of cutaneous melanoma. *J. Plast. Reconstr. Aesthetic Surg.* **63**, 1401–1419 (2010).
5. Abbas, O., Miller, D. D. & Bhawan, J. Cutaneous malignant melanoma: Update on diagnostic and prognostic biomarkers. *Am. J. Dermatopathol.* **36**, 363–379 (2014).
6. Ohsie, S. J., Sarantopoulos, G. P., Cochran, A. J. & Binder, S. W. Immunohistochemical characteristics of melanoma. *J. Cutan. Pathol.* **35**, 433–444 (2008).
7. Eisenstein, A. *et al.* Emerging biomarkers in cutaneous melanoma. *Mol. Diagnosis Ther.* **22**, 203–218 (2018).
8. Halaban, R. Signal transduction in normal and malignant melanocytes. *Pigment Cell Res.* **7**, 89–95 (1994).
9. Revach, O.-Y., Sandler, O., Samuels, Y. & Geiger, B. Cross-talk between receptor tyrosine kinases AXL and ERBB3 regulates invadopodia formation in melanoma cells. *Cancer Res.* **79**, 2634–2648 (2019).
10. Kroiher, M., Miller, M. A. & Steele, R. E. Deceiving appearances: Signaling by 'dead' and 'fractured' receptor protein-tyrosine kinases. *BioEssays* **23**, 69–76 (2001).
11. van der Geer, P., Hunter, T. & Lindberg, R. A. Receptor protein-tyrosine kinases and their signal transduction pathways. *Annu. Rev. Cell Biol.* **10**, 251–337 (1994).
12. Lhoumeau, A. C., Puppo, F., Prébet, T., Kodjabachian, L. & Borg, J. P. PTK7: A cell polarity receptor with multiple facets. *Cell Cycle* **10**, 1233–1236 (2011).
13. Golubkov, V. S. *et al.* Protein-tyrosine pseudokinase 7 (PTK7) directs cancer cell motility and metastasis. *J. Biol. Chem.* **289**, 24238–24249 (2014).
14. Sun, J. J. *et al.* The increased PTK7 expression is a malignant factor in cervical cancer. *Dis. Markers* **2019**, 1–10 (2019).
15. Yu, B. *et al.* Periostin secreted by cancer-associated fibroblasts promotes cancer stemness in head and neck cancer by activating protein tyrosine kinase 7. *Cell Death Dis.* **9**, 1082 (2018).
16. Kampen, K. R. Membrane proteins: The key players of a cancer cell. *J. Membr. Biol.* **242**, 69–74 (2011).
17. Lin, Y. *et al.* PTK7 as a novel marker for favorableGastric cancer patient survival. *J. Surg. Oncol.* **106**, 880–886 (2012).
18. Endoh, H. *et al.* Prognostic model of pulmonary adenocarcinoma by expression profiling of eight genes as determined by quantitative real-time reverse transcriptase polymerase chain reaction. *J. Clin. Oncol.* **22**, 811–819 (2004).
19. Zhang, H. *et al.* Protein tyrosine kinase 7 (PTK7) as a predictor of lymph node metastases and a novel prognostic biomarker in patients with prostate cancer. *Int. J. Mol. Sci.* **15**, 11665–11677 (2014).

78

20. Gärtner, S. *et al.* PTK 7 is a transforming gene and prognostic marker for breast cancer and nodal metastasis involvement. *PLoS One* **9**, e84472 (2014).
21. Saha, S. *et al.* A phosphatase associated with metastasis of colorectal cancer. *Science* **294**, 1343–6 (2001).
22. Fazilaty, H. & Mehdipour, P. Genetics of breast cancer bone metastasis: A sequential multistep pattern. *Clin. Exp. Metastasis* **31**, 595–612 (2014).
23. Lu, X. *et al.* PTK7/CCK-4 is a novel regulator of planar cell polarity in vertebrates. *Nature* **430**, 93–98 (2004).
24. Shnitsar, I. & Borchers, A. PTK7 recruits dsh to regulate neural crest migration. *Development* **135**, 4015–4024 (2008).
25. Shin, W. S. *et al.* Soluble PTK7 inhibits tube formation, migration, and invasion of endothelial cells and angiogenesis. *Biochem. Biophys. Res. Commun.* **371**, 793–798 (2008).
26. Tong, R. *et al.* Polylactide nanoparticles containing stably incorporated cyanine dyes for in vitro and in vivo imaging applications. *Microsc. Res. Tech.* **73**, 901–909 (2010).
27. Weissleder, R. & Mahmood, U. Molecular imaging. *Radiology* **219**, 316–333 (2001).
28. Zhuo, Z. *et al.* Recent advances in SELEX technology and aptamer applications in biomedicine. *Int. J. Mol. Sci.* **18**, 1–19 (2017).
29. Murphy, P. S., Patel, N. & McCarthy, T. J. Has molecular imaging delivered to drug development? *Philos. Trans. R. Soc. A Math. Phys. Eng. Sci.* **375**, 20170112 (2017).
30. Breaker, R. R. Natural and engineered nucleic acids as tools to explore biology. *Nature* **432**, 838–845 (2004).
31. Hwang, D. W. *et al.* A Nucleolin-targeted multimodal nanoparticle imaging probe for tracking cancer cells using an aptamer. *J. Nucl. Med.* **51**, 98–105 (2010).
32. Hicke, B. J. *et al.* Tumor targeting by an aptamer. *J. Nucl. Med.* **47**, 668–678 (2006).
33. Famulok, M. & Mayer, G. Aptamers as tools in molecular biology and immunology. *Curr. Top. Microbiol. Immunol.* **243**, 123–136 (1999).
34. Ellington, A. D. & Szostak, J. W. In vitro selection of RNA molecules that bind specific ligands. *Nature* **346**, 818–822 (1990).
35. Tuerk, C. & Gold, L. Systematic evolution of ligands by exponential enrichment: RNA ligands to bacteriophage T4 DNA polymerase. *Science* **249**, 505–510 (1990).
36. Borbas, K. E., Ferreira, C. S. M., Perkins, A., Bruce, J. I. & Missailidis, S. Design and synthesis of mono- and multimeric targeted radiopharmaceuticals based on novel cyclen ligands coupled to anti-MUC1 aptamers for the diagnostic imaging and targeted radiotherapy of cancer. *Bioconjug. Chem.* **18**, 1205–1212 (2007).
37. Calzada, V. *et al.* Development of new PTK7-targeting aptamer-fluorescent and -radiolabelled probes for evaluation as molecular imaging agents: Lymphoma and melanoma in vivo proof of concept. *Bioorg. Med. Chem.* **25**, 1163–1171 (2017).
38. Calzada, V. *et al.* Preliminary in vivo characterization of a theranosticaptamer : Sgc8-c-DOTA-⁶⁷Ga. *Aptamers* **1**, 19–27 (2017).
39. Sicco, E. *et al.* Derivatizations of Sgc8-c aptamer to prepare metallic radiopharmaceuticals as imaging diagnostic agents: Syntheses, isolations, and physicochemical characterizations. *Chem. Biol. Drug Des.* **91**, 747–755 (2018).
40. Sicco, E. *et al.* Sgc8-c aptamer as a potential theranostic agent for hemato-oncological malignancies. *Cancer Biother. Radiopharm.* **35**, 262–270 (2020).
41. Shangguan, D., Tang, Z., Mallikaratchy, P., Xiao, Z. & Tan, W. Optimization and modifications of aptamers selected from live cancer cell lines. *ChemBioChem* **8**, 603–606 (2007).
42. Schaafsma, B. E. *et al.* Near-infrared fluorescence sentinel lymph node biopsy in vulvar cancer: A randomised comparison of lymphatic tracers. *BJOG An Int. J. Obstet. Gynaecol.* **120**, 758–764 (2013).
43. KleinJan, G. H., Hellingman, D., Van den Berg, N. S., Van Oosterom, M. N., Hendricksen, K., Horenblas, S., Valdes Olmos, R. A. & vanLeeuwen, F. W. Hybrid surgical guidance: Does hardware integration of γ- and fluorescence imaging modalities make sense? *J. Nucl. Med.* **58**, 646–650 (2017).
44. Liberale, G., Bourgeois, P., Larsimont, D. & Moreau, M. Indocyanine green fluorescence-guided surgery after IV injection in metastatic colorectal cancer: A systematic review. *Eur. J. Surg. Oncol.* **43**, 1656–1667 (2017).
45. Mous, K. *et al.* Intracellular detection of differential APOBEC3G, TRIM5alpha, and LEDGF/p75 protein expression in peripheral blood by flow cytometry. *J. Immunol. Methods* **372**, 52–64 (2011).
46. Na, H., Shin, W., Ludwig, A. & Lee, S. The cytosolic domain of protein-tyrosine kinase 7 (PTK7), generated from sequential cleavage by a disintegrin and metalloprotease 17 (ADAM17) and γ-secretase, enhances cell proliferation and migration in colon cancer cells. *J. Biol. Chem.* **287**, 25001–25009 (2012).
47. Xiao, Z., Shangguan, D., Cao, Z., Fang, X. & Tan, W. Cell-specific internalization study of an aptamer from whole cell selection. *Chem. A Eur. J.* **14**, 1769–1775 (2008).
48. Porciani, D. *et al.* Modular cell-internalizing aptamer nanostructure enables targeted delivery of large functional RNAs in cancer cell lines. *Nat. Commun.* **9**, 2283 (2018).
49. Berger, H. *et al.* PTK7 localization and protein stability is affected by canonical Wnt ligands. *J. Cell Sci.* **130**, 1890–1903 (2017).
50. Pautu, V. *et al.* Melanoma tumour vasculature heterogeneity: From mice models to human. *J. Cancer Res. Clin. Oncol.* **145**, 589–597 (2019).
51. Liu, Y. *et al.* Hands-free, wireless goggles for near-infrared fluorescence and real-time image-guided surgery. *Surgery* **149**, 689–698 (2011).
52. Yin, J., He, X., Wang, K., Xu, F., Shangguan, J., He, D. & Shi, H. Label-free and turn-on aptamer strategy for cancer cells detection based on a DNA–silver nanocluster fluorescence upon recognition-induced hybridization. *Anal. Chem.* **85**, 12011–12019 (2013).
53. Jacobson, O. *et al.* ¹⁸F-labeled single-stranded DNA aptamer for PET imaging of protein tyrosine kinase-7 expression. *J. Nucl. Med.* **56**, 1780–1785 (2015).

Acknowledgements

Author contributions

M.M, V.C. and H.C. conceived all the experiments; E.S. conducted all the experiments; M.F. contributed in the animal experiments; A.M. contributed in the confocal microscopy experiments. All authors reviewed the manuscript.

Competing interests

The authors declare no competing interests.

Additional information

79

Correspondence and requests for materials should be addressed to V.C.

Reprints and permissions information is available at www.nature.com/reprints.

Publisher's note Springer Nature remains neutral with regard to jurisdictional claims in published maps and institutional affiliations.

80

4.3.1. Material suplementario del artículo_III

SUPPLEMENTARY MATERIAL

Metastatic and non-metastatic melanoma imaging using Sgc8-c aptamer PTK7-recognizer

Estefanía Sicco[1,2], Amy Mónaco[2], Marcelo Fernandez[3], María Moreno[2], Victoria Calzada[1,*], and Hugo Cerecetto[1]

[1]Área de Radiofarmacia, Centro de Investigaciones Nucleares, Facultad de Ciencias, Universidad de la República, 11400 Montevideo, Uruguay
[2]Departamento de Desarrollo Biotecnológico, Instituto de Higiene, Facultad de Medicina, Universidad de la República, 11600 Montevideo, Uruguay
[3]Laboratorio de Experimentación Animal, Centro de Investigaciones Nucleares, Facultad de Ciencias, Universidad de la Republica, 11400 Montevideo, Uruguay
[*]vcalzada@cin.edu.uy
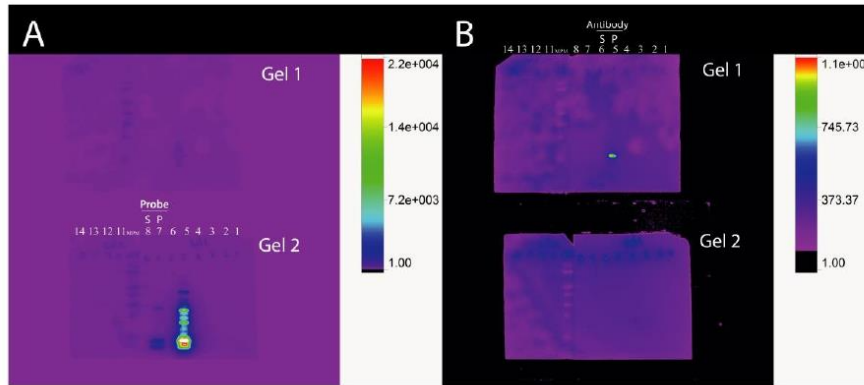
Figure S1. Full-length gels of proteins extracted from the supernatant (S) and pellet (P) of B16F10 cells culture. Exposition was performed with **A.** the Sgc8-c-Alexa647 probe, or **B.** the anti-PTK7-PE antibody. Gel 1 has been incubated with the antibody and Gel 2 with the probe. Both gels show the grouping of Western blot cropped of proteins extracted from the supernatant (S) and pellet (P) of B16F10 cells culture, used to generate Figure 1B of the article. Gel 1 lanes (from left to right): 14-11, negative control (samples incubated without the probe); 9, molecular weight marker; 8, B16F10 cell supernatants; 7, B16F10 cell pellets; 6-3, A20 cell supernatants and pellets. Gel 2 lanes (left to right): 14-11, negative controls (samples incubated without the antibody); 9, molecular weight marker; 6, B16F10 cell supernatants; 5, B16F10 cell pellets.
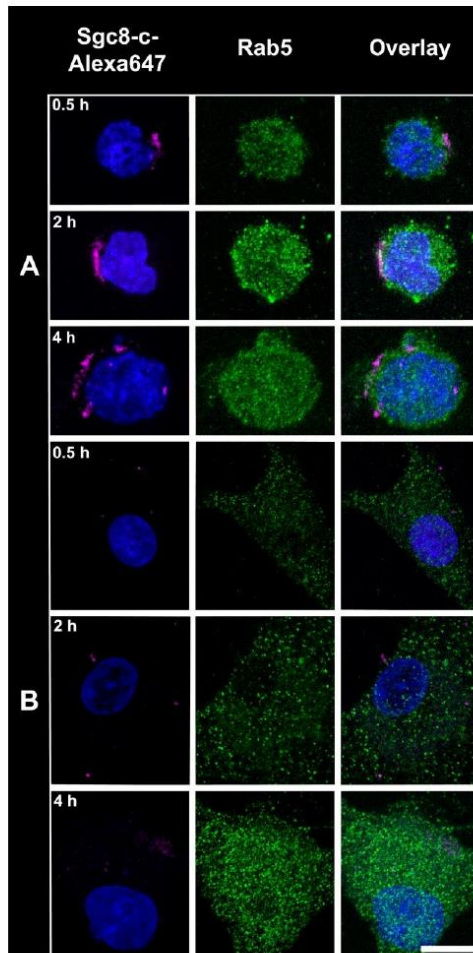
Figure S2. Sgc8-c-Alexa647 co-localize within endosomes. Confocal microscopy of **A.** CCRF-CEM and **B.** U87MG tumor cells incubated for 0.5, 2 and 4 h with the probe. Magenta: Sgc8-c-Alexa647, Blue: *Hoechst* and Green: *Rab5*. Scale bar: 10 μm.

S2
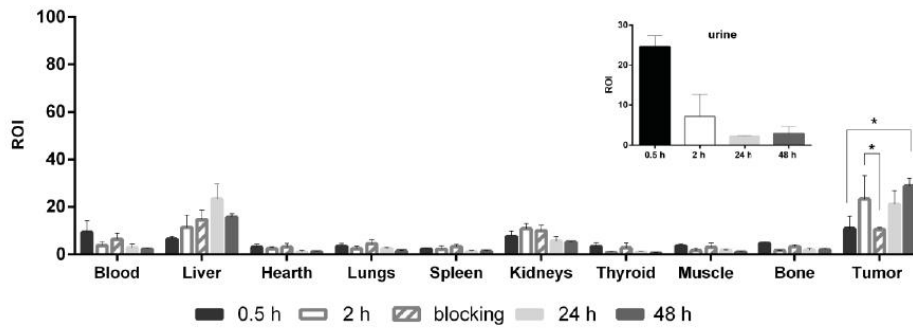
Figure S3. Biodistribution of Sgc8-c-Alexa647 probe in B16F1 tumors. * p < 0.05
(Student's t-test).
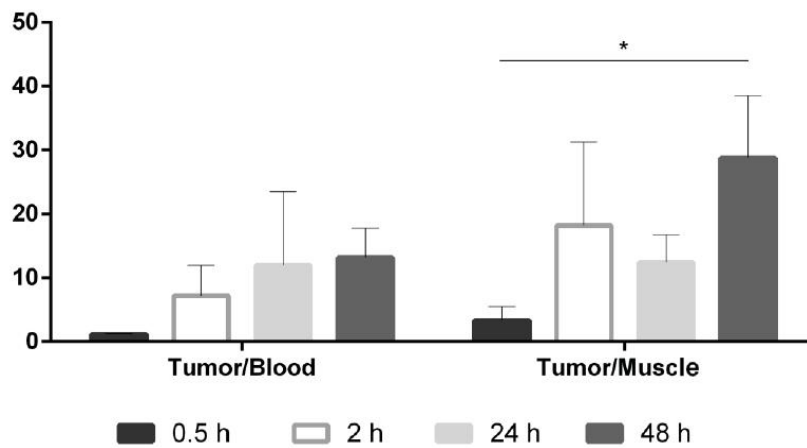
**Figure S4. Tumor/blood and tumor/muscle ratios in the tumor model generated
with B16F1 cells using Sgc8-cAlexa647 probe.** * p < 0.05 (Student's t-test).
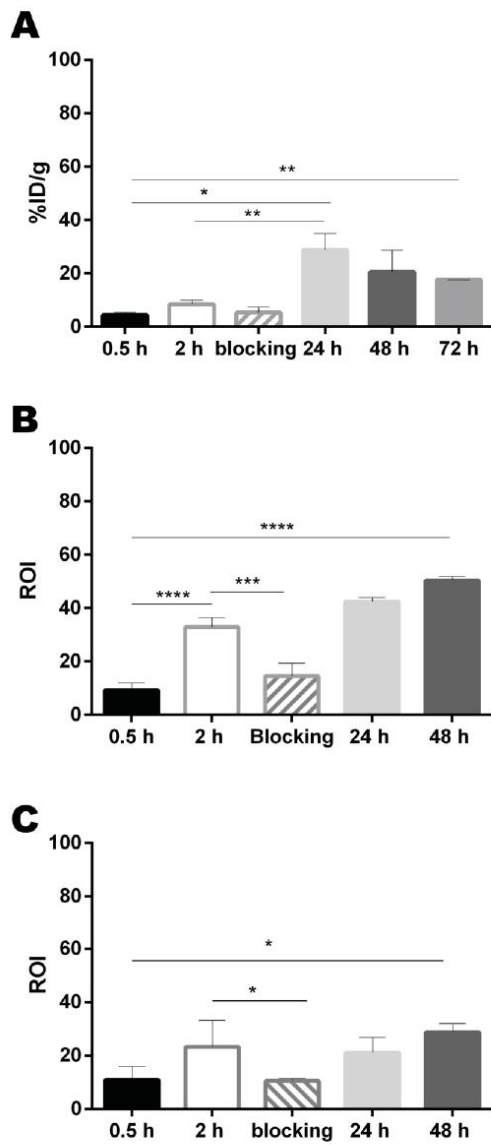
Figure S5. Biodistribution of the probes in tumor. In **A.** Biodistribution of Sgc8-c-NOTA-^{67}Ga and in **B.** Sgc8-cAlexa647 in the tumor model generated with B16F10 cells. In **C.** Biodistribution of Sgc8-cAlexa647 in the tumor model generated with B16F1 cells. **** $p < 0.0001$, *** $p < 0.001$, ** $p < 0.01$, * $p < 0.05$ (Student's t-test).

5. Capítulo II: Sgc8-c como agente potencial bioterapéutico selectivo en cáncer

5.1. Artículo IV: Síntesis, purificación y caracterización de conjugados aptámero-fármaco.

RESEARCH ARTICLE

Chemical conjugations of Sgc8-c with the lymphoma drug dasatinib to generate selective biotherapeutics

Estefanía Sicco[1], Lucía Almeida[1], María Moreno[2], Victoria Calzada[1,*], Hugo Cerecetto[1,*]

[1]Área de Radiofarmacia, Centro de Investigaciones Nucleares, Facultad de Ciencias, Universidad de la República, Mataojo 2055, 11400 Montevideo, Uruguay

[2]Departamento de Desarrollo Biotecnológico, Instituto de Higiene, Facultad de Medicina, Universidad de la República, 11600 Montevideo, Uruguay

*Correspondence to: Victoria Calzada, Email: vcalzada@cin.edu.uy; Hugo Cerecetto, Email: hcerecetto@cin.edu.uy

ABSTRACT

The conjugation of drugs to target therapeutics has become a promising method that could improve the efficacy of therapy and reduce side effects. Herein, we describe the efforts to covalently link the anti-lymphoma agent dasatinib to the truncated aptamer Sgc8-c, expecting the new hybrids to specifically damage lymphoma cells but with minimal toxicity towards non-target cells. Two linkages, ester and carbamate, with variable pH labilities were used to connect Sgc8-c with dasatinib. Different reaction conditions were studied by varying the solvent, time, temperature, heat source, pH and counter-ions. Each product from the reaction mixture was analysed by qualitative electrospray ionization time-of-flight mass spectrometry, identifying the nucleic acid modifications formed under the different experimental conditions. Among the reactions, depurinations from the 3´-extreme mainly occurred as lateral processes. Preparation of the carbamate-linked Sgc8-c–dasatinib hybrid **Sgc8-c-carb-da** was successful but the ester-linked hybrid only produced lateral undesired products. The potential biotherapeutic **Sgc8-c-carb-da** displayed the ability to trigger dasatinib at endosomal pH, which is optimal because this could be the aptamer's cellular uptake route.

KEYWORDS: biotherapeutics, Sgc8-c, dasatinib, drug delivery, synthesis, depurination

INTRODUCTION

The advantages of aptamers in terms of size, ease of production and ease of chemical modification (Breaker, 2004; Hwang et al, 2010) make them excellent candidates for the development of new biotechnological platforms to produce biotherapeutics (Famulok and Mayer, 1999; Hicke et al, 2006; Tong et al, 2010). Specifically, the use of aptamers as a vehicle for the selective delivery of drugs for clinical use has been described in the literature (Patil et al, 2005; Yazdian-Robati et al, 2017). The first examples included the use of DNA-intercalating drugs (Bagalkot et al, 2006; Taghdisi et al, 2010) such as doxorubicin and daunorubicin; however, these drugs could affect aptamer recognition by its target, leading to a loss of specificity. Advantages have been found using a series of covalent binding strategies between drug and aptamer at a site not relevant for recognition, thus avoiding loss of bioactivity (Zhao et al, 2015). However, the partially stable covalent bonds used, such as amides (Zhao et al, 2015), do not allow release of the drug under physiological conditions, potentially losing the activity provided by this component of the molecule.

The truncated DNA aptamer Sgc8-c, which has 41 bases and specifically binds to the PTK7 receptor (Shangguan et al, 2007), has been studied in our laboratory to develop tumour imaging agents (Calzada et al, 2017a; Calzada et al, 2017b; Sicco et al, 2018; Sicco et al, 2020). We found that

Sgc8-c was able to recognize PTK7 *in vivo* in murine melanoma and lymphoma models (Calzada et al, 2017a; Calzada et al, 2017b; Sicco et al, 2020). This behaviour provided us with the basis to develop potential therapeutic agents, using this truncated aptamer to direct anti-tumour drugs specifically to the site of action.

Herein, we propose covalently incorporating an anti-tumour agent into the structure of Sgc8-c using molecular hybridization strategies. The selected anti-tumour agent was dasatinib, which is a BCR-ABL kinase inhibitor approved by the Food and Drug Administration (USA) for the treatment of chronic myelogenous leukaemia (D'Cruz and Uckun, 2013; McCLafferty et al, 2018) and Philadelphia chromosome-positive acute lymphoblastic leukaemia (Jabbour and Kantarjian, 2016; Sasaki et al, 2020). Dasatinib is also a potent inhibitor of five other critical oncogenic tyrosine kinase families: SRC, c-KIT, PDGF receptors, Bruton tyrosine kinase (BTK) and ephrin receptor kinases (Hantschel et al, 2007; Araujo and Logothetis, 2010; Umakanthan et al, 2019). For example, inhibition of BTK can lead to the downstream mitigation of cell growth, proliferation, adhesion, migration and survival of B-cell malignancies, including chronic lymphocytic leukaemia, mantle cell lymphoma, marginal zone lymphoma and Waldenström macroglobulinaemia (Moore and Thompson, 2021). In view of this, dasatinib was incorporated into Sgc8-c using different (i.e. ester and carbamate) covalent connectors. These connectors were considered because they display different abilities to be hydrolysed, chemically or enzymatically, and hence promote the release of the drug at the site of action (Babu et al, 2020). Therefore, these potential therapeutic agents will use the aptamer as a vehicle for the selective delivery of dasatinib in tumour cells with overexpression of PTK7.

MATERIALS AND METHODS

Chemicals
All chemicals necessary for the reactions and to prepare suitable buffers were purchased from Sigma-Aldrich (St. Louis, MO, USA). Water was purified and deionized (18MΩ/cm^2) in a Milli-Q water filtration system (Millipore Corp., Milford). Dasatinib was purchased from Hong Kong Guokang Bio-Technology Co., Ltd (Baoji City, China). The 5'-(6-aminohexyl)-modified Sgc8-c truncated aptamer (12813 Da, **Sgc8-c-NH$_2$**) was purchased commercially from IDT Technologies (Integrated DNA Technologies, Inc., IA, USA).

Synthesis of dasatinib intermediates
Dasatinib phenylcarbonate (2)
This intermediate was prepared according to Carpino et al (Method II, Carpino et al, 1973) using dasatinib (**1**) in alcohol (1 equiv) and phenylchloroformate (1 equiv), modifying the reaction time (2hr) and the base (trimethylamine, 2 equiv). The reaction was monitored by thin layer chromatography (TLC) (dichloromethane:methanol = 95:5). The final product (**2**) was structurally characterized using nuclear magnetic resonance spectroscopy (^{1}H and^{13}C) and heteronuclear single quantum coherence (HSQC) and heteronuclear multiple bond correlation (HMBC) experiments.

Chloroacetyl dasatinib (3)
This intermediate was prepared according to Baker and Bordwell (Method II, Baker and Bordwell, 1955) using **1** (1 equiv) and chloroacetyl chloride (1 equiv), modifying the base (trimethylamine, 3.5 equiv) and the solvent (dry dichloromethane). The reaction was monitored by TLC (dichloromethane:methanol = 95:5). The final product (**3**) was structurally characterized using nuclear magnetic resonance spectroscopy (^{1}H and^{13}C) and HSQC and HMBC experiments.

Synthesis of Sgc8-c-carb-da
First, commercial **Sgc8-c-NH$_2$** (0.5mg) was washed with Milli-Q water and reaction buffer using Microcon® centrifugal filters (10kDa cut-off) or a PD-10 column (GE Healthcare Life Sciences, Little Chalfont, UK).

Intermediate **2** (200equiv) dissolved in dimethylsulphoxide (DMSO; 400µl for each 0.5mg of aptamer) was added to washed **Sgc8-c-NH$_2$** (1equiv) dissolved in a mixture of equal volumes (50:50) of sodium phosphate buffer (0.1M) and sodium bicarbonate buffer (0.1M) at pH 8.3 (200µl for each 0.5mg of aptamer) (Sicco et al, 2018). This mixture was left to react for 1 h at 60°C and *N,N*-dimethylformamide (DMF; 100µl for each 0.5mg of aptamer) was added, with the reaction maintained at 60°C for an additional 47hr. The reaction was stopped by washing **Sgc8-c-carb-da** with Milli-Q water using Microcon® centrifugal filters (10kDa cut-off). The reaction was monitored by reversed-phase high-performance liquid chromatography (RP-HPLC; Agilent 1200 Series Infinity Star, Santa Clara, USA) with a 5µm C-18 Kinetex column (150 x 4.6 mm; Phenomenex) run with an aqueous solution of triethylamine (50mM, pH 7.5)/5% (v/v) acetonitrile (solvent A) and methanol (solvent B) at a flow rate of 1ml/min and an A:B gradient of 90:10 to 40:60 for 30min (UV detection). Purification of **Sgc8-c-carb-da** was performed in the same RP-HPLC conditions. The desired product and subproducts were characterized using electrospray time-of-flight mass spectrometry (ESI-TOF-MS; IDT Technologies).

Physicochemical characterization of Sgc8-c-carba-da
Thermal stability (Sicco et al, 2018)
Sgc8-c-carba-da was incubated in Milli-Q water at 25°C, 37°C, 45°C, 60°C and 75°C for 30min. Subsequently, the mixtures were filtered (0.22µm) and analysed by RP-HPLC (see previous conditions) and gel electrophoresis. Briefly, for gel electrophoresis, 1.0µg of the sample was suspended in Milli-Q water (10µl), heated at 75°C for 10min, chilled on ice for 10min and added to electrophoresis buffer (1 µl). The samples were loaded into the gel. The gel electrophoreses were performed on 15% (w/v) native polyacrylamide gel in 1X TAE buffer using a constant voltage of 100V and a current of 0.04A. Silver nitrate staining was used for visualization. BioRad 170-8201 (20bp) was used as a molecular weight marker. These tests were carried out in duplicate.

Storage stability (Sicco et al, 2018)
The stability of **Sgc8-c-carba-da** in Milli-Q water at -20°C and 4°C for 30 days was checked weekly. At these time points, aliquots of the reaction mixture were filtered (0.22µm) and

analysed using RP-HPLC (see previous conditions) and gel electrophoresis as described above. These tests were carried out in duplicate.

Lipophilicity

Sgc8-c-carba-da was placed in an Eppendorf tube with 500µl of 1X phosphate-buffered saline (PBS, pH 7.4) and 500µl of *n*-octanol, centrifuged at 13000 rpm for 10min at room temperature and 200µL aliquots were removed for quantification on a spectrophotometer at 260nm. This test was carried out five times.

Dasatinib-releasing ability studies

To study the *in vitro* releasing capacity of the carbamate group at different pH, **Sgc8-c-carba-da** was challenged against a mixture of equal volumes (50:50) of sodium phosphate buffer (0.1M) and sodium bicarbonate buffer (0.1M) adjusted to pH 5.0, 5.5 and 7.4 with hydrochloric acid. The solutions were kept at a constant temperature of 37°C and fractions were removed at different times (0.5, 3, 6, 24, 30 and 48hr) for analysis by RP-HPLC (see previous conditions).

RESULTS

Chemical conjugations

The syntheses of the differently designed Sgc8-c–dasatinib conjugates were planned as two-step procedures. First, we prepared two different dasatinib derivatives (**2** and **3**; Figure 1) in excellent yields to study two different releasing moieties (ester and carbamate) that give us different biological responses of the bio-conjugates. Then, using RP-

HPLC, we analysed the optimal experimental conditions to link **Sgc8-c-NH$_2$** to **2** or **3**. For this, we initially studied the coupling of **Sgc8-c-NH$_2$** to carbonate **2** in order to test the reaction solvents, molar ratios of reactants, time, temperature, heat source and other reaction conditions (Sicco et al, 2017; Sicco et al, 2020).

According to previous results with the coupling of **Sgc8-c-NH$_2$** (Sicco et al, 2017), we selected an initial reactant molar ratio of 1:50 (aptamer:**2**) and room temperature to study the optimum reaction solvents. In this regard, we chose a mixture of equal volumes of sodium bicarbonate buffer (0.1M, pH 8.3) and sodium phosphate buffer (0.1M, pH 8.3) as the solvent for **Sgc8-c-NH$_2$** and different organic solvents were studied to dissolve **2**. The use of DMSO, triethylamine (Et$_3$N) or DMF did not produce consumption of **Sgc8-c-NH$_2$** in the first 24hr of reaction (runs 2–4, Table 1) whereas acetone produced complete **Sgc8-c-NH$_2$** decomposition (run 1, Table 1). However, when long reaction times were studied (*i.e.,* 120hr), the use of DMSO, Et$_3$N or DMF generated new compounds in very low yield, one of them being the product of interest, **Sgc8-c-carba-da** (see ESI-TOF-MS characterization below) (runs 5-7, Table 1). In order to improve the yield of **Sgc8-c-carba-da**, we studied a mixture of organic solvents and a selected mixture of buffers working at higher temperature. For example, at 60°C new products began to appear after 3hr of reaction (runs 8-10, Table 1). In these cases, the worst results were observed with the higher amount of Et$_3$N and the best results were obtained when a mixture of the four solvents was used (run 10, Table 1).
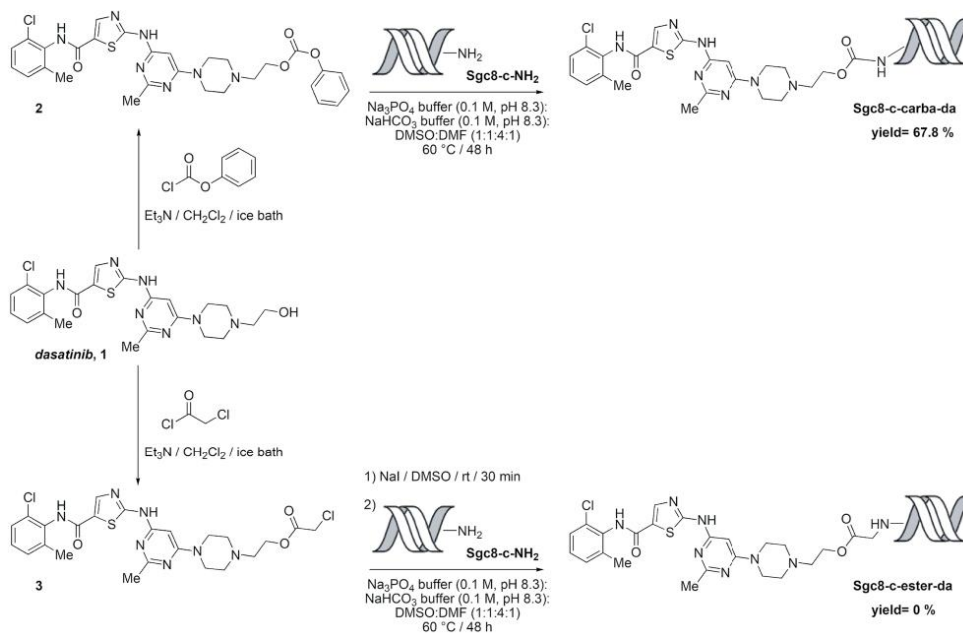
Figure 1. Schematic procedures designed and studied for the preparation of **Sgc8-c-carba-da** and **Sgc8-c-ester-da**.

Table 1. Selected initial experimental conditions assayed to optimize the preparation of **Sgc8-c-carba-da.**

run	solvent	reactants molar ratio (Sgc8-c-NH$_2$:2)	temperature (°C)	time (hr)	yield of Sgc8-c-carba-da	yield of secondary products[a]
1	mix buf[b]:acetone (30:1)					
2	mix buf:DMSO (30:1)[c]			24	0	0
3	mix buf:Et$_3$N (30:1)		25			
4	mix buf:DMF (30:1)					
5	mix buf:DMSO (30:1)	1:50			1.3	0.6
6	mix buf:Et$_3$N (30:1)			120	0.9	0
7	mix buf:DMF (30:1)				0	0.7
8	mix buf:DMF:Et$_3$N (4:1:5.5)				0.3	0.4
9	mix buf:DMF:Et$_3$N (3:4:1)		60	3	2.3	0
10	mix buf:DMSO:DMF:Et$_3$N (3:3:1:1)				6.1	0

[a]See (ESI-TOF-MS characterization); [b]Mixture of equal volumes of sodium bicarbonate buffer (0.1M, pH 8.3) and sodium phosphate buffer (0.1M, pH 8.3); [c]volume:volume

Table 2. Selected experimental conditions assayed to optimize the preparation of **Sgc8-c-carba-da** when varying the ratio of reactants and reaction time.

run	solvent	reactants molar ratio (Sgc8-c-NH$_2$:2)	temperature (°C)	time (hr)	yield of Sgc8-c-carba-da	yield of secondary products[ab]
1		1:2			0	0
2		1:10			0.8	0
3		1:50			4.2	0
4		1:100	60	24	8.0	2.4
5		1:200			48.8	2.9
6		1:300			39.0	0
7	mix buf[cc]:DMSO:DMF (2:4:1) (v:v:v)	1:400			22.0	0.7
8				2	3.0	0
9				4	7.0	0
10				6	11.6	0
11		1:200	60	8	17.0	0
12				30	51.8	1.9
13				**48**	**67.8**	**2.9**
14				72	49.4	0

[a]See (ESI-TOF-MS characterization); [b]Unreacted **Sgc8-c-NH$_2$** completes the 100% yield; [c]Mixture of equal volumes of sodium bicarbonate buffer (0.1M, pH 8.3) and sodium phosphate buffer (0.1M, pH 8.3)

For these reasons, our next goal was to optimize the amount of reactants and the reaction time using as solvent the mixture of buffer together with DMSO and DMF (Table 2). With reference to the amount of reactants (runs 1-7, Table 2), working at 60°C for 24hr the best result was obtained with a ratio of 1:200 (aptamer:**2**) (run 5, Table 2), a result that was completely in agreement with our previous findings with other organic reagents instead of **2** (Sicco et al, 2017). Regarding reaction times (runs 5 and 8-14, Table 2), working with the reactant ratio of 1:200 at 60°C the optimal time was 48hr of incubation. Other analyses were also performed, such as variation of temperature,

microwave irradiation as mode of heating, different reaction conditions (e.g. variation in pH), incorporation of additives (i.e. propylene glycol, Tween-20 or MgCl$_2$) and reagent **2** addition scheme (see Supporting Information, Table S1). All these analyses demonstrated that the best conditions to obtain **Sgc8-c-carba-da** were to use reactants in the ratio 1:200 (aptamer:**2**) and a mixture of buffer:DMSO:DMF (2:4:1, v:v:v) as solvent at 60°C for 48hr.

For the desired product **Sgc8-c-ester-da**, designed by the reaction between **Sgc8-c-NH$_2$** and intermediate **3** (Figure 1), the best conditions described above for **Sgc8-c-carba-**

da were used. In the first stage, sodium iodide was added to increase the reactivity of chloroacetyl chloride. Unfortunately, under the studied experimental conditions it was not possible to generate **Sgc8-c-ester-da**. The main products detected (see ESI-TOF-MS characterization below) were mainly the result of acetylations of the desired product, showing that the reactivity of the ester group of intermediate **3** (or the corresponding iodo-analogue) is very high compared with the aptamer-nucleophilic moieties (see below).

ESI-TOF-MS characterization of reaction products

To establish the identity of the final products of the reaction and consequently isolate the desired product, the different entities generated under particular conditions were separated by RP-HPLC and characterized by ESI-TOF-MS, with gel electrophoresis additionally used as a complementary evaluation. For example, Figure S1A (Supplementary Data) shows the reaction mixture for the preparation of **Sgc8-c-carba-da** in the conditions of run 11 of Table 2, whereas Figure S1C (Supplementary Data) shows the reaction mixture for the attempt to prepare this biotherapeutic in acetic acid (see Supplementary Data, Table S1, run S11), where a very different compound appeared as the main product. After isolation from the reaction mixture and ESI-TOF-MS characterization of each compound, the following conclusions could be reached (see Supplementary Figure S2): (i) the compound with a retention time (t_R) near to 11min (peak **A** in Supplementary Figure S1A) corresponded to **Sgc8-c-NH₂**; (ii) the compounds with t_R near to 12 and 14min (peaks **B** and **C** in Supplementary Figure S1A corresponded to the desired product, but with 3′-depurinations (**B**) possibly by the loss of deoxyadenosine and OH; **C** possibly by the loss of formyladenine and four H); (iii) the compound with t_R near to 21min (peak **D** in Supplementary Figure S1A) corresponded to the desired product but with fragmentation/hydrolysis of the pyrimidine ring from 3′-adenine and the addition of PO_2; (iv) the product with t_R near to 24min (peak **E** in Supplementary Figure S1A) corresponded to the desired product, **Sgc8-c-carba-da** (ESI-TOF-MS spectrum in Supplementary Figure S1D); and (v) the product in acidic milieu with t_R near to 26min (peak **F** in Supplementary Figure S1C) could correspond to the desired product but has a new purine fragment added (deoxyadenosine 3′-diphosphite) (see Supplementary Figure S2). The analyses by gel electrophoresis were completely in agreement with the MS studies (Figure 2).

The same analysis procedure was performed for the reaction mixtures used to obtain **Sgc8-c-ester-da**. In these cases, none of the isolated products corresponded to the desired one. We were unable to identify the product **Sgc8-c-ester-da** from the reaction mixtures, the isolated compounds being the result of both 3′-depurinations and iodo- or chloroacetylation processes (see analysis of the most relevant products in Supplementary Figure S3). As mentioned above, the iodo- or chloroacetyl esters were so reactive that they promoted iodo- or chloroacetylations as side reactions on phosphates or nucleophilic bases of the aptamer. Attempts to improve the reaction conditions were not performed.

The desired product, **Sgc8-c-carba-da**, was purified by RP-HPLC (t_R = 24.4min; see Materials and Methods, chromatographic conditions, peak **E** in Supporting Information, Figure S1A) in 67.8% yield and with purity higher than 99% (see Supplementary Figure S1B).

Physicochemical characterization of Sgc8-c-carba-da

The physical stability of **Sgc8-c-carba-da** was analysed in Milli-Q water at different temperatures and under different storage conditions over time. The RP-HPLC and gel electrophoresis results confirmed integrity in all cases. Furthermore, the electrophoresis profiles were consistent with the absence of low-molecular-weight fragmentation. **Sgc8-c-carba-da** was stable in water up to 75°C for 30min of incubation and under the different storage conditions analysed (dissolved in Milli-Q water and lyophilized) (Figure 3).

The lipophilicity of **Sgc8-c-carba-da**, calculated as $logD_{7.5}$, was -1.35 ± 0.04. The potential biotherapeutic **Sgc8-c-carba-da** was hydrophilic and a little more lipophilic than other Sgc8-c-probes previously developed by us (Table 3) (Calzada et al, 2017a, Calzada et al, 2017b; Sicco et al, 2020). The slightly less hydrophilic character could be the result of incorporation of the apolar framework from dasatinib. The $logD_{7.5}$ value, of the same order as for other probes, could indicate that the biological behaviour of **Sgc8-c-carba-da** was similar to that of other imaging agents.

Dasatinib-releasing ability of Sgc8-c-carba-da

The hydrolysis ability of the carbamate moiety in **Sgc8-c-carba-da,** releasing dasatinib from the biotherapeutic, was evaluated *in vitro* at different pH. The selected values
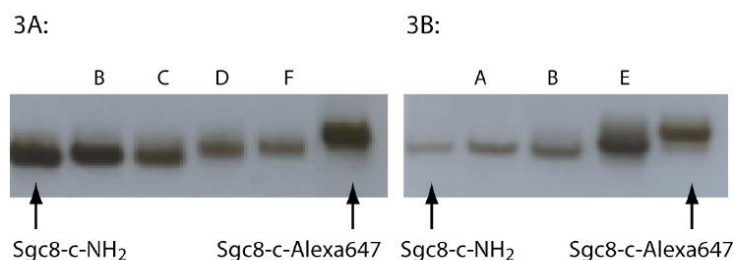

Figure 2. Gel electrophoresis analyses. Examples of two different electrophoretic analyses, including the products isolated from the reaction mixtures shown in Supporting Information, Figures S1A and S1C (isolated peaks **A–F**). In both runs, standards were included: **Sgc8-c-NH₂** and **Sgc8-c-Alex647** (MW = 13678D) (Calzada et al, 2017a; Sicco et al, 2018).

Table 3. Lipophilicities of different **Sgc8-c-NH$_2$** derivatives.

	Sgc8-c-NH$_2$ derivative				
	Sgc8-c-Alex647	**Sgc8-c-HYNIC-^{99m}Tc**	**Sgc8-c-DOTA-^{67}Ga**	**Sgc8-c-NOTA-^{67}Ga**	**Sgc8-c-carba-da**
LogD$_{7.5}$	- 1.90±0.30	- 2.36±0.29	- 1.87±0.05	- 2.41±0.11	- 1.35±0.04
Reference	Calzada et al, 2017a		Calzada et al, 2017b	Sicco et al, 2020	This paper
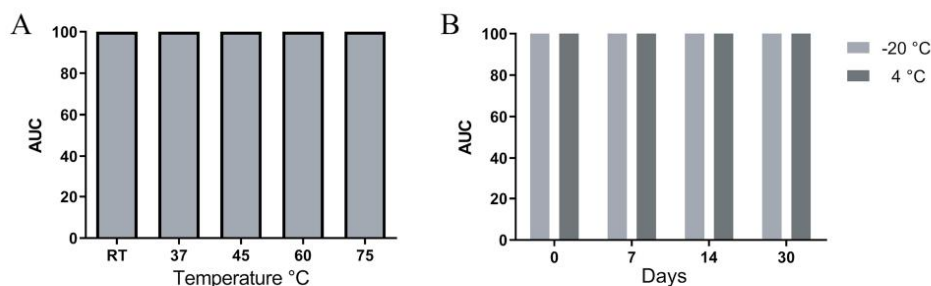
Figure 3. Stability studies. (**A**) **Sgc8-c-carba-da** was stable at different temperatures when incubated for 30min. (**B**) **Sgc8-c-carba-da** was stable under different storage conditions (dissolved in Milli-Q water or lyophilized, both at −20°C and 4°C) for 30 days. AUC: area under the curve from the RP-HPLC analysis. The measurements were carried out in duplicate.

correspond to physiological (7.4), intratumoural (5.5) and endosomal (5.0) pH. Complete **Sgc8-c-carba-da** hydrolysis was observed at 30hr after incubation but only at endosomal pH was dasatinib released in a short time (from 0.5hr). For cytoplasmatic and intratumoural pH, it was observed that dasatinib release began at times close to 24hr but this was not complete at 30hr.

CONCLUSIONS

Aptamers are promising molecular drug-delivery vehicles (Tang et al, 2020; Sameiyan et al, 2021), possessing optimal properties that include a ligand-specific response, short sequence, low immunogenic potential and easy functionalization. In our previous studies, we modified the Sgc8-c aptamer to generate imaging probes (Calzada et al, 2017a, Calzada et al, 2017b; Sicco et al, 2018, 2020). Synthesized and evaluated *in vivo*, Sgc8-c-fluorescent and -radioactive agents showed the ability to recognize different tumoural systems (*i.e.*, melanoma and lymphoma). Herein, a Sgc8-c-dasatinib hybrid was designed, synthesized and studied as a potential dasatinib-releasing biotherapeutic. A 5'-amino derivative of Sgc8-c was used to conjugate to dasatinib using two different linkages: carbamate and ester. The biotherapeutic with a carbamate connector was efficiently prepared with near to 70% yield under optimal conditions (*i.e.*, using a 200-fold excess of dasatinib derivative **2** in a mixture of adequate solvents). The biotherapeutic was successfully purified using RP-HPLC to obtain a product with high purity (near to 100%). The physicochemical properties of the biotherapeutic, such as stability and lipophilicity, are adequate for its use as a future drug. Additionally, the ability to release dasatinib was pH-dependent, the endosome being the best place to release the drug as cytoplasmatic and intratumoural pH gives only slow and

incomplete hydrolysis. These data are very interesting: (i) as we have previously reported that probes based on the Sgc8-c aptamer have rapid tumour uptake and blood clearance (Calzada et al, 2017a, Calzada et al, 2017b; Sicco et al, 2020), when **Sgc8-c-carba-da** is evaluated *in vivo* it will be expected to reach the site of action with minimal hydrolysis at the non-target sites; and (ii) as the route of some aptamers' internalization has been confirmed as endosomal (Xiao et al, 2008; Porciani et al, 2018), when **Sgc8-c-carba-da** penetrates the tumour cell via the endosome the release of dasatinib will take place.

The findings reported here highlight the potential of a simple aptamer as an anti-tumour delivery vehicle. Experiments related to the bioactivity of **Sgc8-c-carba-da** are currently underway.

ACKNOWLEDGEMENTS

COMPETING INTERESTS

None declared.

LIST OF ABBREVIATIONS

DMF: *N,N*-**D**i**m**ethylformamide
DMSO: **D**i**m**ethyl**s**ulf**o**xide
ESI-TOF: **E**lectrospray **I**onization **T**ime-**o**f-**F**light
FDA: **F**ood and **D**rug **A**dministration
HMBC: **H**eteronuclear **M**ultiple **B**ond **C**orrelation

HPLC: **H**igh **P**erformance **L**iquid **C**hromatography
HSQC: **H**eteronuclear **S**ingle **Q**uantum **C**oherence
MeOH: **M**e**th**an**o**l
MS: **M**ass **S**pectrometry
PBS: **P**hosphate **B**uffered **S**aline
PTK7: **P**rotein **T**yrosine **K**inase **7**
RP: **R**everse **P**hase
TAE: **T**ris base, **a**cetic acid and **E**DTA
TLC: **T**hin **L**ayer **C**hromatography

REFERENCES

Araujo J and Logothetis C. 2010. Dasatinib: A Potent SRC Inhibitor in Clinical Development for the Treatment of Solid Tumors. Cancer Treat Rev, 36, 492-500.

Babu T, Sarkar A, Karmakar S, Schmidt C and Gibson D. 2020. Multiaction Pt(IV) Carbamate Complexes Can Codeliver Pt(II) Drugs and Amine Containing Bioactive Molecules. Inorg Chem, 59, 5182-5193.

Bagalkot V, Farokhzad OC, Langer R and Jon S. 2006. An Aptamer-Doxorubicin Physical Conjugate as a Novel Targeted Drug-Delivery Platform. Angew Chem Int Ed Engl, 45, 8149-8152.

Baker RH and Bordwell FG. 1955. tert-Butyl Acetate. Organic Syntheses, Bristol, USA, Online Edition, pp 141.

Breaker RR. 2004. Natural and Engineered Nucleic Acids as Tools to Explore Biology. Nature, 432, 838-845.

Calzada V, Moreno M, Newton J, González J, Fernández M, Gambini JP, et al. 2017. Development of New PTK7-targeting Aptamer-Fluorescent and -Radiolabelled Probes for Evaluation as Molecular Imaging Agents: Lymphoma and Melanoma In Vivo Proof of Concept. Bioorg Med Chem, 25, 1163-1171.

Calzada V, Báez J, Sicco E, Margenat J, Fernández M, Moreno M, et al. 2017. Preliminary In Vivo Characterization of a Theranostic Aptamer: Sgc8-c-DOTA-^{67}Ga. Aptamers, 1, 19-27.

Carpino LA, Collins D, Göwecke S, Mayo J, Thatte SD and Tibbetts F. 1973. t-Butyl Carbazate. Organic Syntheses, UMass Boston, USA, Online Edition, pp 166.

D´Cruz OJ and Uckun FM. 2013. Protein Kinase Inhibitors Against Malignant Lymphoma. Expert Opin Pharmacother, 14, 707-721.

Famulok M and Mayer G. 1999. Aptamers as Tools in Molecular Biology and Immunology. Curr Top Microbiol Immunol, 123-136.

Hantschel O, Rix U, Schmidt U, Bürckstümmer T, Kneidinger M, Schütze G, et al. 2007. The Btk Tyrosine Kinase is a Major Target of the Bcr-Abl Inhibitor Dasatinib. Proc Natl Acad Sci USA, 104, 13283-13288.

Hicke BJ, Stephens AW, Gould T, Chang YF, Lynott CK, Heil J, et al. 2006. Tumor Targeting by an Aptamer. J Nucl Med, 47, 668-678.

Hwang DW, Ko HY, Lee JH, Kang H, Ryu SH, Song IC, et al. 2010. A Nucleolin-Targeted Multimodal Nanoparticle Imaging Probe for Tracking Cancer Cells Using an Aptamer. J Nucl Med, 51, 98-105.

Jabbour E and Kantarjian H. 2016. Chronic Myeloid Leukemia: 2016 Update on Diagnosis, Therapy, and Monitoring. Am J Hematol, 91, 252-265.

McCafferty EH, Dhillon S and Deeks ED. 2018. Dasatinib; A Review in Pediatric Chronic Myeloid Leukemia. Pediatr Drugs, 20, 593-600.

Moore DC and Thompson D. 2021. A Review of the Bruton tyrosine kinase inhibitors in B-cell malignancies. J Adv Pract Oncol, 12, 439-447.

Patil SD, Rhodes DG and Burgess DJ. 2005. DNA-based Therapeutics and DNA Delivery Systems : A Comprehensive Review. AAPS J, 7, E61-E77.

Porciani D, Cardwell LN, Tawiah KD, Alam KK, Lange MJ, Daniels MA, et al. 2018. Modular Cell-internalizing Aptamer Nanostructure Enables Targeted Delivery of Large Functional RNAs in Cancer Cell Lines. Nat Commun, 9, 2283.

Sameiyan E, Bagheri E, Dehghani S, Ramezani M, Alibolandi M, Abnous K, et al. 2021. Aptamer-based ATP-responsive Delivery Systems for Cancer Diagnosis and Treatment. Acta Biomater, 123, 110-122.

Sasaki K, Kantarjian H, Wierda W, Ravandi-Kashani F, Jorgensen J, Wang SA, et al. 2020. Phase 2 Study of Hyper-CMAD with Liposomal Vincristine for Patients with Newly Diagnosed Acute Lymphoblastic Leukemia. Am J Hematol, 95, 734-739.

Shangguan D, Tang Z, Mallikaratchy P, Xiao Z and Tan W. 2007. Optimization and Modifications of Aptamers Selected from Live Cancer Cell Lines. ChemBioChem, 8, 603-606.

Sicco E, Báez J, Margenat J, García F, Ibarra M, Cabral P, et al. 2018. Derivatizations of Sgc8-c Aptamer to Prepare Metallic Radiopharmaceuticals as Imaging Diagnostic Agents: Syntheses, Isolations, and Physicochemical Characterizations. Chem Biol Drug Des, 91, 747-755.

Sicco E, Baez J, Ibarra M, Fernández M, Cabral P, Moreno M, et al. 2020. Sgc8-c Aptamer as a Potential Theranostic Agent for Hemato-Oncological Malignancies. Cancer Biother Radiopharm, 35, 262-270.

Taghdisi SM, Abnous K, Mosaffa F and Behravan J. 2010. Targeted delivery of daunorubicin to T-cell acute lymphoblastic leukemia by aptamer. J Drug Target, 18, 277-281.

Tang Y, Liu H, Chen H, Chen Z, Liu Y, Jin L, et al. 2020. Advances in Aptamer Screening and Drug Delivery. J Biomed Nanotechnol, 16, 763-788.

Tong R, Coyle VJ, Tang L, Barger AM, Fan TM, Cheng J. 2010. Polylactide Nanoparticles Containing Stably Incorporated Cyanine Dyes for In Vitro and In Vivo Imaging Applications. Microsc Res Tech, 73, 901-909.

Umakanthan JM, Iqbal J, Batlevi CL, Bouska A, Smith LM, Shostrom V, et al. 2019. Phase I/II Study of Dasatinib and Exploratory Genomic Analysis in Relapsed or Refractory Non-Hodgkin Lymphoma. Br J Haematol, 184, 744-752.

Xiao Z, Shangguan D, Cao Z, Fang X, Tan W. 2008. Cell-specific Internalization Study of an Aptamer from Whole Cell Selection. Chem A Eur J, 14, 1769-1775.

Yazdian-Robati R, Arab A, Ramezani M, Abnous K and Mohammad S. 2017. Application of Aptamers in Treatment and Diagnosis of Leukemia. Int J Pharm, 529, 44-54.

Zhao N, Pei S-N, Qi J, Zeng Z, Iyer SP, Lin P, et al. 2015. Oligonucleotide Aptamer-drug Conjugates for Targeted Therapy of Acute Myeloid Leukemia. Biomaterials, 67, 42-51.

5.1.1. Material suplementario del artículo_IV

SUPPLEMENTARY DATA

RESEARCH ARTICLE

Chemical conjugations of Sgc8-c with the lymphoma drug dasatinib to generate selective biotherapeutics

Estefanía Sicco[1], Lucía Almeida[1], María Moreno[2], Victoria Calzada[1,*], Hugo Cerecetto[1,*]

[1]Área de Radiofarmacia, Centro de Investigaciones Nucleares, Facultad de Ciencias, Universidad de la República, Mataojo 2055, 11400 Montevideo, Uruguay

[2]Departamento de Desarrollo Biotecnológico, Instituto de Higiene, Facultad de Medicina, Universidad de la República, 11600 Montevideo, Uruguay

Correspondence to: Victoria Calzada, Email: vcalzada@cin.edu.uy; Hugo Cerecetto, Email: hcerecetto@cin.edu.uy

Table S1. Selected of other experimental conditions studied to optimize the preparation of **Sgc8-c-carba-da**.

run	Solvent	reactants molar ratio (**Sgc8-c-NH$_2$:2**)	temperature (°C)/mwi[a]	time	yield of **Sgc8-c-carba-da**	yield of secondary products[b]
S1	mix buf[c]:DMSO:DMF (2:4:1) (v:v:v)	1:200	25	24 hr	0	0
S2			37		2.0	0
S3			50		1.9	0
S4			80[d]		5.2	0
S5			100[d]		0	0
S6			mwi / low potency[e]	8 min	0	0
S7			mwi / low potency	5 min	5.9	0
S8			mwi / high potency[e]	5 min	0	0
S9	mix buf[c]:DMSO:DMF (2:4:1) (v:v:v) + Et$_3$N (0.5)		60	48 hr	24.5	0
S10			60	72 hr	8.1	60.5
S11	mix buf[c]:DMSO:DMF (2:4:1) (v:v:v) + acetic acid (0.1)		60	48 hr	0.8	94.5
S12	mix buf[c]:DMSO:DMF (1:1:0.5) (v:v:v) + propylene glycol (1)		60	24 hr	1.8	0
S13	mix buf[c]:DMSO:DMF (1:1:0.5) (v:v:v) + Tween 20 (0.2)				0	0
S14	mix buf[c]:DMSO:DMF (2:4:1) (v:v:v) + MgCl$_2$ (5mM)				4.8	0
S15	mix buf[c]:DMSO:DMF (2:4:1) (v:v:v)	2 addition - Initial: 20 eq - 2 h: 50 eq - 4 h: 50 eq - 22 h: 50 eq - 26 h: 30 eq	60	30 hr	18.1	0

[a]mwi: microwave irradiation. [b] See ESI-TOF mass spectrometry characterization. [c]Mixture of equal volume of sodium bicarbonate buffer (0.1M, pH 8.3) and sodium phosphate buffer (0.1M, pH 8.3). [d]Degradation of **Sgc8-c-NH$_2$** was observed. [d] Complete degradation of **Sgc8-c-NH$_2$** was observed.
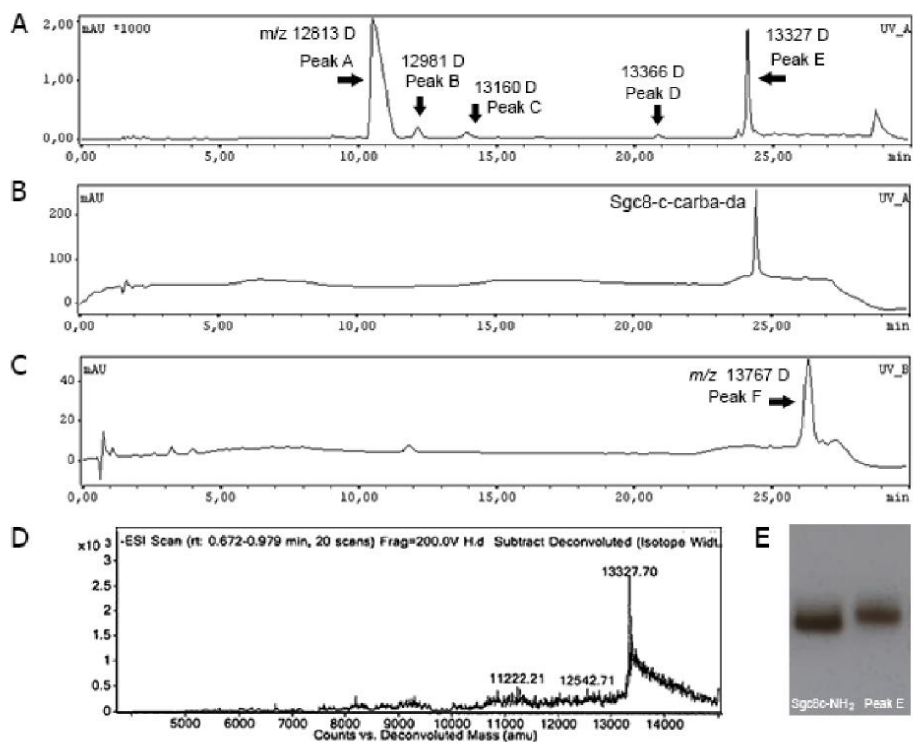
Figure S1. Studies of the reactions in order to identify the desired product, **Sgc8-c-carba-da**: (**A**) RP-HPLC profile of the reaction according to run 11 of Table 2; (**B**) desired product after purification by RP-HPLC; (**C**) RP-HPLC profile of the reaction in acetic acid (run S11, Table S1, Supporting Information); (**D**) ESI-TOF-MS spectrum of the product corresponding to peak **E** in Figure 2A; and (**E**) gel electrophoresis of **Sgc8-c-NH₂** and purified peak **E**.

Peak B (MW: 12981 D)

loss of 346 D

Peak C (MW: 13160 D)

loss of 167 D

Peak D (MW: 13366 D)

gain of 39 D

Peak F (MW: 13767 D)

gain of 440 D
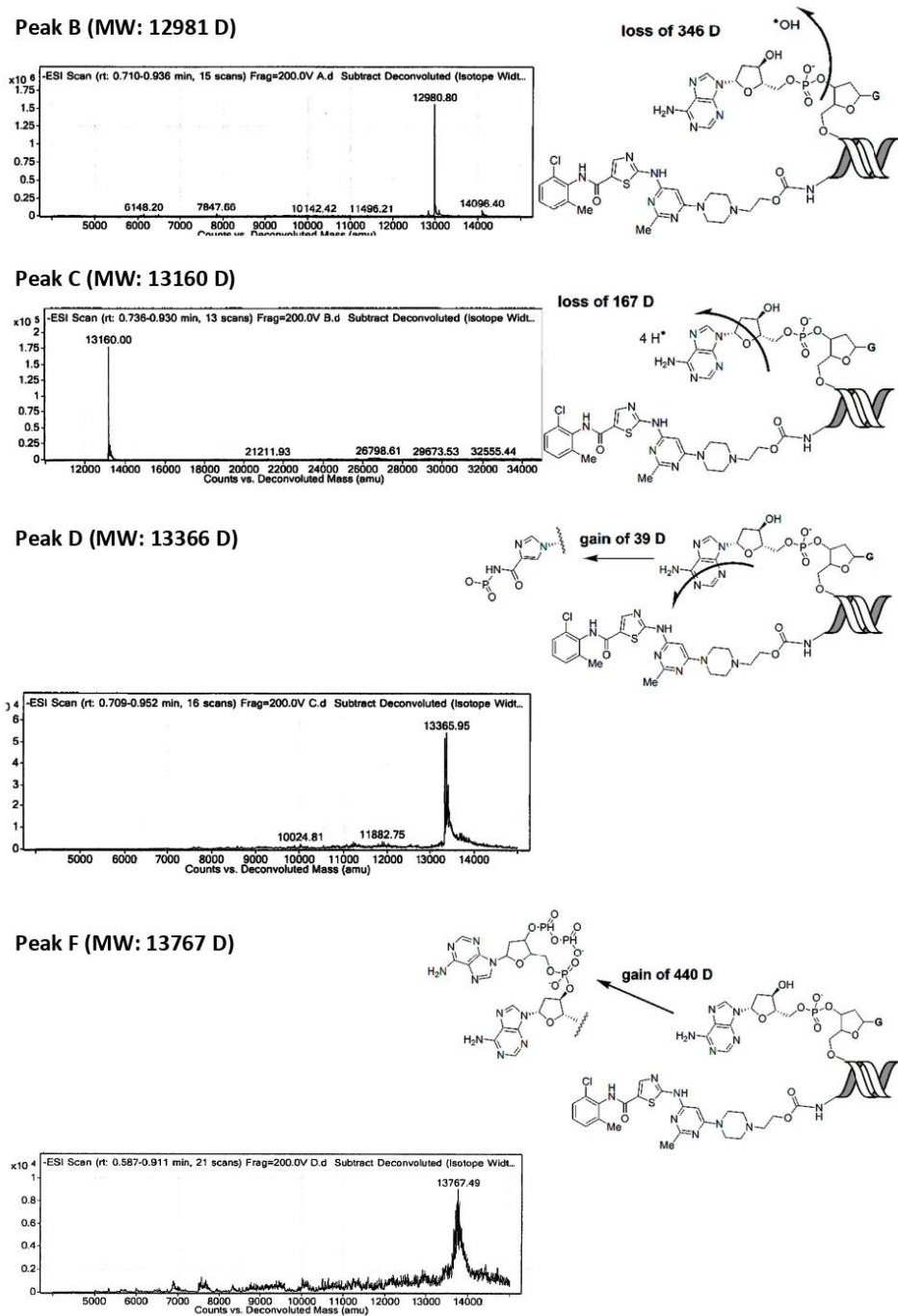
Figure S2. Proposal of secondary products isolated in the **Sgc8-c-carba-da** preparation optimization conditions.
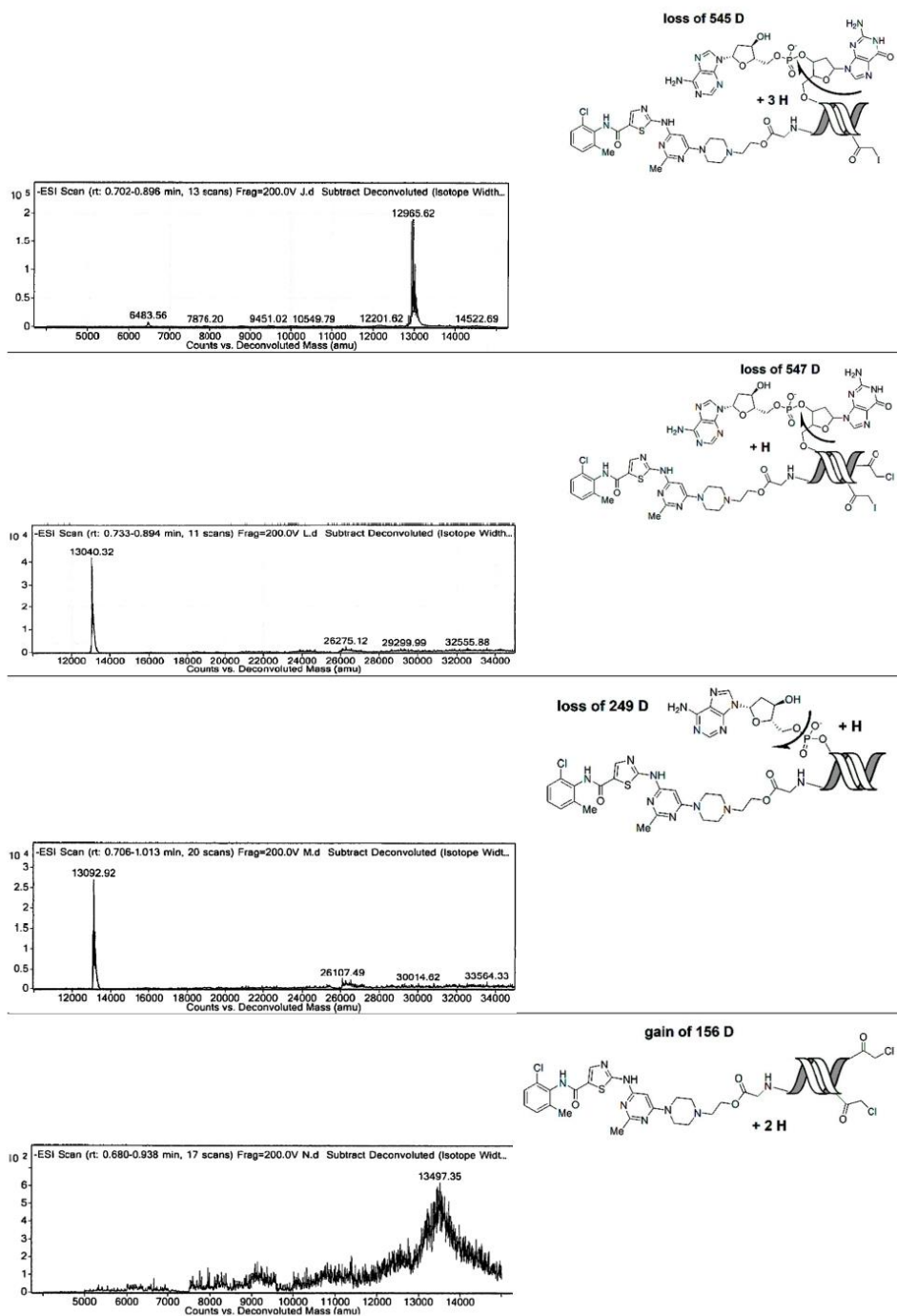
Figure S3. Proposal of products isolated in the **Sgc8c-ester-da** preparation optimization conditions.

5.2. Artículo V: Prueba de concepto del conjugado aptámero-fármaco Sgc8-c-carb-da en linfoma.

Article

Targeted-Lymphoma Drug Delivery System Based on the Sgc8-c Aptamer

Estefanía Sicco [1,2], Hugo Cerecetto [1] , Victoria Calzada [1,*] and María Moreno [2,*]

1   Área de Radiofarmacia, Centro de Investigaciones Nucleares, Facultad de Ciencias,
     Universidad de la República, Montevideo 11400, Uruguay
2   Departamento de Desarrollo Biotecnológico, Instituto de Higiene, Facultad de Medicina,
     Universidad de la República, Montevideo 11600, Uruguay
*   Correspondence: vcalzada@cin.edu.uy (V.C.); mmoreno@higiene.edu.uy (M.M.); Tel.: +598-25250800 (V.C.);
     +598-24871288 (M.M.); Fax: +598-25250895 (V.C.); +598-24873073 (M.M.)

Simple Summary: Aptamers are oligonucleotides that recognise their target with high specificity and affinity, having properties comparable to those of antibodies; however, they present important advantages in terms of their size, production, and modification. These characteristics make them excellent candidates for the development of new biotechnological platforms and their application as imaging or therapy agents. The Sgc8-c aptamer binds to PTK7, allowing the recognition of haemato-oncological malignancies, among others. Thus, we have developed aptamer-drug conjugates by chemical synthesis, hybridizing Sgc8-c and dasatinib, a drug proposed for lymphoma chemotherapy. Here, we demonstrated that the aptamer-drug conjugate, **Sgc8-c-carb-da**, specifically inhibited lymphocyte growth, produced cell death, caused cell proliferation arrest, and affected mitochondrial potential. In addition, **Sgc8-c-carb-da** showed higher (2.5-fold) cytotoxic effects than dasatinib in an in vitro cell-directed assay that mimics in vivo conditions. These findings provide proof-of-concept of the therapeutic value of **Sgc8-c-carb-da** for lymphoma, creating new opportunities for the chemical synthesis of novel targeted biotherapeutics.

Abstract: Aptamers are emerging as a promising new class of functional nucleic acids because they can specifically bind to any target with high affinity and be easily modified chemically with different pharmacophoric subunits for therapy. The truncated aptamer, Sgc8-c, binds to tyrosine-protein kinase-like 7 receptor, a promising cancer therapeutic target, allowing the recognition of haemato-oncological malignancies, among others. We have previously developed aptamer-drug conjugates by chemical synthesis, hybridizing Sgc8-c and dasatinib, a drug proposed for lymphoma chemotherapy. One of the best-characterised Sgc8-c-dasatinib hybrids, namely **Sgc8-c-carb-da**, was capable of releasing dasatinib at an endosomal-pH. Herein, we probed the therapeutic potential of this aptamer-drug conjugate. **Sgc8-c-carb-da** specifically inhibited murine A20 B lymphocyte growth and produced cell death, mainly by late apoptosis and necrosis. In addition, **Sgc8-c-carb-da** generated an arrest in cell proliferation, with a cell cycle arrest in the Sub-G1-peak. The mitochondrial potential was altered accordingly to these pathways. Moreover, using an in vitro cell-targeting assay that mimics in vivo conditions, we showed that **Sgc8-c-carb-da** displayed higher (2.5-fold) cytotoxic effects than dasatinib. These findings provide proof-of-concept of the therapeutic value of **Sgc8-c-carb-da** for lymphoma, creating new opportunities for the chemical synthesis of targeted biotherapeutics.

Keywords: lymphoma; aptamer; drug delivery; aptamer-drug conjugates; biotherapeutics; PTK7

1. Introduction

Aptamers are oligonucleotides that recognise their target with high affinity and specificity and have properties comparable to antibodies; however, they have significant advantages in terms of size, production, and chemical modifications [1–3]. Therefore, they are

excellent candidates for the development of new biotechnological platforms for applications as imaging or therapeutic agents [3–6].

Sgc8-c is a DNA aptamer, a truncated form of Sgc8, which has 41 bases and specifically binds to the tyrosine-protein kinase-like 7 (PTK7) receptor [7], also known as colon carcinoma kinase 4 (CCK4). This receptor, which acts as a co-receptor in several cell pathways, is a tumour biomarker that is overexpressed in different types of leukaemia, gastric tumours, colon, lung, breast, and prostate cancers, and even in metastases [8–12]. Likewise, it is involved in the migration and endothelial invasion of tumour cells [8,13,14].

Our research group has studied the truncated DNA aptamer Sgc8-c as a tool for the development of tumour imaging agents [15–21]. We found that Sgc8-c was able to recognise the PTK7 receptor in vivo in murine melanoma and lymphoma models. These findings provided us with the basis to develop potential therapeutic agents, using this truncated aptamer to direct anti-tumour drugs specifically to the site of action via the PTK7 receptor.

The use of aptamers as probes for the selective delivery of drugs for clinical use has already been described in the literature [22,23]. Among the first examples, the use of DNA-intercalating drugs, like doxorubicin and daunorubicin, has been reported [22,24,25]; however, due to the intercalation process, such agents could affect aptamer target recognition, leading to a loss of specificity. A series of covalent binding strategies between the drug and the aptamer at a non-relevant site for recognition have been explored to avoid bioactivity loss [26]. Partially stable covalent bonds were used, such as amides [26]. Nevertheless, these constructions do not ensure the release of the drug under physiological conditions, potentially losing the activity provided by the drug component of the molecule. We recently described a molecular hybridisation strategy to covalently incorporate the anti-tumour agent dasatinib into the structure of Sgc8-c to generate potential biotherapeutics for haemato-oncology [27].

Dasatinib is a BCR-ABL kinase inhibitor approved by the Food and Drug Administration (FDA; USA) for the treatment of chronic myelogenous leukaemia and Philadelphia chromosome-positive acute lymphoblastic leukaemia [28]. We analysed different covalent connectors between dasatinib and the truncated aptamer and found that a carbamate moiety was able to preferentially release the drug at endosomal pH, which is optimal as the endosome is the Sgc8-c cellular uptake route [27]. Thus, we envisioned the generated hybrid agent, **Sgc8-c-carb-da** (Figure 1), to be highly attractive for therapeutic intervention. Therefore, we selected a lymphoma model to evaluate the potential of **Sgc8-c-carb-da** as a proof-of-concept for an aptamer-drug conjugate (ApDC) for biotherapy.
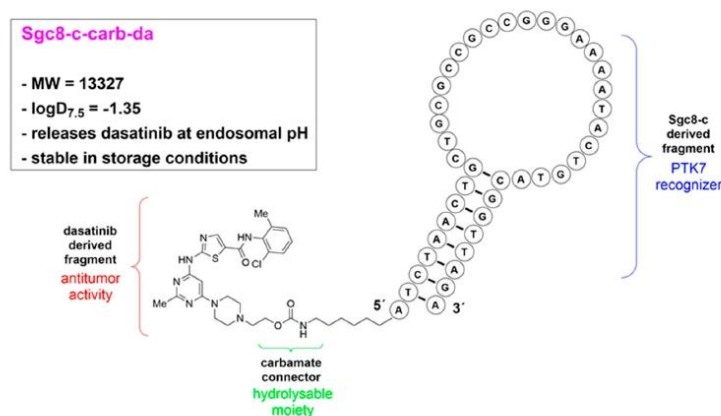
Figure 1. Schematic representation of **Sgc8-c-carb-da** structure and characteristics. Fragments correspond to anti-tumour activity (dasatinib-derived moiety), target recognition (Sgc8-c-derived fragment), and carbamate connectors (hydrolysable at endosomal pH [27]).

2. Material and Methods

2.1. Chemical Components

Dasatinib was purchased from Hong Kong Guokang Bio-Technology Co., Ltd. (Baoji City, China).

The 5′-(6-aminohexyl)-modified Sgc8-c aptamer [12813 Da, 5′-(aminohexyl) ATC TAA CTG CTG CGC CGC CGG GAA AAT ACT GTA CGG TTA GA -3′, Sgc8-c-NH$_2$] was purchased from IDT Technologies (Coralville, IA, USA).

Sgc8-c-carb-da (Figure 1) was synthesised and purified as described previously [27]. Briefly, dasatinib was coupled to a reactive pool, carbonate [29]. This intermediate product, dasatinib phenyl carbonate, was dissolved in dimethyl sulfoxide (DMSO). The aptamer Sgc8-c-NH$_2$ was dissolved in a sodium phosphate buffer (0.1 M) and a sodium bicarbonate buffer (0.1 M) (50:50 *v:v*) (pH 8.3) and then mixed with dasatinib phenyl carbonate, and the mixture was maintained at 60 °C. After 1 h, N,N-dimethylformamide was added, and the reaction was maintained at 60 °C for 47 h. The reaction was stopped by washing **Sgc8-c-carb-da** with Milli-Q water using Microcon® centrifugal filters. Finally, the product was purified by reversed-phase high-performance liquid chromatography.

Water was purified and deionised (18 MΩ/cm^2) in a Milli-Q water filtration system (Millipore Corp., Milford, UK).

2.2. Biological Components

All cell lines were obtained from the American Type Culture Collection (ATCC; Manassas, VA, USA): *Mus musculus* B lymphoma A20 cell line (TIB-208), *Homo sapiens* acute lymphoblastic leukaemia CCRF-CEM cell line (CCL-119) as the PTK7-positive control [30], and *Homo sapiens* glioblastoma U87 MG cell line (HTB-14) as the PTK7-negative control [31]. A20 and CCRF-CEM were cultured in Roswell Park Memorial Institute (RPMI)-1640 medium (Sigma-Aldrich, St. Louis, MO, USA) supplemented with 10% (*v/v*) foetal calf serum (FCS; Capricorn, Ebsdorfergrund, Germany) and 2 mM L-glutamine (Sigma-Aldrich) at 37 °C with 5% CO$_2$. U87 MG was grown in Dulbecco's Modified Eagle's Medium (DMEM; Capricorn) supplemented with 10% FCS and 2 mM L-glutamine.

2.3. In Vitro Biological Assays

2.3.1. Cytotoxicity Assay

Cells (5×10^4 cells/well) were seeded in a 96-well plate and cultured for 48 h at 37 °C in 5% CO$_2$, with different concentrations of **Sgc8-c-carb-da**, Sgc8-c, or dasatinib, ranging from 400 to 80,000 nM. In addition, cells were incubated with 20% DMSO (Sigma-Aldrich) and culture medium as controls. Then, the medium was removed, and cells were washed with 1X phosphate buffered saline (PBS), and 5 mg/mL of 3-(4,5-dimethylthiazol-2-yl)-2,5-diphenyltetrazolium bromide (MTT; Sigma-Aldrich) was added to each well. The plates were incubated for 4 h at 37 °C in 5% CO$_2$. To dissolve MTT crystals, a 20% sodium dodecyl sulfate (SDS) solution (Sigma-Aldrich) was added to the plates and further incubated overnight at room temperature in dark conditions. Finally, the plates were read at 570 nm to determine the optical density (OD) in each well. Cell cytotoxicity (%) was calculated using the following formula: [(OD in the studied condition—OD with DMSO)/(OD in control medium—OD with DMSO)] × 100. The half maximal inhibitory concentrations (IC$_{50}$), defined as the concentrations that induce 50% cytotoxicity, were determined from the viability vs. concentration curves using the software GraphPad8 (version 8.0.1).

2.3.2. Washing Method

To study the role of Sgc8-c as a delivery system, we used an adaptation of a previously described Washing Method (WM) [32], which mimics the in vivo conditions. Cells were incubated with the studied agents (**Sgc8-c-carb-da**, Sgc8-c, or dasatinib) for 30, 60, or 120 min to allow specific binding to PTK-7. Afterward, the media was removed, and the cells were washed with PBS. Then, cells were incubated at 37 °C in the corresponding culture medium for up to 48 h. The MTT assay was developed as described above.

2.3.3. Cell Death Studies

Induction of cell death was studied by flow cytometry to detect early and late apoptosis and necrosis using Annexin V conjugated to FITC (AV; BD Pharmingen) and propidium iodide (PI; Sigma-Aldrich). For this, cells (5×10^5 cells/well in 24-well plates) were incubated with 200, 400, and 800 nM of **Sgc8-c-carb-da** or dasatinib for 24 h at 37 °C with 5% CO_2. The washing method was also carried out in these studies to evaluate the role of Sgc8-c as a delivery system.

After the incubation period, the cells and supernatant were washed with cold FACS buffer ($1\times$ PBS, 2% FCS, and 25 mM EDTA), then centrifuged at 1800 rpm for 3 min at 4 °C. After that, the pellets were resuspended in 200 μL of FACS buffer and incubated with 2 μL of AV for 30 min in ice. Two more washes were performed with cold FACS buffer, and cells were further incubated with 5 μL of IP for 5 min. Samples were acquired in a FACS Canto II (BD Biosciences, San Diego, CA, USA). The results were analysed using FACS Diva (version 6.1.3) and FlowJo software (version 7.6).

2.3.4. Mitochondrial Membrane Potential Assay

Changes in the mitochondrial membrane potential (Δψm) were analysed using the cationic carbocyanine dye JC-1. A20 cells were seeded in a 24-well plate (5×10^5 cells/well) and incubated with 200, 400, and 800 nM of **Sgc8-c-carb-da** or dasatinib for 24 h at 37 °C with 5% CO_2. To assess the potential of Sgc8-c as a delivery system, after 1 h of incubation with the compounds, cell cultures were washed with PBS and further incubated in the culture medium for 24 h. Likewise, cells were incubated with 1000 nM of the uncoupler carbonyl cyanide-*p*-trifluoromethoxy phenylhydrazone (FCCP; Sigma-Aldrich) for 15 min at 37 °C, as a positive control (100% JC-1 monomer retention, background of J-aggregate formation), or with culture medium, as a negative control (100% J-aggregate formation, background of JC-1 monomers). All samples were washed with PBS, centrifuged at 1800 rpm for 3 min, and incubated with 500 nM of 5,5′,6,6′-tetrachloro-1,1′,3,3′-tetraethylbenzimidazolylcarbocyanine iodide (JC-1; Sigma-Aldrich, St. Louis, MO, USA) [33,34] in culture medium for 30 min at 37 °C. Cells were washed again with PBS and analysed by flow cytometry, determining green monomers (Ex 485 nm/Em 535 nm) and red J-aggregates (Ex 560 nm/Em 595 nm). Ten thousand events were acquired and analysed using the Diva and FlowJo software (version 7.6). The percentage of JC-1 monomer retention was calculated using the following formula: % JC-1 monomer in the studied condition—% JC-1 monomer FCCP. Likewise, the percentage of J-aggregate formation was calculated using the following formula: % J-aggregates in the studied condition—% J-aggregates in control media.

2.3.5. Arrest of Cell Proliferation Assay

To evaluate cell proliferation, cells (2.6×10^5 cells/mL) were stained with 3 μM of the fluorescent compound succinimidyl-carboxyfluorescein ester (CFSE; Sigma-Aldrich) for 10 min at 37 °C with 5% CO_2. Afterward, cells were washed with 1 mL of FCS for every 3 mL of cell suspension, then with PBS. Cells were resuspended in the corresponding medium, seeded in 24-well plates, and incubated with the IC_{50} of the agents (**Sgc8-c-carb-da** or dasatinib, determined for each of the cell lines) and two serial dilutions. In addition, cells were incubated with 20% DMSO or culture medium as controls for cell arrest and proliferation, respectively. Once again, the washing method was performed to assess the potential of Sgc8-c as a delivery system. After 48 h, cells and supernatants were collected together, washed with PBS, and analysed by flow cytometry. For each sample, 10,000 events were acquired in a FACS Canto II. The results were analysed using FACS Diva and FlowJo software. Cell proliferation (%) was calculated using the following formula: [(% cell proliferation in the studied condition—% cell proliferation with DMSO)/(% cell proliferation in control medium—% cell proliferation with DMSO)] × 100.

2.3.6. Cell Cycle Analysis by DNA Content

A20 cells were seeded in 24-well plates (5×10^5 cells/well) and incubated with 200, 400, and 800 nM of **Sgc8-c-carb-da** or dasatinib at 37 °C with 5% CO_2 for 24 h. To determine the role of Sgc8-c as a delivery system, samples were washed with PBS after one hour of incubation to remove compounds and further incubated with only the culture medium until 24 h were completed. Then, all samples were fixed with cold 70% ethanol at 4 °C for 2 h. To avoid the formation of lumps and guarantee cell fixation, the cell suspension was added dropwise to the ethanol with continuous, gentle shaking. Samples were washed twice with PBS and centrifuged at 2000 rpm at 4 °C for 3 min, then incubated with 0.1 mg/mL of Ribonuclease A (RNAse A; from bovine pancreas, Sigma-Aldrich, St. Louis, MO, USA) in 0.1% Triton X-100 (in PBS) at 37 °C for 30 min. After that, samples were stained with 5 μL of PI in cold RNAse buffer and incubated at 4 °C for 5 min. Samples were analysed by flow cytometry, acquiring 10,000 events, and the height, width, and area of the PI curve were acquired to perform an adequate analysis [35] using FACS Diva (version 6.1.3) and FlowJo software (version 7.6).

2.4. Statistical Analysis

Statistical analysis was performed using the Student's *t*-test, and the *p* values of significance are indicated in each figure.

3. Results and Discussion

3.1. *Sgc8-c-carb-da Displays Cytotoxic Activity against A20 Cells*

The capability of **Sgc8-c-carb-da** to act as a biotherapeutic agent was determined. First, its cytotoxic potential was evaluated against A20 lymphoma cells by MTT assay, showing an IC_{50} of 820 nM (Figure 2, Table 1). In parallel, the cytotoxic potential of dasatinib against A20 cells was assessed (IC_{50} of 740 nM) (Figure 2, Table 1), demonstrating that **Sgc8-c-carb-da** maintained the cytotoxic activity of dasatinib ($IC_{50,dasatinib}/IC_{50,Sgc8-c-carb-da} = 0.91$) (Figure 2, Table 1). Therefore, this drug-delivery system would not affect the biological activity of dasatinib. Additionally, dasatinib does not have the ability to intercalate with DNA since it is not a pi-rich system [36,37]. Therefore, we expect no topological modifications of the aptamer and, consequently, no loss of target recognition.
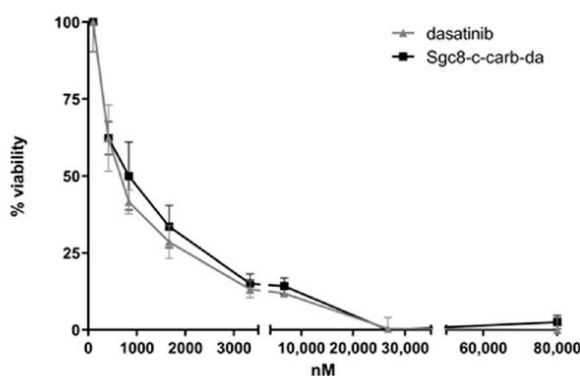
Figure 2. Doses-response curves for dasatinib and **Sgc8-c-carb-da** in A20 cells using the MTT method. Cytotoxicity was evaluated by MTT. Graph shows mean ± standard deviation (SD), n = 10 per condition.

Table 1. Cytotoxic effects of **Sgc8-c-carb-da**, dasatinib, and Sgc8-c against A20 cells, PTK7-positive CCRF-CEM, and negative U87 MG controls, expressed as IC_{50}.

	IC$_{50}$ (nM)			IC$_{50,dasatinib}$/IC$_{50,Sg8-c-carb-da}$
Cell Line	Sgc8-c-carb-da	Sgc8-c	Dasatinib	
A20	820 ± 30	>80,000	740 ± 20	0.91
CCRF-CEM	7477 ± 80	>80,000	$12,260 \pm 30$	1.64
U87 MG	$16,350 \pm 30$	>80,000	$20,160 \pm 70$	1.23

To further test whether **Sgc8-c-carb-da** activity was the result of each component of the hybrid agent (i.e., dasatinib and Sgc8-c), the cytotoxicity of Sgc8-c was also evaluated, being higher than 80,000 nM (Table 1, Figure S1A in Supplementary Materials). These results clearly showed that the **Sgc8-c-carb-da** cytotoxic activity against A20 lymphocytes is the result of the dasatinib component since the truncated aptamer Sgc8-c did not display cytotoxic activity in the experimental assayed conditions. Hence, Sgc8-c was not included in the following mechanistic experiments.

As expected, the IC_{50} for **Sgc8-c-carb-da** in PTK7-negative U87 MG cells [31] was higher than in A20 cells (IC_{50} 16,350 nM) (Table 1, Figure S1C in Supplementary Materials), and no difference was observed for **Sgc8-c-carb-da** and dasatinib activities ($IC_{50,dasatinib}$/$IC_{50,Sgc8-c-carb-da}$ = 1.23), with both IC_{50} values being extremely high. These cells are considered negative controls, as they are not susceptible to any of these agents.

On the other hand, the IC_{50} for **Sgc8-c-carb-da** in PTK7-positive CCRF-CEM cells [30] was also higher than in A20 cells (IC_{50} 7477 nM) (Table 1, Figure S1B in Supplementary Materials), revealing that this biotherapeutic agent is less effective in these cells, albeit CCRF-CEM cells express the PTK7 receptor, unlike U87 MG cells.

However, **Sgc8-c-carb-da** displayed almost 2-fold higher activity than dasatinib ($IC_{50,dasatinib}$/$IC_{50,Sgc8-c-carb-da}$ = 1.64), suggesting the relevance of the PTK7 receptor in facilitating drug delivery into these cells, which are less sensitive to dasatinib.

The lack of differences in cytotoxic activity between dasatinib and the new ApDC ($IC_{50,dasatinib}$/$IC_{50,Sgc8-c-carb-da}$ = 0.91) could suggest the absence of Sgc8-c's functional effect. In order to investigate whether the cellular binding of **Sgc8-c-carb-da** via PTK7 enhances its bio-response, an in vitro cell-binding study was performed. For that, a washing protocol was applied (see Materials and Methods Section 2.3.2), where cells were incubated with different concentrations of **Sgc8-c-carb-da** for 30, 60, or 120 min to allow binding to PTK7, then the assay media containing the biotherapeutic agents were removed, and the cells were washed. The IC_{50} values were determined as described before [32] (Table 2, Figure S2 in Supplementary Materials). **Sgc8-c-carb-da** increased the activity of dasatinib against A20 cells in all studied incubation times (Table 2, Figure 3, and Figure S2A,D in Supplementary Materials), being four times more cytotoxic after 120 min of incubation. Even at shorter incubation periods, the cytotoxic activities expressed as $IC_{50,dasatinib}$/$IC_{50,Sgc8-c-carb-da}$, were higher (2.82 and 2.42 for 30 and 60 min, respectively). Moreover, **Sgc8-c-carb-da** showed an increase in cytotoxic activity in PTK7-positive CCRF-CEM cells compared to dasatinib, particularly after 120 min of incubation ($IC_{50,dasatinib}$/$IC_{50,Sgc8-c-carb-da}$ = 2.08, Table 2, Figure S2B,E in Supplementary Materials). However, **Sgc8-c-carb-da** did not display different activity than dasatinib, with or without the washing step, in PTK7-negative U87 MG cells ($IC_{50,dasatinib}$/$IC_{50,Sgc8-c-carb-da}$ ~ 1, Table 2, Figure S2C,F in Supplementary Materials). The reduced $IC_{50,Sgc8-c-carb-da}$ in these cells could be explained by the lack of receptor mediation in the biopharmaceutical uptake ($IC_{50,Sgc8-c-carb-da}$ 16,350 nM versus 32,580 nM after 48 h and 120 min of incubation, respectively), confirming that this limited activity is PTK7-independent.

Table 2. Cytotoxic effects of dasatinib and **Sgc8-c-carb-da** against A20 cells, PTK7-positive CCRF-CEM, and negative U87 MG controls after different drug exposure times, expressed as IC_{50}.

Exposure Time (min)	IC_{50} (nM)		$IC_{50,dasatinib}/IC_{50,Sgc8-c-carb-da}$
A20	**Dasatinib**	**Sgc8-c-carb-da**	
30	1070 ± 20	380 ± 20	2.82
60	1650 ± 80	680 ± 130	2.43
120	1750 ± 20	440 ± 20	3.98
CCRF-CEM			
30	$18,460 \pm 40$	$15,110 \pm 20$	1.22
60	$11,800 \pm 20$	9520 ± 20	1.24
120	$12,650 \pm 20$	6060 ± 20	2.08
U87 MG			
30	$30,120 \pm 20$	$31,310 \pm 40$	0.96
60	$33,950 \pm 30$	$32,230 \pm 10$	1.05
120	$32,010 \pm 20$	$32,580 \pm 20$	0.98
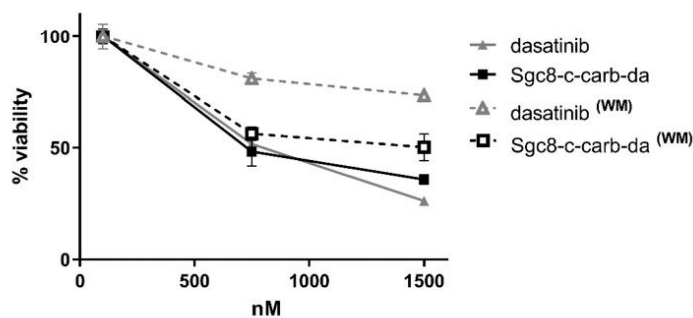
Figure 3. Evaluation of **Sgc8-c-carb-da** binding via PTK7 in A20 cells. Dose-response curves for dasatinib or **Sgc8-c-carb-da** after 48 h of incubation with A20 cells, with (WM) or without the washing method (60 min of drug exposure followed by a wash and further incubation). Cytotoxicity was evaluated by MTT. Graph shows mean $\pm$ SD, n = 10 per condition.

Altogether, these results show the potential of **Sgc8-c-carb-da** as a biotherapeutic agent since it promotes A20 cell cytotoxicity in a PTK-7-mediated manner; however, the MTT assay is a comprehensive measurement of cell cytotoxicity and reflects many altered pathways, including cell death, cell proliferation arrest, and changes in mitochondria dynamics, among others. Therefore, the next experiments were addressed to unravel the mechanisms behind **Sgc8-c-carb-da**'s cytotoxic effect.

3.2. *Sgc8-c-carb-da Promotes A20-Cell Apoptosis and Necrosis*

The mechanisms of A20 cell death (i.e., early and late apoptosis and necrosis) promoted by **Sgc8-c-carb-da** were assessed by flow cytometry using AV and PI. For that, A20 cells were incubated with 800 nM of **Sgc8-c-carb-da** or dasatinib in the same conditions as described above. After 24 h of incubation, 45.6% of dasatinib-treated A20 cells died, mainly by late apoptosis (17.8%) and necrosis (20.6%), whereas 69.3% of **Sgc8-c-carb-da**-treated cells died, triggering a significant increase in late apoptosis (33.6%, $p < 0.01$) and necrosis (30.5%, $p < 0.01$) (Figure 4). Note 11.2% of cell death was observed in the control conditions. When A20 cells were exposed to the biomolecules for only 60 min, then washed away and incubated for another 23 h, a reduction in cell death was observed ($p < 0.01$). Dasatinib induced early apoptosis (9.5%) as much as late apoptosis (10.4%) and necrosis (9.9%), while for **Sgc8-c-carb-da,** early apoptosis was significantly lower (6.0%, $p < 0.01$), slightly shifting the death process toward late apoptosis (11.2%) and especially to necrosis (13.6%, $p < 0.05$).
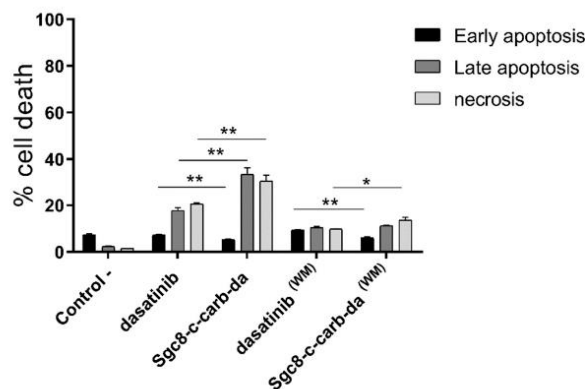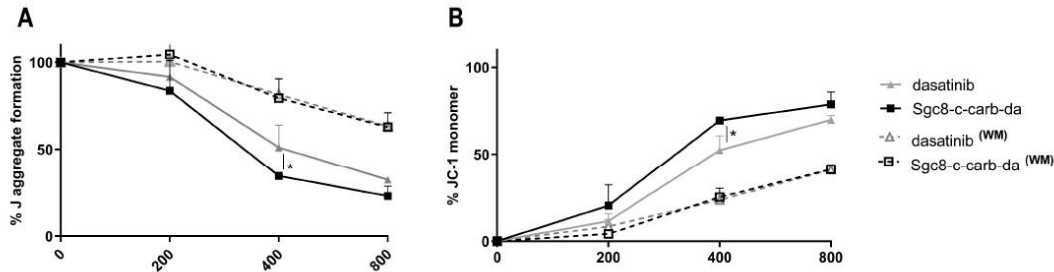
Figure 4. Percentage of cell death of A20 cells obtained after incubation with 800 nM dasatinib or **Sgc8-c-cab-da** for 24 h, with (WM) or without the washing method (60 min of drug exposure followed by a wash and further incubation). Graph shows mean $\pm$ SD, n = 3 per condition. * $p < 0.05$, ** $p < 0.01$ (Student's *t*-test).

To assess whether the observed cell death was preceded by alterations in mitochondrial structure and transmembrane potential, changes in mitochondrial membrane potential were analysed using the JC-1 assay. In living cells (normal $\Delta\Psi M$), the JC-1 dye enters and accumulates in the mitochondria and spontaneously forms red fluorescent J-aggregates. Conversely, in unhealthy (apoptotic) cells (altered $\Delta\Psi M$), the JC-1 dye does not reach sufficient concentration at the mitochondrial to promote J-aggregate formation, thus retaining its original green fluorescence [38]. This assay was performed after the treatment of A20 cells with different doses of **Sgc8-c-carb-da** or dasatinib, as described above. **Sgc8-c-carb-da** caused a decrease in J-aggregate formation (Figure 5A) and an increase in the retention of JC-1 monomers, slightly greater than that of dasatinib in a dose-dependent manner (Figure 5B); however, no differences were observed when cells were treated with **Sgc8-c-carb-da** or dasatinib for only 60 min, washed, and later incubated for another 23 h (Figure 5A,B). These results showed a $\Delta\psi m$ that is indicative of a mitochondrial membrane compromise, in agreement with previous data for dasatinib in other cellular systems [39]. This behaviour could be related to the activation of cellular pathways, particularly apoptosis, which is associated with the response to this drug and generates an uncoupling of the mitochondrial potential [33,34]. In this regard, no differences in the percentage of (early plus late) apoptotic cells were observed when cells were treated with **Sgc8-c-carb-da** or dasatinib for only 60 min, washed, and later incubated for another 23 h (Figure 4).

3.3. *Sgc8-c-carb-da Triggers Cell Proliferation Arrest, Mainly in the subG1 Phase*

Along with cell death, we assessed the potential of **Sgc8-c-carb-da** to promote cell proliferation arrest. A20, CCRF-CEM, and U87 MG cells were stained with CFSE to track cell division. In each cell division, daughter cells will receive half of the CFSE label of their parent cell and so on, allowing the tracking of different cell generations. Thus, when cells proliferate, CFSE fluorescence decreases. CFSE-stained tumour cells were treated with the IC$_{50}$ of **Sgc8-c-carb-da** or dasatinib for 48 h. The results showed that both compounds caused the arrest of A20- and CCRF-CEM-cell proliferation, revealed by a higher percentage of cells that did not undergo division (Figure 6A and Figure S3A in Supplementary Materials). On the other hand, no differences were observed between U87 MG cells treated with **Sgc8-c-carb-da** or dasatinib with the control condition (Figure S3B in Supplementary Materials).

Figure 5. Changes in mitochondrial membrane potential induced by **Sgc8-c-carb-da**. Quantification of the JC-1 assay obtained from incubation of the A20 cell line with 200, 400, and 800 nM of dasatinib or **Sgc8-c-carb-da** for 24 h, with (WM) or with the washing method (60 min of drug exposure followed by a wash and further incubation). (**A**) Percentages of J-aggregate formation and (**B**) percentages of JC-1 monomer retention are shown. Graph shows mean ± SD, n = 3 per condition. * $p < 0.05$ (Student's *t*-test).
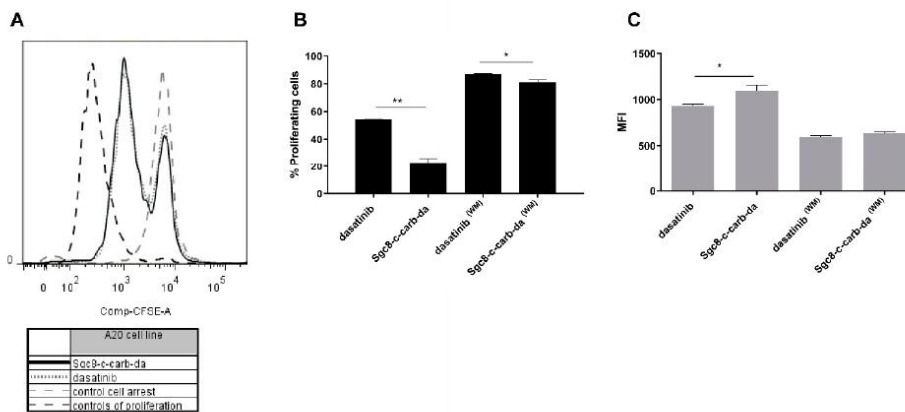
Figure 6. Arrest of cell proliferation in A20 cells after incubation with **Sgc8-c-carb-da** and dasatinib (800 nM) for 48 h, with (WM) or without the washing method (60 min of drug exposure followed by a wash and further incubation). (**A**) Cell proliferation histogram, controls of proliferation, and cell arrest: incubation with medium (100% proliferating cells) and 20% of DMSO (0% proliferating cells), respectively. (**B**) Percentages of proliferating cells are shown. (**C**) Mean fluorescence indices (MFI) for CFSE. Graph shows mean ± SD, n = 3 per condition. * $p < 0.05$, ** $p < 0.01$ (Student's *t*-test).

The percentage of proliferating cells was lower, and concordantly, the CFSE mean fluorescence index (MFI) was higher after treatment with 800 nM **Sgc8-c-carb-da** than dasatinib for 48 h (Figure 6B,C). Likewise, when A20 cells were incubated for 60 min (washing method), **Sgc8-c-carb-da** promoted a higher cell arrest than dasatinib, with the percentage of proliferative cells being 81.0% and 87.0% for **Sgc8-c-carb-da** and dasatinib, respectively (Figure 6B). These observations could be explained by the ability of the aptamer to interact with PTK7 and facilitate the delivery of dasatinib intracellularly, arresting cell proliferation.

Since A20 cell proliferation arrest was detected upon **Sgc8-c-carb-da** treatment, the cell cycle distribution was assessed via flow cytometry. **Sgc8-c-carb-da** generated significant changes in the cell cycle with respect to dasatinib, observing a decrease in the G1, S, and G2/M phases and an increase in the Sub-G1 (Figure 7A–C,F). After 24 h of incubation with **Sgc8-c-carb-da** (800 nM), 51.10% of the cell population had stopped in Sub-G1, while

30.30% of the cells were in G1, 8.60% in S, and 10.15% in the G2/M phases (Figure 7C,F). This cell cycle distribution differed from that found after 24 h of incubation with dasatinib (800 nM) (37.60% of the cell population stopped in Sub-G1, while 56.05% were in G1, 3.25% in S, and 3.00% in the G2/M phases; Figure 7B,F). The Sub-G1 peak is associated with cell apoptosis [40], confirming that **Sgc8-c-carb-da** facilitated dasatinib-mediated apoptosis. In line with previous assays, when A20 cells were incubated with **Sgc8-c-carb-da** (800 nM) for only 60 min, followed by a washing method, only 17.85% of the cell population was arrested in Sub-G1, while 71.20% of the cells were in G1, 5.75% in S, and 5.15% in the G2/M phases (Figure 7D–F). These analyses confirmed that both agents have similar effects on the cell cycle progression in a dose-dependent manner (Figure S4 in Supplementary Materials).
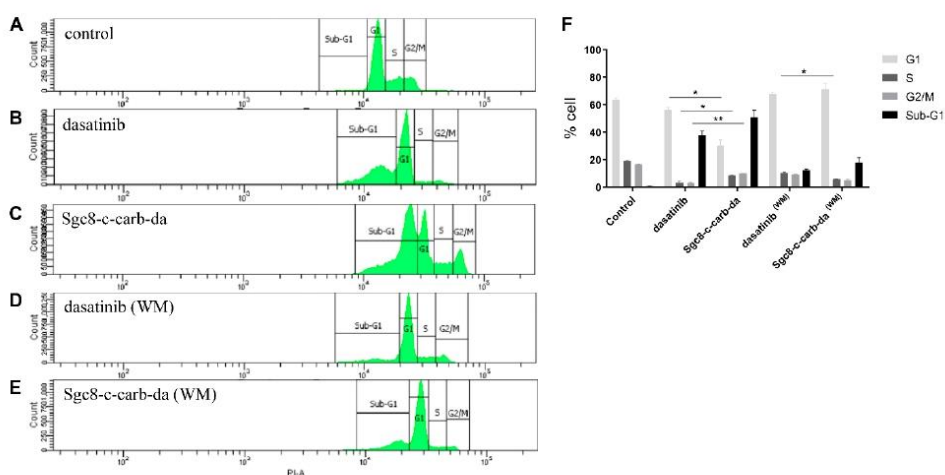
Figure 7. Analysis of cell cycle phases. Assay was performed on A20 cells after incubation with 800 nM **Sgc8-c-carb-da** and dasatinib for 24 h, with (WM) or without the washing method (60 min of drug exposure followed by a wash and further incubation). Histograms of cells incubated with (**A**) control culture medium, (**B**) dasatinib for 24 h, (**C**) **Sgc8-c-carb-da** for 24 h, (**D**) dasatinib for 60 min then washed, and (**E**) **Sgc8-c-carb-da** for 60 min then washed. (**F**) Percentages of cells in the different cell cycle phases after incubation under the mentioned conditions. Graph shows mean $\pm$ SD, n = 3 per condition. * $p < 0.05$, ** $p < 0.01$ (Student's *t*-test).

4. Conclusions

Here, we report the potential **Sgc8-c-carb-da** ApDC, which combines a truncated aptamer that recognises the PTK7 receptor as a target-specific component and dasatinib sub-structure as a cytotoxic component. The site-specific drug attachment was achieved by covalent conjugation via a carbamate moiety of the amino aptamer to the dasatinib primary alcohol [27]. One of the relevant properties of **Sgc8-c-carb-da** is its capability to release dasatinib in a pH-dependent manner, with the endosome (pH 5.0) being the optimal place for drug release. This property is highly relevant because it implies some advantages to traditional treatment. On the one hand, Sgc8-c aptamer-based probes have significant tumour uptake and blood clearance [16,19,21]. Hence, the in vivo use of **Sgc8-c-carb-da** would facilitate drug delivery to the site of action with minimal hydrolysis at the non-target sites, enhancing drug availability at the tumour site and reducing systemic toxicity. On the other hand, since the endosomal route has been confirmed for some aptamers' internalisation [16,41,42], and particularly endosomal Sgc8-c-uptake in A20 cells [15], once **Sgc8-c-carb-da** penetrates lymphoma cells, dasatinib release would take place, facilitating drug delivery at the appropriate site of action. Thus, this system merits further exploration in haemato-oncology indications.

The objective of the current study was to establish the potential of **Sgc8-c-carb-da** as an ApDC on A20 lymphoma cells. Here, we demonstrated these hypotheses: (i) the dasatinib does not undergo biological activity loss; (ii) higher cytotoxic activity is observed in the PTK7-over-expressing cells (A20 and CCRF-CEM vs. U87 MG cells); and (iii) the ApDC displays higher activity than dasatinib in a washing method set-up, highlighting the relevance of Sgc8-c as a delivery system.

In addition, we explored the mode of action of this ApDC in different biological-behaviour studies (i.e., the PTK7-dependence of cytotoxic effects, cell death pathways, and cell cycle perturbation) and compared it to the drug alone. **Sgc8-c-carb-da** reveals significant cytotoxicity against A20 cells, potentiating dasatinib biological activity. **Sgc8-c-carb-da** promotes cell death by necrosis and apoptosis, accompanied by changes in the mitochondrial membrane potential. It also generates cell proliferation arrest, which results in an increase in the Sub-G1 peak and decreases in the S and G2/M phases. Collectively, these results confirm the hypothesis that the Sgc8-c aptamer acts as a tumour-specific vehicle for dasatinib, binding to PTK7 and delivering the drug into the cell, enhancing its biological activity. To further translate the Sgc8-c platform as a drug delivery system into tumours, there is still a need for pre-clinical and, ultimately, clinical investigations.

Supplementary Materials: The following supporting information can be downloaded at: https://www.mdpi.com/article/10.3390/cancers15030922/s1, Figure S1: Dose-response curves for dasatinib, **Sgc8-c-carb-da**, and Sgc8-c-NH$_2$ using the MTT method in (A) A20, (B) CCRF-CEM, and (C) U87 MG cells. Figure S2: Dose-response curves for dasatinib or **Sgc8-c-carb-da** after 48 h of incubation, with (WM) or without the washing method (60 or 120 min of drug exposure followed by a wash and further incubation), in the different cell lines: (A) A20 (60 min), (B) CCRF-CEM (60 min), (C) U87 MG (60 min), (D) A20 (120 min), (E) CCRF-CEM (120 min) and (F) U87 MG (120 min). Cytotoxicity was evaluated by MTT. Graph shows mean ± SD, n = 10 per condition. Figure S3: Arrest of cell proliferation induced by **Sgc8-c-carb-da** and dasatinib in (A) CCRF-CEM and (B) U87 MG cell lines. Figure S4: Phases of the cell cycle induced by **Sgc8-c-carb-da** and dasatinib in A20 cells. Assay performed on the A20 cells after incubation with 200, 400, and 800 nM **Sgc8-c-carb-da** and dasatinib for 24 h, with (WM) or without the washing method (60 min of drug exposure followed by a wash and further incubation). Graph shows mean ± SD, n = 3 per condition.

Author Contributions: Conceptualization, E.S., H.C., V.C. and M.M.; Methodology, E.S., H.C., V.C. and M.M.; Formal analysis, E.S. and M.M.; Investigation, E.S., V.C. and M.M.; Writing—original draft, E.S., H.C., V.C. and M.M.; Visualization, E.S., H.C., V.C. and M.M.; Supervision, H.C., V.C. and M.M.; Project administration, V.C.; Funding acquisition, H.C. and V.C. All authors have read and agreed to the published version of the manuscript.

Institutional Review Board Statement: Not applicable.

Informed Consent Statement: Not applicable.

Data Availability Statement: The data presented in this study are available in this article.

Conflicts of Interest: The authors declare no conflict of interest.

References

1. Qu, N.; Ying, Y.; Qin, J.; Chen, A.K. Rational design of self-assembled RNA nanostructures for HIV-1 virus assembly blockade. *Nucleic. Acids Res.* **2021**, *50*, e44. [CrossRef] [PubMed]
2. Yamada, K.; Hildebrand, S.; Davis, S.M.; Miller, R.; Conroy, F.; Sapp, E.; Caiazzi, J.; Alterman, J.F.; Roux, L.; Echeverria, D.; et al. Structurally constrained phosphonate internucleotide linkage impacts oligonucleotide-enzyme interaction, and modulates siRNA activity and allele specificity. *Nucleic. Acids Res.* **2021**, *49*, 12069–12088. [CrossRef] [PubMed]
3. Qi, S.; Duan, N.; Khan, I.M.; Dong, X.; Zhang, Y.; Wu, S.; Wang, Z. Strategies to manipulate the performance of aptamers in SELEX, post-SELEX and microenvironment. *Biotechnol. Adv.* **2022**, *55*, 107902. [CrossRef] [PubMed]

4.   Calzada, V. Aptamers in Diagnostic and Molecular Imaging Applications. In *Aptamers in Biotechnology*; Springer: Cham, Switzerland, 2019; pp. 141–160.

5.   Tong, R.; Coyle, V.J.; Tang, L.; Barger, A.M.; Fan, T.M.; Cheng, J. Polylactide nanoparticles containing stably incorporated cyanine dyes for in vitro and in vivo imaging applications. *Microsc. Res. Tech.* **2010**, *73*, 901–909. [CrossRef]

6.   Liu, M.; Wang, L.; Lo, Y.; Shiu, S.C.; Kinghorn, A.B.; Tanner, J.A. Aptamer-Enabled Nanomaterials for Therapeutics, Drug Targeting and Imaging. *Cells* **2022**, *11*, 159. [CrossRef] [PubMed]

7.   Shangguan, D.; Tang, Z.; Mallikaratchy, P.; Xiao, Z.; Tan, W. Optimization and Modifications of Aptamers Selected from Live Cancer Cell Lines. *ChemBioChem* **2007**, *8*, 603–606. [CrossRef] [PubMed]

8.   Ganier, L.; Morelli, X.; Borg, J.-P. Rôle en cancérologie et ciblage du récepteur à activité tyrosine kinase PTK7. *Méd./Sci.* **2020**, *36*, 42–46. [CrossRef]

9.   Gärtner, S.; Gunesch, A.; Knyazeva, T.; Wolf, P.; Högel, B.; Eiermann, W.; Ullrich, A.; Knyazev, P.; Ataseven, B. PTK 7 Is a Transforming Gene and Prognostic Marker for Breast Cancer and Nodal Metastasis Involvement. *PLoS ONE* **2014**, *9*, e84472. [CrossRef] [PubMed]

10.   Zhang, H.; Wang, A.; Qi, S.; Cheng, S.; Yao, B.; Xu, Y. Protein Tyrosine Kinase 7 (PTK7) as a Predictor of Lymph Node Metastases and a Novel Prognostic Biomarker in Patients with Prostate Cancer. *Int. J. Mol. Sci.* **2014**, *15*, 11665–11677. [CrossRef]

11.   Lin, Y.; Zhang, L.H.; Wang, X.H.; Xing, X.F.; Cheng, X.J.; Dong, B.; Hu, Y.; Du, H.; Li, Y.A.; Zhu, Y.B.; et al. PTK7 as a novel marker for favorable gastric cancer patient survival. *J. Surg. Oncol.* **2012**, *106*, 880–886. [CrossRef]

12.   Golubkov, V.; Prigozhina, N.; Zhang, Y.; Stoletov, K.; Lewis, J.; Schwartz, P.; Hoffman, R.; Strongin, A. Protein-tyrosine pseudokinase 7 (PTK7) directs cancer cell motility and metastasis. *J. Biol. Chem.* **2014**, *289*, 24238–24249. [CrossRef] [PubMed]

13.   Berger, H.; Breuer, M.; Peradziryi, H.; Podleschny, M.; Jacob, R.; Borchers, A. PTK7 localization and protein stability is affected by canonical Wnt ligands. *J. Cell Sci.* **2017**, *130*, 1890–1903. [CrossRef] [PubMed]

14.   Shin, W.; Maeng, Y.; Jung, J.; Min, J.; Kwon, Y.; Lee, S. Soluble PTK7 inhibits tube formation, migration, and invasion of endothelial cells and angiogenesis. *Biochem. Biophys. Res. Commun.* **2008**, *371*, 793–798. [CrossRef] [PubMed]

15.   Castelli, R.; Ibarra, M.; Faccio, R.; Miraballes, I.; Fernández, M.; Moglioni, A.; Cabral, P.; Cerecetto, H.; Glisoni, R.J.; Calzada, V. T908 polymeric micelles improved the uptake of Sgc8-c aptamer probe in tumor-bearing mice: A co-association study between the probe and preformed nanostructures. *Pharmaceuticals* **2022**, *15*, 15. [CrossRef]

16.   Sicco, E.; Mónaco, A.; Fernandez, M.; Moreno, M.; Cerecetto, H. Metastatic and non-metastatic melanoma imaging using Sgc8-c aptamer PTK7-recognizer. *Sci. Rep.* **2021**, *11*, 19942. [CrossRef] [PubMed]

17.   Sicco, E.; Baez, J.; Ibarra, M.; Fernández, M.; Cabral, P.; Moreno, M.; Cerecetto, H.; Calzada, V. Sgc8-c Aptamer as a Potential Theranostic Agent for Hemato-Oncological Malignancies. *Cancer Biother. Radiopharm.* **2020**, *35*, 262–270. [CrossRef] [PubMed]

18.   Sicco, E.; Báez, J.; Margenat, J.; García, F.; Ibarra, M.; Cabral, P.; Moreno, M.; Cerecetto, H.; Calzada, V. Derivatizations of Sgc8-c aptamer to prepare metallic radiopharmaceuticals as imaging diagnostic agents: Syntheses, isolations, and physicochemical characterizations. *Chem. Biol. Drug Des.* **2018**, *91*, 747–755. [CrossRef]

19.   Calzada, V.; Moreno, M.; Newton, J.; González, J.; Fernández, M.; Gambini, J.P.; Ibarra, M.; Chabalgoity, A.; Deutscher, S.; Quinn, T.; et al. Development of new PTK7-targeting aptamer-fluorescent and -radiolabelled probes for evaluation as molecular imaging agents: Lymphoma and melanoma in vivo proof of concept. *Bioorganic. Med. Chem.* **2017**, *25*, 1163–1171. [CrossRef]

20.   Arevalo, A.P.; Castelli, R.; Ibarra, M.; Crispo, M.; Calzada, V. In vivo evaluation of Sgc8-c aptamer as a molecular imaging probe for colon cancer in a mouse xenograft model. *Int. J. Mol. Sci. Press* **2022**, *23*, 2466. [CrossRef]

21.   Calzada, V.; Báez, J.; Sicco, E.; Margenat, J.; Fernández, M.; Moreno, M.; Ibarra, M.; Gambini, J.; Cabral González, P.; Cerecetto, H. Preliminary in vivo characterization of a theranostic aptamer: Sgc8-c-DOTA-67Ga. *Aptamers* **2017**, *1*, 19–27.

22.   Yazdian-robati, R.; Arab, A.; Ramezani, M.; Abnous, K.; Mohammad, S. Application of aptamers in treatment and diagnosis of leukemia. *Int. J. Pharm.* **2017**, *529*, 44–54. [CrossRef] [PubMed]

23.   Patil, S.D.; Rhodes, D.G.; Burgess, D.J. DNA-based therapeutics and DNA delivery systems: A comprehensive review. *AAPS J.* **2005**, *7*, E61–E77. [CrossRef]

24.   Bagalkot, V.; Farokhzad, O.C.; Langer, R.; Jon, S. An Aptamer–Doxorubicin Physical Conjugate as a Novel Targeted Drug-Delivery Platform. *Angew. Chemie. Int. Ed.* **2006**, *45*, 8149–8152. [CrossRef]

25.   Taghdisi, S.M.; Abnous, K.; Mosaffa, F.; Behravan, J. Targeted delivery of daunorubicin to T-cell acute lymphoblastic leukemia by aptamer. *J. Drug Target.* **2010**, *18*, 277–281. [CrossRef] [PubMed]

26.   Zhao, N.; Pei, S.N.; Qi, J.; Zeng, Z.; Iyer, S.P.; Lin, P.; Tung, C.H.; Zu, Y. Oligonucleotide aptamer-drug conjugates for targeted therapy of acute myeloid leukemia. *Biomaterials* **2015**, *67*, 42–51. [CrossRef]

27.   Sicco, E.; Almeida, L.; Moreno, M.; Calzada, V.; Cerecetto, H. Chemical conjugations of Sgc8-c with the lymphoma drug dasatinib to generate selective biotherapeutics. *Aptamers* **2021**, *5*, 15–21.

28.   De Novellis, D.; Cacace, F.; Caprioli, V.; Wierda, W.G.; Mahadeo, K.M.; Tambaro, F.P. The tki era in chronic leukemias. *Pharmaceutics* **2021**, *13*, 2201. [CrossRef]

29.   Carpino, L.; Collins, D.; Göwecke, S.; Mayo, J.; Thatte, S.; Tibbetts, F. t-Butyl carbazate. In *Organic Syntheses*; Academic Press: New York, NY, USA, 1973; p. 166.

30.   Yin, J.; He, X.; Wang, K.; Xu, F.; Shangguan, J.; He, D.; Shi, H. Label-Free and Turn-on Aptamer Strategy for Cancer Cells Detection Based on a DNA–Silver Nanocluster Fluorescence upon Recognition-Induced Hybridization. *Anal. Chem.* **2013**, *85*, 12011–12019. [CrossRef]

31. Jacobson, O.; Weiss, I.D.; Wang, L.; Wang, Z.; Yang, X.; Dewhurst, A.; Ma, Y.; Zhu, G.; Niu, G.; Kiesewetter, D.O.; et al. 18F-Labeled Single-Stranded DNA Aptamer for PET Imaging of Protein Tyrosine Kinase-7 Expression. *J. Nucl. Med.* **2015**, *56*, 1780–1785. [CrossRef] [PubMed]

32. Alawak, M.; Abu Dayyih, A.; Mahmoud, G.; Tariq, I.; Duse, L.; Goergen, N.; Engelhardt, K.; Reddy Pinnapireddy, S.; Jedelská, J.; Awak, M.; et al. ADAM 8 as a novel target for doxorubicin delivery to TNBC cells using magnetic thermosensitive liposomes. *Eur. J. Pharm. Biopharm.* **2021**, *158*, 390–400. [CrossRef]

33. Cossarizza, A.; Salvioli, S. Flow Cytometric Analysis of Mitochondrial Membrane Potential Using JC-1. *Curr. Protoc. Cytom.* **2000**, *13*, 9–14. [CrossRef] [PubMed]

34. Perelman, A.; Wachtel, C.; Cohen, M.; Haupt, S.; Shapiro, H.; Tzur, A. JC-1: Alternative excitation wavelengths facilitate mitochondrial membrane potential cytometry. *Cell Death Dis.* **2012**, *3*, e430. [CrossRef] [PubMed]

35. Hof, J.V. Cell Cycle Analysis. In *Tissue Culture*; Elsevier: Amsterdam, The Netherlands, 1973; pp. 423–428.

36. Korashy, H.M.; Rahman, A.F.M.M.; Kassem, M.G.; Dasatinib. *Profiles of Drug Substances, Excipients and Related Methodology*; Academic Press: New York, NY, USA, 2014; Volume 39, pp. 205–237.

37. Luo, Y.; Liao, F.; Lu, W.; Chang, G.; Sun, X. Coordination polymer nanobelts for nucleic acid detection. *Nanotechnology* **2011**, *22*, 195502. [CrossRef]

38. Sivandzade, F.; Bhalerao, A.; Cucullo, L. Analysis of the Mitochondrial Membrane Potential Using the Cationic JC-1 Dye as a Sensitive Fluorescent Probe. *Bio-Protocol* **2019**, *9*, e3128. [CrossRef] [PubMed]

39. Bouitbir, J.; Panajatovic, M.V.; Frechard, T.; Roos, N.J.; Krähenbühl, S. Imatinib and Dasatinib Provoke Mitochondrial Dysfunction Leading to Oxidative Stress in C2C12 Myotubes and Human RD Cells. *Front. Pharmacol.* **2020**, *11*, 1106. [CrossRef]

40. Yu, R.; Zhang, Y.; Xu, Z.; Wang, J.; Chen, B.; Jin, H. Potential antitumor effects of panaxatriol against DU-15 human prostate cancer cells is mediated via mitochondrial mediated apoptosis, inhibition of cell migration and sub-G1 cell cycle arrest. *J. BUON* **2018**, *23*, 200–204. [PubMed]

41. Porciani, D.; Cardwell, L.N.; Tawiah, K.D.; Alam, K.K.; Lange, M.J.; Daniels, M.A.; Burke, D.H. Modular cell-internalizing aptamer nanostructure enables targeted delivery of large functional RNAs in cancer cell lines. *Nat. Commun.* **2018**, *9*, 2283. [CrossRef]

42. Xiao, Z.; Shangguan, D.; Cao, Z.; Fang, X.; Tan, W. Cell-specific internalization study of an aptamer from whole cell selection. *Chem.-A Eur. J.* **2008**, *14*, 1769–1775. [CrossRef]

5.2.1. Material suplementario del artículo V

Targeted-lymphoma drug delivery system based on the Sgc8-c aptamer.

Estefanía Sicco[1,2], Hugo Cerecetto[1], Victoria Calzada[1,*] and María Moreno[2,*]

SUPPLEMENTARY MATERIALS
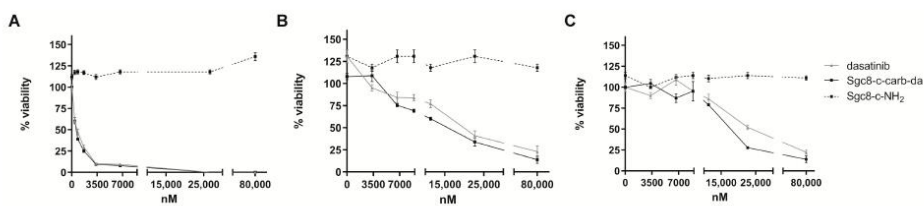
Figure S1: Dose-response curves for dasatinib, **Sgc8-c-carb-da,** and Sgc8-c-NH$_2$ using the MTT method in (**A**) A20, (**B**) CCRF-CEM, and (**C**) U87 MG cells. Graph shows mean ± SD, n = 10 per condition.
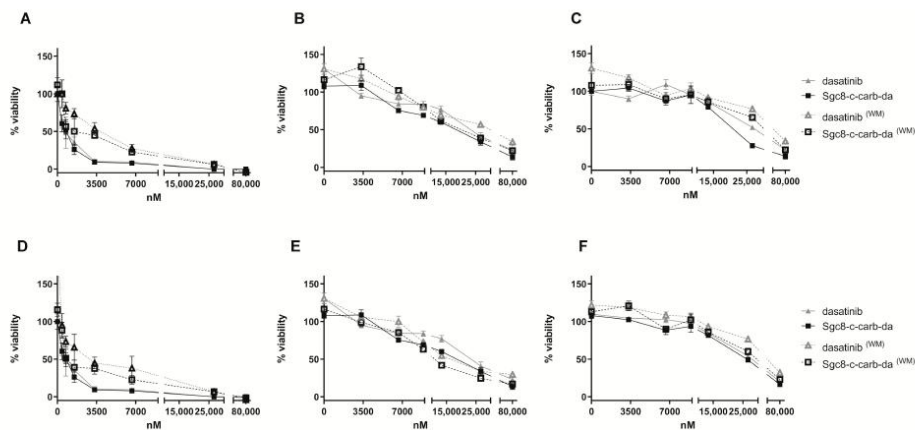
Figure S2. Dose-response curves for dasatinib or **Sgc8-c-carb-da** after 48 h of incubation, with (WM) or without the washing method (60 or 120 min of drug exposure followed by a wash and further incubation), with the different cell lines: (**A**) A20 (60 min), (**B**) CCRF-CEM (60 min), (**C**) U87 MG (60 min), (**D**) A20 (120 min), (**E**) CCRF-CEM (120 min), and (**F**) U87 MG (120 min). Cytotoxicity was evaluated by MTT. Graph shows mean ± SD, n = 10 per condition.
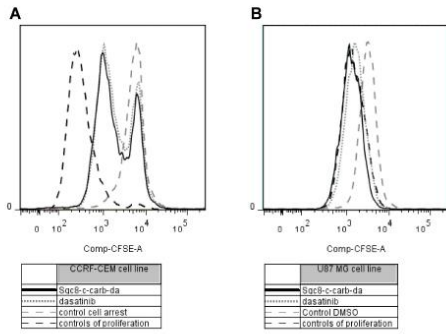
Figure S3. Arrest of cell proliferation induced by **Sgc8-c-carb-da** and dasatinib in (**A**) CCRF-CEM and (**B**) U87 MG cell lines. Cell proliferation arrest histogram, controls of proliferation, and cell arrest: incubation with medium (100% proliferating cells) and 20% of DMSO (0% proliferating cells), respectively.
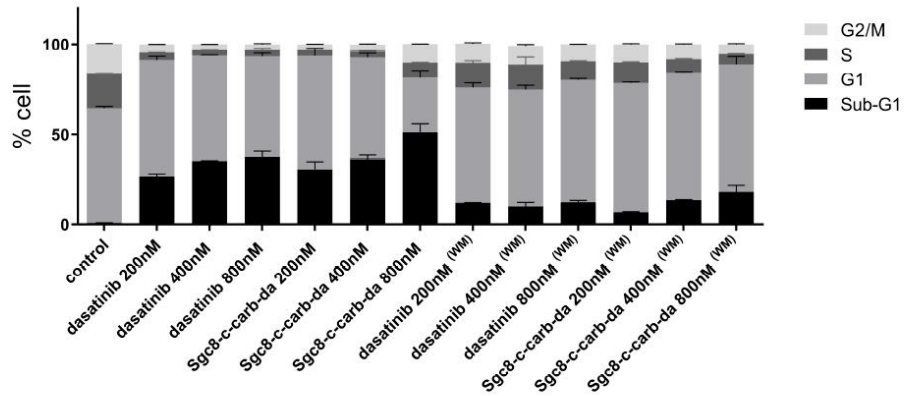
Figure S4. Phases of the cell cycle induced by **Sgc8-c-carb-da** and dasatinib in A20 cells. Assay performed on the A20 cells after incubation with 200, 400, and 800 nM **Sgc8-c-carb-da** and dasatinib for 24 h, with (WM) or without the washing method (60 min of drug exposure followed by a wash and further incubation). Graph shows mean ± SD, n = 3 per condition.

6. Discusión general

Capítulo I: Sgc8-c como agente de imagenología molecular en cáncer

En base a los alentadores antecedentes generados por el laboratorio sobre la implementación de nuevas estrategias de Imagenología Molecular en cáncer basados en aptámeros y a la excelente experiencia en marcación de moléculas (Calzada, 2012; Camacho, 2013; García, 2014; Calzada, 2017a; Calzada, 2017b) es que se planteó, en una primera instancia, profundizar con el desarrollo de sondas para imagenología molecular utilizando como plataforma estructural estos bio-sistemas.

En el artículo I, se diseñaron, sintetizaron y caracterizaron tres derivados del aptámero Sgc8-c y quelantes bifuncionales, para la preparación posterior de sondas radiomarcadas. Además, se profundizó en la síntesis y caracterización de una sonda fluorescente, previamente generada por nuestro grupo (Calzada, 2017a). Estas síntesis químicas se lograron estandarizar y sistematizar, obteniendo excelentes rendimientos para la incorporación de todos los quelantes. Se generó una metodología versátil, lo que permitirá su utilización con otros aptámeros. Del protocolo se destaca que se realizó a temperatura ambiente y que los tiempos de reacción química utilizados fueron cortos, con ausencia de degradación del aptámero y sin reacciones secundarias. Asimismo, la reacción es compatible con disolventes orgánicos, como dimetilsulfóxido (DMSO) o dimetilformamida (DMF), clásicos disolventes utilizados en sustancias hidrofílicas (Arakawa, 2018), e incluso DMF también presenta funciones importantes como catalizador y estabilizador (Heravi, 2018).

Los derivados del aptámero que se generaron tienen una modificación estructural muy pequeña en término de su masa molecular, sin embargo, mostraron diferentes tiempos de retención en las corridas por RP-HPLC. Se logró generar una metodología de RP-HPLC que distinguió los diferentes conjugados estudiados y, también, la sonda fluorescente. Esta característica podría explicarse por diferencias significativas en las lipofilias de los diferentes quelantes utilizados y por las distintas masas moleculares que presentaron los derivados y la sonda. Esto, por tanto, podría modificar el comportamiento biológico *in vivo*, especialmente la biodistribución y depuración de las sondas que se generen con estos derivados. En este trabajo de posgrado se continuó con el estudio del comportamiento biológico del derivado generado con el quelante bifuncional NOTA, Sgc8-c-NOTA.

La pureza de las sondas fue una de las características que se consideró relevante para obtener un buen contraste en las imágenes (Chen, 2010b; Calzada, 2020). En este sentido, el proceso de purificación que se utilizó, RP-HPLC, permitió obtener los tres conjugados deseados y la sonda fluorescente con una pureza próxima al 100 % (según la técnica de cuantificación utilizada). No se detectaron, en ningún caso, fragmentos de aptámero de baja masa molecular o agregados de aptámero de gran masa molecular. Esto podría significar que se obtuvieron todos los aptámeros en estequiometría 1:1 (aptámero:quelante bifuncional).

La estabilidad es otra característica deseable, ya que los transforma en potenciales sistemas para la generación futura de sondas (Chen, 2010b). Los derivados mostraron excelentes estabilidades en condiciones para generar las sondas radiomarcadas, siendo estables en medios acuosos y en un amplio rango de temperaturas (desde temperatura ambiente hasta 70 ºC). Adicionalmente, presentaron estabilidad en condiciones clásicas de almacenamiento.

En el artículo II, se diseñó, sintetizó, caracterizó y evaluó una sonda radiomarcada con ^{67}Ga, generada a partir de un derivado del aptámero Sgc8-c, Sgc8-c-NOTA, para su empleo en diagnóstico de neoplasias hemato-oncológicas.

Para este trabajo se utilizó el derivado Sgc8-c-NOTA generado en el artículo I (Sicco, 2018). La conjugación NOTA se eligió debido a sus buenas propiedades como quelante bifuncional para M^{3+}, ideal para emisores gamma como ^{67}Ga, que se utiliza para generar imágenes durante días y ha sido estudiado para tomografía por emisión de positrones y teranóstico (Kang, 2019; Woo, 2019). Además, se ha observado que este quelante bifuncional presenta una rápida cinética de complejación a temperatura ambiente y una excelente estabilidad *in vivo* (Okoye, 2019).

Con la finalidad de confirmar la estructura de la radio-sonda desarrollada y asegurar la incorporación de un solo átomo de galio por molécula de aptámero, Sgc8-c-NOTA se coordinó con galio estable ($^{69/71}$GaCl$_3$) en idénticas condiciones que las utilizadas en el radiomarcado. Así, se corroboró la estructura del compuesto obtenido por espectrometría de masas ESI-MS y, por la coincidencia en tiempos de retención en RP-HPLC, se plantea que la radio-sonda es estructuralmente idéntica al complejo con galio estable. En este sentido, se propone que la coordinación con ^{67}Ga es la deseada.

El procedimiento de marcación se optimizó mostrando que el pH del buffer es relevante para obtener una óptima marcación. Esto concuerda con lo descripto en la literatura, donde se observa que el quelante bifuncional NOTA puede formar diferentes quelatos estables con galio, cuya estructura es dependiente del pH (Shetty, 2010).

Se evaluó la pureza radioquímica y la actividad específica para Sgc8-c-NOTA-^{67}Ga. En cuanto a la pureza radioquímica de Sgc8-c-NOTA-^{67}Ga fue superior a 95 %. La sonda radiomarcada mostró alta estabilidad en el buffer de reacción, a diferentes temperaturas y en el tiempo. Al estudiar la estabilidad de la sonda en suero fetal bovino, se observó una alta unión a proteínas séricas, > 90 %, y además se observó inestabilidad del aptámero libre (66 %) después de 2 h de incubación. Se obtuvieron resultados similares en ensayos previos con sistemas similares (Calzada, 2017b).

La sonda marcada presentó un coeficiente de distribución, $logD_{7,5}$ = -2,41± 0,11, siendo más hidrofílico que el análogo DOTA, previamente descripto, $logD_{7,5}$= -1,87 ± 0,05 (Sgc8-c-DOTA-^{67}Ga) (Calzada, 2017b). Este cambio podría modular el comportamiento *in vivo* de la sonda. Los estudios de afinidad mostraron un valor de K_d para el receptor PTK7 de 0,019 nM, lo que indica que la afinidad de unión no se modificó al incorporar el quelante y el radiometal. Este valor de K_d es consistente con lo descripto por los investigadores que seleccionaron el aptámero Sgc8-c (Shangguan, 2007).

Los estudios de unión de la sonda radiomarcada a líneas de células tumorales mostraron un aumento de la señal con el tiempo para la línea murina de linfoma no-Hodgkin a células B, A20, y con la línea de célula tumoral A20/GFP (transfectada con *Green Fluorescent Protein*), lo que demuestra la capacidad de unión de la sonda. El análisis farmacocinético mostró que la sonda se ajustó a un modelo farmacocinético bi-compartimental en el cuerpo, con eliminación del compartimento central, es decir, por sangre y órganos muy perfundidos como riñón e hígado.

Se demostró que el modelo tumoral era adecuado para el estudio de prueba de concepto, ya que se confirmó, mediante citometría de flujo, que la línea celular tumoral A20/GFP expresa PTK7. En el modelo de animales portadores de tumores A20/GFP, la sonda presentó una biodistribución con captación tumoral, sin captación significativa en células no blanco y una eliminación por vía hepatobiliar y por vía renal; esto último se encuentra en concordancia con la farmacocinética. Esto confirmó que el cambio en el

quelante bifuncional, de DOTA (Calzada, 2017b) a NOTA, no modificó la biodistribución *in vivo* como era de esperar, según los valores de logD obtenidos.

La captación del tumor aumentó con un tiempo significativamente mayor durante las 48 h post-inyección. Sin embargo, las actividades ID/g de la sangre y del músculo disminuyeron con el tiempo, lo que dio como resultado que las relaciones de tumor/no tumor sean más altas a 24 h post-inyección de la sonda. Consecuentemente, esto mejoró el contraste de las imágenes, observándose así una notable mejoría en la captación tumoral. Estos resultados se compararon con un grupo control de bloqueo con aptámero sin modificar (Sgc8-c-NH$_2$), obteniendo una disminución no significativa de la captación tumoral. Lo que podría deberse a que el aptámero libre Sgc8-c-NH$_2$ se está uniendo a las proteínas séricas y, por ende, no consigue competir con los receptores PTK7 de las células tumorales. Asimismo, una sobreexpresión de este receptor en las células también podría resultar en un bloqueo leve. Por lo que estos ensayos deben mejorarse, en principio, con cambios en las dosis inyectadas tanto de la sonda como del aptámero libre. También se podría cambiar la molécula de bloqueo, pero los anticuerpos anti-PTK7 reconocen sitios de unión al ligando diferentes que el aptámero Sgc8 (Shangguan, 2008; Chen, 2010a).

Los resultados de la biodistribución de la sonda radiomarcada fueron consistentes con las imágenes *in vivo* logradas, donde se observó una óptima captación tumoral y una señal abdominal a las 24 h post-inyección de la sonda. Se lograron imágenes tumorales bien definidas a las 24, 48 y 72 h. Mediante las imágenes *ex vivo* se evidenció que la captación de la sonda provenía del tumor, resultados que fueron obtenidos mediante el uso de co-localización con el GFP que expresaban las células tumorales A20/GFP utilizadas para generar el modelo. Para generar estas imágenes se utilizó una combinación multimodal de imágenes de fluorescencia, de radioactividad (gamma) y de rayos X; resultando en un apropiado control positivo de interacción específica. Además, con estos estudios *ex vivo* fue posible distinguir las señales fuertes provenientes del tumor y del hígado, y en menor medida de riñones e intestino; coincidente con los resultados de los ensayos de biodistribución. Si bien se adquirieron imágenes con una considerable captación tumoral, es necesario ajustar la dosis de las sondas o el tiempo de adquisición para mejorarlas, incluso el microambiente tumoral podría estar afectando la penetración de la sonda en el tejido tumoral. Por lo que es necesario recurrir a otros modelos tumorales que permitan evaluar el potencial de las sondas imagenológicas. Recientemente, nuestro

grupo describió la evaluación de Sgc8-c en cáncer de colon en un modelo de xenoinjerto de ratón, donde se observó que presentan excelentes captaciones tumorales a las 2 horas post-inyección de la sonda fluorescente y una óptima relación tumor/músculo a este tiempo (Arévalo, 2021; Arévalo, 2022). En base a estos resultados, se podría evaluar la sonda radiomarcada en modelos murinos de xenoinjerto tumorales, para mejorar la captación tumoral y relaciones tumor/no tumor a tiempos post-inyección más cortos que los obtenidos hasta el momento.

Finalmente, para este modelo tumoral de ratón la relación de tumor/no tumor con la sonda Sgc8-c-NOTA-^{67}Ga fue muy alta, mejorando, por consecuencia, el contraste en las imágenes. Estos resultados demuestran el potencial del aptámero Sgc8-c como agente diagnóstico para estas neoplasias hemato-oncológicas, lo cual fue destacado en una carta al editor (Filippi, 2020).

En el artículo III, se evaluó por primera vez el aptámero Sgc8-c en un modelo de melanoma metastásico como sonda de imagen molecular para diagnóstico *in vivo*, así como en un modelo de melanoma no metastásico. Los antecedentes para el uso de este modelo tumoral fueron los trabajos previos del grupo (Calzada, 2017a).

Se emplearon dos estrategias diferentes y complementarias para analizar la capacidad de las sondas para interactuar con las células de melanoma metastático (B16F10): (1) el uso de la sonda radiomarcada (Sgc8-c-NOTA-^{67}Ga) que permitió medir mediante el sistema de contador gamma y (2) el uso de la sonda fluorescente (Sgc8-c-Alexa647) que permitió el análisis por citometría de flujo y Western blot.

Primeramente, se verificó la sobreexpresión de PTK7 en las células de melanoma metastático mediante la incubación con un anticuerpo o la sonda fluorescente (Sgc8-c-Alexa647), tanto en los ensayos por citometría de flujo como los estudios por Western blot. Incluso, el índice de fluorescencia medio específico (MFI) que se obtuvo para la población de células B16F10, sugiere que estas células expresan niveles altos de PTK7. En el ensayo de Western blot, se observó que la sonda fluorescente reconoció dos fracciones de PTK7. Esto se puede deber a que PTK7 presenta sitios de escisión (Lichtig, 2019) y, además, como se mencionó, el anticuerpo y el aptámero reconocen sitios distintos de PTK7 (Shangguan, 2008; Chen, 2010a). A su vez, se comprobó que la sonda Sgc8-c-NOTA-^{67}Ga se une a la línea celular B16F10 y los ensayos de competencia

realizados con el aptámero sin marcar, Sgc8-c-NH$_2$, mostraron diferencias significativas, confirmando la interacción de la sonda con PTK7.

La internalización compleja por la interacción Sgc8-PTK7 es un mecanismo que se confirmó mediante microscopía confocal, donde se observó la sonda fluorescente de forma intracelular en diferentes líneas tumorales. Este mecanismo ya ha sido descripto para algunos aptámeros (Xiao, 2008). A su vez, se confirmó que la internalización a la célula es por vía endosomal. Esto también ha sido descripto en otras sondas basadas en aptámeros (Jacobson, 2015).

Se realizó una prueba de concepto *in vivo* en modelos de melanoma metastático y no metastático en ratones. Ambas sondas presentaron una excelente relación tumor/no tumor, con una rápida depuración sanguínea. Los resultados de los estudios *in vitro* fueron consistentes con los obtenidos para las biodistribuciones y las imágenes *in vivo*. En la biodistribución, nuevamente, para ambas sondas se observó una captación tumoral casi exclusiva a las 24 horas post-inyección. Al igual que para el modelo de linfoma, es primordial desarrollar nuevas evaluaciones para mejorar los tiempos de adquisición. Todos estos hallazgos permitieron explorar nuevas herramientas para mejorar la farmacocinética y la captación tumoral, mediante la co-asociación de estas sondas de aptámeros a nanoestructuras. En particular, la co-asociación de la micela polimérica T908 con la sonda mostró una biodistribución y un perfil farmacocinético diferentes y deseables, lo que podría contribuir a la permanencia en el organismo y la entrega de direccionamiento pasivo en un microambiente tumoral (Castelli, 2021).

Por otro lado, las metodologías aplicadas permitieron detectar diferencias en la expresión del marcador tumoral PTK7 en los dos modelos tumorales de melanoma. Por ello, es importante profundizar en el estudio de la expresión de PTK7, con el objetivo de conocer si las diferencias en la expresión que se observaron en los ensayos están realmente involucradas en vías de señalización que, en consecuencia, otorgan un mayor poder metastásico a las células tumorales.

Los resultados que se presentan en los artículos I (Sicco, 2018), II (Sicco, 2020) y III (Sicco, 2021a) de este trabajo de posgrado, junto con los resultados de los trabajos del área (Calzada, 2017a; Calzada, 2017b; Castelli, 2021; Arévalo, 2021; Arévalo, 2022), respaldan el papel potencial de Sgc8-c-NOTA-[67]Ga y Sgc8-c-Alexa647 como herramientas

de imagenología molecular óptimas para mejorar las estrategias en el diagnóstico molecular no invasivo en melanoma y linfoma, así como los potenciales enfoques teranósticos. Otorgan, además, las bases para desarrollar el diseño de nuevos agentes bioterapéuticos basados en aptámeros.

Capítulo II: Sgc8-c como agente potencial bioterapéutico selectivo en cáncer

En el artículo IV, se diseñó, sintetizó y caracterizó un conjugado covalente aptámero-fármaco basado en Sgc8-c para su uso como bioterapéutico selectivo en cáncer.

Para generar el nuevo conjugado, Sgc8-c-carb-da, se incorporó covalentemente a la estructura del aptámero un fragmento derivado del fármaco dasatinib, mediante un conector carbamato. Este agrupamiento tiene la característica de que es hidrolizable química y enzimáticamente, por ende, tiene la capacidad de liberar el fármaco a distintos pH (Bartoschek, 2000; Xia, 2022).

Se transformó dasatinib en un intermedio reactivo, fenilcarbonato, vía el grupo alcohol primario presente en la estructura del fármaco. Se confirmó espectroscópicamente la estructura (^{1}H-RMN, ^{13}C-RMN, HSQC y HMBC). Posteriormente, este intermedio se hizo reaccionar covalentemente con Sgc8-c-NH$_2$. Para optimizar la síntesis se analizaron diferentes condiciones de reacción variando: el disolvente, el tiempo, la temperatura, la fuente de calor, el pH y los contraiones. De los diferentes productos generados durante la reacción, se identificó el producto de interés, Sgc8-c-carb-da, a través de espectrometría ESI-MS. El mayor rendimiento que se alcanzó en la síntesis del conjugado aptámero-fármaco, en escala de 0,5 mg, fue del 67,8 %. Se purificó por RP-HPLC, siguiendo las condiciones previas utilizadas para el desarrollo de las sondas y se obtuvo con una pureza del 99 %. El escalado, en escala de 100 mg (ya que, debido a la alta masa molecular de Sgc8-c-carb-da, se requiere una importante cantidad del mismo para trabajar con un número estadísticamente significativo de animales en los estudios *in vivo*) conllevó a un importante detrimento en el rendimiento de reacción (28,3 %, datos no publicados), lo que se convirtió en una limitante para el posterior estudio sobre animales de experimentación (ver más adelante).

Adicionalmente, mediante electroforesis y RP-HPLC se complementó la información sobre la integridad de Sgc8-c-carb-da, los perfiles fueron consistentes con la ausencia de fragmentos de baja masa molecular en el pico de RP-HPLC que correspondió al producto

de interés. El conjugado presentó estabilidad frente a diferentes temperaturas y en condiciones de almacenamiento estándar para aptámeros. El valor $logD_{7.5}$ es de -1,35 ± 0,04, que resulta ser del mismo orden que las sondas imagenológicas, lo que podría indicar que el comportamiento biológico *in vivo* de Sgc8-c-carba-da puede ser similar al de otros agentes de imagen. Las propiedades fisicoquímicas del bioterapéutico son adecuadas para su uso como futuro fármaco.

Adicionalmente, Sgc8-c-carb-da fue capaz de liberar dasatinib completamente *in vitro* a pH endosomal (5,0), luego de 0,5 h de incubación, sin liberación a pH fisiológico (7,4) o intratumoral (5,5). Esta propiedad de Sgc8-c-carb-da de liberar dasatinib dependiente del pH, es muy relevante porque implica algunas ventajas para el tratamiento tradicional. Por un lado, las sondas basadas en aptámeros Sgc8-c tienen una captación tumoral y una depuración sanguínea significativas (Calzada, 2017a; Calzada, 2017b; Sicco, 2020; Sicco, 2021a; Castelli, 2021; Arévalo, 2021; Arévalo, 2022), por lo que se espera que Sgc8-c-carb-da facilite la administración del fármaco al sitio de acción, a través de la interacción aptámero-PTK7, con una mínima hidrólisis en los sitios inespecíficos; mejorando así, la disponibilidad del fármaco y reduciendo la toxicidad sistémica. Por otro lado, al confirmarse que las sondas generadas se internalizan por vía endosomal (Sicco, 2021a), se espera que, una vez internalizado Sgc8-c-carb-da en las células tumorales, se provoque la liberación de dasatinib favoreciendo la administración del fármaco en el sitio de acción apropiado. El sistema desarrollado cumple con las características previstas, y por tanto merece una mayor exploración en las indicaciones hemato-oncológicas. Esto permitirá evaluar el potencial del aptámero como un vehículo de administración de fármacos en el órgano blanco.

En el artículo V, se evaluó el potencial terapéutico de Sgc8-c-carb-da, conjugado aptámero-fármaco desarrollado en el artículo IV, que combina un aptámero que reconoce el receptor PTK7, como un componente específico del blanco (células tumorales) y la subestructura de dasatinib, como un componente citotóxico (Sicco, 2021b).

El conjugado aptámero-fármaco mostró actividad citotóxica contra las células A20, sugiriendo que dasatinib no pierde actividad biológica al acoplarse a la estructura del aptámero. También, se observó mayor actividad citotóxica en células que sobreexpresaban PTK7. Por lo tanto, este sistema de entrega de fármacos no afectaría la actividad biológica del mismo. De igual manera, no se esperaba que el aptámero sufriera modificaciones

topológicas, ni pérdidas en el reconocimiento por su blanco, ya que dasatinib no se incorporó por intercalación con el oligonucleótido (Luo, 2011; Korashy, 2014). En este estudio, además Sgc8-c no presentó actividad citotóxica en las concentraciones estudiadas, como sí sucede con otros aptámeros (Kim, 2018); indicando que funcionaría únicamente como vehículo para dasatinib en el conjugado aptámero-fármaco.

Por otro lado, la falta de diferencias en la actividad citotóxica entre dasatinib y el conjugado aptámero-fármaco Sgc8-c-carb-da, podría deberse a la ausencia del efecto funcional de vehículo de Sgc8-c, debiéndose exclusivamente a una ruptura del oligonucleótido en el medio biológico y a la liberación de dasatinib. Para investigar si la unión celular de Sgc8-c-carb-da a través de PTK7 es responsable de su biorrespuesta, se realizó un estudio de unión celular *in vitro*, donde se aplicó un protocolo de lavado post-exposición de potencial agente citotóxico a las células en estudio. En estos ensayos, se observó que Sgc8-c-carb-da fue más citotóxico que en los tratamientos con dasatinib solo. El conjugado Sgc8-c-carb-da resultó ser cuatro veces más citotóxico que dasatinib después de 120 min de incubación y lavado posterior. Estos resultados destacaron la relevancia de Sgc8-c como sistema de administración mediada por PTK7.

Los resultados obtenidos por ensayos de MTT muestran el potencial de Sgc8-c-carb-da como agente bioterapéutico. Sin embargo, el ensayo MTT es una medida integral de la citotoxicidad celular y refleja muchas vías alteradas. Por lo tanto, se ahondó en el estudio de los mecanismos detrás del efecto citotóxico de Sgc8-c-carb-da.

Así se evidenció que Sgc8-c-carb-da promueve la muerte celular, de manera dosis dependiente, en tiempos tempranos por apoptosis y en tiempos tardíos por necrosis. Asimismo, se encontró un porcentaje de muerte celular distinto al observado por MTT. Esto puede deberse a que éste último depende de la actividad mitocondrial. Cuando se aplicó el método de lavado de los compuestos, nuevamente el porcentaje de muerte celular aumentaba significativamente para Sgc8-c-carb-da con respecto al dasatinib. Por otro lado, se corroboró que la muerte celular observada estuvo precedida por alteraciones en la estructura mitocondrial, debido a que se encontraron cambios en el potencial mitocondrial para ambos compuestos, siendo levemente mayor para Sgc8-c-carb-da.

Sgc8-c-carb-da generó un arresto celular, dosis-dependiente, significativamente mayor que dasatinib, gracias a la capacidad del aptámero para interactuar con PTK7 y

facilitar la administración intracelular de dasatinib, deteniendo la proliferación celular. Por último, el arresto de la proliferación celular generada por Sgc8-c-carb-da, también resultó en un aumento significativo y dosis-dependiente del pico Sub-G1 y disminuciones en las fases G1, S y G2/M. El pico Sub-G1 está asociado a la apoptosis celular (Yu, 2008), en este caso generada por Sgc8-c-carb-da.

Dados estos resultados, se estaría confirmando la hipótesis de que el aptámero Sgc8-c actúa como vehículo para el dasatinib, interaccionando con PTK7, ingresando a la célula y mejorando su actividad biológica. Además, con los lavados realizados en los ensayos, se corroboro que Sgc8-c-carb-da sigue ejerciendo su efecto citotóxico porque ya se encuentra dentro de la célula o unido al receptor. A pesar de la exitosa demostración del concepto, el potencial de Sgc8-c-carb-da no pudo ser aún evaluado *in vivo*.

El principal obstáculo para la no realización de estudios *in vivo* fue económico. Ya que, en el escalado de la síntesis del conjugado de 0,5 mg a 100 mg, del aptámero de partida Sgc8-c-NH$_2$, no fue posible reproducir el rendimiento de la síntesis a pequeña escala (disminución del rendimiento de 67,8 a 28,3 %). Debido a la alta masa molecular del conjugado, y a la estequiometria de 1:1, la cantidad necesaria para realizar futuros estudio con animales de experimentación implicaría partir de cantidades próximas a los 500 mg del aptámero Sgc8-c-NH$_2$ (considerando una única administración de Sgc8-c-carb-da, a una dosis equivalente a la identificada como activa para dasatinib, en 10 animales de 20 g de masa corporal, datos no publicados). Esto implicaba un elevadísimo costo del aptámero de partida (U\$S 3100, Proforma de julio de 2020, BIOSPRING The Oligo Company).

Continuar profundizando en su evaluación biológica nos permitirá conocer adecuadamente este sistema de administración de fármacos en tumores.

7. Conclusiones

En el presente trabajo de posgrado se profundizó en el estudio del potencial que presenta el aptámero Sgc8-c para su aplicación en imagenología molecular y en terapia de cáncer.

- **Capítulo I: Sgc8-c como agente de imagenología molecular en cáncer**

Se desarrollaron y estudiaron dos sondas con alto grado de pureza, una portadora de un emisor gamma, Sgc8-c-NOTA-^{67}Ga y otra fluorescente, Sgc8-c-Alexa647. Las preparaciones y purificaciones se lograron sistematizar, consiguiendo reacciones de tiempos cortos, rendimientos excelentes, con compatibilidad con disolvente orgánicos y sin presencia de reacciones secundarias. Además, la versátil metodología desarrollada permite la aplicación con otros aptámeros.

Ambas sondas se caracterizaron fisicoquímicamente y presentaron una excelente estabilidad frente a diferentes temperaturas, medios acuosos y condiciones clásicas de almacenamiento. Presentaron una lipofilicidad óptima para el comportamiento biológico *in vivo*.

Las sondas mantienen la afinidad y especificidad por el blanco molecular PTK7, y se demostró que se internalizan por vía endosomal, en las distintas líneas celulares tumorales estudiadas.

En las evaluaciones biológicas *in vivo* ambas sondas mostraron una óptima captación tumoral, con una rápida depuración sanguínea, indicando que ambas son herramientas potenciales para su uso específico en la detección precoz del melanoma y linfoma. Asimismo, la sonda Sgc8-c-NOTA-^{67}Ga presentó una relación tumor/no tumor muy alta para el modelo de linfoma, mejorando el contraste de las imágenes. Confirmamos así, la utilidad del aptámero Sgc8-c como agente diagnóstico para neoplasias hemato-oncológicas.

- **Capítulo II: Sgc8-c como agente potencial bioterapéutico selectivo en cáncer**

Se generó, con un alto grado de pureza, un conjugado aptámero-fármaco Sgc8-c-carb-da, mediante la incorporación de un fragmento derivado de dasatinib conectado covalentemente al aptámero Sgc8-c. Esta reacción también se logró estandarizar.

Sgc8-c-carb-da presentó óptimas propiedades fisicoquímicas, como la estabilidad y la lipofilia.

Se observó que el conjugado covalente aptámero-fármaco tiene la capacidad de liberar dasatinib a pH endosomal, siendo el lugar óptimo para la liberación del fármaco.

En los diferentes estudios del comportamiento biológico de Sgc8-c-carb-da, se observó que dasatinib no pierde su actividad biológica y que la actividad citotóxica es mayor cuando la célula sobreexpresa PTK7.

Sgc8-c-carb-da promueve la muerte celular por apoptosis y necrosis, acompañada de cambios en el potencial de la membrana mitocondrial. También genera una detención de la proliferación celular, lo que resulta en un aumento en el pico Sub-G1 y disminuciones en las fases S y G2 / M.

Sgc8-c-carb-da presenta mayor actividad anti-tumoral que dasatinib, en una modelo que simula la depuración del compuesto (protocolo de lavado), lo que destaca la relevancia de Sgc8-c como sistema de entrega de fármacos por interacción con un receptor específico sobreexpresado en la línea celular de estudio. Por esto último, se estaría confirmando la hipótesis que el aptámero Sgc8-c actúa como vehículo para el dasatinib, interaccionando con PTK7, ingresando a la célula.

En este trabajo se exploraron diferentes enfoques del uso de aptámeros en aplicaciones biomédicas. Sin dudas, tras varios años de investigación el sistema de estudio, aptámero Sgc8-c, resulta ser muy prometedor y consistente en cuanto a su potencial como agente de reconocimiento por PTK7 con todos los beneficios para diagnóstico por imágenes y terapia mediada que eso conlleva. Además, de este trabajo se concluye que los aptámeros resultan ser moléculas sumamente versátiles y una gran oportunidad para el desarrollo en diversas áreas, sin descuidar la rigurosidad en los puntos que se han destacado en el manuscrito y en concordancia con las recientes recomendaciones de la *International Society of Aptameros* (McKeague 2022).

8. Perspectivas

En base a los excelentes resultados tanto en la síntesis como en las imágenes y biodistribuciones;

i) profundizar en la evaluación preclínica y en el desarrollo de sondas para imagenología molecular basadas en aptámeros;

ii) analizar diferentes dosis de administración, tiempos de adquisición de imágenes, otros radionucleidos con fines teranósticos;

iii) diseñar nuevos conjugados covalentes aptámero-fármacos, con nuevas moléculas citotóxicas. Si bien en este posgrado se logró una síntesis óptima del conjugado aptámero-dasatinib y presentó potenciales características para ser usado como bioterápico, no fue posible durante el desarrollo de la tesis continuar con los estudios en animales (por el inadecuado rendimiento en el escalado del biofármaco Sgc8-c-carb-da). Por lo que, sería interesante realizar conjugados con otras moléculas u otro tipo de conjugación aptámero-fármacos que permita, por ejemplo, una mayor estequiometria fármaco: aptámero;

iv) profundizar en la administración selectiva de fármacos mediada por aptámeros. Los óptimos resultados de la síntesis química y purificación, la confirmación de la internalización de Sgc8-c por vía endosomal, no solo en la línea celular A20 sino que también para las líneas celulares CCRF-CEM, B16 F10 y B16F1, y la demostración de la liberación del fármaco a pH endosomal, sientan las bases para continuar trabajando en esta línea de investigación.

9. Referencias bibliográficas

Adachi, T.; Nakamura, Y. Aptamers: A Review of Their Chemical Properties and Modifications for Therapeutic Application. Molecules. 2019; 24(23):4229.

Aebersold, R.; Anderson, L.; Caprioli, R.; Druker, B.; Hartwell, L.; Smith, R. Perspective: a program to improve protein biomarker discovery for cancer. J Proteome Res. 2005; 4(4):1104-9.

Alberts, B.; Johnson, A.; Lewis, J.; Raff, M.; Roberts, K.; Walter, P. Biología molecular de la célula. In; Omega, Ed.; 2004. pp. 1314–1320.

Alford, R.; Ogawa, M.; Choyke, P.L.; Kobayashi, H. Molecular probes for the in vivo imaging of cancer. Mol Biosyst. 2009; 5(11):1279-91.

American Cancer Society. Cancer facts & figures. The Society. 2008.

Anderson, C.J.; Welch, M.J. Radiometal-labeled agents (non-technetium) for diagnostic imaging. Chem Rev. 1999; 99(9):2219-34.

Arakawa, T. Acetonitrile as solvent for protein interaction analysis. Int J Biol Macromol. 2018; 114:728-732.

Araujo, J.; Logothetis, C. Dasatinib: a potent SRC inhibitor in clinical development for the treatment of solid tumors. Cancer Treat Rev. 2010; 36(6):492-500.

Arévalo, A. P.; Castelli, R.; Ibarra, M.; Crispo, M.; Calzada, V. *In Vivo* Evaluation of Sgc8-c Aptamer as a Molecular Imaging Probe for Colon Cancer in a Mouse Xenograft Model. Int J Mol Sci. 2022; 23(5):2466.

Arévalo, A., P. Evaluación de agentes marcadores de cáncer por imagenología molecular en modelos murinos. Tesis de maestría. ProInBio. 2021.

Ataseven, B.; Gunesch, A.; Eiermann, W.; Kates, R.E.; Högel, B.; Knyazev, P.; Ullrich, A.; Harbeck, N. PTK7 as a potential prognostic and predictive marker of response to adjuvant chemotherapy in breast cancer patients, and resistance to anthracycline drugs. Onco Targets Ther. 2014; 7:1723–31.

Attie, M.; Koskinas, M.; Dias, M.; Fonseca, K. Absolute disintegration rate measurements of Ga-67. Appl. Radiat. Isot. 1998; 49, (9)11, pp. 1175-1177.

Baba, A.I.; Câtoi, C. Comparative Oncology. Bucharest (RO): The Publishing House of the Romanian Academy; 2007.

Bagalkot, V.; Farokhzad, O.C.; Langer, R.; Jon, S. An aptamer-doxorubicin physical conjugate as a novel targeted drug-delivery platform. Angew Chem Int Ed Engl. 2006; 45(48):8149-52.

Bartoschek, S.; Vorholt, J.A.; Thauer, R.K.; Geierstanger, B.H.; Griesinger, C. N-carboxymethanofuran (carbamate) formation from methanofuran and CO2 in methanogenic archaea. Thermodynamics and kinetics of the spontaneous reaction. Eur J Biochem. 2000; 267(11):3130-8.

Berlier, J.E.; Rothe, A.; Buller, G.; Bradford, J.; Gray, D.R.; Filanoski, B.J.; Telford, W.G.; Yue, S.; Liu, J.; Cheung, C-Y.; Chang, W.; Hirsch, J.D.; Beechem, J.M.; Haugland, R.P.; Haugland, R.P. Quantitative Comparison of Long-wavelength Alexa Fluor Dyes to Cy Dyes: Fluorescence of the Dyes and Their Bioconjugates. Journal of Histochemistry & Cytochemistry. 2003; 51(12):1699-1712.

Bohrmann, L.; Burghardt, T.; Haynes, C.; Saatchi, K.; Häfeli, U.O. Aptamers used for molecular imaging and theranostics - recent developments. Theranostics. 2022; 12(9):4010-4050.

Borlan, R.; Focsan, M.; Maniu, D.; Astilean, S. Interventional NIR Fluorescence Imaging of Cancer: Review on Next Generation of Dye-Loaded Protein-Based Nanoparticles for Real-Time Feedback During Cancer Surgery. Int J Nanomedicine. 2021; 16:2147-2171.

Bouchard, P.R.; Hutabarat, R.M.; Thompson, K.M. Discovery and development of therapeutic aptamers. Annu Rev Pharmacol Toxicol. 2010; 50:237-57.

Boumaza, S.; Arribas, S.M.; Osborne-Pellegrin; M.; McGrath, J.C.; Laurent, S.; Lacolley, P.; Challande, P. Fenestrations of the carotid internal elastic lamina and structural adaptation in stroke-prone spontaneously hypertensive rats. Hypertension. 2001; 37(4):1101-7.

Braun, T.P.; Eide, C.A.; Druker, B.J. Response and Resistance to BCR-ABL1-Targeted Therapies. Cancer Cell. 2020; 37(4):530-542.

Butti, R.; Das, S.; Gunasekaran, V. P.; Yadav, A. S.; Kumar, D.; Kundu, G. C. Receptor tyrosine kinases (RTKs) in breast cancer: Signaling, therapeutic implications and challenges. Molecular Cancer, 2018; 17(1), 34.

Cai, W.; Rao, J.; Gambhir, S.S.; Chen, X. How molecular imaging is speeding up antiangiogenic drug development. Mol Cancer Ther. 2006; 5(11):2624-33.

Calzada, V. Aptamers in Diagnostic and Molecular Imaging Applications. Advances in Biochemical Engineering/Biotechnology. 2020; 174:141-160.

Calzada, V.; Báez, J.; Sicco, E.; Margenat, J.; Fernández, M.; Moreno, M.; Ibarra, M.; Quinn, T.; Gambini, J.P.; Cabral, P.; Cerecetto, H. Preliminary *In Vivo* Characterization of a Theranostic Aptamer: Sgc8-c-DOTA-67Ga. Aptamers. 2017b; 1, 19-27.

Calzada, V.; Moreno, M.; Newton, J.; González, J.; Fernández, M.; Gambini, J.P.; Ibarra, M.; Chabalgoity, A.; Deutscher, S.; Quinn, T.; Cabral, P.; Cerecetto, H. Development of new PTK7-targeting aptamer-fluorescent and -radiolabelled probes for evaluation as molecular imaging agents: Lymphoma and melanoma *in vivo* proof of concept. Bioorg Med Chem. 2017a; 25(3):1163-1171.

Calzada, V.; Zhang, X.; Fernandez, M.; Diaz-Miqueli, A.; Iznaga-Escobar, N.; Deutscher, S.L.; Balter, H.; Quinn, T.P.; Cabral P. A potencial theranostic agent for EGF-R expression tumors: (177)Lu-DOTA-nimotuzumab. Curr Radiopharm. 2012; 5(4):318-24.

Camacho, X.; García, M.F.; Calzada, V.; Fernández, M.; Chabalgoity, J.A.; Moreno, M.; Barbosa de Aguiar, R.; Alonso, O.; Gambini, J.P.; Chammas, R.; Cabral, P. [(99m)Tc(CO)(3)]-radiolabeled bevacizumab: *in vitro* and *in vivo* evaluation in a melanoma model. Oncology. 2013; 84(4):200-9.

Castelli, R.; Ibarra, M.; Faccio, R.; Miraballes, I.; Fernández, M.; Moglioni, A.; Cabral, P.; Cerecetto, H.; Glisoni, R.J.; Calzada, V. T908 Polymeric Micelles Improved the Uptake of Sgc8-c Aptamer Probe in Tumor-Bearing Mice: A Co-Association Study between the Probe and Preformed Nanostructures. Pharmaceuticals (Basel). 2021; 15(1):15.

Catana, C.; Wu, Y.; Judenhofer, M.S.; Qi, J.; Pichler, B.J.; Cherry, S.R. Simultaneous acquisition of multislice PET and MR images: initial results with a MR-compatible PET scanner. J Nucl Med. 2006; 47(12):1968-76.

Chen, C.; Wu, C.Q.; Chen, T.W.; Tang, M.Y.; Zhang, X.M. Molecular Imaging with MRI: Potential Application in Pancreatic Cancer. Biomed Res Int. 2015; 2015:624074.

Chen, K.; Chen, X. Design and development of molecular imaging probes. Curr Top Med Chem. 2010b; 10(12):1227-36.

Chen, M.; Yu, Y.; Jiang, F.; Zhou, J.; Li, Y.; Liang, C.; Dang, L.; Lu, A.; Zhang, G. Development of Cell-SELEX Technology and Its Application in Cancer Diagnosis and Therapy. Int J Mol Sci. 2016; 17(12):2079.

Chen, M-K.; Hung, M-C. Proteolytic cleavage, trafficking, and functions of nuclear receptor tyrosine kinases. FEBS J. 2015; 282(19):3693-721.

Chen, Y.; O'Donoghue, M.B.; Huang, Y.F.; Kang, H.; Phillips, J.A.; Chen, X.; Estevez, M.C.; Yang, C.J.; Tan, W. A surface energy transfer nanoruler for measuring binding site distances on live cell surfaces. J Am Chem Soc. 2010a; 132(46):16559-70.

CHLCC. Resumen Estadístico – Todos los cánceres. Incidencia y Mortalidad periodo 2015-2019. Tendencia de la Mortalidad hasta 2020. https://www.comisioncancer.org.uy/Ocultas/RESUMENES-ESTADISTICOSpara-los-canceres-mas-frecuentes--uc264

Ciancio, D.R.; Vargas, M.R.; Thiel, W.H.; Bruno, M.A.; Giangrande, P.H.; Mestre, M.B. Aptamers as Diagnostic Tools in Cancer. Pharmaceuticals (Basel). 2018; 11(3):86.

Civit, L.; Theodorou, I.; Frey, F.; Weber, H.; Lingnau, A.; Gröber, C.; Blank, M.; Dambrune, C.; Stunden, J.; Beyer, M.; Schultze, J.; Latz, E.; Duconge, F.; Kubbutat, M.H.G.; Mayer, G. Targeting hormone refractory prostate cancer by *in vivo* selected DNA libraries in an orthotopic xenograft mouse model. Sci Rep. 2019; 9(1):4976.

Comeo, E.; Kindon, N.D.; Soave, M.; Stoddart, L.A.; Kilpatrick, L.E.; Scammells, P.J.; Hill, S.J.; Kellam, B. Subtype-Selective Fluorescent Ligands as Pharmacological Research Tools for the Human Adenosine A2A Receptor. J Med Chem. 2020; 63(5):2656-2672.

Da Pieve, C.; Williams, P.; Haddleton, D.M.; Palmer, R.M.; Missailidis, S. Modification of thiol functionalized aptamers by conjugation of synthetic polymers. Bioconjug Chem. 2010; 21(1):169-74.

Dong, Y.; Chen, X.; Li, H.; Ni, Y.; Han, W.; Wang, J. PTK7 is a molecular marker for metastasis, TNM stage, and prognosis in oral tongue squamous cell carcinoma. Pol J Pathol. 2017; 68(1): 49-54.

Drugs and Lactation Database (LactMed®). Bethesda (MD): National Institute of Child Health and Human Development; 2006–. Gallium Citrate Ga 67. 2021.

Eley, T.; Luo, F.R.; Agrawal, S.; Sanil, A.; Manning, J.; Li, T.; Blackwood-Chirchir, A.; Bertz, R. Phase I study of the effect of gastric acid pH modulators on the bioavailability of oral dasatinib in healthy subjects. J Clin Pharmacol. 2009; 49(6):700-9.

Ellington, AD.; Szostak, JW. *In vitro* selection of RNA molecules that bind specific ligands. Nature. 1990. 346(6287):818-22.

Endoh, H.; Tomida, S.; Yatabe, Y.; Konishi, H.; Osada, H.; Tajima, K.; Kuwano, H.; Takahashi, T.; Mitsudomi, T. Prognostic model of pulmonary adenocarcinoma by expression profiling of eight genes as determined by quantitative real-time reverse transcriptase polymerase chain reaction. J Clin Oncol. 2004; 22(5):811–9.

Even-Sapir, E.; Lerman, H.; Lievshitz, G.; Khafif, A.; Fliss, D.M.; Schwartz, A.; Gur, E.; Skornick, Y.; Schneebaum, S. Lymphoscintigraphy for sentinel node mapping using a hybrid SPECT/CT system. J Nucl Med. 2003; 44(9):1413-20.

Famulok, M.; Mayer, G. Aptamer modules as sensors and detectors. Acc Chem Res. 2011; 44(12):1349-58.

Ferlay, J.; Colombet, M.; Soerjomataram, I.; Parkin, D.M.; Piñeros, M.; Znaor, A.; Bray, F. Cancer statistics for the year 2020: An overview. Int J Cancer. 2021.

Filippi, L.; Bagni, O.; Schillaci, O. Re: "Sgc8-c Aptamer as a Potential Theranostic Agent for Hemato-Oncological Malignancies" by Sicco et al. Cancer Biother Radiopharm. 2020; 35(8):626.

Furmanski, B.D.; Hu, S.; Fujita, K-I.; Li, L.; Gibson, A.A.; Janke, L.J.; Williams, R.T.; Schuetz, J.D.; Sparreboom, A.; Baker, S.D. Contribution of ABCC4-mediated gastric transport to the absorption and efficacy of dasatinib. Clin Cancer Res. 2013; 19(16):4359-4370.

Galmarini, C.M.; Mackey, J.R.; Dumontet, C. Nucleoside analogues and nucleobases in cancer treatment. Lancet Oncol. 2002; 3(7):415-24.

Gambhir, S.S. Molecular imaging of cancer with positron emission tomography. Nat Rev Cancer. 2002; 2(9):683-93.

Gao, S.; Zheng, X.; Jiao, B.; Wang, L. Post-SELEX optimization of aptamers. Anal Bioanal Chem. 2016; 408(17):4567-73.

Garau, M.; Alonso, R.; Musetti, C.; Barrios, E. Cancer incidence and mortality in Uruguay: 2013-2017. Colomb Med (Cali). 2022; 53(1):e2014966.

García, M.F.; Calzada, V.; Camacho, X.; Goicochea, E.; Gambini, J.P.; Quinn, T.P.; Porcal, W.; Cabra,l. P. Microwave-assisted synthesis of HYNIC protected analogue for 99mTc labeled antibody. Curr Radiopharm. 2014; 7(2):84-90.

García, M.F.; Moreno, M.; Cerecetto, H.; Calzada, V. Aptamer-Based Immunotheranostic Strategies. Cancer Biother Radiopharm. 2023; 38(4):246-255.

Gärtner, S.; Gunesch, A.; Knyazeva, T.; Wolf, P.; Högel, B.; Eiermann, W.; Ullrich, A.; Knyazev, P.; Ataseven, B. PTK 7 is a transforming gene and prognostic marker for breast cancer and nodal metastasis involvement. PLoS One. 2014; 9(1): e84472.

Gibbs, S.L. Near infrared fluorescence for image-guided surgery. Quant Imaging Med Surg. 2012; 2(3):177-87.

Globocan. Global Cancer Observatory World. Source: Globocan. Incidence, Mortality and Prevalence by cancer site. New cases. Deaths. 5-year prevalence (all ages). Cancer. 2020. https://gco.iarc.fr›data›900-world-fact-sheets

González, V.M.; Martín, M.E.; Fernández, G.; García-Sacristán, A. Use of Aptamers as Diagnostics Tools and Antiviral Agents for Human Viruses. Pharmaceuticals (Basel). 2016; 9(4):78.

Gorringe, K.L.; Boussioutas, A.; Bowtell, D.L.; Melbourne Gastric Cancer Group; Peter Mac Micro Array Facility. Novel regions of chromosomal amplifi cation at 6p21, 5p13, and 12q14 in gastric cancer identifi ed by array comparative genomic hybridization. Genes Chromosomes Cancer. 2005; 42(3):247–59.

Grassot, J.; Gouy, M.; Perrière, G.; Mouchiroud, G. Origin and molecular evolution of receptor tyrosine kinases with immunoglobulin-like domains. Mol Biol Evol., 2006; 23(6): 1232-1241.

Gryziewicz, L. Regulatory aspects of drug approval for macular degeneration. Adv Drug Deliv Rev. 2005; 57(14):2092-8.

Guo, H.; Shenoy, N.; Gershman, B.M.; Yang, J.; Sklar, L.A.; Miao, Y. Metastatic melanoma imaging with an (111) In-labeled lactam bridge-cyclized alpha-melanocyte-stimulating hormone peptide. Nucl Med Biol. 2009; 36(3):267-76.

Hanahan, D. Hallmarks of Cancer: New Dimensions. Cancer Discov. 2022; 12(1):31-46.

Hanahan, D.; Weinberg, R.A. Hallmarks of cancer: the next generation. Cell. 2011; 144(5):646-74.

Hartwell, L.; Mankoff, D.; Paulovich, A.; Ramsey, S.; Swisher, E. Cancer biomarkers: a systems approach. Nat Biotechnol. 2006; 24(8):905-8.

Haruta, K.; Otaki, N.; Nagamine, M.; Kayo, T.; Sasaki, A.; Hiramoto, S.; Takahashi, M.; Hota, K.; Sato, H.; Yamazaki, H. A Novel PEGylation Method for Improving the Pharmacokinetic Properties of Anti-Interleukin-17A RNA Aptamers. Nucleic Acid Ther. 2017; 27(1):36-44.

Heo, D.; Lee, E.; Ku, M.; Hwang, S.; Kim, B.; Park, Y.; Han Lee, Y.; Huh, Y-M.; Haam, S.; Cheong, J-H.; Yang, J.; Suh, J-S. Maleimidyl magnetic nanoplatform for facile molecular MRI. Nanotechnology. 2014; 25(27):275102.

Heravi, M.M.; Ghavidel, M.; Mohammadkhani. L. Beyond a solvent: triple roles of dimethylformamide in organic chemistry. RSC Adv. 2018; 8(49):27832-27862.

Hernández-Jiménez, M.; Abad-Santos, F.; Cotgreave, I.; Gallego, J.; Jilma, B.; Flores, A.; Jovin, T.G.; Vivancos, J.; Hernández-Pérez, M.; Molina, C.A.; Montaner, J.; Casariego, J.; Dalsgaard, M.; Liebeskind, D.S.; Cobo, E.; Castellanos, M.; Portela, P.C.; Masjuán, J.; Moniche, F.; Tembl, J.I.; Terceño, Izaga, M.; Arenillas, J.F.; Callejas, P.; Olivot, J-M.; Calviere, L.; Henon, H.; Mazighi, M.; Piñeiro, D.; Pugliese, M.; González, V.M.; Moro, M.A.; Garcia-Tornel, A.; Lizasoain, I.; Ribo, M. Safety and Efficacy of ApTOLL in Patients With Ischemic Stroke Undergoing Endovascular Treatment: A Phase 1/2 Randomized Clinical Trial. JAMA Neurol. 2023; e231660.

Hernández-Jiménez, M.; Abad-Santos, F.; Cotgreave, I.; Gallego, J.; Jilma, B.; Flores, A.; Jovin, T.G.; Vivancos, J.; Hernández-Pérez, M.; Molina, C.A.; Montaner, J.; Casariego, J.; Dalsgaard, M.; Liebeskind, D.S.; Cobo, E.; Castellanos, M.; Portela, P.C.; Masjuán, J.; Moniche, F.; Tembl, J.I.; Terceño, Izaga, M.; Arenillas, J.F.; Callejas, P.; Olivot, J-M.; Calviere, L.; Henon, H.; Mazighi, M.; Piñeiro, D.; Pugliese, M.; González, V.M.; Moro, M.A.; Garcia-Tornel, A.; Lizasoain, I.; Ribo, M. Safety and Efficacy of ApTOLL in Patients With Ischemic Stroke Undergoing Endovascular

Treatment: A Phase 1/2 Randomized Clinical Trial. JAMA Neurol. 2023; e231660.

Hilderbrand, S.A.; Weissleder, R. Near-infrared fluorescence: application to *in vivo* molecular imaging. Curr Opin Chem Biol. 2010; 14(1):71-9.

Hiwase, D.K.; Saunders, V.; Hewett, D.; Frede, A.; Zrim, S.; Dang, P.; Eadie, L.; To, L.B.; Melo, J.; Kumar, S.; Hughes, T.P.; White, D.L. Dasatinib cellular uptake and efflux in chronic myeloid leukemia cells: therapeutic implications. Clin Cancer Res. 2008; 14(12):3881-8.

Huang, F.; You, M.; Chen, T.; Zhu, G.; Liang, H.; Tan, W. Self-assembled hybrid nanoparticles for targeted co-delivery of two drugs into cancer cells. Chem Commun (Camb). 2014; 50(23):3103-5.

Huang, Y.F.; Shangguan, D.; Liu, H.; Phillips, J.A.; Zhang, X.; Chen, Y.; Tan, W. Molecular assembly of an aptamer-drug conjugate for targeted drug delivery to tumor cells. Chembiochem. 2009; 10(5):862-8.

Ireson, C.R.; Kelland, L.R. Discovery and development of anticancer aptamers. Mol Cancer Ther. 2006; 5(12):2957-62.

Islami, F.; Ward, E.M.; Sung, H.; Cronin, K.A.; Tangka, F.K.L.; Sherman, R.L.; Zhao, J.; Anderson, R.N.; Henley, S.J.; Yabroff, K.R.; Jemal, A.; Benard, V.B. Annual Report to the Nation on the Status of Cancer, Part 1: National Cancer Statistics. J Natl Cancer Inst. 2021; 113(12):1648-1669.

Jacobson, O.; Weiss, I.D.; Wang, L.; Wang, Z.; Yang, X.; Dewhurst, A.; Ma, Y.; Zhu, G.; Niu, G.; Kiesewetter, D.O.; Vasdev, N.; Liang, S.H.; Chen, X. 18F-Labeled Single-Stranded DNA Aptamer for PET Imaging of Protein Tyrosine Kinase-7 Expression. J Nucl Med. 2015; 56(11):1780-1785.

Jain, A.; Chakraborty, S.; Sarma, H.D.; Dash, A. A Systematic Comparative Evaluation of 68Ga-Labeled RGD Peptides Conjugated with Different Chelators. Nucl Med Mol Imaging. 2018; 52(2):125-134.

Jiang, G.; Zhang, M.; Yue, B.; Yang, M.; Carter, C.; Al-Quran, S.Z.; Li, B.; Li, Y. PTK7: a new biomarker for immunophenotypic characterization of maturing T cells and T cell acute lymphoblastic leukemia. Leuk Res. 2012; 36(11): 1347-1353.

Jin, J.; Ryu, H.S.; Lee, K.B.; Jang, J-J. High expression of protein tyrosine kinase 7 signifi cantly associates with invasiveness and poor prognosis in intrahepatic cholangiocarcinoma. PLoS One. 2014; 9(2): e90247.

Jung, J.W.; Ji, A.R.; Lee, J.; Kim, U.J.; Lee, S.T. Organization of the human PTK7 gene encoding a receptor protein tyrosine kinase-like molecule and alternative splicing of its mRNA. Biochim Biophys Acta. 2002; 1579(2–3):153–63.

Kang, L.; Rosenkrans, Z.T.; Cai, W. 64Cu-Labeled Aptamers for Tumor-Targeted Radionuclide Delivery. Methods Mol Biol. 2019; 1974:223.

Kaur, H. Recent developments in cell-SELEX technology for aptamer selection. Biochim Biophys Acta Gen Subj. 2018; 1862(10):2323-2329.

Khoshfetrat, S.M.; Mehrgardi, M.A. Amplified detection of leukemia cancer cells using an aptamer-conjugated gold-coated magnetic nanoparticles on a nitrogen-doped graphene modified electrode. Bioelectrochemistry. 2017; 114:24-32.

Kim, B.; Yang, J.; Hwang, M.; Choi, J.; Kim, H-O.; Jang, E.; Lee, J.H.; Ryu, S-H.; Suh, J-S.; Huh, Y-M.; Haam, S. Aptamer-modified magnetic nanoprobe for molecular MR imaging of VEGFR2 on angiogenic vasculature. Nanoscale Res Lett. 2013; 8(1):399.

Kim, D-H.; Seo, J-M.; Shin, K-J.; Yang S-G. Design and clinical developments of aptamer-drug conjugates for targeted cancer therapy. Biomater Res. 2021; 25(1):42.

Kim, M.; Kim, D-M.; Kim, K-S.; Jung, W.; Kim, D-E. Applications of Cancer Cell-Specific Aptamers in Targeted Delivery of Anticancer Therapeutic Agents. Molecules. 2018; 23(4):830.

Kinghorn, A.B.; Fraser, L.A.; Lang, S.; Shiu, S. C-C.; Tanner, J.A. Aptamer Bioinformatics. Int J Mol Sci. 2017; 18(12):2516.

Klein, C.A. Cancer progression and the invisible phase of metastatic colonization. Nat Rev Cancer. 2020; (11):681-694.

Korashy, H.M.; Rahman, A.F.M.M.; Kassem, M.G. Dasatinib. Profiles Drug Subst Excip Relat Methodol. 2014; 39:205-37.

Krebs, S.; Veach, D.R.; Carter, L.M.; Grkovski, M.; Fornier, M.; Mauro, M.J.; Voss, M.H.; Danila, D.C.; Burnazi, E.; Null, M.; Staton, K.; Pressl, C.; Beattie, B.J.; Zanzonico, P.; Weber, W.A.; Lyashchenko, S.K.; Lewis, J.S.; Larson, S.M.; Dunphy, M.P.S. First-in-Humans Trial of Dasatinib-Derivative Tracer for Tumor Kinase-Targeted PET. J Nucl Med. 2020; 61(11):1580-1587.

Kumar, V.; Singh, P.; Gupta, S.K.; Ali, V.; Verma, M. Transport and metabolism of tyrosine kinase inhibitors associated with chronic myeloid leukemia therapy: a review. Mol Cell Biochem. 2022 Apr;477(4):1261-1279.

Kurt, H.; Yüce, M.; Hussain, B.; Budak, H. Dual-excitation upconverting nanoparticle and quantum dot aptasensor for multiplexed food pathogen detection. Biosens Bioelectron. 2016; 81:280-286.

Lakhin, A.V.; Tarantul, V.Z.; Gening, L.V. Aptamers: problems, solutions and prospects. Acta Naturae. 2013; 5(4):34-43.

Lapraz, F.; Röttinger, E.; Duboc, V.; Range, R.; Duloquin, L.; Walton, K.; Wu, S.Y.; Bradham, C.; Loza, M.; Hibino, T.; Wilson, K.; Poustka, A.; McClay, D.; Angerer, L.; Gache, C.; Lepage, T. RTK and TGF-beta signaling pathways genes in the sea urchin genome. Dev. Biol., 2006; 300(1):132-52.

Lee, H.K.; Chauhan, S.K.; Kay, E.; Dana, R. Flt-1 regulates vascular endothelial cell migration via a protein tyrosine kinase-7-dependent pathway. Blood. 2011; 117(21):5762-71.

Lhoumeau, A.C.; Martinez, S.; Boher, J.M.; Monges, G.; Castellano, R.; Goubard, A.; Doremus, M.; Poizat, F.; Lelong, B.; Chaisemartin, C.; Bardin, F.; Viens, P.; Raoul, J.L.; Prebet, T.; Aurrand-Lions, M.; Borg, J.P.; Gonçalves, A. Overexpression of the Promigratory and Prometastatic PTK7 Receptor Is Associated with an Adverse Clinical Outcome in Colorectal Cancer. PLoS One. 2015; 10(5): e0123768.

Lhoumeau, A-C.; Borg, J-P. PTK7 (PTK7 protein tyrosine kinase 7) Atlas Genet Cytogenet Oncol Haematol. 2012. http://atlasgeneticsoncology.org/gene/41901/ptk7

Li, W.; Bing, T.; Wang, R.; Jin, S.; Shangguan, D.; Chen, H. Cell-SELEX-based selection of ssDNA aptamers for specifically targeting BRAF V600E-mutated melanoma. Analyst. 2021; 147(1):187-195.

Lichtig, H.; Cohen, Y.; Bin-Nun, N.; Golubkov, V.; Frank, D. PTK7 proteolytic fragment proteins function during early Xenopus development. Developmental Biology. 2019; 453(1), 48-55.

Lin, Y.; Zhang, L.H.; Wang, X.H.; Xing, X.F.; Cheng, X.J.; Dong, B.; Hu, Y.; Du, H.; Li, Y.A.; Zhu, Y.B.; Ding, N.; Du, Y.X.; Li, J.Y.; Ji, J.F. PTK7 as a novel marker for favorable gastric cancer patient survival. J Surg Oncol. 2012; 106(7):880-6.

Liu, H.; Zhang, Y.; Zhang, Z.; Deng, Z.; Bu, J.; Li, T.; Nie, J.; Qin, X.; Yang, Y.; Zhong, S. Self-assembly of DNA nanospheres with controllable size and self-degradable property for enhanced antitumor chemotherapy. Colloids Surf B Biointerfaces. 2023; 222:113122.

Liu, J.; Zhang, Y.; Liu, A.; Wang, J.; Li, L.; Chen, X.; Gao, X.; Xue, Y.; Zhang, X.; Liu, Y. Distinct Dasatinib-Induced Mechanisms of Apoptotic Response and Exosome Release in Imatinib-Resistant Human Chronic Myeloid Leukemia Cells. Int J Mol Sci. 2016; 17(4):531.

Liu, Q.; Zhang, C.; Yuan, J.; Fu, J.; Wu, M.; Su, J.; Wang, X.; Yuan, X.; Jiang, W. PTK7 regulates Id1 expression in CD44-high glioma cells. Neuro-Oncol. 2015; 17(4):505–15.

Liu, S. The role of coordination chemistry in the development of target-specific radiopharmaceuticals. Chem Soc Rev. 2004; 10;33(7):445-61.

Luo, Y.; Liao, F.; Lu, W.; Chang, G.; Sun, X. Coordination polymer nanobelts for nucleic acid detection. Nanotechnology. 2011; 22(19):195502.

Ma, H.; Gao, Z.; Yu, P.; Shen, S.; Liu, Y.; Xu, B. A dual functional fluorescent probe for glioma imaging mediated by blood-brain barrier penetration and glioma cell targeting. Biochem Biophys Res Commun. 2014; 449(1):44-8.

Massoud, T.F.; Gambhir, S.S. Molecular imaging in living subjects: seeing fundamental biological processes in a new light. Genes Dev. 2003; 17(5):545-80.

Mattsson, S.; Johansson, L.; Leide Svegborn, S.; Liniecki, J.; Noßke, D.; Riklund, K.Å.; Stabin, M.; Taylor, D.; Bolch, W.; Carlsson, S.; Eckerman, K.; Giussani, A.; Söderberg, L.; Valind, S.; ICRP. Radiation Dose to Patients from Radiopharmaceuticals: a Compendium of Current Information Related to Frequently Used Substances. Ann ICRP. 2015; 44(2 Suppl):7-321.

McCormack, P.L.; Keam, S.J. Dasatinib: a review of its use in the treatment of chronic myeloid leukaemia and Philadelphia chromosome-positive acute lymphoblastic leukaemia. Drugs. 2011; 71(13):1771-95.

McKeague, M.; Calzada, V.; Cerchia, L.; DeRosa, M.; Heemstra, J.M.; Janjic, N.; Johnson, P.E.; Kraus, L.; Limson, J.; Mayer, G.; Nilsen-Hamilton, M.; Porciani, D.; Sharma, T.K.; Suess, B.; Tanner, J.A.; Shigdar, S. The minimum aptamer publication standards (MAPS guidelines) for de novo aptamer selection. Aptamers. 2022; 6, 10-18.

Meng, L.; Sefah, K.; O'Donoghue, M.B.; Zhu, G.; Shangguan, D.; Noorali, A.; Chen, Y.; Zhou, L.; Tan, W. Silencing of PTK7 in colon cancer cells: caspase-10-dependent apoptosis via mitochondrial pathway. PLoS One. 2010; 5(11): e14018.

Miao, D.; Yu, Y.; Chen, Y.; Liu, Y.; Su, G. Facile Construction of i-Motif DNA-Conjugated Gold Nanostars as Near-Infrared and pH Dual-Responsive Targeted Drug Delivery Systems for Combined Cancer Therapy. Mol Pharm. 2020; 17(4):1127-1138.

Michor, F.; Iwasa, Y.; Nowak, M.A. Dynamics of cancer progression. Nat Rev Cancer. 2004; (3):197-205.

Mossie, K.; Jallal, B.; Alves, F.; Sures, I.; Plowman, G.D.; Ullrich, A. Colon carcinoma kinase-4 defi nes a new subclass of the receptor tyrosine kinase family. Oncogene. 1995; 11(10): 2179–84.

Murphy, J.M.; Zhang, Q.; Young, S.N.; Reese, M.L.; Bailey, F.P.; Eyers, P.A.; Ungureanu, D.; Hammaren, H.; Silvennoinen, O.; Varghese, L.N.; Chen, K.; Tripaydonis, A.; Jura, N.; Fukuda, K.; Qin, J.; Nimchuk, Z.; Mudgett, M.B.; Elowe, S.; Gee, C.L.; Liu, L.; Daly, R.J.; Manning, G.; Babon, J.J.; Lucet, I.S. A robust methodology to subclassify pseudokinases based on their nucleotide-binding properties. Biochem J. 2014; 457(2):323-34.

Musumeci, D.; Platella, C.; Riccardi, C.; Moccia, F.; Montesarchio, D. Fluorescence Sensing Using DNA Aptamers in Cancer Research and Clinical Diagnostics. Cancers (Basel). 2017; 9(12):174.

Ni, S.; Zhuo, Z.; Pan, Y.; Yu, Y.; Li, F.; Liu, J.; Wang, L.; Wu, X.; Li, D.; Wan, Y.; Zhang, L.; Yang, Z.; Zhang, B-T.; Lu, A.; Zhang, G. Recent Progress in Aptamer Discoveries and Modifications for Therapeutic Applications. ACS Appl Mater Interfaces. 2021; 13(8):9500-9519.

Ning, Y.; Hu, J.; Lu, F. Aptamers used for biosensors and targeted therapy. Biomed Pharmacother. 2020; 132:110902.

Odeh, F.; Nsairat, H.; Alshaer, W.; Ismail, M. A.; Esawi, E.; Qaqish, B.; Bawab, A. A.; Ismail, S. I. Aptamers Chemistry: Chemical Modifications and Conjugation Strategies. Molecules. 2020; 25(1), 3.

O'Hare, T.; Walters, D.K.; Stoffregen, E.P.; Taiping, J.; Manley, P.W.; Mestan, J.; Cowan-Jacob, S.W.; Lee, F.Y.; Heinrich, M.C.; Deininger, M.W.N.; Druker, B.J. *In vitro* activity of Bcr-Abl inhibitors AMN107 and BMS-354825 against clinically relevant imatinib-resistant Abl kinase domain mutants. Cancer Res. 2005; 65(11):4500-5.

Okoye, N.C.; Baumeister, J.E.; Khosroshahi, F.N.; Hennkens, H.M.; Jurisson, S.S. Chelators and metal complex stability for radiopharmaceutical applications. Radiochim Acta. 2019; 107, 1087-1121.

Ospina, J.D. Aptamers as a novel diagnostic and therapeutic tool and their potential use in parasitology. Biomedica. 2020; 40(1):148-165.

Othman, M.F.; Mitry, N.R.; Lewington, V.J.; Blower, P.J.; Terry, S.Y. Re-assessing gallium-67 as a therapeutic radionuclide. Nucl Med Biol. 2017; 46:12-18.

PDQ Cancer Genetics Editorial Board. Cancer Genetics Overview (PDQ®): Health Professional Version. 2023 Mar 16. In: PDQ Cancer Information Summaries [Internet]. Bethesda (MD): National Cancer Institute (US); 2002.

Peradziryi, H.; Tolwinski, N.S.; Borchers, A. The many roles of PTK7: a versatile regulator of cell-cell communication. Arch Biochem Biophys. 2012; 524: 71–76.

Pereira, R.L.; Nascimento, I.C.; Santos, A.P.; Ogusuku, I.E.Y.; Lameu, C.; Mayer, G.; Ulrich, H. Aptamers: novelty tools for cancer biology. Oncotarget. 2018; 9(42):26934-26953.

Pinheiro, P.S. Cancer Surveillance Opportunities to Meet Prevention and Control Challenges. J Natl Cancer Inst. 2021; 113(12):1604-1605.

Prebet, T.; Lhoumeau, A.C.; Arnoulet, C.; Aulas, A.; Marchetto, S.; Audebert, S.; Puppo, F.; Chabannon, C.; Sainty, D.; Santoni, M.J.; Sebbagh, M.; Summerour, V.; Huon, Y.; Shin, W.S.; Lee, S.T.; Esterni, B.; Vey, N.; Borg, J.P. The cell polarity PTK7 receptor acts as a modulator of the chemotherapeutic response in acute myeloid leukemia and impairs clinical outcome. Blood. 2010; 116(13): 2315-23.

Qi, J.; Zeng, Z.; Chen, Z.; Nipper, C.; Liu, X.; Wan, Q.; Chen, J.; Tung, C-H.; Zu, Y. Aptamer-Gemcitabine Conjugates with Enzymatically Cleavable Linker for Targeted Delivery and Intracellular Drug Release in Cancer Cells. Pharmaceuticals (Basel). 2022; 15(5):558.

Qi, J.; Zeng, Z.; Chen, Z.; Nipper, C.; Liu, X.; Wan, Q.; Chen, J.; Tung, C-H.; Zu, Y. Aptamer-Gemcitabine Conjugates with Enzymatically Cleavable Linker for Targeted Delivery and Intracellular Drug Release in Cancer Cells. Pharmaceuticals (Basel). 2022; 15(5):558.

Regad, T. Targeting RTK Signaling Pathways in Cancer. Cancers. 2015; 7(3), 1758-1784.

Reinemann, C.; Strehlitz, B. Aptamer-modified nanoparticles and their use in cancer diagnostics and treatment. Swiss Medical Weekly. 2014; 144:13908.

Reissig, D.; Clement, J.; Sänger, J.; Berndt, A.; Kosmehl, H.; Böhmer, F.D. Elevated activity and expression of Src-family kinases in human breast carcinoma tissue versus matched non-tumor tissue. J Cancer Res Clin Oncol. 2001;127(4):226-30.

Rowe, S.P.; Pomper, M.G. Molecular imaging in oncology: Current impact and future directions. CA Cancer J Clin. 2022; 72(4):333-352.

Saccomano, M.; Dullin, C.; Alves, F.; Napp, J. Preclinical evaluation of near-infrared (NIR) fluorescently labeled cetuximab as a potential tool for fluorescence-guided surgery. Int J Cancer. 2016; 139(10):2277-89.

Sanchez, C. N. Knowing and understanding the cancer cell: Physiopathology of cancer. Rev. Med. Clin. Condes. 2013; 24(4): 553-562.

Shangguan, D.; Cao, Z.; Meng, L.; Mallikaratchy, P.; Sefah, K.; Wang, H.; Li, Y.; Tan, W. Cell-Specific Aptamer Probes for Membrane Protein Elucidation in Cancer Cells. Journal of proteome research. 2008; 7(5), 2133-2139.

Shangguan, D.; Li, Y.; Tang, Z.; Cao, Z. C.; Chen, H. W.; Mallikaratchy, P.; Sefah, K.; Yang, C. J.; Tan, W. Aptamers evolved from live cells as effective molecular probes for cancer study. Proceedings of the National Academy of Sciences of the United States of America. 2006; 103(32), 11838-11843.

Shangguan, D.; Tang, Z.; Mallikaratchy, P.; Xiao, Z.; Tan, W. Optimization and Modifications of Aptamers Selected from Live Cancer Cell Lines. ChemBioChem. 2007; 8(6), 603-606.

Shetty, D.; Choi, S.Y.; Jeong, J.M.; Hoigebazar, L.; Lee, Y-S.; Lee, D.S.; Chung, J-K.; Lee, M.C.; Chung, Y.K. Formation and Characterization of Gallium (III) Complexes with Monoamide Derivatives of 1,4,7-Triazacyclononane-1,4,7-Triacetic Acid: A Study of the Dependency of Structure on Reaction pH. European Journal of Inorganic Chemistry. 2010; 5432-5438.

Shin, W-S.; Kwon, J.; Lee, H.W.; Kang, M.C.; Na, H-W.; Lee, S-T.; Park, J.H. Oncogenic role of protein tyrosine kinase 7 in esophageal squamous cell carcinoma. Cancer Sci. 2013; 104(8):1120–6.

Shin, W-S.; Maeng, Y.S.; Jung, J.W.; Min, J.K.; Kwon, Y.G.; Lee, S.T. Soluble PTK7 inhibits tube formation, migration, and invasion of endothelial cells and angiogenesis. Biochem. Biophys. Res. Commun. 2008; 371(4):793-8.

Sicco, E.; Almeida, L.; Moreno, M.; Calzada, V.; Cerecetto, H. Chemical conjugations of Sgc8-c with the lymphoma drug dasatinib to generate selective biotherapeutics. Aptamers. 2021b; 5, 15–21.

Sicco, E.; Baez, J.; Ibarra, M.; Fernández, M.; Cabral, P.; Moreno, M.; Cerecetto, H.; Calzada, V. Sgc8-c Aptamer as a Potential Theranostic Agent for Hemato-Oncological Malignancies. Cancer Biother Radiopharm. 2020; 35(4):262-270.

Sicco, E.; Báez, J.; Margenat, J.; García, F.; Ibarra, M.; Cabral, P.; Moreno, M.; Cerecetto, H.; Calzada, V. Derivatizations of Sgc8-c aptamer to prepare metallic radiopharmaceuticals as imaging diagnostic agents: Syntheses, isolations, and physicochemical characterizations. Chem Biol Drug Des. 2018; 91(3):747-755.

Sicco, E.; Mónaco, A.; Fernandez, M.; Moreno, M.; Calzada, V.; Cerecetto, H. Metastatic and non-metastatic melanoma imaging using Sgc8-c aptamer PTK7-recognizer. Sci Rep. 2021a; 11(1):19942.

Šimeček, J.; Schulz, M.; Notni, J.; Plutnar, J.; Kubíček, V.; Havlíčková, J.; Hermann, P. Complexation of metal ions with TRAP (1,4,7-triazacyclononane phosphinic acid) ligands and 1,4,7-triazacyclononane-1,4,7-triacetic acid: phosphinate-containing ligands as unique chelators for trivalent gallium. Inorg Chem. 2012; 51(1):577-90.

Simoneau, C-A. Treating Chronic Myeloid Leukemia: Improving Management through Understanding of the Patient Experience. Clin. J. Oncol. Nurs. 2013, 17, E13–E20.

Smith, J.D.; Cardwell, L.N.; Porciani, D.; Nguyen, J.A.; Zhang, R.; Gallazzi, F.; Tata, R.R.; Burke, D.H.; Daniels, M.A.; Ulery, B.D. Aptamer-displaying peptide amphiphile micelles as a cell-targeted delivery vehicle of peptide cargoes. Physical Biology. 2018; 15(6):065006.

Speransky, S.; Serafini, P.; Caroli, J.; Bicciato, S.; Lippman, M.E.; Bishopric, N.H. A novel RNA aptamer identifies plasma membrane ATP synthase beta subunit as an early marker and therapeutic target in aggressive cancer. Breast Cancer Res Treat. 2019; 176(2):271-289.

Sun, C.; Bernards, R. Feedback and redundancy in receptor tyrosine kinase signaling: relevance to cancer therapies. Trends Biochem Sci. 2014; 39(10): 465-474.

Sun, J.; Wang, X.; Tang, B.; Liu, H.; Zhang, M.; Wang, Y.; Ping, F.; Ding, J.; Shen, A.; Geng, M. A tightly controlled Src-YAP signaling axis determines therapeutic response to dasatinib in renal cell carcinoma. Theranostics. 2018; 8(12), 3256–3267.

Sung, H.; Ferlay, J.; Siegel, R.L.; Laversanne, M.; Soerjomataram, I.; Jemal, A.; Bray, F. Global Cancer Statistics 2020: GLOBOCAN Estimates of Incidence and Mortality Worldwide for 36 Cancers in 185 Countries. CA Cancer J Clin. 2021;71(3):209-249.

Taghdisi, S.M.; Abnous, K.; Mosaffa, F.; Behravan, J. Targeted delivery of daunorubicin to T-cell acute lymphoblastic leukemia by aptamer. J Drug Target. 2010; 18(4):277-81.

Talpaz, M.; Shah, N.P.; Kantarjian, H.; Donato, N.; Nicoll, J.; Paquette, R.; Cortes, J.; O'Brien, S.; Nicaise, C.; Bleickardt, E.; Blackwood-Chirchir, M.A.; Iyer, V.; Chen, T-T.; Huang, F.; Decillis, A.P.; Sawyers, C.L. Dasatinib in imatinib-resistant Philadelphia chromosome-positive leukemias. N Engl J Med. 2006; 354(24):2531-41.

Tan, J.; Yang, N.; Hu, Z.; Su, J.; Zhong, J.; Yang, Y.; Yu, Y.; Zhu, J.; Xue, D.; Huang, Y.; Lai, Z.; Huang, Y.; Lu, X.; Zhao, Y. Aptamer-Functionalized Fluorescent Silica Nanoparticles for Highly Sensitive Detection of Leukemia Cells. Nanoscale Res Lett. 2016; 11(1):298.

Thakur, M.; Lentle, B.C. Report of a summit on molecular imaging. Radiology. 2005; 236(3):753-5.

Tolmachev, V. Choice of Radionuclides and Radiolabelling Techniques. En: Targeted Radionuclide Tumor Therapy. Biological Aspects; 1st ed.; Stigbrand, T., Carlsson, J., Adams, G.P., Eds.; Springer: 2008; pp. 145-174.

Trinh, T.L.; Zhu, G.; Xiao, X.; Puszyk, W.; Sefah, K.; Wu, Q.; Tan, W.; Liu, C. A Synthetic Aptamer-Drug Adduct for Targeted Liver Cancer Therapy. PLoS One. 2015; 10(11):e0136673.

Tuerk, C.; Gold, L. Systematic evolution of ligands by exponential enrichment: RNA ligands to bacteriophage T4 DNA polymerase. Science. 1990. 249(4968):505-10.

Vaidya, T.; Kamta, J.; Chaar, M.; Ande, A.; Ait-Oudhia, S. Systems pharmacological analysis of mitochondrial cardiotoxicity induced by selected tyrosine kinase inhibitors. J Pharmacokinet Pharmacodyn. 2018; 45(3):401-418.

Valdovinos, H.F.; Hernandez, R.; Graves, S.; Ellison, P.A.; Barnhart, T.E.; Theuer, C.P.; Engle, J.W.; Cai, W.; Nickles, R.J. Cyclotron production and radiochemical separation of 55Co and 58mCo from 54Fe, 58Ni and 57Fe targets. Appl Radiat Isot. 2017; 130:90-101.

Weissleder, R. Molecular imaging in cancer. Science. 2006; 312(5777):1168-71.

Weissleder, R.; Mahmood, U. Molecular imaging. Radiology. 2001; 219(2):316-33.

Williams, L.E.; DeNardo, G.L.; Meredith, R.F. Targeted radionuclide therapy. Med Phys. 2008; 35(7):3062-8.

Woo, S-K.; Jang, S.J.; Seo, M-J.; Park, J.H.; Kim, B.S.; Kim, E.J.; Lee, Y.J.; Lee, T.S.; An, G.I.; Song, I.H.; Seo, Y.; Kim, K.I.; Kang, J.H. Development of ^{64}Cu-NOTA-Trastuzumab for HER2 Targeting: A Radiopharmaceutical with Improved Pharmacokinetics for Human Studies. J Nucl Med. 2019; 60(1):26-33.

Wu, X.; Zhao, Z.; Bai, H.; Fu, T.; Yang, C.; Hu, X.; Liu, Q.; Champanhac, C.; Teng, I-T.; Ye, M.; Tan, W. DNA Aptamer Selected against Pancreatic Ductal Adenocarcinoma for *in vivo* Imaging and Clinical Tissue Recognition. Theranostics. 2015; 5(9):985-94.

Xia, L.; Yang, Y.; Yang, H.; Tang, Y.; Zhou, J.; Wu, Y. Screening and identification of an aptamer as novel recognition molecule in the test strip and its application for visual detection of ethyl carbamate in liquor. Anal Chim Acta. 2022; 1226:340289.

Xiao, Z.; Shangguan, D.; Cao, Z.; Fang, X.; Tan, W. Cell-specific internalization study of an aptamer from whole cell selection. Chemistry. 2008; 14(6):1769-75.

Xu, B.; Washington, A.M.; Domeniconi, R.F.; Ferreira Souza, A.C.; Lu, X.; Sutherland, A.; Hinton, B.T. Protein tyrosine kinase 7 is essential for tubular morphogenesis of the Wolffian duct. Dev Biol. 2016; 412(2): 219-33.

Xue, T.; Luo, P.; Zhu, H.; Zhao, Y.; Wu, H.; Gai, R.; Wu, Y.; Yang, B.; Yang, X.; He, Q. Oxidative stress is involved in Dasatinib-induced apoptosis in rat primary hepatocytes. Toxicol Appl Pharmacol. 2012; 261(3):280-91.

Yang, T.; Wan, Z.; Liu, Z.; Li, H.; Wang, H.; Lu, N.; Chen, Z.; Mei, X.; Ren, X. In situ mineralization of anticancer drug into calcium carbonate monodisperse nanospheres and their pH-responsive release property. Mater Sci Eng C Mater Biol Appl. 2016; 63:384-92.

Yang, Y.; Zhao, W.; Tan, W.; Lai, Z.; Fang, D.; Jiang, L.; Zuo, C.; Yang, N.; Lai, Y. An Efficient Cell-Targeting Drug Delivery System Based on Aptamer-Modified Mesoporous Silica Nanoparticles. Nanoscale Res Lett. 2019; 14(1):390.

Yildizhan, H.; Uslu, B.; Ozkan, S.A. Chapter 1 e treatment strategies in cancer from past to present, in: A.M. Grumezescu (Ed.), Drug Targeting and Stimuli Sensitive Drug Delivery Systems, William Andrew Publishing, Norwich, United States. 2018; pp. 1e37.

Yu, L.X.; Akseli, I.; Allen, B.; Amidon, G.; Bizjak, T.G.; Boam, A.; Caulk, M.; Doleski, D.; Famulare, J.; Fisher, A.C.; Furness, S.; Hasselbalch, B.; Havel, H.; Hoag, S.W.; Iser, R.; Johnson, B.D.; Ju, R.; Katz, P.; Lacana, E.; Lee, S.L.; Lostritto, R.; McNally, G.; Mehta, M.; Mohan, G.; Nasr, M.; Nosal, R.; Oates, M.; O'Connor, T.; Polli, J.; Raju, G.K.; Ramanadham, M.; Randazzo, G.; Rosencrance, S.; Schwendeman, A.; Selen, A.; Seo, P.; Shah, V.; Sood, R.; Thien, M.P.; Tong, T.; Trout, B.L.; Tyner, K.; Vaithiyalingam, S.; VanTrieste, M.; Walsh, F.; Wesdyk, R.; Woodcock, J.; Wu, G.; Wu, L.; Yu, L.; Zezza, D. Advancing Product Quality: a Summary of the Second FDA/PQRI Conference. AAPS J. 2016; 18(2):528-43.

Yu, M.K.; Kim, D.; Lee, I-H.; So, J-S.; Jeong, Y.Y.; Jon, S. Image-guided prostate cancer therapy using aptamer-functionalized thermally cross-linked superparamagnetic iron oxide nanoparticles. Small. 2011; 7(15):2241-9.

Yu, R.; Zhang, Y.; Xu, Z.; Wang, J.; Chen, B.; Jin, H. Potential antitumor effects of panaxatriol against DU-15 human prostate cancer cells is mediated via mitochondrial mediated apoptosis, inhibition of cell migration and sub-G1 cell cycle arrest. J BUON. 2018; 23(1):200-204.

Zeng, Z.; Parekh, P.; Li, Z.; Shi, Z-Z.; Tung, C-H.; Zu, Y. Specific and sensitive tumor imaging using biostable oligonucleotide aptamer probes. Theranostics. 2014; 4(9):945-52.

Zeng, Z.; Qi, J.; Wan, Q.; Zu, Y. Aptamers with Self-Loading Drug Payload and pH-Controlled Drug Release for Targeted Chemotherapy. Pharmaceutics. 2021; 13(8):1221.

Zhang, C.; Lin, K.S.; Bénard, F. Molecular Imaging and Radionuclide Therapy of Melanoma Targeting the Melanocortin 1 Receptor. Mol Imaging. 2017; 16:1536012117737919.

Zhang, H.; Wang, A.; Qi, S.; Cheng, S.; Yao, B.; Xu, Y. Protein tyrosine kinase 7 (PTK7) as a predictor of lymph node metastases and a novel prognostic biomarker in patients with prostate cancer. Int J Mol Sci. 2014; 15(7):11665–77.

Zhang, K.; Li, Y.; Liu, J.; Yang, X.; Xu, Y.; Shi, J.; Liu, W.; Li, J. Y-shaped circular aptamer DNAzyme conjugates for highly efficient in vivo gene silencing. CCS Chem. 2020; 2:631–641.

Zhang, Y.; Lai, B.S.; Juhas, M. Recent Advances in Aptamer Discovery and Applications. Molecules. 2019; 24(5):941.

Zhao, J.; Chen, J.; Ma, S.; Liu, Q.; Huang, L.; Chen, X.; Lou, K.; Wang, W. Recent developments in multimodality fluorescence imaging probes. Acta Pharmaceutica Sinica B. 2018; 8(3), 320–338.

Zhu, G.; Chen, X. Aptamer-based targeted therapy. Adv Drug Deliv Rev. 2018; 134:65-78.

Zhu, G.; Zheng, J.; Song, E.; Donovan, M.; Zhang, K.; Liu, C.; Tan, W. Self-assembled, aptamer-tethered DNA nanotrains for targeted transport of molecular drugs in cancer theranostics. Proc Natl Acad Sci U S A. 2013; 110(20):7998-8003.

Zong, S.; Wang, L.; Yang, Z.; Wang, H.; Wang, Z.; Cui, Y. Black Phosphorus-Based Drug Nanocarrier for Targeted and Synergetic Chemophotothermal Therapy of Acute Lymphoblastic Leukemia. ACS Appl Mater Interfaces. 2019; 11(6):5896-5902.

10. Anexo

10.1. Presentaciones en congresos y artículos publicados en el marco de este posgrado.

Presentaciones en congresos:

- Presentación **formato poster** en el 8th Brazilian Symposium on Medicinal Chemistry. Búzios, Rio de Janeiro, Brasil. 2016. "Sgc8-c-aptamer derivatives as molecular imaging agents: Optimization of preparation conditions". Estefanía Sicco, Jessica Báez, Jimena Margenat, Fernanda García, Manuel Ibarra, Pablo Cabral, María Moreno, Hugo Cerecetto, Victoria Calzada.

- Presentación **formato poster** en el 4th International INSOAP symposium on Aptamers. Oxford, UK. 2017. "Syntheses optimizations of Sgc8-c aptamer as multimodal imaging probes for cancer". Estefanía Sicco, Jessica Báez, Jimena Margenat, Fernanda García, Manuel Ibarra, Pablo Cabral, María Moreno, Hugo Cerecetto, Victoria Calzada.

- Presentación **formato oral** en el I Congreso Nacional de Biociencias. Montevideo, Uruguay. 2017. "Imagenología molecular en cáncer usando como agente el aptámero Sgc8-c". Estefanía Sicco, Jessica Báez, Marcelo Fernández, Juan Pablo Gambini, María Moreno, Victoria Calzada, Hugo Cerecetto.

- Presentación **formato oral** en el II Congreso Nacional de Biociencias. Montevideo, Uruguay. 2019. "Generación de un biofármaco basado en el aptámero Sgc8-c: Potencial agente terapéutico en cáncer". Estefanía Sicco, María Moreno, Victoria Calzada, Hugo Cerecetto.

- Presentación **formato oral** en el Segundo Encuentro Bienal de la Sociedad de Bioquímica y Melecular. Montevideo, 2020. "Potencial agente terapéutico en cáncer desarrollado en base al aptámero Sgc8-c". Estefanía Sicco, María Moreno, Victoria Calzada, Hugo Cerecetto. **Esta exposición recibió el primer premio a mejor presentación oral.**

- Presentación **formato oral** en el I Encuentro Red Iberoamericana de Aptámeros, virtual. 2021. "Desarrollo de un potencial agente terapéutico en cáncer basado en el aptámero Sgc8-c". Estefanía Sicco, María Moreno, Victoria Calzada, Hugo Cerecetto.

Artículos publicados:

- Sicco, E., Báez, J., Margenat, J., García, F., Ibarra, M., Cabral, P., Moreno, M., Cerecetto, H., & Calzada, V. (2018). Derivatizations of Sgc8-c aptamer to prepare metallic radiopharmaceuticals as imaging diagnostic agents: Syntheses, isolations, and physicochemical characterizations. Chemical biology & drug design, 91(3), 747–755. https://doi.org/10.1111/cbdd.13135

- Sicco, E., Baez, J., Ibarra, M., Fernández, M., Cabral, P., Moreno, M., Cerecetto, H., & Calzada, V. (2020). Sgc8-c Aptamer as a Potential Theranostic Agent for Hemato-Oncological Malignancies. Cancer biotherapy & radiopharmaceuticals, 35(4), 262–270. https://doi.org/10.1089/cbr.2019.3402. **<u>Los resultados publicados en este artículo fueron destacados en una carta al editor (Filippi, 2020).</u>**

- Sicco, E., Mónaco, A., Fernandez, M., Moreno, M., Calzada, V., & Cerecetto, H. (2021). Metastatic and non-metastatic melanoma imaging using Sgc8-c aptamer PTK7-recognizer. Scientific reports, 11(1), 19942. https://doi.org/10.1038/s41598-021-98828-6

- Sicco, E.; Almeida, L.; Moreno, M.; Calzada, V.; Cerecetto, H. Chemical conjugations of Sgc8-c with the lymphoma drug dasatinib to generate selective biotherapeutics. Aptamers 2021, 5, 15–21.

- Sicco, E.; Cerecetto, H.; Calzada, V.; Moreno, M. Targeted-Lymphoma Drug Delivery System Based on the Sgc8-c Aptamer. Cancers 2023, 15, 922. https://doi.org/10.3390/cancers15030922

- Calzada, V.; Báez, J.; Sicco, E.; Margenat, J.; Fernández, M.; Moreno, M.; Ibarra, M.; Quinn, T.; Gambini, J.P.; Cabral, P.; Cerecetto, H. (2017). Preliminary *In Vivo* Characterization of a Theranostic Aptamer: Sgc8-c-DOTA-[67]Ga. Aptamers. 1, 19-27.

10.2. Financiación y becas de posgrado

La financiación necesaria para la realización de este posgrado, se obtuvo de los siguientes programas y proyectos:

11. Agradecimientos

A mis coach y gente adorada de crossfit, principalmente por ayudar a despejar mi mente en los momentos más difíciles.

A mis amigas y amigos del alma, "Juntadera.com, Cobras, Amiguis, Feliz cumple, Puerquilandia, El mejor drupo y Team ansiedad (Mex-Uru)", por su cariño, sus charlas y palabras de aliento.

A mi familia, muy especialmente a mi Madre, Hermana y Hermanos, que me acompañaron todo este tiempo y brindaron su apoyo, hasta cebando mates.

A mis gatitas, por su peludito amor tan incondicional.

A mi ahijadita, por brindarme siempre su ternura y amor.

¡Muchísimas gracias!